DUAL-VIEW CATADIOPTRIC IMAGING SYSTEM DESIGN FOR ENDOSCOPY

DUAL-VIEW CATADIOPTRIC IMAGING SYSTEM DESIGN FOR ENDOSCOPY

By

ROY CHIH CHUNG WANG, B. ENG.

A Thesis

Submitted to the School of Graduate Studies

in Partial Fulfilment of the Requirements

for the Degree

Master of Applied Science

McMaster University

MASTER OF APPLIED SCIENCE (2010) McMaster University
(Engineering Physics) Hamilton, Ontario

TITLE: Dual-View Catadioptric Imaging System Design for Endoscopy

AUTHOR: Roy Chih Chung Wang, B. Eng.
(McMaster University)

SUPERVISOR: Professor Qiyin Fang

CO-SUPERVISOR: Professor M. Jamal Deen

NUMBER OF PAGES: xviii, 162

Abstract

Fluorescence endoscopy is a promising functional imaging technique to improve screening of early cancer lesions in the gastrointestinal (GI) tract. The intensity of tissue autofluorescence is weak and conventional forward viewing endoscopes are inefficient in light collection from objects of interest located on the GI tract wall. This thesis work presents the design and optimization of a catadioptric endoscope objective lens that is capable of acquiring simultaneous forward and radial views. The radial view optics is optimized for a balance between image quality and light collection by utilizing a pair of folded parabolic mirrors for redirecting the field of view and lenses for aberration control. The modulation transfer function, numerical aperture, track length, and field of view are parameters used in the optimization. Non-sequential ray tracing simulations of the light collection of various field locations along a cylindrical surface that simulates the GI tract suggest that the proposed design is more practical in light collection when compared to typical wide-angle, forward-viewing endoscope objectives. A prototype with additional optimization in an enlarged 3:1 scale design is manufactured by the Instrument Technology Research Center of the National Applied Research Laboratories (Hsinchu, Taiwan, Republic of China). Empirical verification of the modulation transfer function as well as relative light collection across the field of view is performed on the manufactured prototype. View synthesis digital image processing algorithms are proposed and tested using imagery acquired by the manufactured prototype.

Acknowledgments

My experience as a graduate student at McMaster University has been an exciting and fruitful one. I express sincere gratitude to Professor Qiyin Fang, who has provided me with the opportunity, resources, and guidance to make this research possible. Many of the lessons patiently taught by Professor Fang have helped me develop my research abilities and as well as other skills valuable to becoming a true engineering professional. I greatly appreciate the helpful suggestions Professor Jamal Deen has offered me throughout my research. I am indebted to Professor Joseph Hayward for the many advices he has given me as well as the insightful discussions we shared. I am thankful to Professor Chang-Qing Xu for reviewing my thesis and for being on my committee.

I am grateful to the Instrument Technology Research Center (ITRC) of the National Applied Research Laboratories (Hsinchu, Taiwan, Republic of China) in providing an academic discount on the manufacturing of the prototype used in this research. I would like to thank Dr. Donyau Chiang, Mr. Cheng-Fong Ho, and Mr. Zong-Ru Yu for their technical input that aided me in the revision of the prototype design for feasible manufacturing.

I would like to thank Mr. Jin Ng and Mr. Gord Harris for sharing their wealth of optical industry experience. I would also like to thank my brother, Mr. Louis Chih-Yoa Wang, for being a very supportive and good brother. I wish him well in his future endeavors. Lastly, I would like to extend my gratitude to my parents, Mr. Wen-Yun Wang and Ms. Su-Fang Wang-Hu, for the guidance, support, and love they have shown me.

Abstract iii

Acknowledgements iv

Table of Contents v

List of Figures ix

List of Tables xv

List of Acronyms and Abbreviations xvii

Chapter 1. Introduction 1

1.1 Motivation 1
1.2 Existing Endoscope Designs 3
1.3 Proposed Approach 7
1.4 Thesis Organization 8
1.5 References 9

Chapter 2. Background 11

2.1 Optical Design 11
2.1.1 Chief Rays 12
2.1.2 F-number and Numerical Aperture 13
2.1.3 Entrance Pupil 14
2.1.4 Light Collection vs. Optical Throughput 15
2.1.5 Aberration vs. Light Collection 16
2.1.6 Necessary Workarounds to Assumptions 16
2.2 Lens Design Background 17
2.2.1 Petzval Curvature 18
2.2.2 Lateral Chromatic Aberration 19
2.2.3 Coma Aberration 20
2.2.4 Evaluation Methods 20
2.2.5 Relevant Lens Forms 22
2.3 Image Understanding 23
2.3.1 Projections: Perspective vs. Orthographic 23
2.3.2 Mosaic Panoramic Generation 24
2.3.3 Functional Overview of Perspective Projection 25
2.3.4 Catadioptric Imaging System Design 25
2.4 References 26

Chapter 3. 1:1 Scale Endoscope Objective Simulation Design 29

3.1 Problem Definition 29
3.2 Design Specification 30
3.3 Approach 32

3.3.1 Mirror Template Selection 32
3.3.2. Finalization of the Mirror Form 39
3.3.3 Sequential Ray Trace: Catadioptric Simulation 42
3.3.4 Radial View Design Refinement 43
3.3.5. Forward View Lens Design 46
3.4. Sequential Ray Trace Simulation Results 47
3.5 Radiometry Simulation Method & Simulation Results 52
3.6. Discussion & Conclusion 56
3.7 References 58

Chapter 4. Prototype Development 59

4.1 Prototype Design Specification 60
4.2 Prototype Design 61
4.2.1. Design Modification 63
4.2.2. Sequential Ray Trace Simulation Results 65
4.2.3. Tolerance Simulations 65
4.3 Test Chart Measurements 72
4.3.1 Setup 73
4.3.2 Results 77
4.3.3 Discussion 80
4.4 Radiometry: Simulations & Measurements 87
4.5 Reference 89

Chapter 5. View Synthesis Algorithms 91

5.1 Perspective View Synthesis Algorithm 92
5.1.1 Pre-process 95
5.1.2 Viewpoint Calculation 95
5.1.3 Perspective View Coordinates Generation 97
5.1.4 Object Sample Coordinates Generation 98
5.1.5 Object-Image Mapping 99
5.1.6 Results 99
5.2 Estimated Orthographic View Synthesis 101
5.2.1 Algorithm Approach 101
5.2.2 Results 103
5.3 Discussion 104
5.4 References 104

Chapter 6. Conclusion 105

6.1 References 108

Appendix A. Chief Raytrace MATLAB™ Code 109

A.1 main.m 109

A.2 engine.m 111
A.3 getEllipse.m 115
A.4 getHyperbola.m 115
A.5 getCone.m 116
A.6 getSphere2.m 117
A.7 EulerR.m 117
A.8 PlanarR.m 118

Appendix B. Tolerance Simulation Summary 119

B1. Forward View, Averaged Diffractive MTF at 35 lp/mm 119
B2. Forward View, Averaged Diffractive MTF at 70 lp/mm 120
B3. Radial View, Averaged Diffractive MTF at 30 lp/mm 122
B4. Forward View, Averaged Diffractive MTF at 60 lp/mm 123

Appendix C. Custom Test Patterns for Radial View MTF Tests 125

Appendix D. Acquired Images for Forward View MTF Tests 133

Appendix E. Acquired Images for Radial View MTF Tests 139

Appendix F. Acquired Images for Radiometry Test 151

Appendix G. View Synthesis MATLAB™ Code 153

G.1 Perspective View Synthesis Algorithm 153
G.2 Estimated Orthographic View Synthesis Algorithm 159

List of Figures

Figure 1.1. Anatomy of (a) common forward-viewing endoscope tip (b) forward-viewing endoscope with fibre optics (c) capsule endoscope. 3

Figure 1.2. Endoscope objective raytrace layout simulated from reference designs (units: mm) (a) Ref. [9] (b) Ref. [10] (c) Ref. [11] (d) Ref. [12] (e) Ref. [13] (f) Ref. [14]. 5

Figure 1.3. Typical endoscope optical system design: (a) Field of view (FOV) of a typical wide-angle endoscope objective. (b) FOV of a radial view endoscope. 6

Figure 1.4. Initial concept diagram for the radial and forward viewing endoscope objective design used for this thesis work. The light emitting diodes (LEDs) near the mirror provide illumination for the forward field of view (FOV). The LEDs near the CCD provide illumination for the radial FOV. Lens R represents the lens group used to focus the objects from the radial view to the CCD. Lens F represents the additional lens group required to bring the forward view in focus with the CCD. 8

Figure 2.1. Ray trace of a Cooke Triplet lens. The object is located to the far left and not shown. 15

Figure 2.2. Coordinate system setup for aberration equations. 18

Figure 2.3. Demonstration of field curvature with a single lens. The dotted red curve outlines the field curvature. 19

Figure 2.4. Demonstration of coma aberration with a single lens. This aberration is significant when the field angle is large. (a) is a zoomed out version of (b). 20

Figure 2.5. Sample telecentric implementation modified from Ref. [10]. The object is to the far left and not shown. The FOV is determined by the size of the clear aperture of the system. 24

Figure 2.6. Functional representation of a perspective lens using (a) pinhole camera (b) perspective projection. 25

Figure 3.1. Design flow chart. 32

Figure 3.2. This plot visualizes the estimated FOV of the single cone reflector concept imaging system by tracing only the chief ray. The parameters are $(k,c) = (4.33,0)$ and this system is a non-SVP constrained imaging system. The camera distance to mirror focus is 9.67 mm. 35

Figure 3.3. This plot visualizes the estimated FOV of the single spherical reflector concept imaging system by tracing only the chief ray. The blue points are locations where the chief ray would intersect the mirror; the green points are locations where the chief rays would intersect the GI tract wall, which is assumed to be cylindrical. The parameters are $(k,c) =$

(50,0) and this system is a non-SVP constrained imaging system. The camera distance to mirror focus is 18 mm. The FOV range at high z values would practically be obstructed by the camera optics... 36
Figure 3.4. This plot visualizes the estimated FOV of the single ellipsoidal reflector concept imaging system by tracing only the chief ray. The parameters are (k,c) = (100,15) and this system is a SVP constrained imaging system. The camera distance to mirror focus is 15 mm. The FOV range at high z values would practically be obstructed by the camera optics. 37
Figure 3.5. This plot visualizes the estimated FOV of the single hyperbolic reflector concept imaging system by tracing only the chief ray. The parameters are (k,c) = (7.33,9.67) and this system is a SVP constrained imaging system. The camera distance to mirror focus is 9.67 mm. 38
Figure 3.6. OSLO simulation results from a hyperbolic mirror with a magnifier lens, the numerical aperture is extremely small and the system has high aberration. (a) Ray trace layout of the simulation. The distance scale units are in millimeters. (b) MTF score, where T is the tangential direction, and S is the sagittal direction. 39
Figure 3.7. Early simulation attempts of a folded elliptical mirror system (units: mm)....40
Figure 3.8. Ray tracing with the aperture stop located at the focus of the convex mirror (units: mm) (a) convex hyperbolic and concave ellipsoidal mirrors (b) parabolic mirrors. 41
Figure 3.9. Ray trace layout diagrams of two proposed radial view optical designs with (a) FOV range near the concave mirror (b) FOV range near the convex mirror. The shaded mirror regions would be hollowed so light from the forward view could pass. For practical lens edge thickness handling during fabrication, the clear aperture of the last doublet in (b) may need to be smaller than specified here. The scale for (a) and (b) as shown here are different. Both (a) and (b) use a similar coordinate system as shown at the bottom of the figure. 44
Figure 3.10. Spot diagram at the image surface with at field point positions sampled across the field of view (a) spot diagram for the system shown in fig. 3.9(a), units in microns (b) spot diagram for the system shown in fig. 3.9(b), units in millimeters. Note the difference in the shape and chromatic aberration between (a) and (b). The black circle is the simulated Airy disc radius. The colours correspond to the wavelength legend at the bottom of the figure.. 45
Figure 3.11. Ray trace layout diagram for the forward view optical design. The radial view lens groups marked in the orange box are the same lenses used in radial view design in fig. 3.9(a). The four elements from the left are unique to the forward view optical design. They provide the necessary degrees of freedom to match the back focus to the image plane.. 47

Figure 3.12. Simulated MTF for (a) forward view and (b) radial view. *T* is tangential MTF curve at the specified field point. *S* is sagittal MTF curve at the specified field point. Field points are specified in terms of field angle (measured in *DEG*, degrees). *DIFF. LIMIT* is the theoretical diffraction-limited MTF curve. The *MODULUS OF THE OTF* is another technical name for the MTF. 50
Figure 3.13. Image surface spot diagram for (a) forward view and (b) radial view. The black circle is the simulated Airy disc radius. The colours correspond to the wavelength legend at the top right of this figure; all units in microns. *RMS radius* is the RMS spot size, *GEO radius* is the distance from the centroid to the furthest ray intersection with the imaging surface. *IMA* describe the location of the centroid on the imaging surface. *OBJ* describe the location of the field points in terms of field angles. The forward view optics has smaller spot sizes than the radial view optics. 51
Figure 3.14. Radiometry simulation setup for radial view optical design. The simulated point source is located at the field position of 6.9 mm from global axis in the negative *z* direction in this figure. Other field positions in table 3.7 are sampled from the region shade in gray, which represents the radial view FOV. The PMMA tube emulates the sidewall of the endoscope..... 52
Figure 3.15. Radiometry simulation setup for the design in Ref. [3]. The field points are measured in the negative *z* direction from the surface of the first lens 53
Figure 3.16. Irradiance plot of the imaging plane of the setup in fig. 3.15..... 53
Figure 3.17. The spot diagram plot of the 50% scaled proposed design. The Airy disc is indicated by the black circle. Its size and the total spot size are similar 55
Figure 3.18. 3D bar chart of the data in table 3.8. 56
Figure 4.1. Photographs of the finished prototype imaging system. The white arrows point to the (a) convex mirror (b) concave mirror. 60
Figure 4.2. Radial view layout of prototype. 62
Figure 4.3. Forward view layout of prototype. 62
Figure 4.4. Simulated MTF for (a) forward view and (b) radial view. *T* is tangential MTF curve at the specified field point. *S* is sagittal MTF curve at the specified field point. Field points are specified in terms of field angle (measured in *DEG*, degrees). *DIFF. LIMIT* is the theoretical diffraction-limited MTF curve. The *MODULUS OF THE OTF* is another technical name for the MTF. 66
Figure 4.5. Image surface spot diagram for (a) forward view and (b) sidewall view. The black circle is the simulated Airy disc radius. The colours correspond to the wavelength legend at the top right of this figure; all units in microns. *RMS radius* is the RMS spot size, *GEO radius* is the distance from the centroid to the furthest ray intersection with the imaging surface. *IMA* describe the location

of the centroid on the imaging surface. *OBJ* describe the location of the field points in terms of field angles. The forward view optics has smaller spot sizes than the radial view optics. 67
Figure 4.6. Photograph of USAF1951 target. 72
Figure 4.7. Setup blueprint for (a) forward view (b) radial view without the illumination. 74
Figure 4.8. Setup photograph for radial view illumination. 75
Figure 4.9. The generation of (a) sagittal (b) tangential MTF test patterns from rolling custom printed single spatial frequency test patterns on paper. 76
Figure 4.10. Gray level information on group 2 element 4 of the USAF 1951 test chart used for the forward view MTF test (a) is resized at 600% zoom to illustrate the red box, which is the region of interest used in computation of the histogram in (b). The dark and bright gray level peaks are taken to be 41 and 174 out of 0 ~ 255 possible levels of gray. 76
Figure 4.11. Gray level information on group 2 element 4 of the USAF 1951 test chart used for the forward view test (a) is resized at 75% zoom to illustrate the yellow box, which is the region of interest used (b) histogram for the sagittal test pattern at 4 lp/mm. The dark and bright gray level peaks are taken to be 39 and 146 out of 0 ~ 255 possible levels of gray. 77
Figure 4.12. Acquired image of the forward view. 78
Figure 4.13. Acquired image of the radial view sagittal test pattern at 2 lp/mm object spatial frequency. 78
Figure 4.14. The magenta outline is similar to the oval selection tool used in ImageJ to generate the mask image. 82
Figure 4.15. Tangential MTF comparison of forward view optics. 83
Figure 4.16. Sagittal MTF comparison of forward view optics. 84
Figure 4.17. Tangential MTF comparison of radial view optics 85
Figure 4.18. Sagittal MTF comparison of radial view optics. 85
Figure 4.19. Radiometry simulation setup for radial view optical design. The simulated point source is located at the field position of 32 mm from global axis in the negative z direction in this figure. Other field positions in table 4.16 are sampled from the region shade in gray, which represents the radial view FOV. The PMMA tube emulates the sidewall of the endoscope. 87
Figure 4.20. Acquired images resized at 50% zoom for field position 18 mm. (a) mask image (b) measurement image. The mean gray level intensity in the measurement image is 88.11 over the region of

interest in defined by the mask image. The dynamic range of the image is 0 ~ 255 discrete levels of gray.....88
Figure 4.21. Acquired images resized at 50% zoom for field position 18 mm. (a) mask image (b) measurement image. The mean gray level intensity in the measurement image is 88.11 over the region of interest in defined by the mask image. 89
Figure 5.1. Perspective view synthesis algorithm flow chart.....92
Figure 5.2. The raytrace database would store the relationship between field positions and their corresponding image positions. Object points with the same colour would map to the same coloured image point. The points on the image are uniformly sampled. 93
Figure 5.3. The object at a fixed depth forms a cylinder around the imaging system. 94
Figure 5.4. The possible outcome of the viewpoint calculation step (a) all objects points across depth with the same corresponding image point form a line of sight that would intersect the optical axis at a location shared by other lines of sight formed by other object points; this is the effective viewpoint (b) a more general case where object points across depth with the same corresponding image point do not form a straight line, and the objects may be better described using curves.....96
Figure 5.5. Viewpoint location and their corresponding image positions using only raytrace simulation data.....97
Figure 5.6. View plane and sample plane in object space. The view coordinates define the view plane, which could be used with the effective viewpoint to define the region of the world the resultant perspective image would sample from. 98
Figure 5.7. Calculated sample points in object space. 99
Figure 5.8. (a) mask image (b) acquired image with McMaster business card (c) synthesized perspective image (d) acquired image with 0.5 lp/mm test pattern (e) synthesized perspective image. 100
Figure 5.9. Estimated orthographic projection vs. perspective projection. (a) perspective projection with the same viewpoint as the optical system (b) orthographic projection where the viewpoint is located at infinity.....102
Figure 5.10. Estimated orthographic view synthesis algorithm flow chart.....102
Figure 5.11. (a) mask image (b) acquired image with 0.5 lp/mm test pattern (c) synthesized estimated orthographic image (d) acquired image with McMaster business card (e) synthesized estimated orthographic image. 103

List of Tables

Table 1.1. Year 2002 world-wide cancer incidence and mortality, using data from Ref. [1] 1
Table 1.2. Estimated Age-adjusted Survival Rate (%), Ref. [1]. 2
Table 1.3. Optical characteristics of several reference endoscope objective designs. 4
Table 3.1. Design constraints based on a balance of image performance, light collection, and practical manufacturing 31
Table 3.2. Reflected ray calculation. 34
Table 3.3. Effect of FOV position on imaging system. 44
Table 3.4. Prescription for the 1:1 scale radial view simulation. 48
Table 3.5. Prescription for the 1:1 scale forward view simulation. 48
Table 3.6. Simulation results of the template lens patent with the proposed system. 49
Table 3.7. Radiometry simulation results from the radial view from the proposed design, proposed design without the PMMA tube, and the reference patent endoscope objective described in Ref. [3] 53
Table 3.8. Radiometry simulation results from different lower scale versions of the proposed design. 54
Table 4.1. Design constraints based on a balance of image performance, similarity to proposed 1:1 scale design, and optimized cost. 61
Table 4.2. Prescription for the 3:1 scale radial view Zemax™ simulation. 63
Table 4.3. Prescription for the forward view Zemax™ simulation. Surfaces 1-2 are the dummy surfaces used for coordinate rotation. Flat surfaces have a ROC of infinity (Inf). 64
Table 4.4. Simulation results of the 3:1 prototype endoscope objective 65
Table 4.5. Tolerance settings for the prototype design. M1 is concave mirror, M2 is convex mirror 69
Table 4.6. Sensitivity tolerance summary for (a) forward view optics (b) radial view optics. The evaluation criterion is average MTF at (a) 30 lp/mm (b) 35 lp/mm. 70
Table 4.7. Monte Carlo tolerance simulation report for the forward view optics at (a) 35 lp/mm (b) 70 lp/mm. Back compensator is the distance the imaging plane would move to refocus the system. 71
Table 4.8. Monte Carlo tolerance simulation report for the radial view optics at (a) 30 lp/mm (b) 60 lp/mm. 71
Table 4.9. USAF 1951 Test chart legend. This legend relates group and element numbers to spatial frequency (lp/mm). The group numbers are horizontal and element numbers are vertical on the test chart. 72
Table 4.10. MTF test procedure. 73

Table 4.11. Forward view MTF measurement results. 79
Table 4.12. Radial view MTF measurement results. 79
Table 4.13. Calculated image height for each test pattern. 82
Table 4.14. Image height of each field point used in the MTF simulation. 83
Table 4.15. Measured and Monte Carlo tolerance simulated average MTF. 86
Table 4.16. Simulated and measured radiometry results. 88
Table 6.1. Performance summary of reference designs. 105
Table 6.2. Performance summary of the proposed 1:1 scale and 3:1 scale designs; (R) is radial view and (F) is forward view. 106

List of Acronyms and Abbreviations

3D	3 dimensional
5-ALA	5-aminolevulinic acid
CCD	Charge-coupled device
CMOS	Complementary metal-oxide-semiconductor
DEG	Degree
DIFF. LIMIT	Diffraction limit
DOF	Depth of field
EFL	Effective focal length
EPR	Entrance pupil radius
FOV	Field of view
GEO	Geometric
GI	Gastrointestinal
Img	Image
IMA	Image
Inf	Infinity
lp/mm	Line pairs per millimetre
LCS	Local Coordinate System
LED	Light-emitting diode
Obj	Object
OPD	Optical path difference
OTF	Optical transfer function
MTF	Modulation transfer function
PMMA	Polymethyl-methacrylate
NA	Numerical aperture
N/A	Not available
ROC	Radius of curvature
RMS	Root mean square
Ref	Reference
SI	Surface irregularities tolerance
Std Dev	Standard deviation
SVP	Single-viewpoint
TFRN	Tolerance on curvature in fringes.
TTHI	Tolerance on thickness.
TSDX	Tolerance on surface decenter in x.
TSDY	Tolerance on surface decenter in y.
TSTX	Tolerance on surface tilt in x (degrees).
TSTY	Tolerance on surface tilt in y (degrees).
TIRR	Tolerance on irregularity (fringes).
TIND	Tolerance on index of refraction.

TABB	Tolerance on Abbe number.
TEDX	Tolerance on element decenter in x.
TEDY	Tolerance on element decenter in y.
TETX	Tolerance on element tilt in x (degrees).
TETY	Tolerance on element tilt in y (degrees).
w/o	Without

Chapter 1
Introduction

There exists a demand for more specific mass diagnostic screening methods for cancers in the gastrointestinal (GI) tract. This thesis work documents the design and simulation of a 1:1 scale endoscope objective for non-real-time autofluorescence imaging based diagnostic screening applications and the empirical verification of a 3:1 scaled-up prototype to demonstrate the validity of the simulation methods proposed.

1.1 Motivation

The most common types of cancer are summarized in table 1.1 using data from Ref. [1]. Cancer in the GI tract is the second most common cause of death from cancer, with the survival rate being 44% in the U.S. and 30% in Western Europe [1], as shown in table 1.2. Mass diagnostic screening based on photofluoroscopy has been implemented in Japan since the 1960s, and their stomach cancer survival rate is 52% [1]. This indicates that readily accessible GI screening could help detect malignant tissues at its early stages of growth, and thus increase the treatment's success rate.

Table 1.1. Year 2002 world-wide cancer incidence and mortality, using data from Ref. [1].

	Incidence (Cases)		Mortality (Deaths)	
Cancer Type	Male	Female	Male	Female
Oral cavity	175,916	98,373	80,736	46,723
Esophagus	315394	146723	261162	124730
Stomach	603419	330518	446052	254297
Colon/rectum	550465	472687	278446	250532
Liver	442119	184043	416882	181439
Lung	965241	386891	848132	330786
Prostate	679023	-	221002	-
Breast	-	1151298	-	410712
Cervix uteri	-	493243	-	273505
Ovary	-	204499	-	124860
Bladder	273858	82699	108310	36699
Leukemia	171037	129485	125142	97364

The traditional clinical practice for screening GI cancer is to acquire biopsies using a white light illuminated endoscope at suspected regions and perform biopsy analysis [2]. This is a hit-and-miss approach since white light endoscopy cannot effectively discern the difference between healthy and

malignant tissues, and tissue sampling positions would be chosen in a predominantly random fashion. This process is time consuming and invasive.

Table 1.2. Estimated Age-adjusted Survival Rate (%), Ref. [1].

	United States		Eastern Europe		Western Europe		Japan	
Cancer Type	Male	Female	Male	Female	Male	Female	Male	Female
Esophagus	14	8	6	2	18	14	25	15
Stomach	44	33	15	16	30	24	54	51
Colon/rectum	66	65	35	36	56	53	65	58
Liver	20	0	~0	~0	~0	~0	9	12
Lung	21	26	9	10	9	14	15	22
Breast	-	81	-	58	-	74	-	75
Prostate	87	-	44	-	72	-	55	-
Leukemia	43	45	29	29	43	45	25	29

Fluorescence imaging has shown good potential to improve the diagnosis sensitivity of early detection of malignant tissues in the GI tract. The origin of the fluorophores may be from the endogenous proteins that constitute the GI tissue such as collagen, or from an exogenous contrast agent, such as 5-aminolevulinic acid (5-ALA) [3]. The ingestion of exogenous contrast agents is usually associated with undesirable side effects such as ultra-sensitivity to light [3]; thus fluorescence imaging using the endogenous contrast agents, or *autofluorescence imaging*, is an attractive option. Existing literatures has suggested that the GI tissue autofluorescence emission may provide physiological and biochemical information necessary for the differentiation between healthy and malignant cells [4]. However, tissue autofluorescence is typically very weak such that its methods usually require high-sensitivity photo detectors and efficient light collection optics [5]. It is difficult to discern geometric information from the noisy autofluorescence images. Therefore, autofluorescence endoscopy usually has a white light illumination channel to acquire white light images. The image from the fluorescence and white light channels could be combined to form the final image that is presented to gastroenterologists [6]. The combination of white light endoscopy, fluorescence imaging, and automated video processing could improve the screening sensitivity, specificity, and throughput.

White light capsule endoscopy provides a convenient diagnostic screening method for lower GI diseases by reducing the long human operation time required in conventional white light endoscopy [2]. If a functional fluorescence imaging channel could be implemented inside capsule endoscopes, it could achieve the screening process by using video processing after the capsule has passed through the GI system [7]. This would make the screening process non-real-time as the video processing would need to be done after data acquisition. The optical design of such an endoscope is difficult due to the short object-to-optics distance and weak autofluorescence emission. The close-up imaging nature of the application

implies the presence of high optical aberrations. The weak autofluorescence emission would require the optical design to be efficient in collecting light from object points along the GI wall. In addition, other miniaturized components, e.g. illumination source, imaging optics, and imager sensor should all fit inside the confined space of an endoscope catheter or capsule.

1.2 Existing Endoscope Designs

The anatomy of a typical catheter-based medical endoscope tip is shown in Fig 1.1(a). Besides the imaging channel occupied by the objective lens, there are usually other channels such as nozzle for spraying air/water to clear debris, forceps for sample retrieval, and a dedicated channel for illumination. The catheter based endoscope could have its imaging charge-coupled device (CCD) sensor located at the end of the objective, or it could be coupled to relay optics such as a bundle of fibre optics to an external system that would contain the CCD sensor. The diameters of the lenses in an endoscope objective are usually very small, so that other channels could fit in an endoscope tube [8].

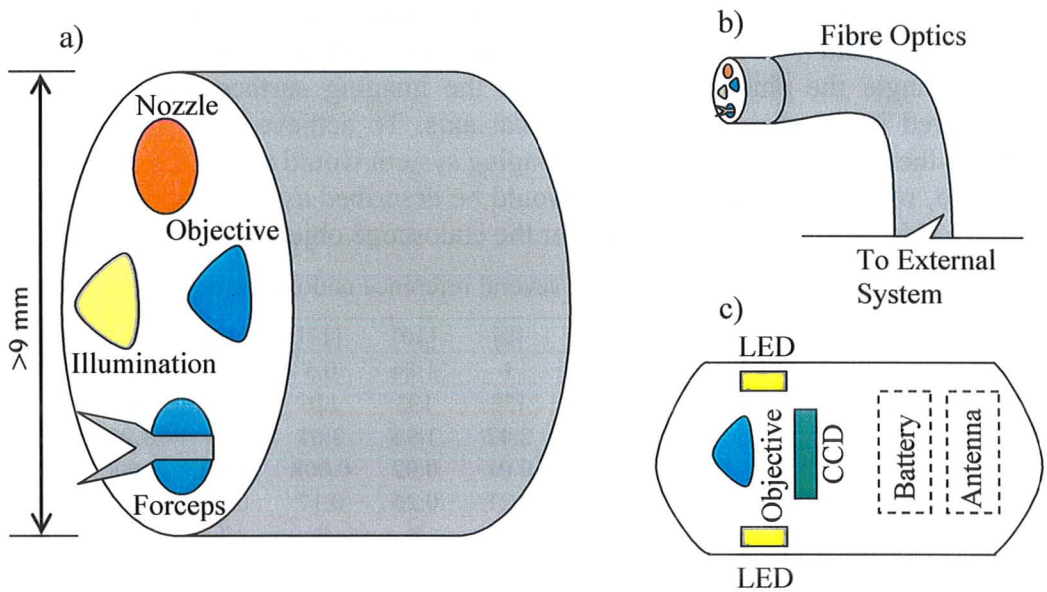

Figure 1.1. Anatomy of (a) common forward-viewing endoscope tip (b) forward-viewing endoscope with fibre optics (c) capsule endoscope.

The light collection ability of several [9-14] typical wide-angle endoscope objective designs are simulated and summarized in table 1.3. Their raytrace layout diagrams are shown in fig. 1.2. The numerical aperture (NA) is a quantity that relates to the angle the light ray makes with the optical system and the f-number is the ratio of effective focal length (EFL) to aperture diameter. These are quantities that characterize the ability of the optical system to collect light; higher values of

numerical aperture in object space and lower values of f-number signify better light collection capability. The object space is the region between the object and the first optical surface. Another parameter of interest is the radius of curvature (ROC); it is difficult to manufacture lenses with short radius of curvature, and it limits the maximum diameter of the lens. A Convex surface would have a positive radius of curvature while a concave surface would have a negative radius of curvature. The root mean square (RMS) spot size is an indication of image quality, where larger sizes correspond to larger blur size from imaging point objects. The RMS spot size and other evaluation parameters are discussed in detail in section 2.2.4. The common optical design philosophy of these endoscope objectives is to keep the focal length short and aperture stop small in order to achieve large depth of field and acceptable image quality.

The wide-angle endoscope objectives in fig. 1.2 are loosely based on a reverse telephoto lens form with the divergent lens group preceding the convergent elements, where the divergent group compresses the ray bundles to achieve wide field of view, and the convergent lens group provides aberration correction. For object points located at the same depth, Smith [15] shows the illumination attenuation of off-axis objects can be approximated by $cos^4\theta$, where θ is the angle the chief ray makes with the imaging surface normal. Depth is measured in the direction of the optical axis. To achieve uniform illumination across the field of view (FOV), the imaging system would need to lower θ to close to zero, where the imaging system would be described as being telecentric on the image side. This is practically true for the endoscope objectives shown in fig. 1.2.

Table 1.3. Optical characteristics of several reference endoscope objective designs.

Reference No.	[9]	[10]	[11]	[12]	[13]	[14]
EFL (mm)	1	1.84	0.5	1	0.5	1
Full FOV (degrees)	133	133	116	116	80	110
F-number	2.42	1.96	3.01	4.1	3.99	4.93
NA, object space	0.01	0.02	0.008	0.011	0.006	0.002
NA, image space	0.21	0.26	0.17	0.12	0.13	0.1
Number of elements	8	8	3	7	3	6
Track length (mm)	7.72	9.01	2.872	6.73	3.25	9.94
Shortest ROC (mm)	0.87	0.85	-0.75	0.848	0.61	0.93
EPR (mm)	0.21	0.32	0.084	0.12	0.06	0.1
RMS spot size at 40° field angle (μm)	3.4	2.2	4.2	3.1	4.1	3.9

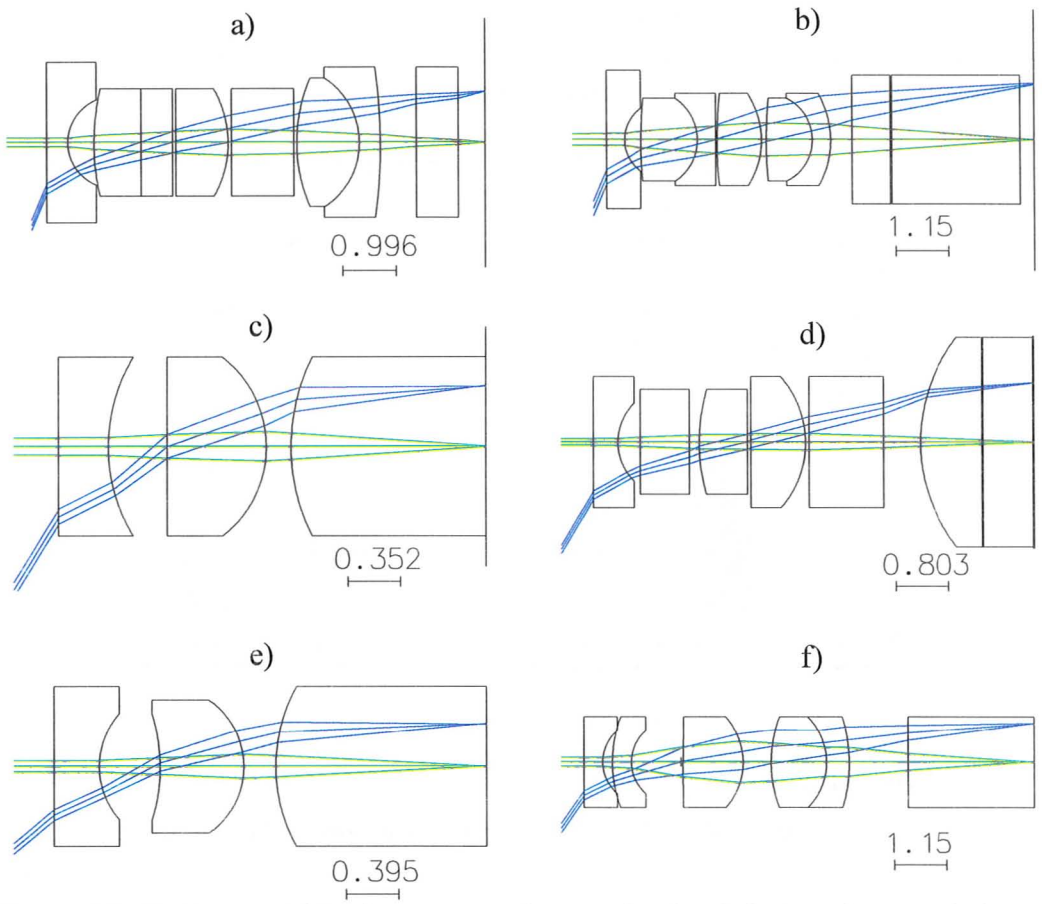

Figure 1.2. Endoscope objective raytrace layout simulated from reference designs (units: mm) (a) Ref. [9] (b) Ref. [10] (c) Ref. [11] (d) Ref. [12] (e) Ref. [13] (f) Ref. [14].

In practice, endoscope diameters often approach the diameter of the GI tract, especially in the case of capsule endoscopy where the GI tract would collapse on the endoscope. This would orient the optical axis of the endoscope to be parallel to the direction of travel of the GI tract. As shown in fig. 1.3(a), objects along the sidewall of the GI tract would be off axis and located at different depths from the endoscope. Due to the regions of interest being the walls of the GI tract, conventional forward-viewing endoscope objectives described in fig. 1.2 are only able to image the regions of interest because of their large field of view and depth of field. Fluorescence emission is isotropic and the irradiance on a detector decreases with distance from the source, thus an efficient fluorescence imaging system would minimize the distance between the source sample and its collection optics. It is evident from fig. 1.3(a) the distance between the GI wall and the endoscope objective is large, thus the forward-viewing endoscopes are not

efficient in collecting autofluorescence. The numerical aperture of objects at distant depths is lower than the numerical aperture of objects at closer depths. The decrease in numerical aperture with increase source distance would cause inefficient light collection. The different numerical apertures for imaging objects along the GI tract wall at different depths would also cause non-uniform light collection across those objects. These reasons render the forward-viewing endoscope inefficient for fluorescence light collection from the GI tract wall surface. Recent advances in foveated wide-angle endoscope objective design such as in Ref. [16], where variable magnification is implemented via controlled lens distortion, may have the potential to provide better light collection of objects along the GI tract wall surface than the conventional forward-viewing endoscopes described in table 1.3.

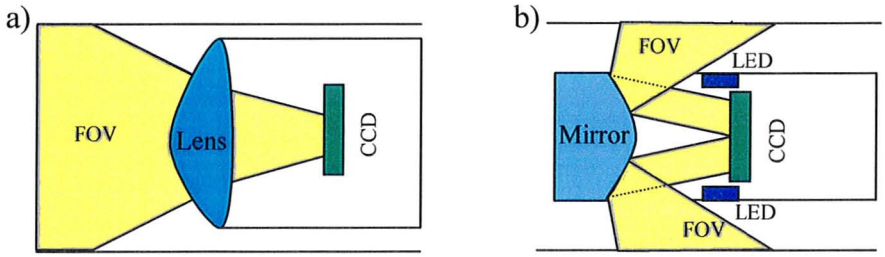

Figure 1.3. Typical endoscope optical system design: (a) Field of view (FOV) of a typical wide-angle endoscope objective. (b) FOV of a radial view endoscope.

Panoramic 360° view imaging using the combination of reflection and refraction optics, or catadioptric systems, has been investigated mostly for surveillance [17] or teleconference applications [18]. The design criteria for these applications are based on objects located meters away from the camera. Most of these catadioptric systems are implemented by pairing commercially available lenses and cameras with customized mirrors to implement a panoramic imaging system [18]. As shown in fig. 1.3(b), a radial view endoscope may be more efficient in terms of collecting light from objects along the GI tract wall. The illumination could be provided by LEDs as illustrated in fig. 1.3(b). Due to the short object-to-lens distance in endoscopy applications, the aberrations introduced by the mirrors are fairly significant for an imaging area small enough to fit inside an endoscope. By customizing all optical components of such a radial panoramic imaging system, there are more design freedoms for balancing the various aberrations and the coplanar focusing of both views.

Ref. [19] describes a panoramic endoscope design that utilizes mirrors to redirect and compress the FOV of the lens group. Their design used a pair of mirrors in folded configuration for radial panoramic imaging, where the paraxial region of the mirror is used for imaging. The rays incident on the lens group is

near paraxial, thus a doublet lens is all that is required for aberration control. The use of the paraxial region of the mirror allowed them to achieve decent image quality and short track length, but their design did not have a forward view, similar to the FOV layout in fig. 1.3(b). Although inefficient in the collection of light from objects along the GI tract surface, a forward view of the GI tract is still desirable for navigation and landmark recognition/co-registration. The forward view could also serve as a reference view during the comparison of images taken from other forward-viewing endoscopes.

Ref. [20] describes the mirror design and the empirical verification of an attachment module that would integrate with existing endoscope objectives for imaging the radial region behind the objective, as well as providing a forward view. In this device, the mirrors are also used to redirect the illumination from the stock endoscope. Their target application is to provide a method of viewing the blind spot located behind the endoscope objective. They did not optimize the entire optical design for light collection.

1.3 Proposed Approach

In comparison to white light endoscopy, tissue autofluorescence emission from the GI tract wall is very weak. Especially in the small intestine, the GI tract is likely to collapse on the endoscope during operation. Therefore the object numerical aperture for imaging the region of interest along the GI tract walls could be optimized more efficiently if the FOV of the endoscope objective is in the radial direction as opposed to being in the forward direction. The object-to-collection optics distance for a radial view imaging system would be short and higher irradiance collection may be achieved than imaging distant objects in a forward-viewing endoscope objective. Fig. 1.4 illustrates the sagittal view of the initial concept diagram of the proposed system.

Similar to fig. 1.3(b), curved mirrors are used in fig. 1.4 to compress and redirect the FOV of the lens elements of the objective. This type of design would provide a radial view of the surrounding tissue, which would have a shorter distance to the endoscope objective than forward-viewing endoscope designs. The portion of the field of view redirected by the apex of the mirror would map onto the lenses in front of the CCD, thus the imaging system would end up imaging itself. To avoid this problem, the apex of the mirror is removed so objects in front of the endoscope could also be imaged. The design in fig. 1.4 would simultaneously image a forward view and a radial view of the GI tract. The lenses would be custom designed to achieve efficient light collection while maintaining acceptable image quality.

This work is an investigation on the optical design of a panoramic and forward-viewing endoscope imaging system with emphasis on the balance between light collection, and achieving comparable image quality with the

forward view wide-angle endoscope objective lenses featured in table 1.1 and fig. 1.2. The proposed design would allow simultaneous imaging of both the forward and the radial panoramic view for non-real-time GI tract screening applications.

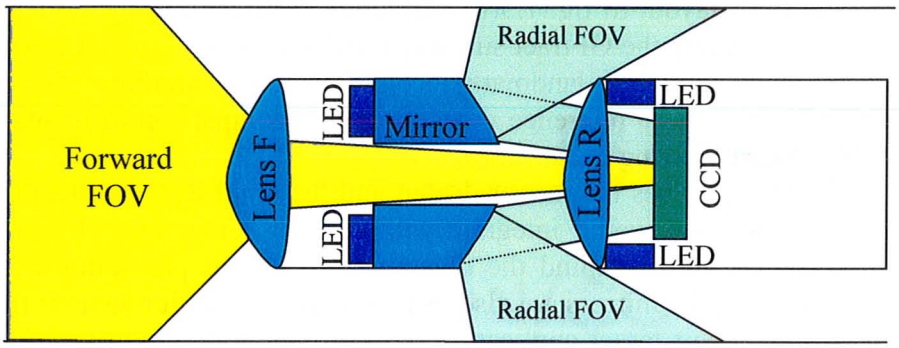

Figure 1.4. Initial concept diagram for the radial and forward viewing endoscope objective design used for this thesis work. The light emitting diodes (LEDs) near the mirror provide illumination for the forward field of view (FOV). The LEDs near the CCD provide illumination for the radial FOV. Lens R represents the lens group used to focus the objects from the radial view to the CCD. Lens F represents the additional lens group required to bring the forward view in focus with the CCD.

1.4 Thesis Organization

Chapter 2 reviews the theories commonly used in optical design as well as their relationship to image formation. Important technical concepts and terminologies used throughout this work are introduced.

Chapter 3 describes the simulation methods used for the design of a 1:1 scale endoscope imaging objective using software simulation packages such as MATLAB™, OSLO™, and Zemax™. The chapter concludes with a radiometry comparison simulation of the proposed design with the wide-angle forward-viewing endoscope objective design described in Ref. [14]. LightTools™ is the radiometry simulation package used for this task. The acquisition of LightTools™ occurred after the design phase of this thesis work and thus did not participate in the optimization of the design.

Chapter 4 briefly describes the simulation design of a 3:1 scale endoscope objective prototype that is similar to the 1:1 scale design. The Instrument Technology Research Center (ITRC) of the National Applied Research Laboratories (Hsinchu, Taiwan, Republic of China) is commissioned to manufacture the prototype from supplied simulation files, ISO10110 lens drawings, as well as optomechanical specifications. ISO10110 lens drawings are the industry standard for specifying lens information for fabrication. The remainder of the chapter describes the empirical work performed on the manufactured prototype to verify the simulation results.

Chapter 5 addresses the view synthesis problem, which is the generation of new views from the acquired images of the manufactured prototype. This has application in the interpretation of the radial view imagery.

Chapter 6 would summarize the work done in this thesis and compare the results with the forward-viewing endoscope objective designs in Ref. [14]. Suggestions for future work would also be discussed.

1.5 References

1. Max Parkin, Freddie Bray, J. Ferlay, Paola Pisani (2005). Global Cancer Statistics 2002. *CA: A Cancer Journal for Clinicians*, 55, 74-108.
2. Amy K. Hara, Jonathan A. Leighton, Russell I. Heigh, Virender K. Sharma, Alvin C. Silva, Giovanni De Petris, Joseph G. Hentz, David E. Fleischer (2006). Crohn Disease of the Small Bowel: Preliminary Comparison among CT Enterography, Capsule Endoscopy, Small-Bowel Follow-through, and Ileoscopy. *Radiology*, 238, 128-134.
3. C.EII (2003). Improving endoscopic resolution and sampling: fluorescence techniques. *GUT An International Journal of Gastroenterology and Hepatology*, 52(4), 30-33.
4. G. W. Falk (2009). Autofluorescence Endoscopy. *Gastrointestinal Endoscopy Clinics of North America*, 19, 209-220.
5. G. E. Cohn, R. Domanik (2003). *In Vitro Clinical Diagnostic Instrumentation*. In T.Vo-Dinh (Ed.), Biomedical Photonics Handbook. CRC Press.
6. Louis-Michel Wong Kee Song, Brian C. Wilson (2005). Endoscopic detection of early upper GI cancers. *Clinical Gastroenterology Best practice & Research*, 19, 833-856.
7. D. K. Iakovidis, S. Tsevas, A. Polydorou (2009). Reduction of capsule endoscopy reading times by unsupervised image mining. *Computerized Medical Imaging and Graphics*, 34, 471-478.
8. Victor L. Fox (2010). Pediatric Endoscopy. In Meinhard Classen; Guldo N.J.Tytgat; Charles J.Lightdale (Eds.), *Gastroenterological Endoscopy*. Thieme.
9. Patent: US 6956703, Objective Lens for Endoscope, 18-10-2005.
10. Patent: US 6994668, Four-Group Endoscope Objective Lens, 7-2-2006.
11. Patent: US 7027231, Endoscope Objective Lens, 11-4-2006.
12. Patent: US 7085064, Object Lens and Endoscope using it, 1-8-2006.
13. Patent: US 7218454, Endoscope Objective Lens, 15-5-2007.
14. Patent: US 7486449, Objective Lens for Endoscope, and Imaging Apparatus for Endoscope using the same, 3-2-2009.
15. Warren J. Smith (2008). *Modern Optical Engineering*. McGraw-Hill professional.
16. Patrice Roulet, Pierre Konen, Mathieu Villegas, Simon Thibault, Pierre Y.Garneau, Gilles Michaud, Ronald Denis (2010). 360° endoscopy using panomorph lens technology. *Proceedings of SPIE*, 7558.
17. Christiane Gimkiewicz, Claus Urban, Edith Innerhofer, Pascal Ferrat, S. Neukom, G. Vanstraelen, Peter Seitz (2008). Ultra-miniature catadioptrical system for an omnidirectional camera, *Proceedings of SPIE*, 6992.

18. S. K. Nayar, V. Peri (1999). Folded Catadioptric Cameras. *IEEE Conference on Computer Vision and Pattern Recognition, CVPR 1999*, 217-223.
19. Contrast Optical Design & Engineering Inc. (2010). *Medical Imaging using a Panoramic Endoscope.* Retrieved Feb.6, 2010. http://www.contrastoptical.com/Services/OpticalDesign/ImagingSystems/MedicalImaging/tabid/88/Default.aspx
20. Ryusuke Sagawa, Takurou Sakai, Tomio Echigo, Keiko Yagi, Masatsugu Shiba, Kazuhide Higuchi, Tetsuo Arakawa, Yasushi Yagi (2008). Omnidirectional Vision Attachment for Medical Endoscopes. *Proc. the Eighth Workshop on Omnidirectional Vision, Camera Networks and Non-classical Cameras, OMNIVIS (2008).*

Chapter 2
Background

This chapter reviews the theories and terminologies used in this thesis work. The design specification and actual simulation methods used in the design work is described in chapter 3, followed by prototype development and empirical tests on the manufactured prototype in chapter 4. Recall from fig. 1.4 that there would be a simultaneous forward and radial view in every image acquired by the proposed endoscope objective design. View synthesis digital image processing algorithms that help to better interpret the radial view imagery are discussed in chapter 5.

The bulk of the design simulation is done in commercial optical design software packages, specifically OSLO™ and ZEMAX™. OSLO™ and ZEMAX™ (sequential mode only) are used to handle all of the lens design because they are among the existing industry standards for lens design. This increases the chance the simulations performed by these software would be realistic, provided that the simulation is properly set up. The basics of using formalized approaches to optical design are reviewed in section 2.1. Optical design software packages typically utilize conventional lens design theory in their simulations, therefore essential concepts and terminology pertaining to this theory is briefly described in section 2.2. Section 2.2.4 would describe the background behind the evaluation methods used in chapters 3 and 4. Mirror form design from the field of catadioptric panoramic imaging system design is reviewed in section 2.3. Catadioptric imaging systems utilize a combination of mirrors and lenses in their optical design. Section 2.3 also describes the functional models of image formation used in the field of digital image processing, which would be used in the proposed view synthesis algorithms discussed in chapter 5.

2.1 Optical Design

The majority of optical design simulations for imaging applications are carried out by a *sequential ray trace* algorithm, where the rays would interact with each surface of the design in a sequential manner. This simplifies the ray trace computation of many optical design parameters, but the designer must ensure the placement of each optical surface occurs in a sensible location and orientation. Failure to do so would imply failure for the algorithm to find a realistic solution to the ray trace, or failure to converge to a solution; for example, it is impossible to have a light ray reflecting off a planar mirror to intersect a surface located behind the mirror, thus the ray trace algorithm would most likely fail.

It is apparent from the initial design concept in fig. 1.4 that although rotationally symmetric mirrors about the optical axis are used, the ray path from individual field points in the radial field of view would only utilize an asymmetric portion of the total mirror surface. The planning and selection of suitable lens forms from lens design theory for use with asymmetric regions of curved mirrors such that the ray trace simulation would be successful proved to be a difficult task. This is encountered during the initial design phase where the general form of the mirrors needs to be chosen. To find potential candidates that might generate a sensible simulation configuration in the optical design software, a simplified imaging model based on the pinhole camera is implemented in MATLAB™ to remove the lenses from the problem. This MATLAB™ routine is used to pre-screen the various panoramic imaging mirror design forms proposed by Nayar [1] that would be impractical for the target thesis application. MATLAB™ is used due to its great flexibility as a general purpose simulation package.

The majority of optical designs for illumination applications are carried out by a non-sequential ray trace algorithm, where massive amounts of rays are traced using Monte Carlo methods to simulate the amount of energy that would arrive at the detector surface. Due to the massive amount of computation required, these algorithms typically do not excel in generating lens design evaluation parameters, and the detector cell cannot realistically approach the size of typical pixel pitch sizes of present day image detectors, which is taken to be less than 10 μm. The binning size is set to 95 × 95 μm at the detector on the image surface is used in this thesis work to ensure practical computation could be achieved. LightTools™ is used in this thesis work to provide an initial estimation of the irradiance one would expect to collect on the imaging plane. LightTools™ is one of the present day industry standards of illumination design simulation packages. The subsequent subsections describe the essential technical background concepts used in these software packages.

2.1.1 Chief Rays

Bundles of light from points on an object pass through an optical imaging system to form the image of the scene. The amount of light that pass through is limited by an aperture referred to as the *aperture stop*. Field of view (FOV) is the amount of the object scene that would appear on a given image dimension. The aperture that controls the FOV is the *field stop*.

Suppose the scene object is completely described by a set of fictitious object points. The individual object points within the working FOV of the imaging system are *field points*. The object surface could take on any shape, but it is usually sampled from a planar shape. The distance from the imaging system to the object plane is the *conjugate distance* [2], or object depth. On-axis field points are objects points that lie on the optical axis of the imaging system, and off-axis

field points are the object points located away from the optical axis. Each field point would generate a different bundle of rays that pass through the imaging system, and the single ray that passes through the center of the aperture stop is the *chief ray* [3]. This implies the aperture stop is located at the intersection of the chief ray and the optical axis of the imaging system. The height position of the chief ray on the image surface is the *image height* [3]. Practically speaking, the other rays in the bundle of light from the same field point would not intersect at the same height as the image height, which may be quantified by a *spot diagram*. This deviation would degrade the resolving power of the imaging system and one representation of this behaviour in lens design is through aberration theory. Even if all the rays are calculated to intersect precisely at a single point, the wave nature of light would cause diffraction effects that would degrade the resolving power of the imaging system [4]. Diffraction induces blur due to the wave nature of light passing through an aperture. The effect diffraction has on an imaging system becomes significant when the aperture stop diameter is comparable to the wavelength of light [4]. The angular radius of the central maximum of the diffraction pattern from a circular aperture is the Airy disc and it can be approximated by Eq. (2.1), where θ is the angular radius of the Airy disc, λ is the wavelength, D is the diameter of the aperture [4]. The *Rayleigh's criterion* for barely resolvable images is a practical method for approximately the diffraction-limited resolving power of an imaging system, and it specifies that the distance between the centers of the image patterns from two different object points to be resolved should not be less than the Airy disc [4]. This translates to the spot diagram of any field point should be greater than the Airy disc, otherwise the dominant contributor to blur is diffraction, and the system is said to be *diffraction-limited.*

$$\Delta\theta = \frac{1.22\lambda}{D} \tag{2.1}$$

2.1.2 F-number and Numerical Aperture

For a single rotationally symmetric refractive lens, the *clear aperture* is the diameter of the bundle of light that would pass through the lens if the light source is located at infinity [3]. A light source at infinity could be thought of as a planar and uniform light source in front of the optical system. The clear aperture of a group of lenses would be the clear aperture of the first lens. Lenses that converge light are convergent or positive lenses. Lenses that diverge light are divergent or negative lenses. The focal length of a given lens is the location the light from infinity would focus, which would be a positive quantity for a convergent lens, and negative for a divergent lens. The relationship between the focal length, refractive index, and radius of curvature of a single thin lens is given

by Eq. (2.2). The focal length is f, the radius of curvature of the front and back surfaces are R_1 and R_2, the refractive index of the front and back medium are n_1 and n_2, respectively [4].

$$\frac{1}{f} = \frac{n_2 - n_1}{n_1}\left(\frac{1}{R_1} - \frac{1}{R_2}\right) \tag{2.2}$$

Note some optical design literature use curvature instead of radius of curvature, and the two are simply inverses of each other. Eq. (2.2) is invalid for a lens whose thickness cannot be ignored, but it is useful in the conceptualization of the relationship between radius of curvature, focal length, and single element optical power. Matrix methods of ray tracing are usually used for computing thick lens properties [4]. The effective focal length (EFL) is the resultant focal length of a group of optical components. The EFL is important in the definition of the *f-number*, which is given by Eq. (2.3).

$$f-number = \frac{focal\ length}{clear\ aperture} \tag{2.3}$$

The concept of f-number could be used to evaluate the amount of light being collected, but its definition is based on light from infinity, which is used for *infinite conjugate optical systems*. The target application of this thesis work is for a finite conjugate system because the object is along the wall of the gastrointestinal (GI) tract. The numerical aperture is a similar quantity to the f-number, but for finite conjugate systems. From Ref. [2], its definition is as follows:

$$NA = n\sin U \tag{2.4}$$

With reference to Eq. (2.4), n is the refractive index of the medium in which the image is formed, and U is the half angle of the imaging cone.

From Ref. [3], the working f-number, one that could be used for finite conjugate systems, is defined as:

$$working\ f-number = \frac{1}{2NA} \tag{2.5}$$

The working f-number is a measure of the angle of light acceptance or emission for optical systems [5]. It is used in the field of photography to characterize the speed of lenses. Lenses that collect more light could afford to have faster shutter times without underexposing. The lower the f-number, the wider the angle it could collect light from a given object scene point.

2.1.3 Entrance Pupil

When observing from the object towards the imaging system, the image of the aperture stop is the *entrance pupil* [4]. When observing from the image towards the image system, the image of the aperture stop is the *exit pupil* [4]. Literatures in panoramic media acquisition specify the camera should be rotated about its entrance pupil for a mosaic stitching style panoramic generation [6]. Fig. 2.1 illustrates a Cooke Triplet lens design form with the entrance pupil plane marked with a purple dashed line.

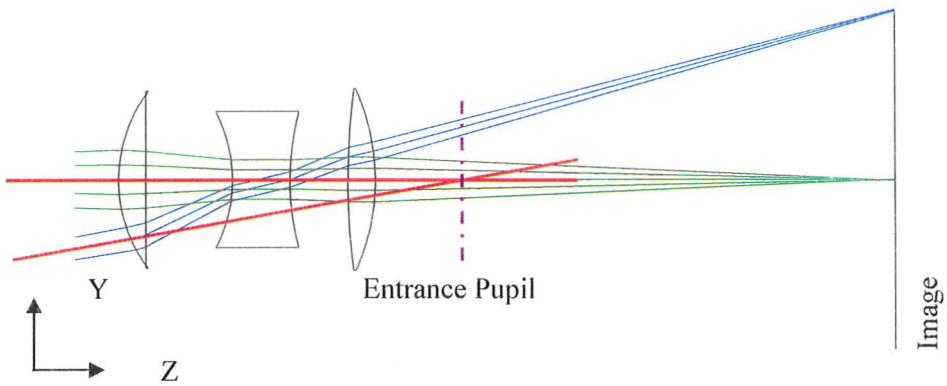

Figure 2.1. Ray trace of a Cooke Triplet lens. The object is located to the far left and not shown.

The object is located to the far left and is not shown. The green bundle of rays represents the on-axis field point and the blue bundle of rays represents the off-axis field point. The chief ray of both bundles is the central ray in each bundle on this figure, and they coincide with the marked red lines before the bundle of rays interact with the first lens from the left. The marked red lines are the line of sight an observer from the object would see. The location where these lines of sight intersect is the image of the aperture stop seen by the observer from the object location, thus it is the location of the entrance pupil.

2.1.4 Light Collection vs. Optical Throughput

In illumination optical system design, a measure of light efficiency would be the *optical throughput*, or *etendue*. However, it is unsuitable for evaluating the light collection of our application. Let n be the refractive index; θ be the angle from the normal; dA be the differential area; and dw be the differential solid angle [7]; the etendue defined of is:

$$E = n^2 \iint_{aperture} \cos\theta \, dA_s \, dw \tag{2.6}$$

It could be seen from Eq. (2.6) that a larger source area would yield a larger etendue value. This implies a larger FOV on the receiver side to image more of the source would yield a larger etendue value. The design proposed in this thesis would work with an illumination system that would optimize its etendue onto the scene object that is within the FOV of the proposed imaging system. Thus, a larger FOV of the proposed imaging system does not necessarily equate to higher light collection from a fictitious point object. The more appropriate parameters for evaluating the imaging optics would be the numerical aperture, working f-number, or the entrance pupil radius. Etendue characterizes an optical system's ability to accept light thus a large FOV to see the light source would increase its value. Numerical aperture as described in Eq. (2.4) characterizes the imaging system's ability to collect light from individual object points within the imaging system's working FOV.

2.1.5 Aberration vs. Light Collection

The purpose of an imaging optical system is to provide adequate amount of exposure and focus of light from the object to the image surface such that details in the object scene would be discernable. It is difficult for a charged-coupled device (CCD) or complementary metal-oxide-semiconductor (CMOS) detector pixels to achieve 100% fill rate, thus the bundle of light passing through an optical system should ideally be focused to an area smaller or at least comparable to the pixel pitch of the detector. This would ensure enough energy from each field point is being concentrated onto an area smaller or comparable to the size of a pixel. This corresponds to having smaller spread sizes on the image surface for various field points, and the spot diagram simulation present in most optical design software offers a method to quantitatively simulate this spread size.

Aberration describes the defect caused by the rays in the bundle of light from a field point not converging at the same image location [2]. One method to correct most types of aberration would be to decrease the diameter of the aperture stop to limit the amount of light so fewer rays would be present in the light bundle. This would decrease the amount of light collected, thus the search for the balance between aberration control and light collection is one of the challenges faced in this thesis work. Details for the type of aberrations most pertinent to this thesis work are described in section 2.2.

2.1.6 Necessary Workarounds to Assumptions

One inconvenience in using optical simulation software based on lens design theory is that certain evaluation parameters such as the entrance and exit pupil location, method of generating rays, and methods of sampling the rays across space may be based on paraxial approximation, depending on the algorithm used in the simulation package. The paraxial approximation is applicable when

the object is near the optical axis, which is an invalid assumption for the proposed radial view optical design due to the asymmetric usage and rotation of the mirrors. Workarounds and detailed study of the simulation package manual is required to accomplish a proper setup for the proposed radial view sequential ray trace simulation. For example, the *field angle* is the angle between the entrance pupil and a field point in the YZ plane of a ray trace layout. Its usefulness diminishes in wide-angle finite conjugate systems where the entrance pupil moves for different field points [8]. However, it is used in order to force the rays to follow a realistic simulation path in Zemax™ for the radial view simulation of the proposed thesis design. The correct entrance pupil locations across the field of view are calculated in MATLAB™ and will be discussed in chapter 5 where they are described as *effective viewpoints* of the imaging system.

2.2 Lens Design Background

The illustration in fig. 2.3 describes a typical coordinate system used by lens design theory upon which sequential optical design software are based on Ref. [2]. The image height are described in Eq. (2.7a) and Eq. (2.7b) and are given in Ref. [2]. A_1 is the transverse measure of the distance from paraxial focus to imaging plane, A_2 is the magnification, B_1 is spherical aberration, B_2 is coma, B_3 is astigmatism, B_4 is Petzval, and B_5 is distortion. The A terms are commonly referred to as first-order optical parameters; the B terms are considered third-order aberrations. Higher order aberrations compensation is built into the default lens merit optimization function in the sequential ray tracer used for this thesis work, OSLO™ and ZEMAX™.

$$y' = A_1 s\cos\theta + A_2 h + B_1 s^3\cos\theta + B_2 s^3 h(2+\cos 2\theta) + \ldots + (3B_3 + B_4)sh^2\cos\theta + B_5 h^3 + \ldots \tag{2.7a}$$

$$x' = A_1 s\sin\theta + B_1 s^3\sin\theta + B_2 s^2 h\sin 2\theta + (B_3 + B_4)sh^2\sin\theta + \ldots \tag{2.7b}$$

Third-order aberrations are easier to reduce by changing individual parameters of the lens design. Common parameters that offer degrees of freedom in lens design include index of refraction, Abbe number, curvature, thickness, and air spaces between elements. The higher order aberrations are not easily correctable since their relationships with each lens element in the lens design are much more complicated than the third order aberrations. It is more practical to first correct significant third order aberration manually with the aid of aberration theory, and then use the computer optimization routine of sequential ray tracers to minimize higher order aberrations.

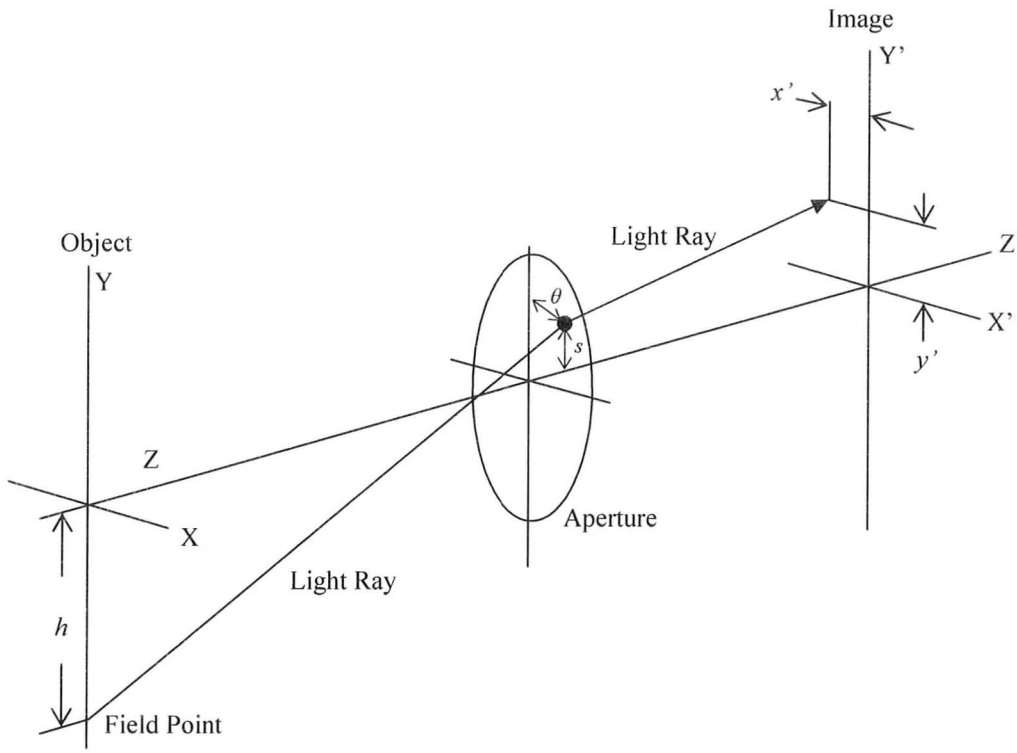

Figure 2.2. Coordinate system setup for aberration equations.

2.2.1 Petzval Curvature

With reference to fig. 2.2, the *tangential rays* are rays from the field point that would lie in the YZ plane, while the *sagittal rays* are rays from the field point that would lie in the XZ plane [2]. Astigmatism aberration occurs when the tangential and sagittal rays do not focus at the same surface. As shown in Eq. (2.7) and fig. 2.2, astigmatism and Petzval curvature would both increase as the distance between the field point and the on-axis object point increases. This effect of astigmatism creates a focus pattern of an ellipse as shown in fig. 2.3, and it is known as the *field curvature* [3]. In practice, the imaging plane is usually planar as opposed to having the field curvature, it could cause the off-axis regions to be out of focus. This is the most problematic aberration for the proposed thesis design due to the high optical power involved in attempt to shorten the focal length of the system in order to image close up objects.

The *Petzval curvature* is a shape unique to every imaging system used in conjunction with astigmatism to predict the location of the sagittal and tangential focal surfaces. Since reducing the field of view to restrain field points that are far from the optical axis would reduce the field curvature aberration, it is not desired in wide FOV applications.

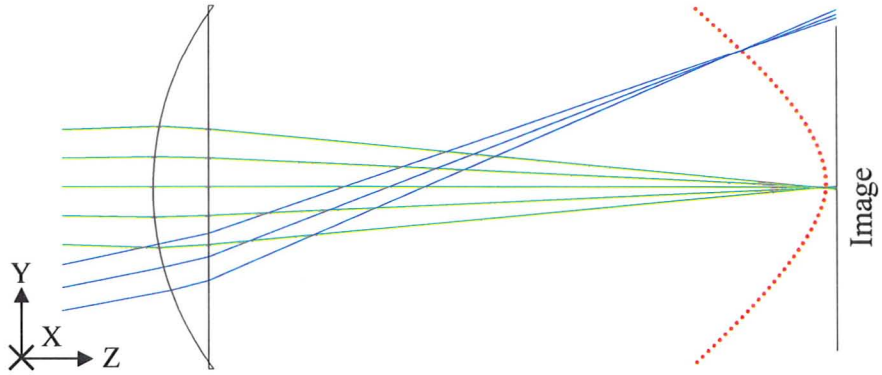

Figure 2.3. Demonstration of field curvature with a single lens. The dotted red curve outlines the field curvature.

The field curvature aberration could also be reduced if the Petzval curvature is flattened. The *Petzval sum* is a concept that quantitatively describe the image curvature of a flat object if all aberrations are absent in the imaging system. The sum equation is given by Eq. (2.8a) and the power of a lens surface is given by Eq. (2.8b) from Ref. [9]. The refractive indices of the two mediums that define an optical surface are denoted n and n'.

$$Petzval\ sum = \sum \frac{\varphi}{nn'} \tag{2.8a}$$

$$\varphi = \sum \frac{(n'-n)}{r} \tag{2.8b}$$

According to Eq. (2.8a), splitting the optical elements would not decrease the Petzval curvature since the contribution they make to the Petzval sum is proportional to its optical power, unlike the correction of spherical aberration [3]. From Ref. [8], $y(n-n')c$ describes the contribution to the system power for one surface, or $y\varphi$ for a component, where y is marginal ray height. The marginal ray is the ray that grazes the edge of the aperture stop. Thus it is possible to have a lens with a large negative optical power that contributes little towards system optical power if the marginal ray height incident on that lens is kept small. In a short focal length system, the Petzval curvature may be reduced if the marginal ray incident on the negative elements could be kept low as to not significantly affect the EFL [8] .

2.2.2 Lateral Chromatic Aberration

This aberration is common in situations where the ray incident on the lens element make a large angle with the surface normal. Shorter wavelength light

refracts more than longer wavelength light, thus rays of different wavelength would focus at different locations on the image and fringe patterns of different colours would appear on the resultant image. This type of situation arise in wide-angle imaging systems where the off-axis field points could make a large angle with the surfaces of elements within the system [3].

2.2.3 Coma Aberration

Consider a bundle of light originating from an off-axis field point passing through an imaging system with a large entrance pupil. Each ray in the bundle would have a very different angle of incidence on the elements, implying the rays would most likely not intersect the imaging plane close to each other. The illustration in fig. 2.4 describes an example with a single element lens. From Eq. (2.7), it can be seen that coma is linearly proportional to the FOV and proportional to the aperture squared [2].

Coma is another significant aberration in the proposed thesis design due to the light bundle from each field point using only an asymmetric portion of the total mirror surface, which causes the optical path length as well as the angle of incidence on the mirror of rays within the light bundles to be very different.

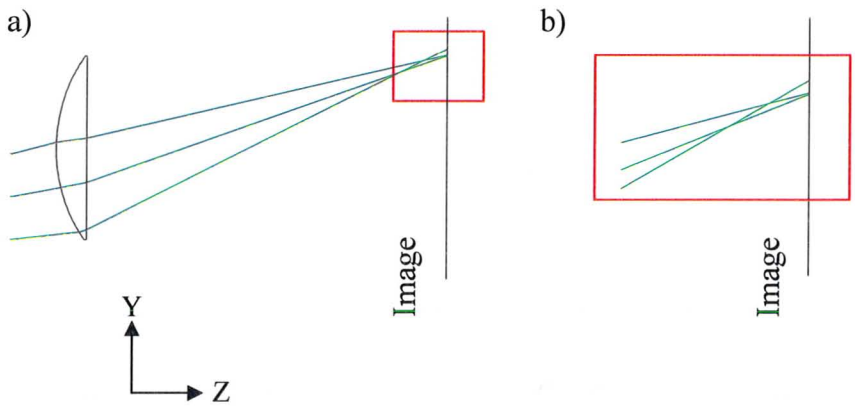

Figure 2.4. Demonstration of coma aberration with a single lens. This aberration is significant when the field angle is large. (a) is a zoomed out version of (b).

2.2.4 Evaluation Methods

The *modulation transfer function* (MTF) characterizes the ability of a lens system to resolve detail by evaluating the contrast of a series of alternating bright and dark pattern [3]. The higher the spatial frequency of the alternating pattern, the more detail it contains. Contrast is described by modulation, which is defined in Eq. (2.9). The *max* and *min* pertain to the image intensity. The MTF is the modulus of the *optical transfer function* (OTF) from *Fourier Optics* theory, but it can also be calculated by Eq. (2.9) [4].

$$Modulation = \frac{\max - \min}{\max + \min} \tag{2.9}$$

The imaging system cannot differentiate any detail if the modulation is zero, whereas a modulation of unity implies the imaging system can reproduce the alternating object pattern perfectly. In practice, it is common to aim for a higher than specified MTF score during design due to the presence of fabrication and assembly tolerances, which would inevitably degrade the actual MTF [3]. Most optical design software packages perform Monte Carlos simulation on the specified tolerance to give an estimate of the most probable MTF performance with the tolerances applied. The topic of different tolerance simulation methodologies is discussed in section 4.2.3.

Depth of field is the range of conjugate distance the imaging system could achieve acceptable image quality without refocusing the lens [4]. In the proposed thesis design, depth of field is determined by varying the object distance to the imaging system and evaluating its corresponding MTF performance without adjusting the imaging surface.

The *spot diagram* is the plot of ray intersection locations on an optical surface in a ray trace simulation [2]. The intersection locations of the rays from the bundle of light of a single field point are represented as spots. Other information that usually accompany a spot diagram analysis include the intersection location of each ray across the design wavelengths, root mean square (RMS) spot size radius, and Airy disc radius. The spots from different wavelengths are plotted with different colours to better visualize the effect of wavelength dependant aberration. The RMS spot size is the area where approximately 68% of the energy from the field point should be contained in. The value of 68% assumes the intersection locations are normally distributed. The OSLO^{TM} Reference in Ref. [10] indicates that its RMS spot size is a weighted standard deviation of all the rays traced.

Eq. (2.10) describes the spot diagram calculation that OSLO^{TM}. Eq. (2.10a) and Eq. (2.10b) describe the variance of the spots in x and y, respectively. The weight assigned to the i^{th} ray is w_i and the sum of all weights is W. The transverse aberration for the i^{th} ray (DX_i, DY_i) is measured with respect to a reference ray. The centroid of the ray intersections is $(\langle x \rangle, \langle y \rangle)$. The radial RMS spot size is given in Eq. (2.10c).

$$\sigma_x^2 = \frac{1}{W} \sum_{i=1}^{n} w_i \left(DX_i - \langle x \rangle \right)^2 \tag{2.10a}$$

$$\sigma_y^2 = \frac{1}{W}\sum_{i=1}^{n} w_i \left(DY_i - \langle y \rangle\right)^2 \tag{2.10b}$$

$$\sigma_{rms} = \sqrt{\sigma_x^2 + \sigma_y^2} \tag{2.10c}$$

Decreasing the aperture would reduce the amount of light collected by the lens but reduce aberration; however it would also bring the optical system closer to the diffraction-limit. The Airy disc and Rayleigh's criterion is used in lens design to indicate the resolving limit due to diffraction. This is applicable for imaging systems with small apertures since in the presence of a large Airy disc yet small RMS spot size, the actual MTF would be dominated by the diffraction induced blur. Thus it is important to ensure the Airy Disc radius is smaller than the RMS spot radius if spot diagram analysis is to be used.

2.2.5 Relevant Lens Forms

Field flattener lenses are used near the imaging surface to provide an adequate amount of compensatory optical power to the off-axis rays to flatten the Petzval curvature of the imaging system [3]. For finite conjugate systems with short conjugate distances and long effective focal length, the presence of the flattener lens often decrease the depth of field to an impractical amount. Its concept is used in the endoscope objective designs in fig. 1.2. These types of imaging systems have parallel chief rays between the last lens element and the imaging surface for coupling onto an infinite conjugate optical system. The exit pupils of these systems are located at infinity. Optical systems with this type of property are referred to as being *telecentric* on the image side.

Reverse telephoto lenses consist of a negative element followed by a positive element [8]. They are the base form for a significant number of lenses with wide FOV. For the wide FOV application, they usually have very strong curvature on the front elements to compress the rays towards the optical axis to achieve wide FOV. Some forms such as the fish eye lens require a long track length and are subjected to lateral chromatic aberration [8]. Other variations of the basic reverse telephoto form have been spotted in endoscope objective lens design patents where the track length is reduced by scaling down the design [11]. This often causes the aperture stop radius to decrease so light collection is reduced.

Eyepiece lens forms are suitable for low FOV, but almost all of its surface parameters such as the curvature, thickness, and airspaces between each element could be used for degrees of freedom in aberration control. This allows flexible control over the magnification and third order aberrations. The Kellner eyepiece form is used in the proposed thesis design to shape an aberration profile that would compensate for the aberration induced by the mirrors.

2.3 Image Understanding

This section introduces the relationship between images and objects for different image projections as well as the corresponding terminologies in their optical implementations. The theory introduced in this section is the basis of the view synthesis image processing algorithm work described in chapter 5.

2.3.1 Projections: Perspective vs. Orthographic

There have been many investigations on the use of curved mirrors for panoramic imagery in the field of image understanding within the past two decades [12-15]. Prior to detailed optical simulation, this thesis followed the single-viewpoint (SVP) catadioptric omnidirectional theory as outlined in Ref. [1] as an initial method of selecting potential mirror forms.

In the field of image understanding and vision applications, only the ray that describes the image formation or location is considered functionally relevant. The other rays in the bundle of light originating from the same field point are usually ignored for simplicity. This is because for an imaging system with low aberrations, these other rays would intersect the imaging plane very close to where the *image formation ray* would intersect the imaging plane. The concept of the image formation ray is similar to the chief ray, except that it is more generalized and not required to pass through the center of the aperture. These simplified camera models functionally describes the purpose of an imaging system and would ultimately be used to characterize its *camera projection.* Camera projections describe the relationship between the object location and the corresponding image location and are important tools for the field of machine vision.

The SVP condition assumes that all image formation rays within the imaging system's working FOV would pass through a common point, or *effective viewpoint* [1], and the subsequent imagery formed may be described by perspective projection [16]. The concept of focal length has different interpretations in the field of image understanding and the field of optical design. For the image understanding terminology, the focal length is the distance from the effective viewpoint to the imaging plane. This implies that the magnification or zoom of the image is affected by the focal length. For optical design, the back focal length is where light from infinity would focus onto the imaging plane, measured from the vertex of the last lens surface [4]. For finite conjugate systems, the back focal length of an imaging system would be different from the distance between the imaging plane and the vertex of the last lens surface in order to achieve adequate focus.

Recall from fig. 2.1, the image of the aperture stop center viewed from the object is the entrance pupil. This implies that for a SVP system, the effective viewpoint is at the entrance pupil and that the image formation rays are chief rays.

The reason perspective projection is widely used to represent most camera systems is because low distortion lenses with finite entrance pupil locations satisfy the SVP constraint. These types of lenses are often referred to as *perspective* lenses in the field of vision engineering. This implies starting a lens ray trace simulation from a SVP constrained lens form greatly increases the chance of the sequential ray tracing algorithm to converge since the image formation rays are by definition, the chief rays and would theoretically pass through the aperture stop somewhere in the system.

When the entrance pupil of an optical system is taken to be at infinity, the chief rays would appear parallel to the optical axis between the object and the first lens surface. This is known as *object side telecentric imaging system* in the field of optical design [2], and *orthographic projection* in the field of image understanding [16]. The consequence for this type of imaging system is that there is no parallax and thus objects across depth retain their size. This is usually used in metrology and some machine vision applications where measurement error induced from different object depth are to be minimized [2]. One major disadvantage is that the clear apertures of these imaging systems need to be larger than the FOV; this is a consequence of the chief ray being parallel to each other in object space, as shown in fig. 2.5.

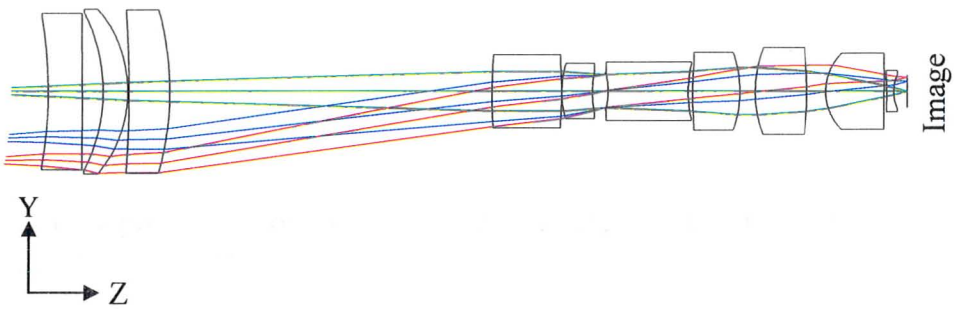

Figure 2.5. Sample telecentric implementation modified from Ref. [10]. The object is to the far left and not shown. The FOV is determined by the size of the clear aperture of the system.

2.3.2 Mosaic Panoramic Generation

The plenoptic function is a conceptual method that characterizes the 3D world from a single-viewpoint, which is essentially a function that describes the information acquired by a pinhole camera with 360° FOV [17]. Therefore, perspective lens cameras with modest FOV may be used to generate panoramas by stitching together acquired images while the camera undergoes rotation about the entrance pupil [6]. This is to avoid parallax when stitching together the different images taken by the camera. Parallax is the discrepancy in the images

produced from multiple different lines of sight viewing the same object. Parallax is essential for stereovision but the discrepancy would cause mosaic panorama to appear unnatural.

2.3.3 Functional Overview of Perspective Projection

In a typical optical ray trace layout diagram of an imaging lens, a real and inverted image is formed at the imaging plane, as shown in fig. 2.1. Ignoring the inverted behaviour, aberrations, and the non-chief rays, the image could functionally be thought of sampling a slice of the rays in front of the first lens. The further the location of this sample plane, the larger the image. This is often represented in perspective projection as a pinhole camera model with the imaging plane in front of the effective viewpoint, as shown in fig. 2.6. The *zoom* or *focal length* terminology used in this representation is the distance from the imaging plane to the effective viewpoint. Its functional purpose is to represent the magnification of the image [6]. Although this method of representing image formation does not obey the laws of physics, it does serve as an accurate functional representation for vision engineering applications that use low distortion perspective lenses. The generation of new views in computer graphics and virtual reality also utilize similar functional camera models [18].

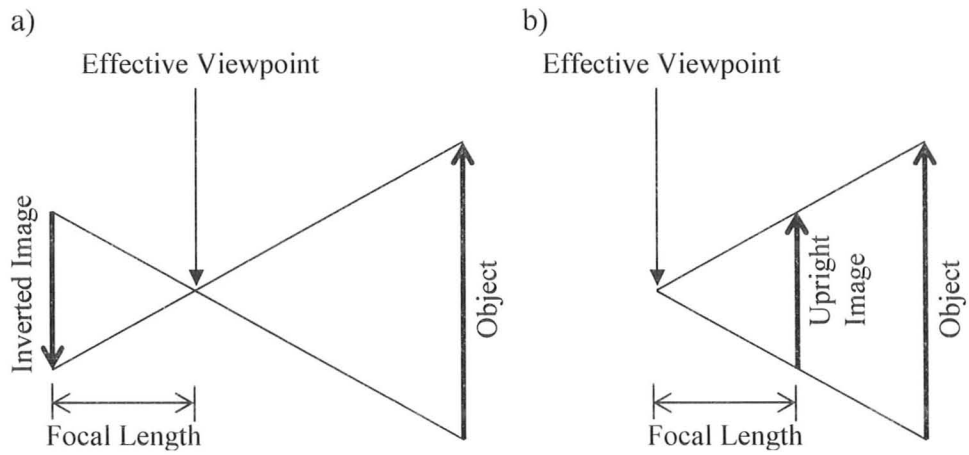

Figure 2.6. Functional representation of a perspective lens using (a) pinhole camera (b) perspective projection.

2.3.4 Catadioptric Imaging System Design

Catadioptric imaging systems are optical systems made from lenses and mirrors. They are historically used in telescope designs such as the Cassegrain telescope [8]. The field points would utilize the entire clear aperture of the mirrors

for image formation. The mirrors typically provide most of the optical power while the lenses serve would provide the majority of the aberration control [8].

Recent investigations of using mirrors for extremely high FOV imaging follow a different design philosophy. The curved mirrors are used to redirect or compress the FOV of lens cameras to objects in the radial 360° direction. The resultant panoramic image would then undergo digital image processing algorithms specific to the mirror and camera placement geometry to obtain a synthesized perspective view of objects in the panorama [12]. These catadioptric imaging devices essentially acquire the visual information of a plenoptic function in a single image. For the target thesis application, the design philosophy of the 360° radial direction panoramic catadioptric systems is used to image the sidewalls of the GI tract. This is assuming the imaging system has its optical axis aligned with the axis of symmetry of a cylindrical pipe, which would most likely be the case when the GI tract is collapsed on the endoscope. Each object point from the GI tract wall would only utilize a portion of the mirrors in an asymmetric manner. This is different from the traditional telescope designs and thus the resulting imagery is likely to have significant coma aberration due to the different optical path length and angle of incidences on each optical element surface for each ray in the bundle of light from the object point. Due to the high amount of aberration involved, the lenses contribute modestly to the overall optical power of the imaging system, more so than the Cassegrain telescope design. The mirrors contribute to the overall optical power as well as redirecting the FOV of the refractive elements in the sidewall direction.

The design philosophy of SVP constrained catadioptric panoramic imaging systems is outlined in Ref. [1], which describes when the entrance pupil of the lens is placed at the secondary focus of the curved mirrors, the ray height could be calculated by solving the perspective projection mapping between the object, mirror, and lens camera. The use of this theory as a starting template helped to secure a successful ray trace solution as opposed to freeform catadioptric designs, since the rays are required to pass through the center of the entrance pupil in a SVP constrained system.

2.4 References

1. S. Baker, S. K. Nayar (1999). A Theory of Single-Viewpoint Catadioptric Image Formation. *International Journal on Computer Vision*, 35, 175-196.
2. Warren J. Smith (2008). *Modern Optical Engineering.* McGraw-Hill Professional.
3. Robert E. Fischer, Biljana Tadie-Galeb, Paul R. Yoder (2008). *Optical System Design*. McGraw-Hill Professional.
4. Frank L. Pedrotti, Leno M. Pedrotti, Leno S. Pedrotti (2006). *Introduction to Optics*, Benjamin Cummings.
5. John E. Greivenkamp (2003). *Field Guide to Geometrical Optics*. SPIE Publications.

6. Fay Huang, Reinhard Klette, Karsten Scheibe (2008). *Panoramic Imaging: Sensor-Line Cameras and Laser Range-Finders*. John Wiley & Sons Ltd.
7. Angelo V. Arecchi, Tahar Messadi, R. John Koshel (2007). *Field Guide to Illumination*. SPIE Publications.
8. Warren J. Smith (2004). *Modern Lens Design*. MgGraw Hill Professional.
9. Rudolf Kingslake (1989). *A History of the Photographic Lens*. Academic Press.
10. Lambda Research Corporation (2005). OSLO Optics Reference. Lambda Research Corporation.
11. Patent: US 7486449, Objective Lens for Endoscope, and Imaging Apparatus for Endoscope using the same, 3-2-2009.
12. J. S. Chahl, M. V. Srinivasan (1997). Reflective surfaces for panoramic imaging. *Applied Optics*, 36, 8275-8285.
13. Robert Andrew Hicks, Ronald K. Perline (2005). Equiresolution catadioptric sensors. *Applied Optics*, 44, 6108-6114.
14. Christiane Gimkiewicz, Claus Urban, Edith Innerhofer, Pascal Ferrat, S. Neukom, G. Vanstraelen, Peter Seitz (2008). Ultra-miniature catadioptrical system for an omnidirectional camera, *Proceedings of SPIE*, 6992.
15. Gurunandan Krishnan, S. K. Nayar (2010). Cata-Fisheye Camera for Panoramic Imaging. *IEEE Workshop on Applications of Computer Vision, WACV 2008*, 1-8.
16. Richard Hartley (2004). *Multiple View Geometry in Computer Vision*. Cambridge University Press.
17. Edward H. Adelson, James R. Bergen (1991). The Plenoptic Function and the Elements of Early Vision. In M. Landy, J. Anthony Movshon (Eds.), *Computational Models of Visual Processing*. MIT Press.
18. S. M. Seitz, C. R. Dyer (1995). Physically-Valid View Synthesis by Image Interpolation. *Proc. Workshop on Representation of Visual Scenes*, 18-25.

Chapter 3
1:1 Scale Endoscope Objective Simulation Design

In comparison to white light endoscopy, tissue autofluorescence emission from the gastrointestinal (GI) tract wall is very weak. During operation, the GI tract is likely to collapse on the endoscope. Panoramic 360° view imaging using the combination of reflection and refraction optics, or catadioptric systems, has been investigated mostly for surveillance [1] or teleconference applications [2]. As shown in fig. 1.3, a radial view endoscope may be more efficient in the collection of light from the GI tract walls, and the illumination could be provided by light emitting diodes (LED) due to the short distance between the endoscope objective and the GI wall. The numerical aperture for imaging the region of interest along the GI tract sidewalls could be optimized more efficiently if the field of view (FOV) of the imaging system is in the radial direction as opposed to being in the forward direction. This shorter object to collection optics distance for a radial view imaging system would be able to achieve higher irradiance collection than a forward view imaging system. However, due to this short conjugate object distance, the aberrations introduced by the mirrors are fairly significant for an imaging area that is small enough to fit inside an endoscope. By customizing all optical components of such a radial panoramic imaging system, there are more design freedoms for balancing the various aberrations and focusing of the radial and the forward views to the same image detector could be achieved, as shown in the proposed initial concept diagram in fig. 1.4. The proposed endoscope objective design in this chapter would address the imaging optics of such a system.

Section 3.1 would define the scope of the problem investigated in this thesis work. The design specifications are laid out in section 3.2, followed by detailed documentation of the simulation methods used to design the proposed endoscope objectives in section 3.3. The simulated results from the sequential ray trace software used are reported in section 3.4. Another simulation approach using non-sequential ray trace software to compare the light collection ability of the proposed endoscope objective design against a wide-angle forward-viewing endoscope objective design from Ref. [3] is described in section 3.5. The results from sections 3.4 and 3.5 are discussed in section 3.6.

3.1 Problem Definition

This thesis investigates the feasibility of designing custom endoscope objective optics for a dual-view imaging system with the emphasis on light collection and comparable image quality with the reference forward wide FOV

endoscope design described in Ref. [3], which is shown in fig. 1.2(f) and table 1.3. This is because the design from Ref. [3] is chosen as the starting template lens form of the proposed thesis design from the six reference endoscope objective designs described in table 1.3 and fig. 1.2. The design from Ref. [3] is chosen for this purpose due to its balance of having few number of elements, mild radius of curvature, and acceptable image quality. Although other reference designs have higher numerical apertures, the mild radius of curvature translates to more design freedom and higher chance to modify the lens design. Designs with mild radius of curvatures are also more feasible in terms of fabrication.

The target application is for non-real-time GI tract diagnostic screening, where a final mosaic map of the GI tract could be generated from images acquired by the endoscope as it traverse through the GI tract. Two views of the GI tract would be present in every acquired image from this endoscope; a forward view for navigational purposes and a 360° radial view for efficient light collection off the tissues on the sidewall of a collapsed GI tract. The radial view is implemented through the use of curved mirrors. This thesis presents two endoscope objective designs. The proposed thesis designs also have a forward view for navigation purposes, with its back focus designed to coincide with the imaging plane of the radial optics. This would allow simultaneous imaging of both the forward and the radial panorama view, as shown in fig. 1.4.

There are two proposed endoscope objective designs in this thesis work. The first design simulation is optimized for 1:1 scale and is described in this chapter. The second design simulation is optimized for 3:1 scale and is described in chapter 4, which is further developed into a manufactured prototype. The manufacture process is outsourced to a third party optics shop. Two view synthesis digital image processing algorithms are proposed in chapter 5 to better interpret the acquired imagery from the radial panorama view of the manufactured prototype.

3.2 Design Specification

Table 3.1 summarizes the evaluation and fabrication constraints for the proposed dual view endoscope design including edge thickness, track length, and radius of curvature. The resulting image quality is evaluated using spot diagrams and modulation transfer function (MTF). Pixel pitch determines the upper bound of the root mean square (RMS) spot sizes for efficient light collection onto one pixel. FOV, depth of field, and entrance pupil radius (EPR) are left to be as large as possible without significant increase in the RMS spot size beyond the target pixel pitch. The pixel pitch of the image detector is assumed to be 5 × 5 μm since that is the estimated pitch size of the hyperspectral complementary metal-oxide-semiconductor (CMOS) image detector under development by another research group at McMaster University. The upper bound of the root mean square (RMS)

spot size is set to 5 μm such that at least 68% of the energy from a field point would be concentrated on one pixel.

Although large light collection is a design goal, the image quality, image dimension, and pixel pitch have to be considered for a successful diagnostic screening device. The more pixels used to sample the image, the more beneficial it would be for the perspective view synthesis algorithm. Since the pixel pitch criteria is fixed at 5 μm, one method to increase the number of pixels available for sampling the FOV is to have a larger image dimension, which translates to larger magnification in the optical design. The target imaging dimension is set to 2 x 2 mm to match the image dimension of the reference endoscope design in Ref. [3]. This would simplify radiometry simulation comparisons between the proposed 1:1 scale design and the design in Ref. [3]. It is found during the design phase that an increase in magnification is difficult to achieve without increasing the track length. The lower bound on the modulation transfer function (MTF) score criteria is set to 100 lp/mm at 50% modulation. From the field of information theory, this requires a sampling frequency of 200 lp/mm. This corresponds to a sampling period of 5 μm, thus the photo detector area of each pixel should be less than 5 μm in order to achieve this MTF score. The MTF would be chosen from the lowest MTF simulation curve at 50% contrast across the specified field points that were ray traced. The 50% contrast was suggested by Ref. [4] for evaluating MTF. The actual MTF would degrade in practice due to the presence of optical fabrication and mechanical assembly tolerances [5].

Table 3.1. Design constraints based on a balance of image performance, light collection, and practical manufacturing

Evaluation Criteria	Target
RMS spot size	< 5 μm
Image dimension	> 2 mm × 2 mm
MTF	> 100 lp/mm at 0.5 modulation
Track length	< 20 mm, ideally < 10 mm
Radius of curvature	> 1 mm
FOV range	> 15° for both views
Edge thickness	> 0.6 mm
Depth of field	± 2 mm, RMS spot size < 10 μm

The full FOV lower bound on the radial and forward view is 15°×360° and 40°, respectively. Due to the non-real-time nature of the target application, a radial FOV of 15° should be adequate for scene interpretation after the mosaic map has been generated. If wider FOV is to be implemented with the same image dimension, the magnification would decrease. Decrease in magnification implies more stringent MTF criteria would need to be used along with smaller pixel pitch in order to maintain the resolving power of the imaging system. Smaller pixel

pitch translates to lower light collection area for individual pixels, which is undesirable in fluorescence imaging applications.

3.3 Approach

The target application of this thesis is to collect in vivo GI auto-fluorescence emission while achieving modest white light endoscopy image quality. The region of interest is the tissue on the sidewall of the GI tract, the emphasis of the design is placed more on the light collection ability of the sidewall optics. The design flow is illustrated in fig. 3.1.

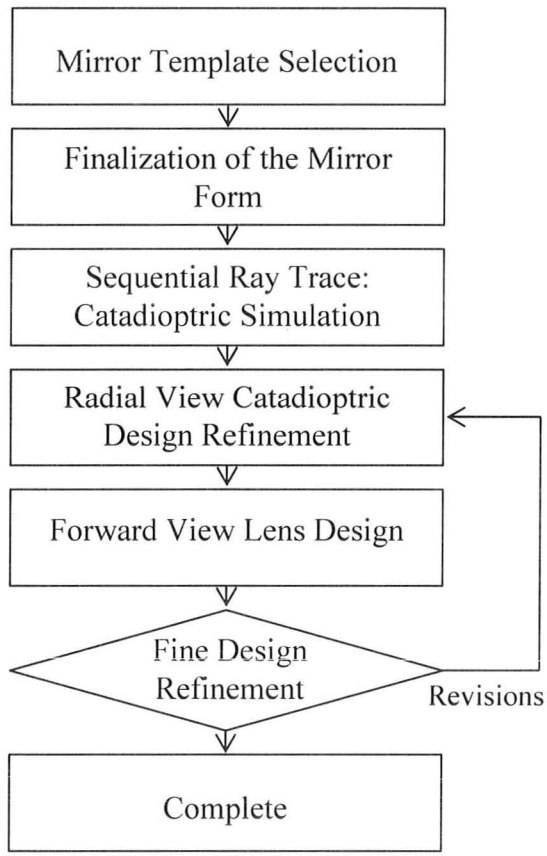

Figure 3.1. Design flow chart.

3.3.1 Mirror Template Selection

Optical design software packages often operate on lens design theory based on concepts such as chief rays, aperture stop, and aberrations. As long the entrance pupil is located at a finite location, the imaging system could be considered as a single-viewpoint (SVP) constrained imaging system; refer to section 2.3.1 for more details. The conic mirror surfaces that satisfy SVP image

formation from Ref. [6] provides a starting point for selecting the mirror. This decision is made to increase the chance of achieving a successful ray trace simulation in sequential ray trace software used in the later steps of design flow as shown in fig. 3.1. Eq. (3.1) and Eq. (3.2) show two independent solutions of the mirror surfaces derived in Ref. [6] that would each independently satisfy the SVP condition. These two independent solutions of mirror surfaces are further isolated and interpreted in terms of the physical shape they represent. It turns out Eq. (3.1) describes hyperbolic and cone surfaces while Eq. (3.2) describes spherical and ellipsoidal surfaces.

$$\left(z-\frac{c}{2}\right)^2-r^2\left(\frac{k}{2}-1\right)=\frac{c^2}{4}\left(\frac{k-2}{k}\right) \qquad k\geq 2 \qquad (3.1)$$

$$\left(z-\frac{c}{2}\right)^2+r^2\left(1+\frac{c^2}{2k}\right)=\left(\frac{2k+c^2}{4}\right) \qquad k>0 \qquad (3.2)$$

When used with a perspective lens camera, or a camera with finite entrance pupil location, the single hyperbolic and single ellipsoidal mirrors could satisfy the SVP condition. When used with an orthographic projection lens camera, or a camera with the entrance pupil located at infinite, the single parabolic mirror could satisfy the SVP condition [6]. The cone mirror can only satisfy the SVP condition at the apex and similarly for the spherical mirror at the center [6]. Thus the cone and spherical mirrors are not practical implementations of SVP constrained imaging system [6]. Details about perspective and orthographic projections are discussed in section 2.3.1.

To help identify potential candidate mirror forms, a chief ray tracer is implemented in MATLAB™; see Appendix A for the complete code. The simulation used a perspective pinhole camera model since only the chief ray need to be traced to estimate the location of the image from given object locations. Recall from section 2.3.1 the perspective projection camera model functionally represents a perspective lens system by tracing only the chief rays. Perspective lens systems have finite entrance and exit pupils. The GI tract is assumed to be cylindrical with radius 7.5 mm and aligned with the optical axis of the mirror and the perspective camera. The mirror surfaces are derived from Eq. (3.2), with the effective pinhole located at the center of the entrance pupil. The amount of chief rays traced is controlled by the FOV of the camera model, which is automatically calculated to utilize the entire mirror of radius 4.5 mm. The SVP degenerate mirror surface solutions, the cone and the sphere, are included in the simulation, but the perspective camera is manually placed at different positions along the optical axis to simulate the non-SVP constrained configures from using the cone and sphere mirror surfaces. The parabolic surface is not included in this chief ray

simulation due to the difficulty in coding locations at infinity and the impracticality of using an orthographic projection lens camera as described in section 2.3.1. Folded parabolic surfaces that satisfy the SVP condition while using a perspective projection camera lens are simulated later in the design phase as described in section 3.3.2.

The chief ray tracer routine first samples the 3D position of the mirror, and then calculates the angle of incidence of the rays that pass through the effective viewpoint of the camera model to the sampled positions on the mirror surface. This information and knowledge of the mirror surface normal vector at each of the sampled positions on the mirror surface would generate the reflected ray vector as described in table 3.2. The reflected rays would undergo a collision detection algorithm with the GI tract cylinder as described in Ref. [7].

Table 3.2. Reflected ray calculation.

Step No.	Procedure
1	Calculate the angle between the surface normal and the z axis of the global coordinate system, which coincides with the optical axis of the mirror. From this information, define a new local coordinate system (LCS) where the z axis coincides with the surface normal. This is a convenient LCS for calculating the angle of reflection due to symmetry about the optical axis.
2	Reference the incident ray with respect to the LCS by rotating the ray vector using the calculated angles from step 1. The incident ray must pass through the effective viewpoint.
3	The reflected ray is calculated by mirroring the coordinates of the incident ray about the optical axis.
4	Reference the calculated reflected ray with respect to the global coordinate system, since the mirror and the object cylinder are reference with respect to the global coordinate system.

The FOV range of the system is calculated in the z direction of the global coordinate system. The FOV start position is taken to be the lowest z value of the ray intersection location with the object cylinder within the simulation. The FOV end position is taken to be the highest z value of the ray intersection location with the object cylinder within the simulation. The FOV range and FOV start position is recorded before the chief ray trace calculation is repeated for different mirror surfaces described by different values of k and c. The k parameter affects the surface shape. The c parameter is the distance from the mirror focus to the effective viewpoint of the camera but it also affects the surface shape. The distance from the camera to the focus of the mirror is also recorded since it gives a sense of the minimum track length required to implement the imaging system. This distance is the parameter c by definition for SVP constrained setups such as single hyperbolic and single ellipsoidal mirror [6], and is manually measured for non-SVP setups that uses the cone and sphere surfaces. The cone, hyperboloid, ellipsoidal, and spherical mirror surfaces are simulated using 16 different

combinations of c and k. The recorded set of FOV start position, FOV range, and estimated track length are then used to determine the most suitable mirror form. First generation M2A^{TM} capsule endoscopes had a track length of 30 mm [8]. The appropriate bounds of the k and c parameters are calculated in MATLAB such that the track length would be below 22 mm. The mirrors have a radius of 4.5 mm and a central opening radius of 1 mm.

The 3D plots in fig. 3.2-3.5 are for visualizing the FOV range and location of selected mirrors. The blue points are the sampled mirror points, the green points are the intersection of the chief rays with the GI tract cylinder.

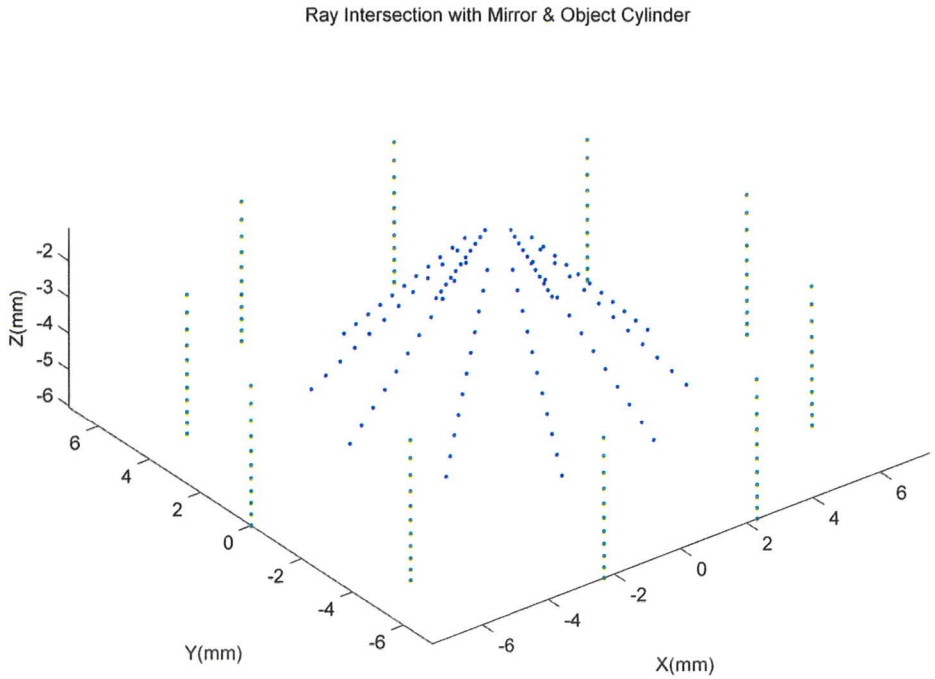

Figure 3.2. This plot visualizes the estimated FOV of the single cone reflector concept imaging system by tracing only the chief ray. The parameters are (k,c) = (4.33,0) and this system is a non-SVP constrained imaging system. The camera distance to mirror focus is 9.67 mm.

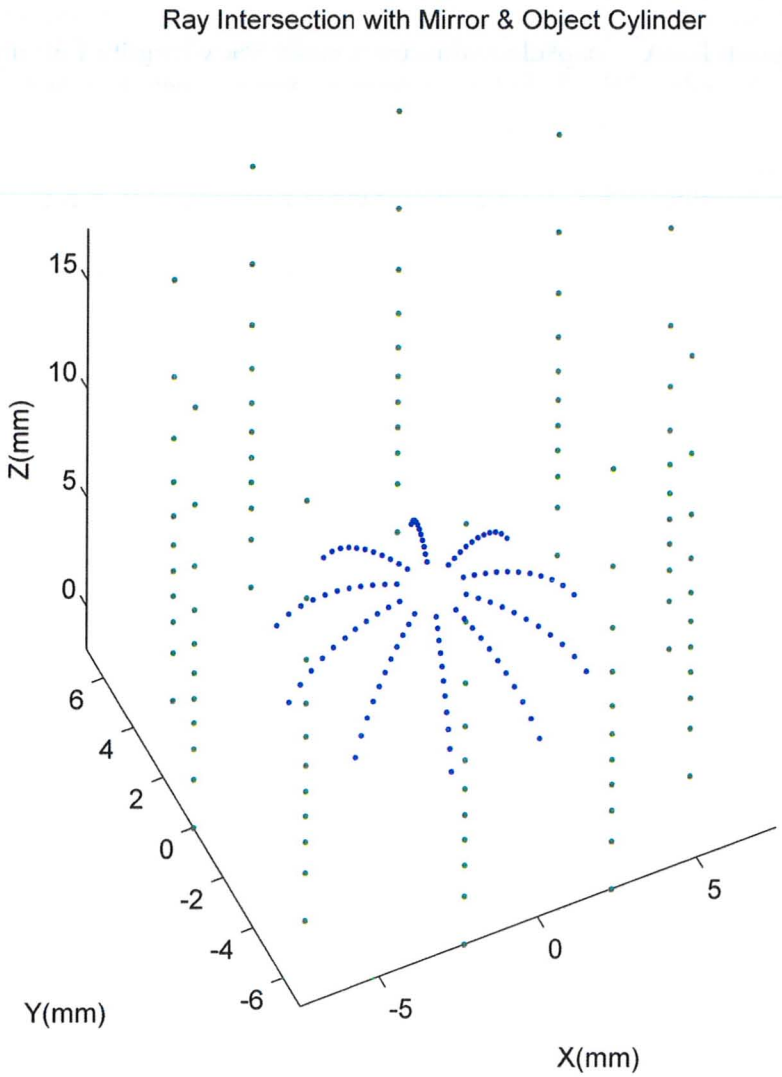

Figure 3.3. This plot visualizes the estimated FOV of the single spherical reflector concept imaging system by tracing only the chief ray. The blue points are locations where the chief ray would intersect the mirror; the green points are locations where the chief rays would intersect the GI tract wall, which is assumed to be cylindrical. The parameters are $(k,c) = (50,0)$ and this system is a non-SVP constrained imaging system. The camera distance to mirror focus is 18 mm. The FOV range at high z values would practically be obstructed by the camera optics.

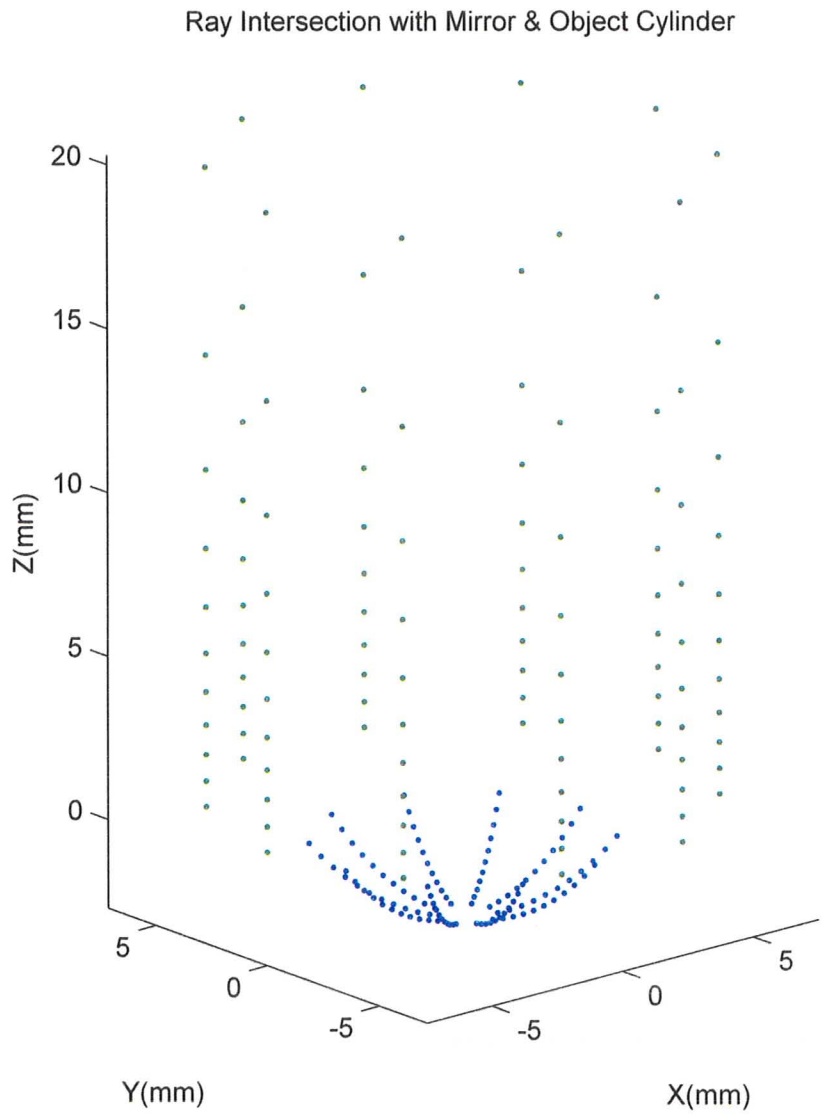

Figure 3.4. This plot visualizes the estimated FOV of the single ellipsoidal reflector concept imaging system by tracing only the chief ray. The parameters are (k,c) = (100,15) and this system is a SVP constrained imaging system. The camera distance to mirror focus is 15 mm. The FOV range at high z values would practically be obstructed by the camera optics.

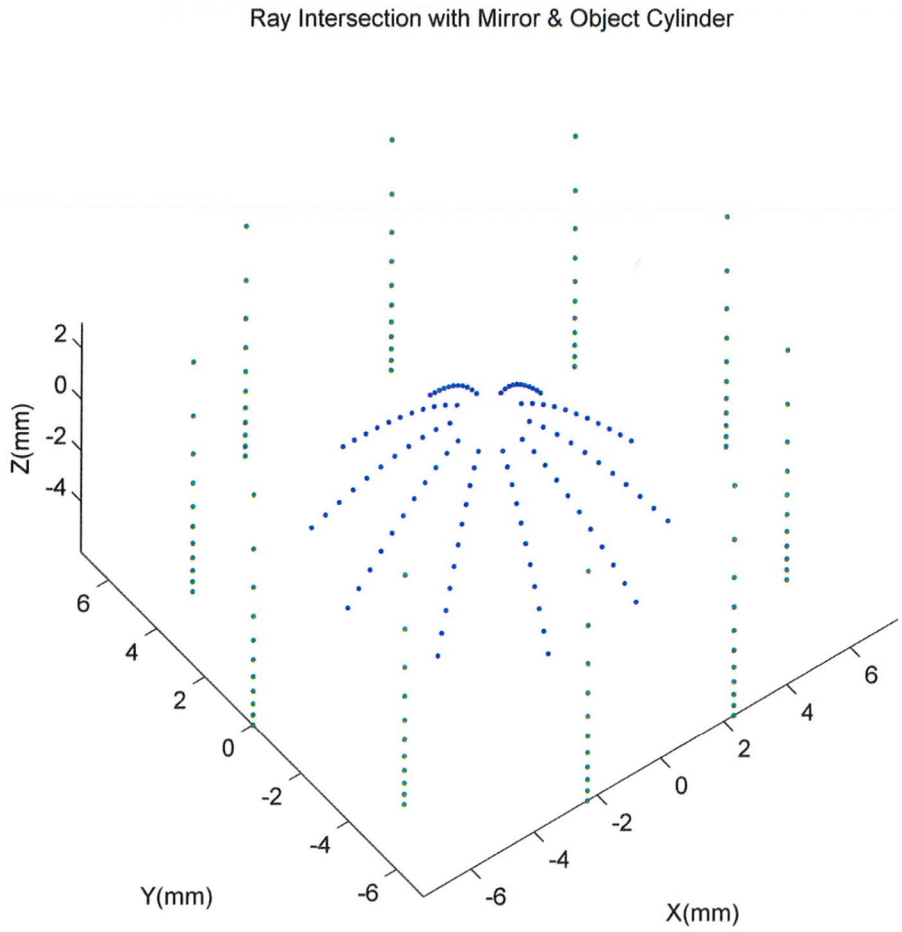

Figure 3.5. This plot visualizes the estimated FOV of the single hyperbolic reflector concept imaging system by tracing only the chief ray. The parameters are (k,c) = (7.33,9.67) and this system is a SVP constrained imaging system. The camera distance to mirror focus is 9.67 mm.

Fig. 3.2-3.5 are chosen from the k and c combination for each surface that had the most uniform sampling of the object cylinder at a radius of 7.5 mm. The elliptical mirror has the largest FOV, but the majority of it would be obstructed by camera optics; and the camera would see itself in the image. The spherical mirror gave large FOV but the camera distance is almost double that of the cone and hyperbolic mirror. The hyperbolic mirror offers a FOV larger than the cone and it is a practical SVP mirror surface solution. The cone mirror and the hyperbolic mirror are the most promising mirror forms for a single mirror based catadioptric system for the target thesis application.

3.3.2. Finalization of the Mirror Form

The simulation of the cone mirror experienced technical difficulties, and it is later confirmed by a support staff that OSLO^{TM} version 6.4.5 has a bug associated with the cone mirror surface, causing the rays to be reflected in non-realistic directions. The hyperbolic mirror is the first mirror surface to be successfully simulated in OSLO^{TM} version 6.4.5. As shown in fig. 3.6, different lens templates are placed in the simulations to evaluate the feasibility of using a single convex hyperbolic mirror for the thesis design. The aberration is found to be unacceptable when compared to table 3.1 for a single mirror with an object to mirror distance of less than 10 mm. The MTF simulation gave 50% modulation at 6 lp/mm for the on-axis field point with the entrance pupil lowered to 50 microns. The other field points generated a ray trace failure due to the presence of severe aberration. It soon became evident that this type of freeform mirror and lens design exploration is inefficient in producing ray trace simulations that would be successful and realistic. The optical design task is thus broken up into two parts; mirror form selection followed by lens design for the selected mirror form.

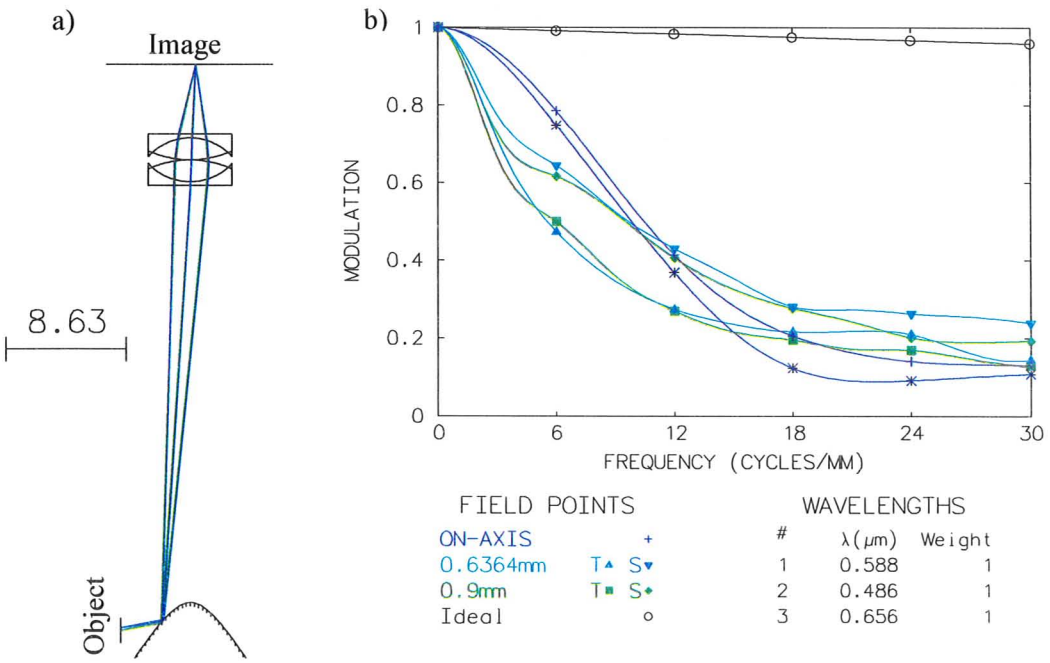

Figure 3.6. OSLO simulation results from a hyperbolic mirror with a magnifier lens, the numerical aperture is extremely small and the system has high aberration. (a) Ray trace layout of the simulation. The distance scale units are in millimeters. (b) MTF score, where *T* is the tangential direction, and *S* is the sagittal direction.

It is explained in section 2.3.4 the use of a mirror to image a field point in an asymmetric way would induce coma aberrations due to large optical path difference between rays within the bundle of light from a single field point. Due to the close proximity of the GI sidewall to the radial view optics, the magnification of the radial view optics would be higher than typical consumer photography cameras where the object is located meters away. Increase in magnification decreases the depth of field [9]. The presence of coma aberration and a short depth of field indicate severe image quality degradation could be expected for the radial optics, as shown in fig. 3.6. Further analysis on the relationship between aberrations and asymmetric usage of curved mirrors conclude an extra mirror with concave reflective surface is required to focus the light diverged from the convex hyperbolic reflector. The use of a folded mirror of opposite concavity in curvature could also partially compensate the aberrations generated from each of the individual mirrors. Another benefit is that light from different field points that pass through folded mirrors of opposite concavity tend to have a more uniform optical path length, which would minimize the aberrations related to uneven optical path length across field points.

Another contributor to severe aberration is the presence of strong lens curvatures, e.g. having a radius of curvature of less than 2 mm. Although strong curvatures on an optical surface contribute to high optical system power and low f-number to help achieve a short track length, the increase in optical system power contributes greatly to the Petzval curvature as well as difficulty in lens fabrication.

Fig. 3.7 is an example of a folded ellipsoidal mirror that has both mirrors and the aperture stop location calculated as described in Ref. [6]. It could be seen here folded ellipsoidal mirrors would utilize the central, or paraxial, region of the second mirror, which would leave no room for the forward view.

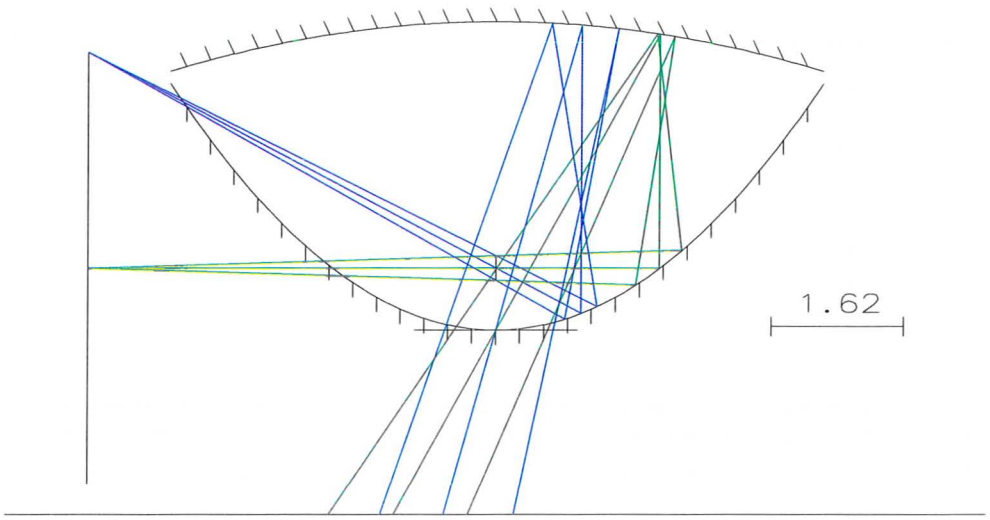

Figure 3.7. Early simulation attempts of a folded elliptical mirror system (units: mm).

The mirror setups shown in fig. 3.8(a) and fig. 3.8(b) are the eventual setup found after exploring several folded designs using SVP mirror theory and lens design theory. The focus of the mirrors and the aperture stop locations are calculated according to the SVP theory and solvable ray trace simulation with smaller aberration than previous attempts.

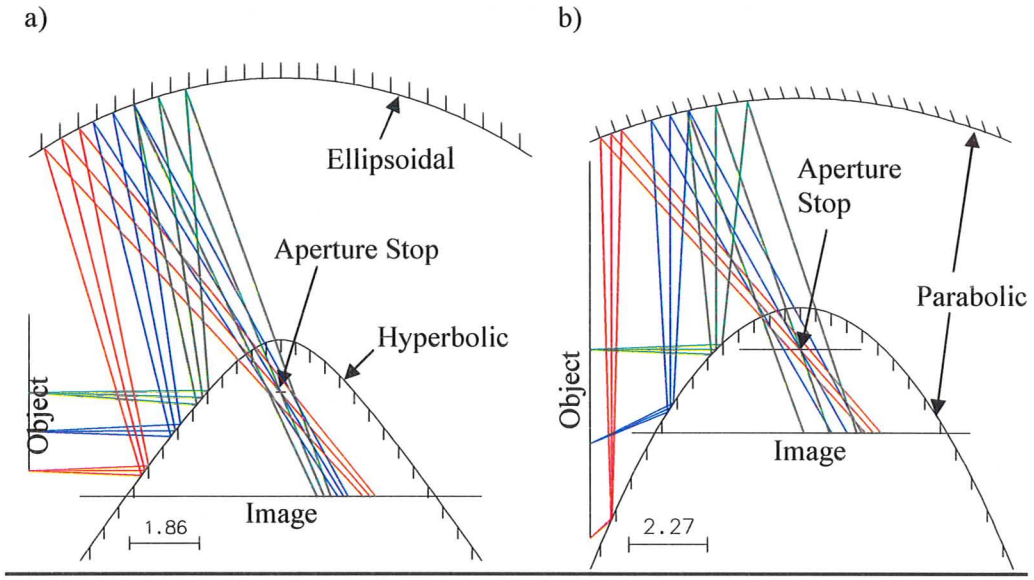

Figure 3.8. Ray tracing with the aperture stop located at the focus of the convex mirror (units: mm) (a) convex hyperbolic and concave ellipsoidal mirrors (b) parabolic mirrors.

Ref. [2] is then discovered at that point in the design process to have already documented the feasibility of using a similar folded mirror design for round table teleconferencing imaging. Ref. [2] also proposed nine other forms of two mirror designs based on different combinations of planar, ellipsoidal, hyperbolic, and parabolic mirrors. In the case of using mirror surfaces that have two finite foci, such as the hyperbolic or ellipsoidal surface, slight modification of the mirror curvature would affect the nominal placement position of the mirror because the focus location would have changed and the second mirror would need to be redesigned or moved to compensate for this. The double parabolic form is chosen to remedy this problem because the chief rays between the mirrors are parallel. The chief rays are parallel because the secondary foci of all parabolic surfaces are at infinity. Fig. 3.8(b) is a ray trace layout of a pair of parabolic mirrors illustrating this effect. Parallel chief rays serve as a convenient visual method of validating the ray trace solution. It also diminishes the effect the distance between the mirrors would have on the chief ray angles. Smaller ray angles translate to less performance degradation susceptibility from the position tolerance of the concave mirror. Parallel chief rays between the mirrors would also simplify the design process because the relationship between FOV and the

individual mirrors are essentially decoupled; focus modification on one of the mirrors would not require a major redesign of the nominal focus of the other mirror. For this thesis work, the ability to design the two mirrors separately adds significant design flexibility.

3.3.3 Sequential Ray Trace: Catadioptric Simulation

The limitations of SVP constrained mirror design described in Ref. [6] are due to the simplified lens camera models used. The perspective projection and orthographic projection functionally represent imaging systems that have finite entrance pupil locations and object space telecentric imaging systems, respectively. These models assume infinite depth of field (DOF) and no aberration. Although there is some discussion about defocusing blur in Ref. [6], there is no detail investigation on the lens implementation. For this thesis work, detailed optical analysis during the lens design is carried out in OSLO^{TM} and ZEMAX^{TM}. The beginning of section 3.3.2 described some preliminary trial and error attempts in the additional of an eyepiece lens template to a hyperbolic mirror, as illustrated in fig. 3.6. However it is only after the folded parabolic mirror form is chosen to be the finalized mirror form, the task of fitting a suitable lens commenced. This is because the focus of both mirrors and the location of the entrance pupil of the lens need to be tuned to match each other, otherwise ray trace failures or presence of severe aberrations would be the likely outcome.

The target application is autofluorescence imaging of the GI tract side wall, which meant the design of the radial view optics would precede the design of the forward view optics. It proved too complicated to simulate two different object planes in the same ray trace simulation in OSLO^{TM} and ZEMAX^{TM}, so the radial panoramic and forward view optical components are simulated in separate files. The back focus distance of the radial view optics would be used as the nominal back focus distance of the forward view optics, so that both views would focus at the same image plane. As discussed in section 2.3.4, the mirrors used in this thesis is utilized asymmetrically in the image formation of a field point, thus the mirrors are primarily used for redirecting the FOV of the lenses while contributing minor focus power to the system optical power in the radial view optical design. Although the lens group is instrumental in correcting the aberrations, but it is a significant contributor of the system optical power in order to keep the track length below 20 mm as specified in table 3.1. The lens group is required to have a sizable FOV because the paraxial region of the mirrors is removed to image the forward view.

Existing wide FOV lens forms from text books and patents are used to integrate into the system as opposed to free form design from scratch. Selected lens forms mentioned in section 2.2.5 as well as other lens forms documented in Ref. [10] such as the dogmar, Cooke Triplet, head-up-display, eyepiece, and

reverse telephoto forms. For the wide FOV lens forms such as dogmar, Cooke Triplet, and reverse telephoto, the track length are too long such that when the design is scaled down to an appropriate size with a track length less than 20 mm, the size of the lens elements approach the manufacture limit. The manufacture limit is taken to be 1 mm radius of curvature and a lens center thickness of 300 microns.

3.3.4 Radial View Design Refinement

Upon integrating the design from Ref. [3] with the folded mirrors, the location of the radial FOV range is found to have an effect on the aberration characteristics. For setups where the FOV positions are located near either of the folded mirrors, the optical path difference (OPD) between the field points is lower than the setup where the FOV positions are located near the center of the two mirrors. Further analysis indicates the OPD relationship between the field points near the two mirrors behave very differently. The OPD is closely related to the formation of several types of aberrations and thus different OPD behaviour would indicate different aberration characteristics [4]. Fig. 3.9(a) illustrates a design where the FOV position is near the bottom convex mirror, and fig. 3.9(b) illustrates a design where the FOV position is near the top concave mirror. Both designs are based on the same folded parabolic mirrors form and uses a starting lens form from Ref. [3], where the final lens form is optimized to minimize aberration. Fig. 3.10(a) is the spot diagram for fig. 3.9(a), and fig. 3.10(b) is the spot diagram for fig. 3.10(b); It is evident that the aberration characteristics are different from the differences in spot diagram shape between fig. 3.10(a) and fig. 3.10(b). This difference in OPD is because the field points make different incidence angles with the bottom mirror as the field point position changes.

The functional effect of three different FOV positions on the radial view is summarized in table 3.3. Case 1 is unsuitable for the final design due to the difficulty in the correction of aberrations of opposite behaviour from the different field point positions across the field of view. Case 2 is featured in fig. 3.9(a) and it has the shortest object to first mirror distance. However, this design requires a larger diameter, longer length, and strongly curved convex mirror. Large OPD between the field points would result from the use of mirrors with strong curvature. In addition, longer longitudinal length mirrors may prove problematic during the removal of the paraxial region as well as the optomechanical assembly of the lens elements. The design in case 3 is featured in fig. 3.9(b) and is chosen for the final design due to the presence of less refractive elements and mild mirror curvature when compared with case 2. The design in case 3 is the one shown in fig. 3.9(a).

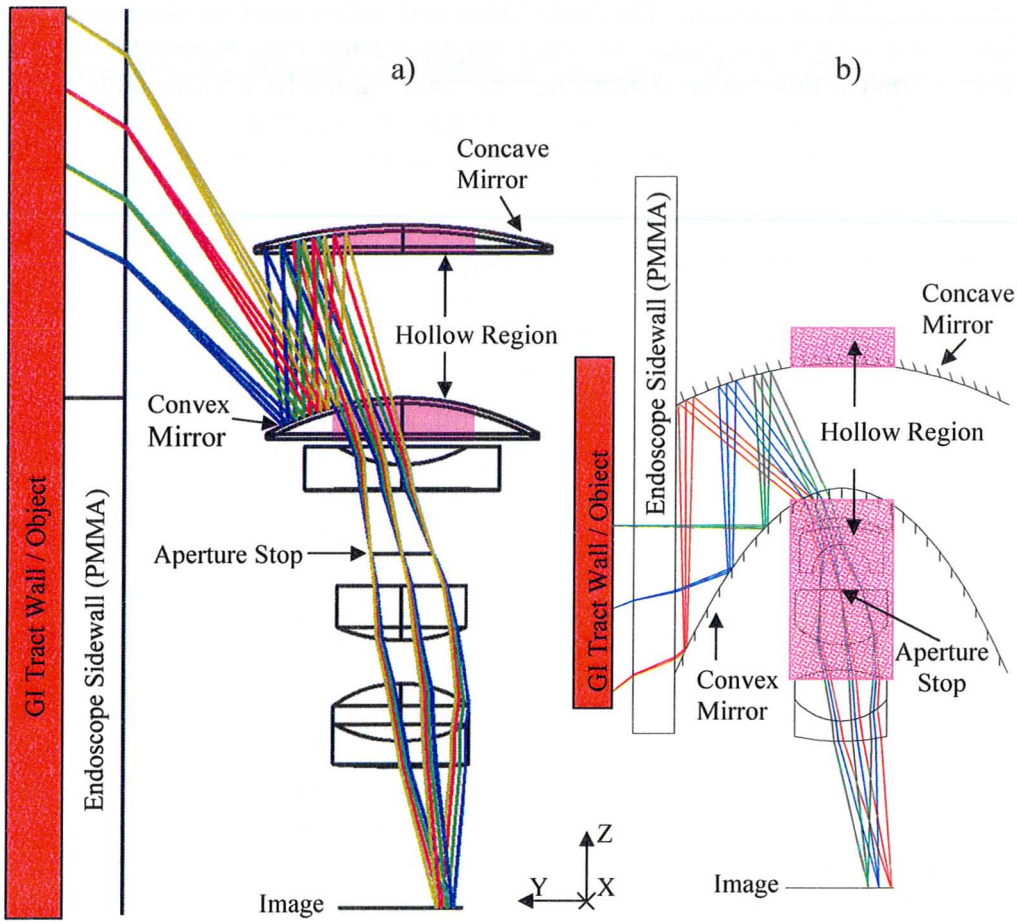

Figure 3.9. Ray trace layout diagrams of two proposed radial view optical designs with (a) FOV range near the concave mirror (b) FOV range near the convex mirror. The shaded mirror regions would be hollowed so light from the forward view could pass. For practical lens edge thickness handling during fabrication, the clear aperture of the last doublet in (b) may need to be smaller than specified here. The scale for (a) and (b) as shown here are different. Both (a) and (b) use a similar coordinate system as shown at the bottom of the figure.

Table 3.3. Effect of FOV position on imaging system.

Case	FOV Location	Effect on imaging system
1	Center of the two mirrors	Two different types of aberration are present, depending on the location of the field points.
2	Near the bottom (convex) mirror	Short distance between optics and object. A large diameter, long longitudinal length, and strongly curved bottom (convex) mirror is required.
3	Near the top (concave) mirror	The top (concave) mirror may obstruct and limit the field of view. Smaller diameter, shorter length, and flatter mirrors can be used.

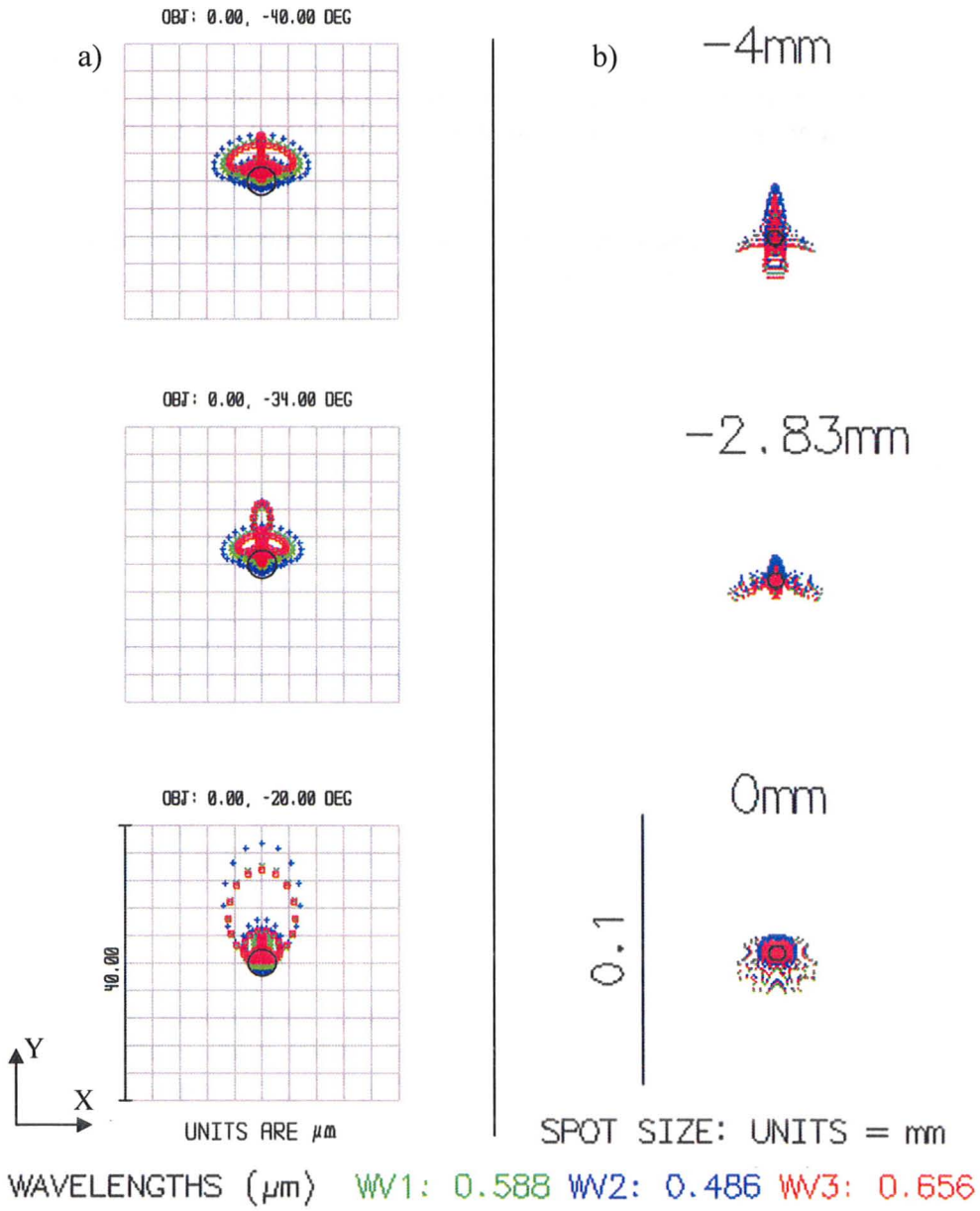

Figure 3.10. Spot diagram at the image surface with at field point positions sampled across the field of view (a) spot diagram for the system shown in fig. 3.9(a), units in microns (b) spot diagram for the system shown in fig. 3.9(b), units in millimeters. Note the difference in the shape and chromatic aberration between (a) and (b). The black circle is the simulated Airy disc radius. The colours correspond to the wavelength legend at the bottom of the figure.

Negative elements are reduced or removed during the lens design modification from the starting template to increase the entrance pupil radius. The final radial view optical design consists of a negative lens in front of a Kellner eyepiece, as illustrated in fig. 3.9(a). The field flattener lens near the imaging plane in the patent is removed to improve the depth of field and to allow practical matching of the back focus between the radial and forward view optics. One method of correcting Petzval curvature without using a field flattener would be to use a strong negative lens with a low incident ray height to avoid significant increase of the overall focal length, similar to the design philosophy of the Cooke Triplet [9]. In the proposed design, the singlet negative lens before the aperture stop contributes to the Petzval curvature reduction, but the EFL is increased by 0.2 mm because the marginal ray height on the singlet is no longer near the paraxial region. This translates to a slight reduction in system optical power, which helped to increase the back focus of the radial view optics to an amount such that it could be matched with the back focus of the forward view optics. This negative lens also regulates other practical design criteria such as the FOV of the refractive group.

The convergent lens elements after the aperture stop in the starting lens template from Ref. [3] shown in fig. 1.2(f) are kept in the proposed design. These elements constitute the Kellner eyepiece lens form. Eyepiece forms are usually suitable for low FOV applications. With reference to fig. 3.9(a), the marginal ray angle incident on the eyepiece is 15°, which is a modest angle of incidence compared to the 63° for the singlet negative lens. The eyepiece is the lens elements below the aperture stop in fig. 3.9(a). The convex surfaces are effective in controlling the coma aberrations while the break in refractive index in the doublet is for astigmatism and field curvature control [10].

3.3.5. Forward View Lens Design

The two major challenges of the forward view optics design is the matching of its back focus to that of the radial view optics, and the implementation of a wide FOV with the central opening of the parabolic mirrors acting as the limiting field stop. The forward view optical design consists of the entire radial view refractive elements as well as four additional refractive elements in front of the mirrors, where the overall form resembles a reverse telephoto design. The first lens is the optical dome of the endoscope with the material set to Zeonex™ R48 medical grade plastics. The first two lenses compress the rays to obtain a moderate FOV. The third lens helps to correct the Petzval curvature. The fourth element has an aspherical front surface that correct other primary aberrations to increase the MTF. The curvature of the back surface of the fourth element controls the back focal length. The ray trace layout of our proposed forward view lens design is shown in fig. 3.11. Note the coordinate

system is different from the radial view simulation because the forward view is conducted in a separate simulation file.

The design goal of the forward view is to implement a wide FOV imaging system while satisfying the image performance criteria specified in table 3.1. Wide FOV is hard to implement since the central opening of the concave mirror acts as the field stop of the forward view optical system, and modification of that mirror opening would affect the radial view optical design drastically. Divergent lenses are added in from of the radial view lens group to compress the FOV. This decrease the size of the image of the aperture stop when viewed from the perspective of an object in the forward field of view. Recall from section 2.1.3, the image of the aperture stop is the *entrance pupil* when the observer is located at the object. The presence of divergent lenses in the forward view lens group would decrease the entrance pupil of the forward view optical design, which implies less light collection, lower numerical aperture, and less aberration. Thus the MTF for the forward view optical design would achieve a higher score than the radial view optical design.

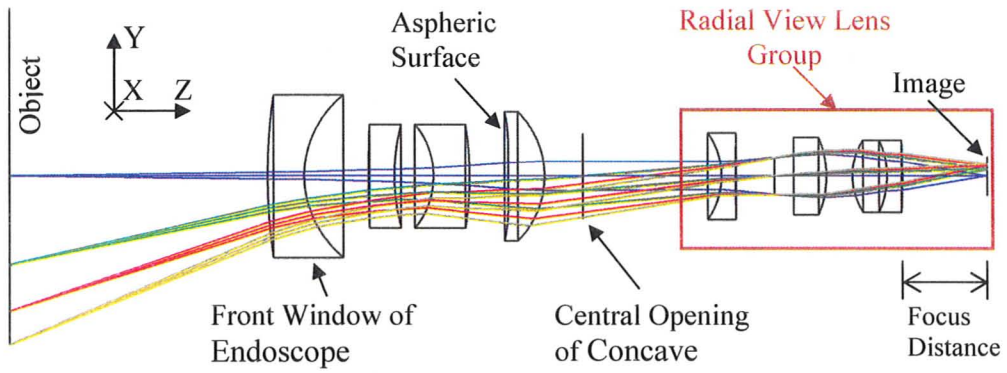

Figure 3.11. Ray trace layout diagram for the forward view optical design. The radial view lens groups marked in the orange box are the same lenses used in radial view design in fig. 3.9(a). The four elements from the left are unique to the forward view optical design. They provide the necessary degrees of freedom to match the back focus to the image plane.

3.4. Sequential Ray Trace Simulation Results

The prescription of the radial view simulation shown in fig. 3.9(a) is summarized in table 3.4. Surface 1 is set to be the global coordinate system and a rotation of 90° in the direction of x is set on surface 3. The prescription of the forward view simulation shown in fig. 3.11 is summarized in table 3.5, with surface 7 being the aspheric surface. These two designs combine to form the proposed 1:1 scale endoscope objective design of this thesis work. The conic

constant refers to the surface type; parabolic surfaces have a conic constant of *-1* and spherical surfaces have a conic constant of *0*.

Table 3.4. Prescription for the 1:1 scale radial view simulation.

Surf No.	Radius of Curvature (mm)	Thickness / Airspace (mm)	Material	Surface Radius (mm)	Conic Constant
Object	Inf	0	-	6.203505	0
1	Inf	1	R48 [1]	10	0
2	Inf	4.5	Air	10	0
3	4.2	-2.688	Mirror	2.205	-1
4	8.4	3.7625	Mirror	2.415	-1
5	-2.044	0.385	N-FK5	1.05	0
6	43.75	1.05	Air	1.57	0
7 (aperture stop)	Inf	0.525	Air	0.5	0
8	Inf	0.875	N-LAK8	1.05	0
9	-2.77	0.7	Air	1.05	0
10	1.8445	0.931	N-FK5	1.1	0
11	-2.3205	0.42	N-SF6	1.1	0
12	-16.5865	2.2785	Air	1.1	0
Image	Inf	-	-	1	0

[1] Refractive index $N_d = 1.533200$, Abbes Number $V_d = 56$, dPgF = 0.5474.

Table 3.5. Prescription for the 1:1 scale forward view simulation.

Surf No.	Radius of Curvature (mm)	Thickness / Airspace (mm)	Material	Surface Radius (mm)	Conic Constant
Object	Inf	7	-	4.537476	0
1	15.75	1	R48	2.2	0
2	2.8	1.75	Air	2.2	0
3	47.75	0.7	R48	1.4	0
4	5.6	1.05	Air	1.4	0
5	-2.2	0.98	N-FK5	1.4	0
6	-9.24	1.05	Air	1.4	0
7 [1]	110.063	0.98	N-FK5	1.75	0
8	-2.47	1.05	Air	1.75	0
9	Inf	3.7625	Air	1.155	0
10	-2.044	0.385	N-FK5	1.176	0
11	43.75	1.05	Air	1.176	0
12 (aperture stop)	Inf	0.525	Air	0.5	0
13	Inf	0.875	N-LAK8	1.05	0
14	-2.77	0.7	Air	1.05	0
15	1.8445	0.931	N-FK5	0.98	0
16	-2.32	0.42	N-SF6	0.98	0
17	-16.5865	2.2785	Air	0.98	0
Image	Inf	-	-	0.525	0

[1] Even aspheric surface with the following parameters; 4^{th} order: -0.011356, 6^{th} order: -3.974953e-004, 8^{th} order: 8.697507e-006.

The simulated MTF is shown in fig. 3.12 and the simualated spot diagrams are shown in fig. 3.13. The MTF is calculated by taking the modulus of

the optical transfer function (OTF), which is derived in the field of Fourier Optics theory [11]. The tangential MTF represents the resolution performance in the y direction and the sagittal MTF represents the resolution performance in the x direction [12]. This translates to the tangential MTF of a lens is the MTF measured in the direction along concentric circles from the image center, and the sagittal MTF is the MTF measured in the direction along the radial direction away from the image center. The image surface coordinate system for radial view and forward view are shown in fig. 3.9(a) and fig. 3.11, respectively.

From table 3.1, the specified pixel pitch is 5 μm with an imaging dimension of 2 mm × 2 mm. From Nyquist information theory, a pixel pitch of 5 μm corresponds to Nyquist spatial frequency of 100 lp/mm and an image of 400 × 400 pixels. The Nyquist frequency is the highest frequency that could be theoretically reconstructed without ambiguity or aliasing. With reference to fig. 3.12 and fig. 3.13, the spatial frequency at 50% modulation is 160 lp/mm and 120 lp/mm for the forward and radial views, respectively. Although this score is higher than 100 lp/mm, it is common for the performance of the lens to drop in practice due to manufacture and alignment tolerances [5]. The largest RMS spot sizes are 1.9 μm and 3.3 μm for the forward and radial views, respectively. Their corresponding Airy disc radiuses are 2.1 μm and 1.8 μm. This translates to more than 68% of the rays from a point object would be concentrated onto an area smaller than the specified pixel pitch of 5 μm. Table 3.6 summarizes the evaluation parameters of the endoscope design from Ref. [3], radial view of the proposed design, and forward view of the proposed design.

Table 3.6. Simulation results of the template lens patent with the proposed system.

	Patent	Radial View	Forward View
Track length (mm)	9.94	13.7	19.5 [1]
Entrance pupil radius (mm)	0.1	0.19	0.15
Working F/#	4.93	2.46	2.99
Full FOV (deg)	110	20 [2]	44
EFL (mm)	1	1.12	0.9
Depth of field (mm) [3]	4.3-inf	0~4.7 [4]	1-1000
NA, object space	0.019	0.026	0.014
NA, image space	0.1	0.16	0.17
Simulated MTF at 0.5 modulation	50 lp/mm	120 lp/mm	160 lp/mm

[1] This is the total track length of the proposed design.

[2] The field angle range is 20°~40°.

[3] This is the distance over which the RMS spot size is below 10 μm.

[4] Measured in the radial direction from the sidewall of the endoscope. The endoscope has a radius of 5.5 mm.

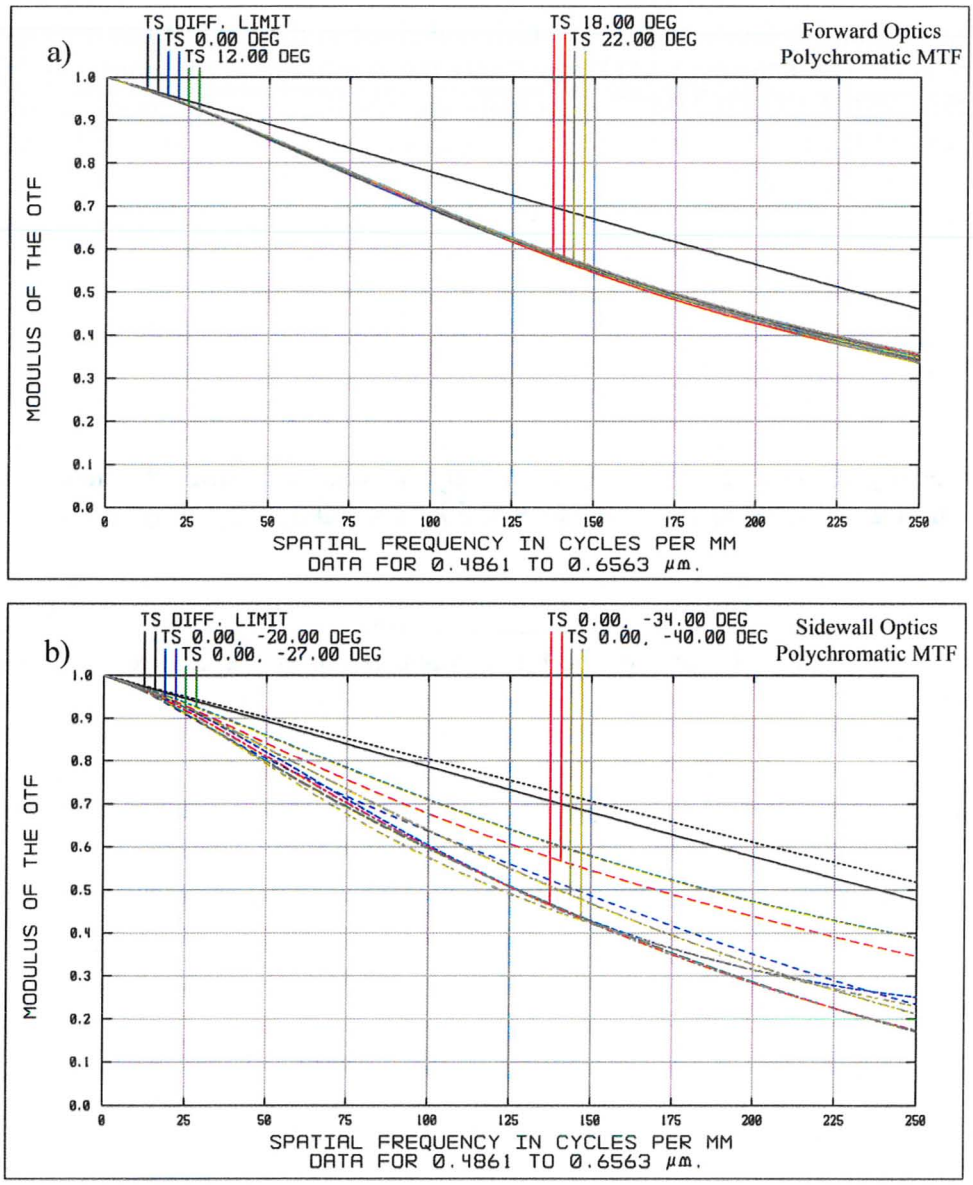

Figure 3.12. Simulated MTF for (a) forward view and (b) radial view. *T* is tangential MTF curve at the specified field point. *S* is sagittal MTF curve at the specified field point. Field points are specified in terms of field angle (measured in *DEG*, degrees). *DIFF. LIMIT* is the theoretical diffraction-limited MTF curve. The *MODULUS OF THE OTF* is another technical name for the MTF.

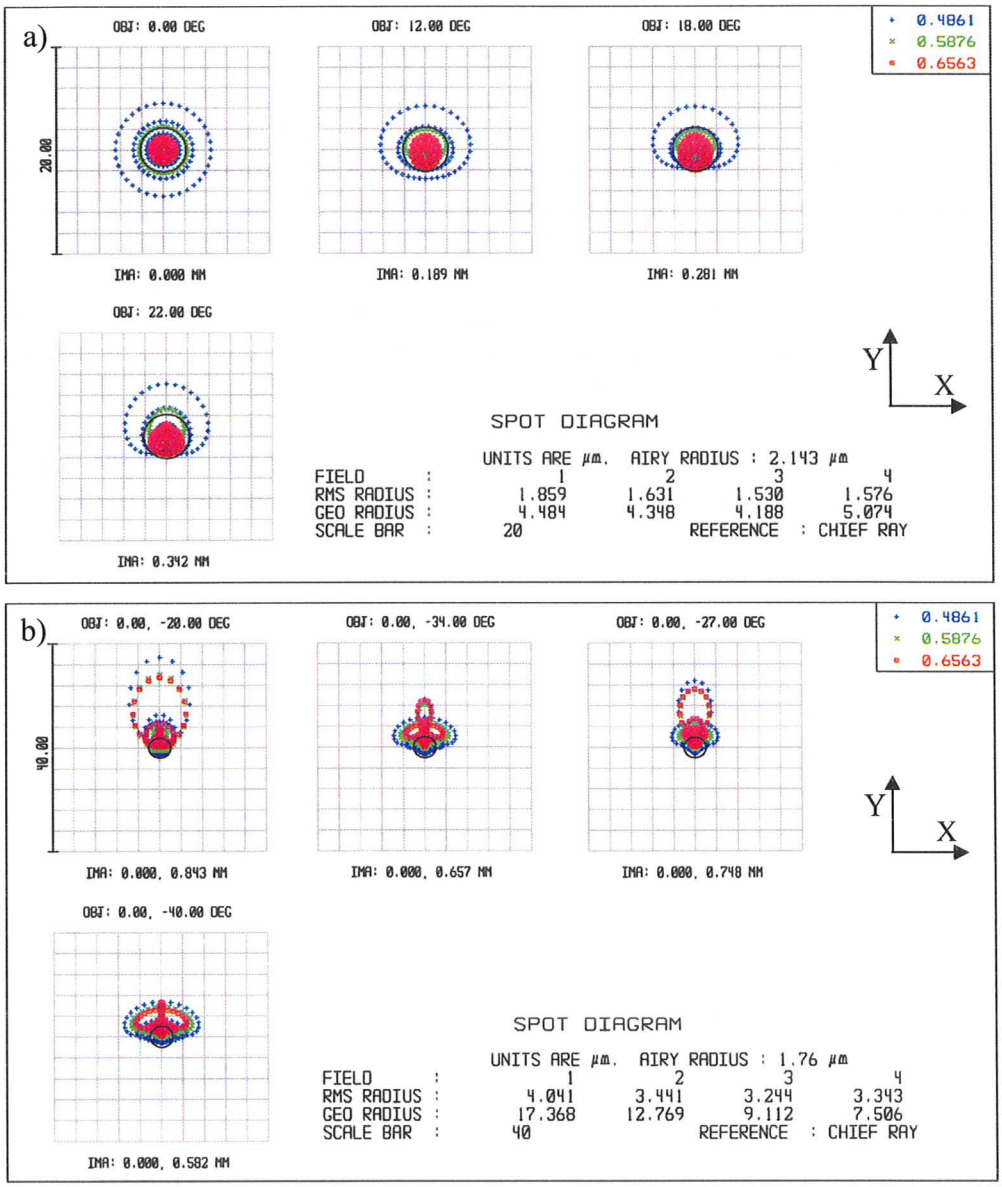

Figure 3.13. Image surface spot diagram for (a) forward view and (b) radial view. The black circle is the simulated Airy disc radius. The colours correspond to the wavelength legend at the top right of this figure; all units in microns. *RMS radius* is the RMS spot size, *GEO radius* is the distance from the centroid to the furthest ray intersection with the imaging surface. *IMA* describe the location of the centroid on the imaging surface. *OBJ* describe the location of the field points in terms of field angles. The forward view optics has smaller spot sizes than the radial view optics.

3.5 Radiometry Simulation Method & Simulation Results

The proposed radial view design and the endoscope objective design described in Ref. [3] are entered into LightTools™ for radiometry simulation. Ref. [3] is chosen since it is the design from which the proposed radial view lens design is derived from. As discussed in section 1.2, the reference endoscope objective designs in table 1.3 and fig. 1.2 all exhibit a similar reverse telephoto form where the divergent lens group is placed in front of the convergent lens group, thus Ref. [3] should be a valid representation for conventional forward-viewing endoscope objectives. Fictitious point sources with 100 watts evenly distributed over its entire projection sphere are used as field points along the GI tract wall. The large power distribution of 100 watts is chosen to avoid the computation of extremely small numbers, thus this measure of light collection serve only as a relative comparison. The range of the simulation field points is marked in fig. 3.14 and fig. 3.15.

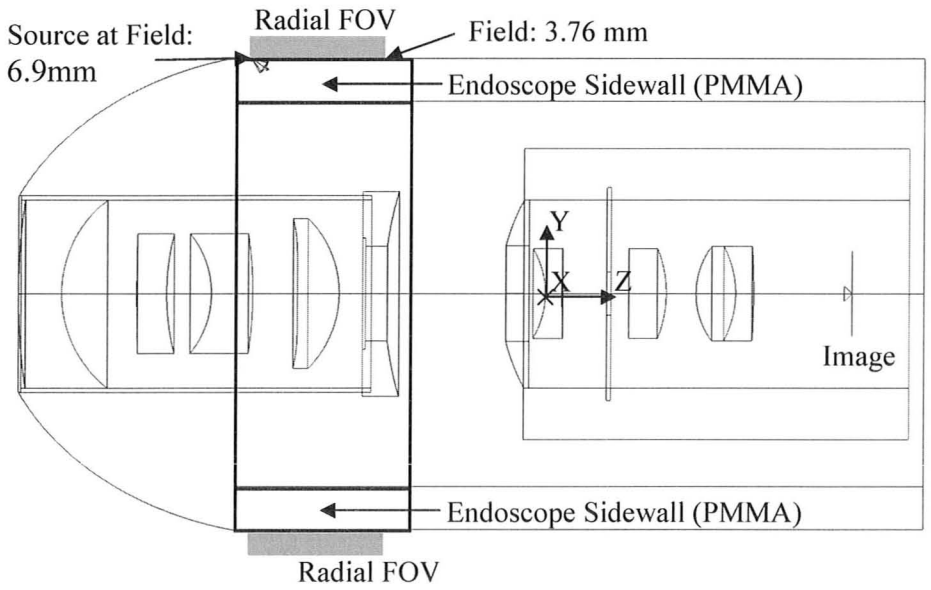

Figure 3.14. Radiometry simulation setup for radial view optical design. The simulated point source is located at the field position of 6.9 mm from global axis in the negative *z* direction in this figure. Other field positions in table 3.7 are sampled from the region shade in gray, which represents the radial view FOV. The PMMA tube emulates the sidewall of the endoscope.

Polymethyl-methacrylate (PMMA) is the material used to simulate the transparent sidewall of the endoscope as suggested in Ref. [13]. The GI tract wall is assumed to be collapsed around the endoscope and approximated by a cylindrical surface, thus the field points are parallel to the optical axis of the endoscope. The irradiance (W/mm^2) at the imaging plane of 2 mm × 2 mm of a

sample field point is shown in fig. 3.16, and the results over a range of field points is summarized in table 3.7. Similar radiometry simulation results of the proposed design without the 1 mm thick PMMA tube are also shown in table 3.7. It demonstrates the behaviour of the light collection simulation is similar when the tubing material is changed to air, thus similar tubing materials may be used with the proposed design with little impact on the overall light collection characteristic.

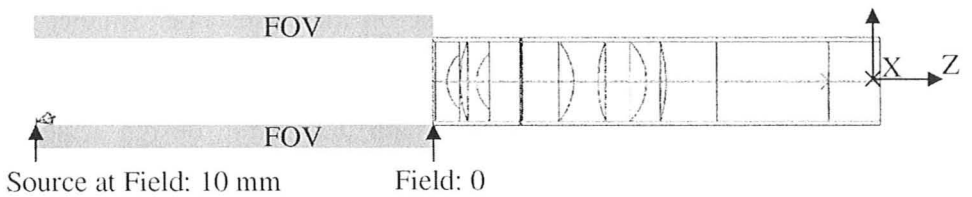

Figure 3.15. Radiometry simulation setup for the design in Ref. [3]. The field points are measured in the negative z direction from the surface of the first lens.

Table 3.7. Radiometry simulation results from the radial view from the proposed design, proposed design without the PMMA tube, and the reference patent endoscope objective described in Ref. [3].

Ref. [3]		Proposed Design		Proposed Design w/o Tube	
Field	W/mm^2	Field	W/mm^2	Field	W/mm^2
0.5	1.5	3.76	0.22	3.76	0.18
1.5	0.53	4.5	0.16	4.5	0.19
3	0.21	5.3	0.14	5.3	0.13
5	0.089	6.1	0.11	6.1	0.12
6.9	0.052	6.9	0.094	6.9	0.095

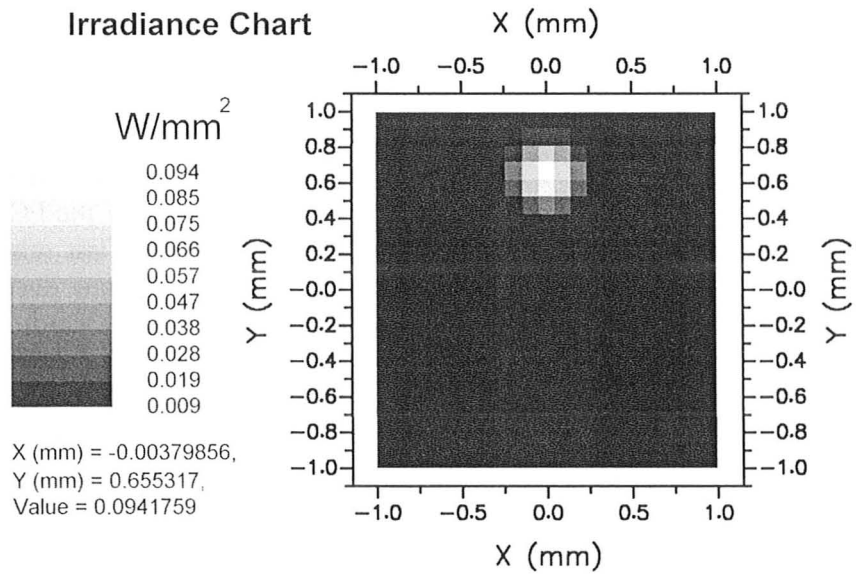

Figure 3.16. Irradiance plot of the imaging plane of the setup in fig. 3.15.

As shown in table 3.6, the track length of the proposed system is 19.5 mm, which is unacceptable for capsule endoscopy. The proposed design is not scaled down further due to practical issues with present day lens fabrication technology [5]. To show the effect on lower scaled design and light collection, designs at 90%, 80%, 70%, 60%, and 50% of the original scale are performed. The point source remained at a radius of 5.5 mm from the optical axis of the endoscope since the endoscope itself will most likely still require a diameter of 8 mm ~ 11 mm, and the GI tract may not totally collapse on the endoscope. Smaller scaled design would have smaller aperture stop diameter, which meant ray trace simulations based on geometric ray propagation would be increasingly unreliable once as the diffraction-limit is approached with decreasing design scales. The radius of the Airy disc is similar in size to the total spot size of the 50% scale design as shown in fig. 3.17, thus LightTools™ should still be able to provide a reliable estimate of the light collection ability up to the 50% scale, but any geometric ray propagation based ray trace analysis without diffraction analysis would be unreliable for designs smaller than 50% scale. The results are summarized in table 3.8.

Table 3.8. Radiometry simulation results from different lower scale versions of the proposed design.

	Irradiance (mW/mm^2)					
Field Position (%)	0.5 Scale	0.6 Scale	0.7 Scale	0.8 Scale	0.9 Scale	1.0 Scale
0	66	88	110	140	160	220
23.6	56	76	98	120	140	160
49.0	52	69	85	99	120	140
74.5	42	55	72	91	95	110
100	44	62	62	70	76	94

Referring to table 3.7 and fig. 3.14, the starting FOV is at 3.76 mm and ending FOV is at 6.9 mm for the original scale. The absolute field positions would change according to each of the scaled down simulations, thus the field positions for these simulations are expressed in terms of percentage; 0% is the field position at the start of the FOV and 100% is the field position at the end of the FOV. At a field position of 100%, or the field position farthest from the first mirror, the bundle of light from a single field point tend to be vignetted, thus during lens optimization the sampling of the field positions is slightly biased towards 0%. An imaging system is *vignetted* when off-axis objects near the edge of the FOV do not pass enough light to the image surface, thus the edge of the image would appear darker.

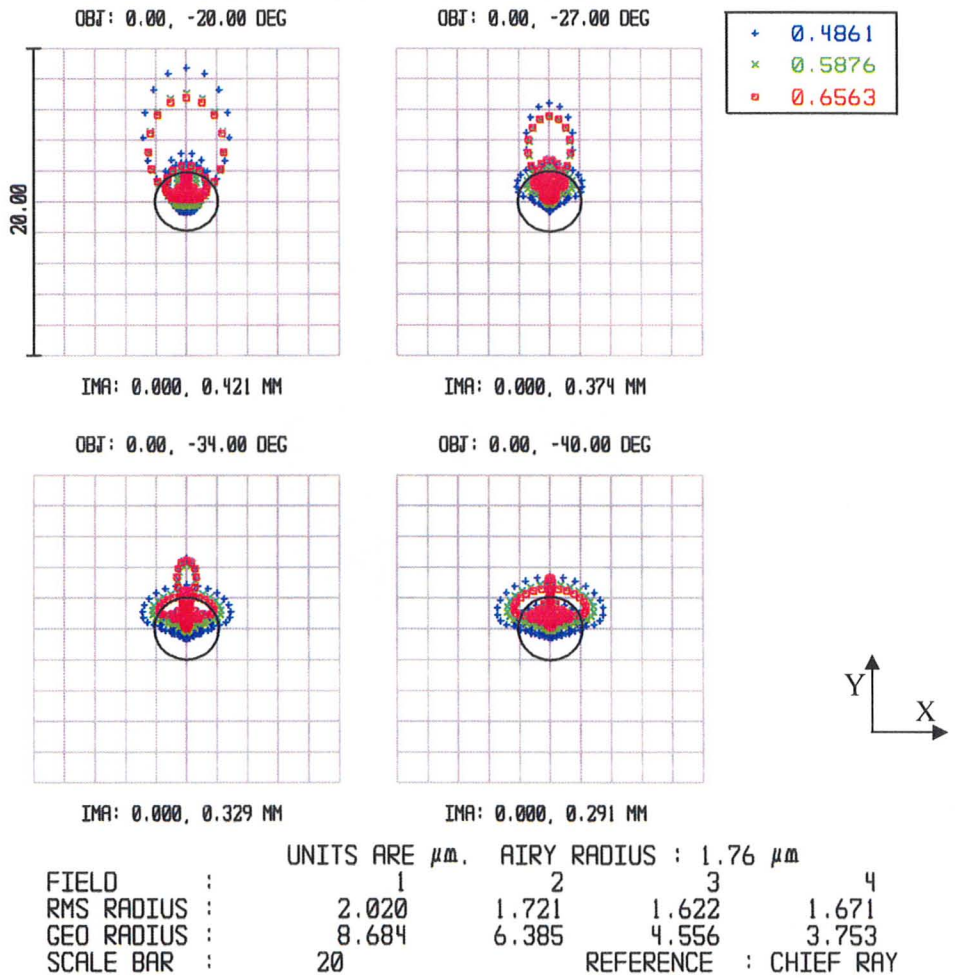

Figure 3.17. The spot diagram plot of the 50% scaled proposed design. The Airy disc is indicated by the black circle. Its size and the total spot size are similar.

Fig. 3.18 is a 3D bar chart visualization of the data in table 3.8. In general, lower light collection occurs for field locations that are further from the first mirror, which are field points near the 100% field position. Lower light collection also occurs as the design is scaled down.

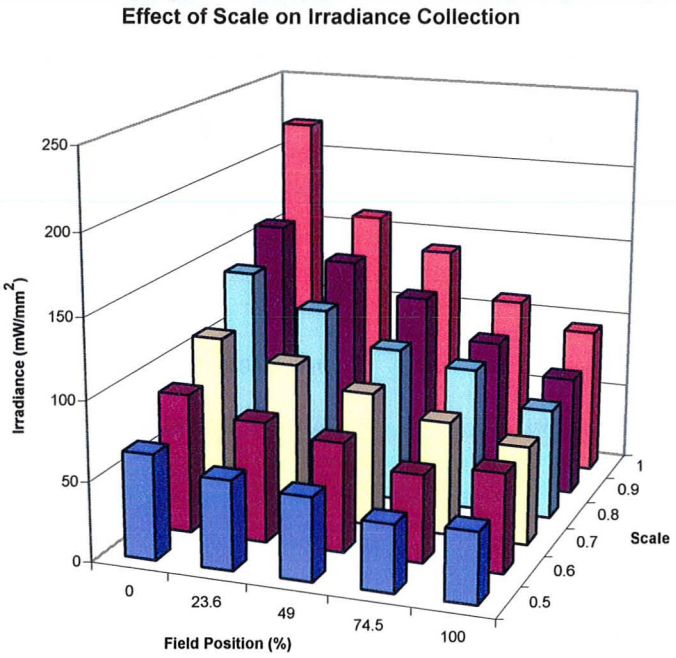

Figure 3.18. 3D bar chart of the data in table 3.8.

3.6. Discussion & Conclusion

The intended application of the proposed design is for non-real-time GI tract screening purposes, where the endoscope would be moved around the GI tract. The image acquired from the proposed system would have the central circular region of the image allocated for the forward view, and the rest of the region of the image allocated for the radial view. The radial imagery would require digital image processing to generate a perspective view of the scene. The ability to do this is important since the human eye interprets imagery based on perspective projection. The FOV between the forward and the radial view is discontinuous, thus there will be a blind spot region. The presence of the blind spot could be remedied by using image processing to generate a mosaic GI tract map using the images acquired as the endoscope traverse through the GI tract. The mosaic of the images would occur in a non-real-time manner as a post processing step to the screening.

With reference to the design prescription in table 3.4 and 3.5, the radius of curvature of the last doublet is severe (1.84 mm). For practical edge thickness, the clear aperture would likely need to be smaller than shown in fig. 3.9(a). Vignetting would occur for the field point represented by the blue rays. Attempts in splitting the power of the doublet proved to be unsuccessful since it is

instrumental in coma aberration correction. The non-reflecting portions of the mirror should undergo anti-reflection treatment to reduce stray light.

From table 3.6, the track length of the proposed design is 19.5 mm, which is double the track length of the design from Ref. [3]. The concave mirror in the proposed design could not have a shorter focal length than the distance between the folded mirrors due to practical optomechanical issues on the assembly of the negative singlet lens. Thus the refractive group contributes a sizable portion of the focus power of the system, while the mirrors provide some focusing power and FOV redirection of the refractive group. The diameter and track length of typical capsule endoscopes lie between 9 mm ~ 11 mm and 12 mm ~ 26 mm, respectively [14,15]. The maximum track length of capsule endoscope optics should be less than 15 mm in order to have room for other components, e.g. antennas and batteries. Although the track length of the proposed design is 19.5 mm, it should be suitable for catheter based devices. The forward view MTF score in table 3.6 is much higher than the MTF of the endoscope patent design described in Ref. [3]. This is a consequence of the reverse telephoto lens form where the divergent lens group is placed before the aperture stop. This decreases the entrance pupil size of the forward view optical design which has a similar effect as stopping down the iris to reduce light and increase the image quality. Since the forward view optics is not optimized for light collection but for large field of view, this trade off of light collection for image quality and wider FOV is deemed acceptable.

As shown in table 3.7, the proposed design would have irradiance values of around 150 ± 70 mW/mm^2 to image 3.14 mm of the GI tract. Forward view wide-angle endoscope objectives could achieve higher light collection than the proposed design at object distances very close to the lens (< 3 mm), and it could achieve comparable irradiance collection at depths 3 mm ~ 5 mm. Its irradiance also decreases drastically with increase distance from the lens. As shown in table 3.6, the design from Ref. [16] does not have a RMS spot size smaller than 10 μm at distances less than 4 mm from the lens. Although the radial FOV of the proposed design can only image 3.14 mm of the GI side wall, it collects light in a more uniform manner compared to the forward endoscope described in Ref. [3].

The results in table 3.8 show maximum light collection occurs at field points closest to the first mirror, due to the shorter optical path length. Recall tissue auto-fluorescence emission is isotropic and thus a point source may be used to approximate its effect, and the irradiance of a point source decays with increasing distance. There is approximately a reduction in maximum light collection reduction by a factor of 3.3, and minimum light collection reduction by a factor of 2.1 when the design is scaled down to 50%. The track length at 50% scale would be 9.75 mm, which is comparable with the track length of Ref. [3].

Although large light collection is a design goal, the image quality, image dimension, and pixel pitch have to be considered for a successful diagnostic

screening device. The more pixels used to sample the image, the more beneficial it would be for the view synthesis algorithms described in chapter 5. Larger imaging dimension and magnification would be set as criteria for future designs. This would allow the pixel pitch to increase and relax the constraints on RMS spot size. The entrance pupil radius could then be increased until the MTF drops below the specified spot size criteria. In the case the pixel pitch is to remain the same, a larger image dimension would provide room for more pixels which could benefit the view synthesis algorithm.

3.7 References

1. Christiane Gimkiewicz, Claus Urban, Edith Innerhofer, Pascal Ferrat, S. Neukom, G. Vanstraelen, Peter Seitz (2008). Ultra-miniature catadioptrical system for an omnidirectional camera, *Proceedings of SPIE*, 6992.
2. S. K. Nayar, V. Peri (1999). Folded Catadioptric Cameras. *IEEE Conference on Computer Vision and Pattern Recognition, CVPR 1999)*, 217-223.
3. Patent: US 7486449, Objective Lens for Endoscope, and Imaging Apparatus for Endoscope using the same, 3-2-2009.
4. Warren J. Smith (2008). *Modern Optical Engineering*. McGraw-Hill Professional.
5. Robert E. Fischer, Biljana Tadie-Galeb, Paul R. Yoder (2008). *Optical System Design*. McGraw-Hill Professional.
6. S. Baker, S. K. Nayar (1999). A Theory of Single-Viewpoint Catadioptric Image Formation. *International Journal on Computer Vision*, 35, 175-196.
7. Christer Ericson (2005). *Real-Time Collision Detection*. Morgan Kaufmann.
8. Moussa Kfouri, Ognian Marinov, Paul Quevedo, Naser Faramarzpour, Student Member, Shahram Shirani, Louis W. C. Liu, Qiyin Fang, M. Jamal Deen (2008). Toward a Miniaturized Wireless Fluorescence-Based Diagnostic Imaging System.
9. Sidney F. Ray (1994). *Applied Photographic Optics: Lenses and Optical Systems for Photography, Film, Video and Electronic Imaging*. Focal Pr.
10. Warren J. Smith (2004). *Modern Lens Design*. MgGraw Hill Professional.
11. Frank L. Pedrotti, Leno M. Pedrotti, Leno S. Pedrotti (2006). *Introduction to Optics*. Benjamin Cummings.
12. Herbert Gross, Hannfried Zugge, Martin Peschka, Fritz Blechinger (2007). Aberrations. In Herbert Gross (Ed.), *Handbook of Optical Systems*. Wiley-VCH.
13. Ou-Yang Mang, Shih-Wei Huang, Yung-Lin Chen, Hsin-Hung Lee, and Ping-Kuo Weng (2007). Design of Wide-Angle Lenses for Wireless Capsule Endoscopes. *Optical Engineering*, 46, 103002-1-103002-11.
14. E. J. Seibel, R. E. Carroll, J. A. Dominitz, R. S. Johnston, C. D. Melville, C. M. Lee, S. M. Seitz, M. B. Kimmey (2008). Tethered capsule endoscopy, a low-cost and high-performance alternative technology for the screening of esophageal cancer and Barrett's esophagus. *IEEE Transactions on Biomedical Engineering*, 55, 1032-1042.
15. M. Simi, P. Valdastri, C. Quaglia, A. Menciassi, P. Dario (2010). Design, Fabrication, and Testing of a Capsule With Hybrid Locomotion for Gastrointestinal Tract Exploration. IEEE/ASME Transactions on Mechatronics, 15, 170-180.

Chapter 4
Prototype Development

Chapter 3 documented the design and optimization of a dual-view endoscope objective through theoretical simulations. This chapter would address the verification of the simulation methods that is introduced in chapter 3. The expected deviations between a manufactured prototype and the simulated design could be caused by the presence of tolerance in the manufactured prototype [1]. The aperture stop diameter is small enough such that the proposed endoscope objective optical design approaches the diffraction-limit, e.g. the Airy disc radius is almost as large as the root mean square (RMS) spot radius. Thus the verification of the proposed simulation methods from chapter 3 is important to determine if the general concept of the dual-view endoscope objective concept presented in fig. 1.4 is feasible in practice.

The proposed 1:1 scale endoscope objective design from chapter 3 use lenses with diameters that range between 1.8 mm ~ 4.4 mm. At lens diameters below 5 mm, lenses may be diamond turned or molded [1] using moldable glass or plastic material. Molded lens fabrication cost is approximately $14,000 USD per mold setup, as verbally suggested by Rochester Precision Optics. All the optics shops we have contacted have declined to provide written quotation on a 1:1 scale prototype due to insufficient budget. To address the validity of the simulation methods within a feasible budget, a 3:1 scaled-up prototype of the proposed design is created with modified design criteria to place an emphasis on manufacture economic feasibility. After discussions with a number of customized optics vendors, we selected the Instrument Technology Research Center (ITRC) of the National Applied Research Laboratories (Hsinchu, Taiwan, Republic of China) to fabricate the prototype. We have closely worked with the ITRC team supervised by Dr. Donyau Chiang on the final optomechanical design and revised the optical design to match the fabrication capabilities of the ITRC. The prototype consists of a set of lens and mirror assembly held in place by multiple lens barrels and spacers that are joined by a single outer barrel casing. Fig. 4.1 is a photograph of the completed prototype.

The revised design specifications for prototype development are described in section 4.1. The prototype design process, as well as the tolerance simulation methods and simulated results are discussed in section 4.2. The empirical verification of the MTF against the simulated results from section 4.2 is carried out in section 4.3. The simulation and empirical verification of the light collection ability of the manufactured prototype across the designed field of view is documented in section 4.4.

a)

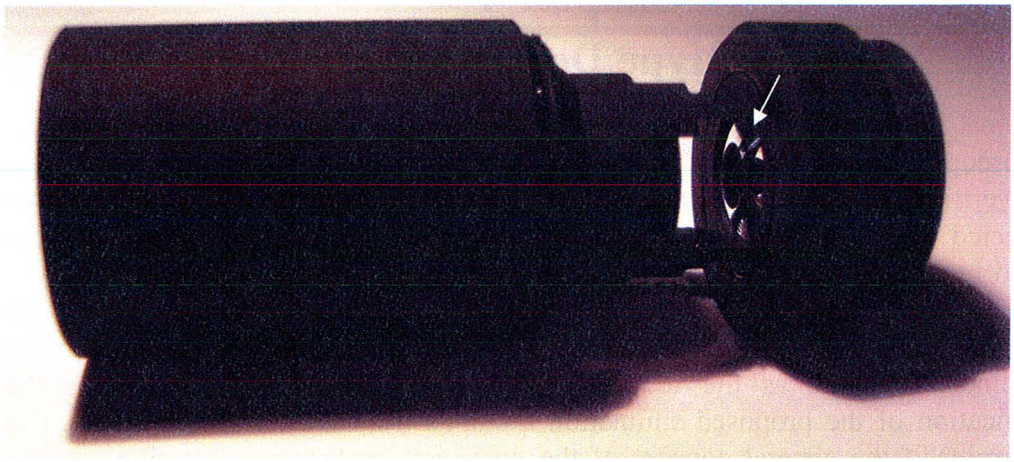

b)

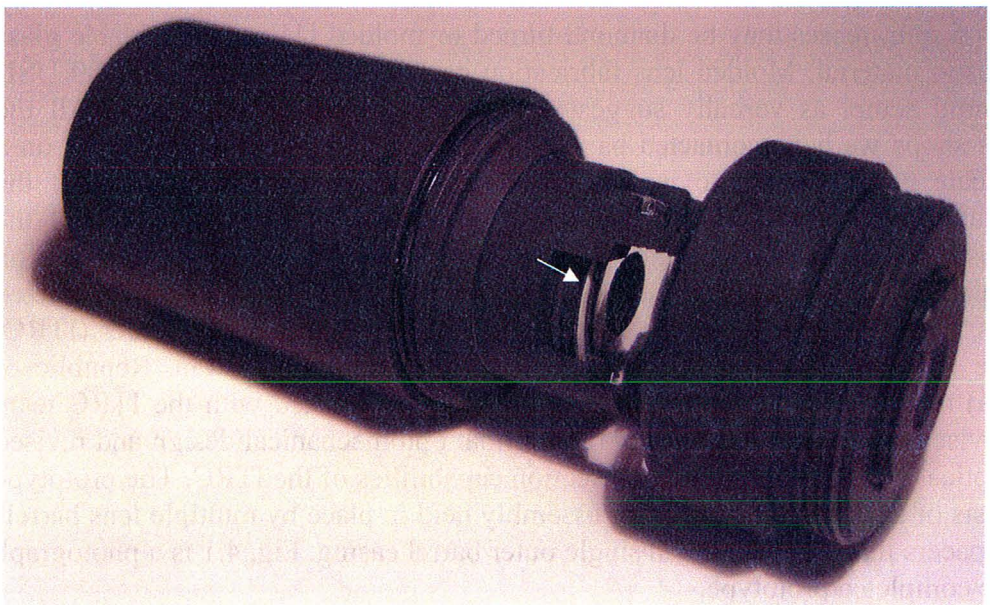

Figure 4.1. Photographs of the finished prototype imaging system. The white arrows point to the (a) convex mirror (b) concave mirror.

4.1 Prototype Design Specification

The prioritized designs goals are to lower the cost of fabrication and assembly as well as to keep the prototype design similar to the proposed 1:1 scale design. Table 4.1 summarizes the evaluation and fabrication constraints for the

prototype. The image quality is evaluated using spot diagrams and modulation transfer function (MTF). The Mightex Monochrome 1.3 Megapixel USB CMOS camera (MCE-B013-U) is used to interface with the prototype imaging system in fig. 4.1. This camera has a pixel pitch of 5.2 μm and an image dimension of 6.66 mm × 5.32 mm. To retain similarity between the 1:1 scale design and the prototype, the upper bound of the RMS spot size is set to 5.2 μm such that at least 68% of the energy from a field point would be concentrated on one pixel. The lower bound of the nominal MTF score before tolerance at 50% modulation is set to 60 lp/mm. The depth of field is the range of object depth position over which a specified performance criterion of having a RMS spot size less than 12 μm is satisfied.

The decrease in tolerance requirements would lead to a decrease in fabrication cost as well as overall image quality, thus after the tolerances are set, Monte Carlo variations of the nominal prototype design are created and the mean MTF over the design variations is set to not drop below 30 lp/mm. Tolerances for each element are either tighten or loosen until the mean MTF is above 30 lp/mm. The depth of field criteria is increased so the empirical verification can be performed over a greater range of distances. Aluminum substrate and enhanced aluminum coating is specified for both mirrors, which provides adequate reflection in the visible range at a cost effective price point. ITRC later upgraded the coating to silver to ensure adequate reflection could be achieved.

Table 4.1. Design constraints based on a balance of image performance, similarity to proposed 1:1 scale design, and optimized cost.

Evaluation Criteria	Target
RMS spot size	< 5.2 μm
Image Dimension	> 5.32 mm × 5.32 mm
Nominal MTF	> 60 lp/mm @ 0.5 modulation
Toleranced Average MTF, Radial View	> 30 lp/mm @ 0.5 modulation
Toleranced Average MTF, Forward View	> 35 lp/mm @ 0.5 modulation
Radius of curvature	> 5 mm
Center thickness	> 1.10
Edge thickness	> 0.6 mm
Radial Depth of Field	± 5 mm or larger, RMS spot size < 12 μm
Forward Depth of Field	± 40 mm or larger, RMS spot size < 12 μm

4.2 Prototype Design

The following topics are investigated for their effectiveness in lowering the manufacture cost and achieve the constraints shown in table 4.1: lens material, tolerance, and the incorporation of stock lenses into the design. Fig. 4.2 is the ray trace layout diagram for the radial view prototype design.

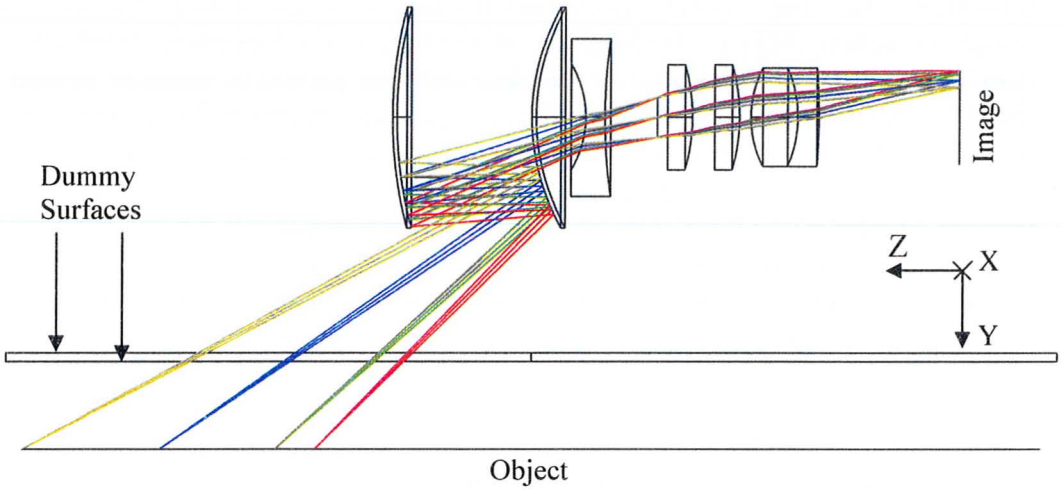

Figure 4.2. Radial view layout of prototype.

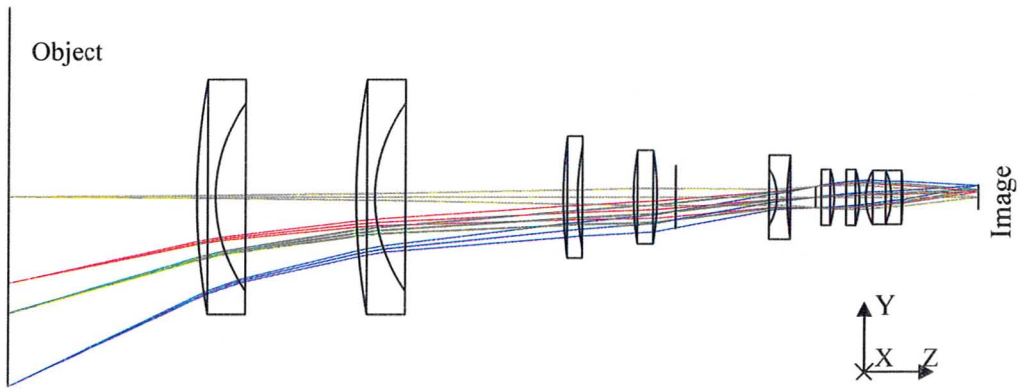

Figure 4.3. Forward view layout of prototype.

Fig. 4.3 is the ray trace layout diagram for the forward view prototype design. The polymethyl-methacrylate (PMMA) tubing that would act as the sidewall of the endoscope as shown in fig. 3.14 is taken out of the prototype design as per the suggestion of the ITRC due to the high possibility of image degradation in the radial view. The simulation surfaces used to simulate the PMMA tubing remains in the prototype simulation but its material is set to air. These dummy surfaces exist in the simulation to enforce a necessary 90° coordinate system rotation in Zemax™. The 3:1 scale prototype design has some minor differences when compared to the 1:1 scale design, but the overall form is similar. The 1:1 scale design layouts are shown in fig. 3.9a and fig. 3.11 for the radial view and the forward view, respectively.

4.2.1. Design Modification

Molded lens fabrication is economically unfeasible for academic research prototyping purposes where low quantities of highly customized lens designs are desired, thus plastic lens materials are excluded from the prototype design. The radial view optical design prescription of the 3:1 scale prototype is shown in table 4.2. Flat surfaces have a radius of curvature (ROC) of infinity (Inf). Surface 1 is set to be the global coordinate system and a rotation of 90° in the direction of x is set on surface 3. Surfaces 1-2 are the dummy surfaces used for coordinate rotation. The forward view optical design prescription of the 3:1 scale prototype is shown in table 4.3. In comparison with the prescription of the 1:1 scale design shown in table 3.4, the Zeonex™ and N-LAK8 materials used in the 1:1 scale design are replaced by N-BK7 in the 3:1 scale design. N-BK7 is one of the most economic optical material according to Ref. [1] and Ref. [2]. The refractive index of N-BK7 is at 1.5168 and the refractive index of N-LAK8 is at 1.713 [2], the ROC would need to be shortened to increase the focus power of the lens.

Table 4.2. Prescription for the 3:1 scale radial view Zemax™ simulation.

Surf No.	Radius of Curvature (mm)	Thickness / Airspace (mm)	Material	Surface Radius (mm)	Conic Constant
Object	Inf	5	-	29.067	0
1	Inf	0.48	Air	30	0
2	Inf	13.4	Air	30	0
3	12	-7.68	Mirror	6.3	-1
4	24	10.75	Mirror	6.3	-1
5	-5.85	1.1	N-FK5	3	0
6	31.12	3	Air	4.5	0
7 (aperture stop)	Inf	0.6	Air	1.128	0
8 (1)	Inf	1.42	N-BK7	3	0
9 (1)	-10.85	1.26	Air	3	0
10 (1)	Inf	1.42	N-BK7	3	0
11 (1)	-10.85	0.66	Air	3	0
12	6.18	2.66	N-FK5	2.8	0
13	-7.02	1.2	N-SF6	2.8	0
14	-34.73	8	Air	2.8	0
Image	Inf	-	-	2.66	0

(1) Surfaces 13-14 and 15-16 represent two Edmund Optics No. 45232 stock lenses.

The only element that used N-LAK8 in the 1:1 scale design is the plano-convex lens right after the aperture stop; refer to table 3.4, table 3.5, fig. 3.9(a), and fig. 3.11 for a review of the 1:1 scale design. It is the first lens in the Kellner eyepiece form and contributes more to focus power than aberration control, thus it is possible to split this optical element into multiple elements of longer focal length to reduce the spherical aberration and Petzval field contribution from having a single short focal length lens [1]. The number of elements after splitting is set to two to lessen the increase on the track length from having more lens

elements. Both of these two elements have their radius of curvature set to be identical and lens optimization is run to find a suitable lens curvature. From table 3.4, the original N-LAK8 plano-convex lens has a radius of curvature of 2.77 mm, which corresponds to a radius of curvature of 8.31 mm in the 3:1 scaled design. The stock lens with the most similar focal length is found to be Edmund Optics 45232, which has a radius of curvature of 10.85 mm [3]. This is not an exact fit to the calculated curvature, so the stock lenses are entered into ZEMAX™ to replace the N-LAK8 lens, and the lens optimization routine is run with the curvature and thickness of the custom rear doublet lens set to variable.

Table 4.3. Prescription for the forward view Zemax™ simulation. Surfaces 1-2 are the dummy surfaces used for coordinate rotation. Flat surfaces have a ROC of infinity (Inf).

Surf No.	Radius of Curvature (mm)	Thickness / Airspace (mm)	Material	Surface Radius (mm)	Conic Constant
Object	Inf	20	-	20.10	0
1	69	2	N-BK7	12.5	0
2	17.12	15	Air	10	0
3	69	2	N-BK7	12.5	0
4	17.12	20	Air	10	0
5	50.33	1.5	N-BK7	6.5	0
6	30	6	Air	5.5	0
7 (1)	30.58	2.5	N-BK7	5	0
8 (1)	-30.58	2	Air	5	0
9	Inf	10.75	Air	3.36	0
10	-5.85	1.1	N-FK5	3	0
11	3112	3	Air	4.5	0
12 (aperture stop)	Inf	0.6	Air	1.128	0
13 (2)	Inf	1.42	N-BK7	3	0
14 (2)	-10.85	1.26	Air	3	0
15 (2)	Inf	1.42	N-BK7	3	0
16 (2)	-10.85	0.66	Air	3	0
17	6.18	2.66	N-FK5	2.9	0
18	-7.02	1.2	N-SF6	2.8	0
19	-34.73	8	Air	2.9	0
Image	Inf	-	-	1.3	0

(1) Surfaces 7-8 represent one Edmund Optics No. 63571 stock lens.
(2) Surfaces 13-14 and 15-16 represent two Edmund Optics No. 45232 stock lenses.

The general procedure used for incorporating stock lenses into the design is to conduct a first wave of lens optimization that generate the nominal stock lens curvatures, and then conduct a second wave of lens optimization that refine other custom lens surfaces to accommodate for the difference in the stock lens and nominal lens curvatures. The Edmund Optics No. 63571 stock lens is incorporated into the design using a similar approach. This procedure is also applicable to the replacement of expensive glass materials to cheaper alternatives. The asphere element used for the forward view from the 1:1 scale design is replaced by a

spherical meniscus lens of cheaper glass material following a similar procedure. Manual constraints are placed on the optimization of the meniscus lens such that the front and back surfaces would not have similar radius of curvatures; it is difficult to center the surfaces during fabrication and testing for meniscus lenses with concentric surfaces [4].

4.2.2. Sequential Ray Trace Simulation Results

The 3:1 prototype simulation results are summarized in table 4.4. Most of the quantities are related to the results from the 1:1 scale design by nearly a factor of three. The simulation results of the 1:1 scale is shown in table 3.5. The average diffraction MTF is the performance criterion used by the tolerance simulations described in section 4.3.3. It is calculated in ZEMAX™ under tolerance criterion simulation with the settings ***Criterion:*** *Diff. MTF Avg*, ***Sampling****: 2*, ***Comp:*** *Paraxial Focus*, and ***Fields:*** *User Defined.* It is important to select user defined fields since the radial view simulation is asymmetric in the *x* and *y* directions. The spot diagrams and the MTF plots are shown in fig. 4.4 and fig. 4.5, respectively.

Table 4.4. Simulation results of the 3:1 prototype endoscope objective

	Radial View	Forward View
Track length (mm) [1]	38.27	83.07
Entrance pupil radius (mm)	0.84	0.67
Working F/#	4.14	4.26
Full FOV (deg) [2]	23	50
EFL (mm)	3.52	2.8
Depth of field (mm) [3]	2-11 [4]	6-73
NA, object space	0.017	0.008
NA, image space	0.12	0.12
Average Diffraction MTF at 0.5 modulation	91 lp/mm	105 lp/mm
Nominal MTF at 0.5 modulation	73 lp/mm	68 lp/mm

[1] This is the total track length of the proposed design.
[2] The field angle range is 26°~49°.
[3] This is the distance over which the RMS spot size is below 10 μm.
[4] Measured in the radial direction from the sidewall of the endoscope. The endoscope has a radius of 13.88 mm.

4.2.3. Tolerance Simulations

Monte Carlo tolerance analysis methods use probability to generate a number of unique variations of the nominal optical design; each design has randomly perturbed surfaces that are governed by a specified probability function. This method essentially simulates a large number of lens simulations that spawn from perturbing each optical surface of the nominal optical design within the specified tolerance. Specified evaluation criterion is then computed across all perturbed variations of the optical design, and the statistics of the evaluation criterion is displayed as the output. The output would provide the most probable

performance one may expect when the specified tolerance is applied to the simulated optical design. Due to the large computational resources required, it is typical to only evaluate and record one performance criterion per simulation.

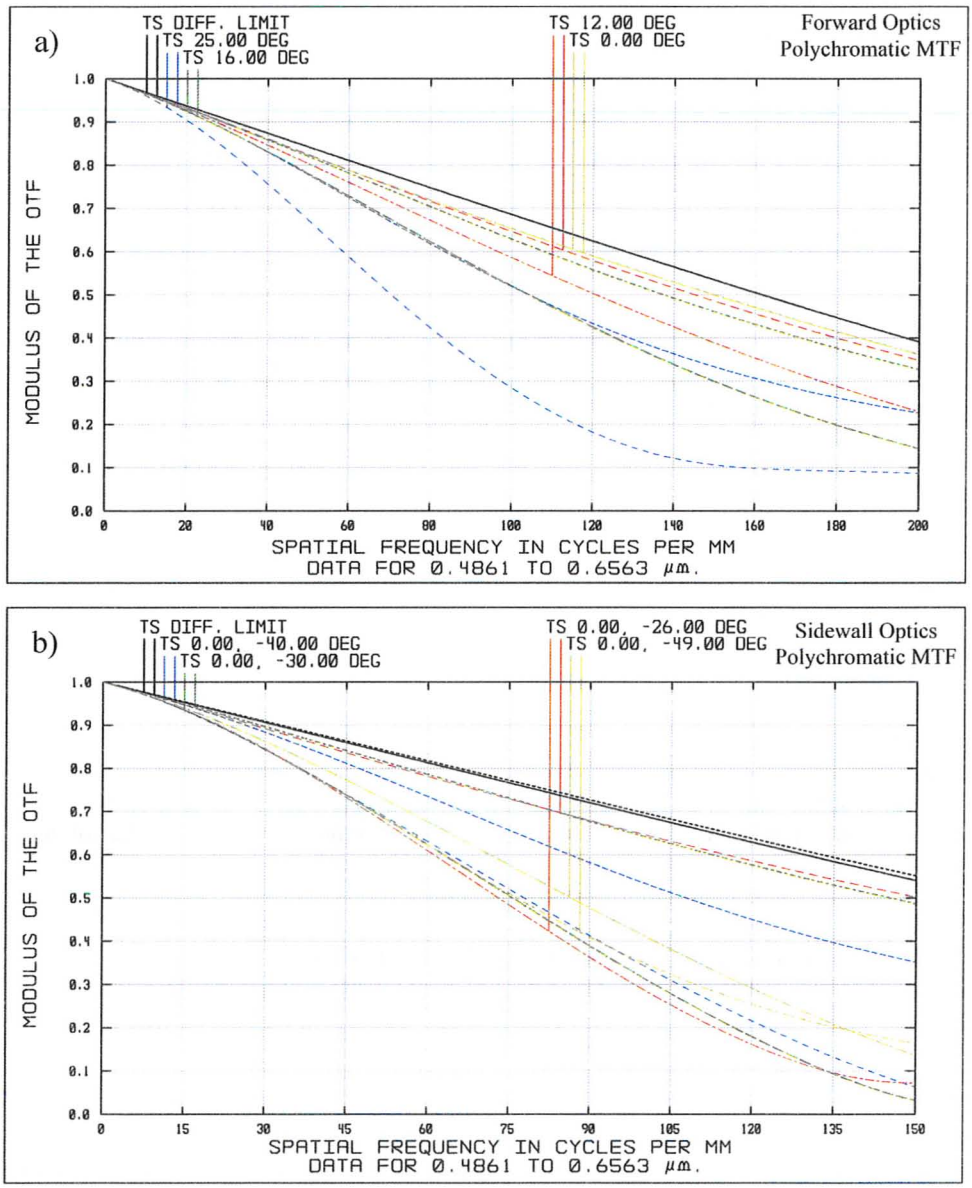

Figure 4.4. Simulated MTF for (a) forward view and (b) radial view. *T* is tangential MTF curve at the specified field point. *S* is sagittal MTF curve at the specified field point. Field points are specified in terms of field angle (measured in *DEG*, degrees). *DIFF. LIMIT* is the theoretical diffraction-limited MTF curve. The *MODULUS OF THE OTF* is another technical name for the MTF.

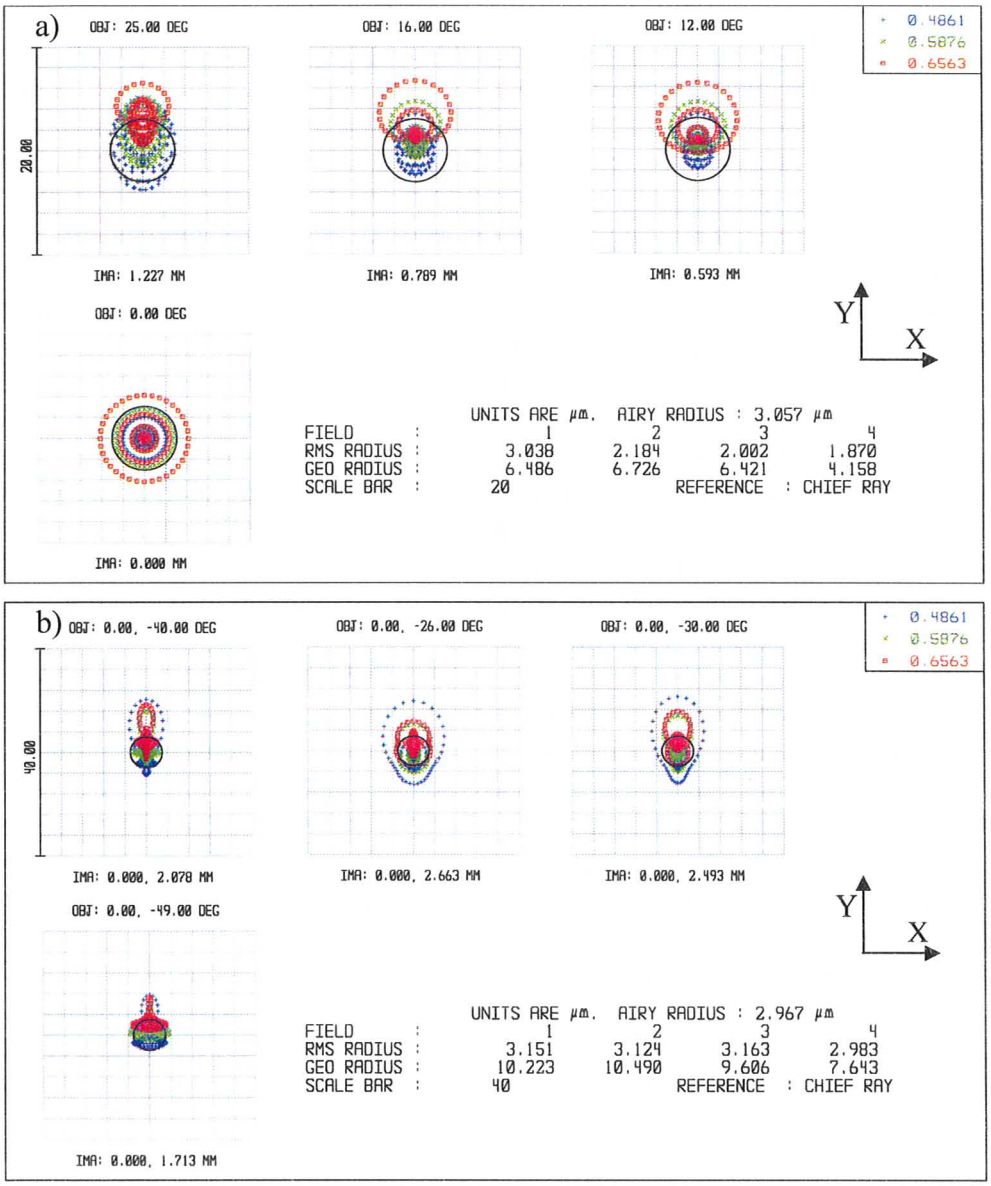

Figure 4.5. Image surface spot diagram for (a) forward view and (b) sidewall view. The black circle is the simulated Airy disc radius. The colours correspond to the wavelength legend at the top right of this figure; all units in microns. *RMS radius* is the RMS spot size, *GEO radius* is the distance from the centroid to the furthest ray intersection with the imaging surface. *IMA* describe the location of the centroid on the imaging surface. *OBJ* describe the location of the field points in terms of field angles. The forward view optics has smaller spot sizes than the radial view optics.

Sensitivity and inverse sensitivity are two other common lens tolerance simulation methods. Sensitivity simulations perturb one optical surface at a time

to the maximum specified tolerance magnitude. The effect on the chosen evaluation parameter is then documented and the process iterates until all optical surfaces have been analyzed. Inverse sensitivity attempts to calculate the tolerance each optical surface should have to ensure the evaluation parameter would satisfy a specified performance drop condition. Regardless of the tolerance simulation method, the image plane could be allowed to move to compensate for a shift in the focus from a tolerance design, which is referred to as the *compensator* in the simulation reports [5]. From analyzing the amount the compensator has to move in a tolerance simulation, an estimate of the optomechanical clearance surrounding the image plane could be obtained.

For this thesis work, inverse sensitivity methods are the first tolerance simulation attempted. However, the presence of the two parabolic mirrors in the simulation proved problematic, and the results would often place large tolerances on the lens elements and impractical stringent tolerances on the mirrors. Therefore a combination of sensitivity methods with repeated manual tuning of the tolerance and Monte Carlo methods are used for this thesis work. This combined approach would start with a set of default tolerance specifications for an initial simulation. The tolerances of each surface would be adjusted depending on the sensitivity simulation report of the default tolerance on each surface. Surfaces where the contribution to system performance degradation is low would have the tolerance adjusted to a more relaxed value to reduce the cost and difficulty in fabrication. Only surfaces that are major contributors to system performance degradation would have its tolerance tightened. These surfaces are referred as *worst offenders* in the tolerance simulation report. Due to the fact only one evaluation criterion could be chosen for each simulation, the averaged MTF is chosen to be the evaluation criterion for both the sensitivity and the Monte Carlo methods. The number of perturbed design variations is set to be 50 for the Monte Carlo method. The computation time for this is approximately 20 ~ 25 minutes on an Intel Core Duo E7200 2.6 GHz dual core CPU with 4 GB of memory. Table 4.5 summarizes the final tolerance specified for each optical component in the prototype design.

The surface reference method in table 4.5 is identical to that of the forward view simulation, as shown in table 4.3. Focus power refers to the tolerance on the radius of curvature and it is typically measured in terms Newton's rings, which are concentric interference fringe patterns created when a curved lens surface is placed against an optical flat [1,6]. Surface irregularities (SI) describe all other residual manufacturing errors which cause a surface to deviate from its nominal shape [1].

The sensitivity simulation results of the radial and forward views are summarized in table 4.6. The tolerance simulation results are symmetric in the forward view, but asymmetric in the radial view. This is because the mirrors are

used in an asymmetric fashion to redirect the FOV of the radial lens group, as discussed in section 2.3.4. The back focus is the distance the image plane would move to refocus the system. Detailed tolerance reports are available in Appendix B. With reference to table 4.6, the most problematic tolerances are decenter related. This is especially true for surface 10 and 11, which is the negative lens after the convex mirror and the plano-convex stock lens after the aperture stop. In general, the elements that contribute the most to the performance degradation are the lenses and the mirrors used in the radial view. This ascertains the choice of using the design in fig. 3.9(a) as opposed to Fig 3.9(b) for the final 1:1 scale thesis design since there would be less room to properly mount and assemble the lenses for the design featured in fig. 3.9(b).

Table 4.5. Tolerance settings for the prototype design. M1 is concave mirror, M2 is convex mirror

Surface Num. [1]	Focus (Fringes)	Thickness (mm)	Decenter (mm)	Tilt	SI (Fringes)	Index of Refraction	Abbe Number
1	± 5	± 0.1	± 0.05	± 0.2°	± 3	± 0.01	± 1%
2	± 5	± 0.1	± 0.05	± 0.2°	± 3	± 0.01	± 1%
3	± 5	± 0.1	± 0.05	± 0.2°	± 3	± 0.01	± 1%
4	± 5	± 0.1	± 0.05	± 0.2°	± 3	± 0.01	± 1%
5	± 5	± 0.05	± 0.05	± 0.2°	± 3	± 0.01	± 1%
6	± 5	± 0.1	± 0.05	± 0.2°	± 3	± 0.01	± 1%
7	± 5	± 0.1	± 0.05	± 0.2°	± 3	± 0.01	± 1%
8	± 5	± 0.1	± 0.05	± 0.2°	± 3	± 0.01	± 1%
9	± 5	± 0.1	± 0.05	± 0.2°	± 3	± 0.01	± 1%
M1 [2]	± 5	± 0.05	± 0.05	± 0.2°	± 3	N/A	N/A
M2 [2]	± 5	± 0.05	± 0.05	± 0.2°	± 3	N/A	N/A
10 [3]	± 5	± 0.05	± 0.05	± 0.2°	± 3	± 0.01	± 1%
11	± 5	± 0.05	± 0.05	± 0.2°	± 3	± 0.01	± 1%
12	± 5	± 0.05	± 0.05	± 0.2°	± 3	± 0.01	± 1%
13	± 5	± 0.05	± 0.05	± 0.2°	± 3	± 0.01	± 1%
14	± 5	± 0.05	± 0.05	± 0.2°	± 3	± 0.01	± 1%
15	± 5	± 0.05	± 0.05	± 0.2°	± 3	± 0.01	± 1%
16	± 5	± 0.05	± 0.05	± 0.2°	± 3	± 0.01	± 1%
17	± 5	± 0.05	± 0.05	± 0.2°	± 3	± 0.01	± 1%
18	± 5	± 0.05	± 0.05	± 0.2°	± 3	± 0.01	± 1%
19	± 5	± 0.05	± 0.05	± 0.2°	± 3	± 0.01	± 1%

[1] Surface numbering is taken to be the same as the forward view simulation, since it contains all lens elements in the prototype. The mirror surfaces are denoted separately.

[2] Mirrors have a scratch-dig of 60-85 and diameter tolerance of 50 microns.

[3] Surfaces after surface 10 are shared by the radial view optics.

The sensitivity tolerance simulation method is useful to compare the surfaces to determine the worst offenders and fine tune the tolerance magnitude for those individual surfaces. The sensitivity simulation only predicts the performance degradation due to the presence of tolerance on one surface, thus to

estimate the overall performance degradation when tolerance is present on multiple surfaces, summation methods such as the root sum square method is used [5]. This summation method over the sensitivity tolerance results does not take into account the presence of tolerances that compensate each other, and thus it tends to overestimate the performance degradation. The Monte Carlo tolerance simulation method is used to estimate the system level performance with the presence of tolerance on every surface.

Table 4.6. Sensitivity tolerance summary for (a) forward view optics (b) radial view optics. The evaluation criterion is average MTF at (a) 30 lp/mm (b) 35 lp/mm.

Mnemonics:	TIRR: Tolerance on irregularity (fringes).
TFRN: Tolerance on curvature in fringes.	TIND: Tolerance on Nd index of refraction.
TTHI: Tolerance on thickness.	TABB: Tolerance on Abbe number.
TSDX: Tolerance on surface decenter in x.	TEDX: Tolerance on element decenter in x.
TSDY: Tolerance on surface decenter in y.	TEDY: Tolerance on element decenter in y.
TSTX: Tolerance on surface tilt in x (degrees).	TETX: Tolerance on element tilt in x (degrees).
TSTY: Tolerance on surface tilt in y (degrees).	TETY: Tolerance on element tilt in y (degrees).

a) Worst Offenders:

Type	Value	Criterion	Change
TEDY 10 11	± 0.05000000	0.84651226	-0.12177497
TEDX 10 11	± 0.05000000	0.84651226	-0.12177497
TSDY 10	± 0.05000000	0.84734760	-0.11581965
TSDX 10	± 0.05000000	0.84734760	-0.11581965
TSDY 18	± 0.05000000	0.84806829	-0.11041884

b) Worst Offenders:

Type	Value	Criterion	Change
TEDY 5 6	0.05000000	0.79314349	-0.34742467
TSDY 5	0.05000000	0.79885761	-0.33407636
TEDY 5 6	-0.05000000	0.80513673	-0.31864611
TSDY 5	-0.05000000	0.81088786	-0.30371265
TEDY 8 9	-0.05000000	0.84022487	-0.20929086
TSDY 9	-0.05000000	0.84022487	-0.20929086
TEDY 10 11	-0.05000000	0.84252464	-0.19983176
TSDY 11	-0.05000000	0.84252464	-0.19983176
TSDY 13	0.05000000	0.84688313	-0.18047013
TSTX 9	-0.20000000	0.85004814	-0.16492014

The Monte Carlo tolerance simulation results for the forward view optics with the evaluation criterion set to averaged MTF at 35 lp/mm and 70 lp/mm is shown in table 4.7. The Monte Carlo tolerance simulation results for the radial view optics with the evaluation criterion set to averaged MTF at 30 lp/mm and 60 lp/mm is shown in table 4.8. The spatial frequencies of the evaluation criterion are chosen to be 33% and 66% of the simulated nominal averaged MTF shown in table 4.4. From table 4.7, the Monte Carlo output indicate there is over 90% probability that the diffraction MTF at 35 lp/mm would achieve better than 74%

contrast for the radial view, and there is over 90% probability that the diffraction MTF at 70 lp/mm would achieve better than 46% contrast for the forward view.

From table 4.8, the Monte Carlo output indicate there is over 90% probability that the diffraction MTF at 30 lp/mm would achieve better than 45% contrast modulation for the radial view, and there is over 90% probability that the diffraction MTF at 60 lp/mm would achieve better than 21% contrast for the forward view. The worst offending surfaces of the radial view optical design are all decenter related and shown in table 4.6. Although 45% contrast at 30 lp/mm is a lower MTF score than the design constraint in table 4.1, it is unrealistic to lower the decenter tolerance further due to the manufacture process used.

Table 4.7. Monte Carlo tolerance simulation report for the forward view optics at (a) 35 lp/mm (b) 70 lp/mm. Back compensator is the distance the imaging plane would move to refocus the system.

a)

Averaged MTF Score				Compensator Statistics	
Summary		Probability	Modulation	Change in back focus (mm)	
Nominal	0.85522637	90%	> 0.74122084	Minimum	-0.597743
Best	0.85067462	80%	> 0.76505361	Maximum	0.446867
Worst	0.72022464	50%	> 0.79874724	Mean	-0.004505
Mean	0.79259745	20%	> 0.81832734	Std Dev	0.269822
Std Dev	0.03037092	10%	> 0.82504789		

b)

Averaged MTF Score				Compensator Statistics	
Summary		Probability	Modulation	Change in back focus (mm)	
Nominal	0.67602981	90%	> 0.46061768	Minimum	-0.604315
Best	0.63801234	80%	> 0.48809009	Maximum	0.598548
Worst	0.41034575	50%	> 0.53455501	Mean	0.040689
Mean	0.53788839	20%	> 0.60533161	Std Dev	0.266730
Std Dev	0.06000854	10%	> 0.61862961		

Table 4.8. Monte Carlo tolerance simulation report for the radial view optics at (a) 30 lp/mm (b) 60 lp/mm.

a)

Averaged MTF Score				Compensator Statistics	
Summary		Probability	Modulation	Change in back focus (mm)	
Nominal	0.86589867	90%	> 0.44859480	Minimum	-0.684442
Best	0.82987789	80%	> 0.52413255	Maximum	0.677583
Worst	0.29322651	50%	> 0.67910888	Mean	-0.032713
Mean	0.65267095	20%	> 0.79237058	Std Dev	0.328241
Std Dev	0.14812317	10%	> 0.81162563		

b)

Averaged MTF Score				Compensator Statistics	
Summary		Probability	Modulation	Change in back focus (mm)	
Nominal	0.68768855	90%	> 0.21209679	Minimum	-0.544278
Best	0.68816750	80%	> 0.27310240	Maximum	0.769625
Worst	0.11331762	50%	> 0.45237084	Mean	0.022282
Mean	0.43339927	20%	> 0.60588376	Std Dev	0.300006
Std Dev	0.16442716	10%	> 0.62693044		

4.3 Test Chart Measurements

The empirical MTF verification method used in this thesis work is based on the use of the USAF test chart as well as custom printed resolution patterns. The forward view tests used a USAF 1951 test chart (Thorlabs R3L3S1N) and the radial view tests used custom printed bar patterns on printing paper (Hewlett-Packard LaserJet 1012) at a resolution of 600 dots per inch. The radial view test patterns are printed on separate 8 × 11 inch printing paper for each of the test spatial frequencies; they can be found in Appendix C. The radial view test pattern spatial frequencies are 0.5 lp/mm, 1 lp/mm, 2 lp/mm, 3 lp/mm, 4 lp/mm, 5 lp/mm, and 6 lp/mm. The USAF 1951 test chart used is shown in fig. 4.6, and its legend is shown in table. 4.9.

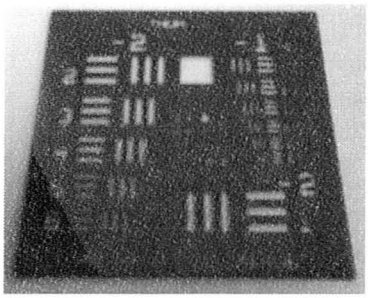

Figure 4.6. Photograph of USAF1951 target.

Table 4.9. USAF 1951 Test chart legend. This legend relates group and element numbers to spatial frequency (lp/mm). The group numbers are horizontal and element numbers are vertical on the test chart.

Element Number	Group Number									
	-2	-1	0	1	2	3	4	5	6	7
1	0.250	0.500	1.00	2.00	4.00	8.00	16.00	32.0	64.0	128.0
2	0.280	0.561	1.12	2.24	4.49	8.98	17.95	36.0	71.8	144.0
3	0.315	0.630	1.26	2.52	5.04	10.10	20.16	40.3	80.6	161.0
4	0.353	0.707	1.41	2.83	5.66	11.30	22.62	45.3	90.5	181.0
5	0.397	0.793	1.59	3.17	6.35	12.70	25.39	50.8	102.0	203.0
6	0.445	0.891	1.78	3.56	7.13	14.30	28.50	57.0	114.0	228.0

These frequencies on the test pattern object would be referred to as *object spatial frequency* and their corresponding image would be referred to as *image spatial frequency*. The object spatial frequency is related to the image spatial frequency through the magnification of the imaging system as shown in Eq. (4.1a)

and Eq. (4.1b). From the radial view simulation, the size of the object and image are 16.63 mm and 0.95 mm, which gave a magnification of 17.5. From the forward view simulation, the size of the object and image are 20.1 mm and 1.23 mm, which gave a magnification of 16.3. Eq. (4.1c) is a sample calculation of the image spatial frequency of the radial view optics from an object side spatial frequency of 0.5 lp/mm.

$$magnification = \frac{size_{img}}{size_{obj}} \tag{4.1a}$$

$$freq_{img} = \frac{freq_{obj}}{magnification} = freq_{obj} \times \frac{size_{obj}}{size_{img}} \tag{4.1b}$$

$$freq_{img} = 0.5 \times 17.5\ (lp/mm) = 8.75\ lp/mm \tag{4.1c}$$

4.3.1 Setup

The test procedure is summarized in table 4.10. The setup blueprint for the MTF test is shown in fig. 4.7 and fig. 4.8.

Table 4.10. MTF test procedure.

Step	Procedure
1	Setup the forward view MTF from the blueprint shown in fig. 4.7(a). Start the Mightex camera software and set the following: ***Continuous video mode:*** *on*, ***1:2 decimation:*** *off*, ***Ignore 1:2 decimation:*** *on*, ***Save as JPEG:*** *off*.
2	Thread the lens prototype onto the Mightex camera by turning it in a circular motion. The amount of turning determines the back focus distance between the last lens surface and the CMOS image detector.
3	Adjust the back focus distance until the USAF 1951 test chart is imaged as sharp as possible.
4	Acquire the image when the test chart is in the best focus. Do not adjust the back focus anymore at this point onwards. This is the acquired image for the forward view and the forward MTF test concludes with this step.
5	Modify the forward view test setup to the radial view test setup shown in fig. 4.7(b) and fig. 4.8.
6	Roll the custom printed test pattern at 0.5 lp/mm into a cylinder as described in fig. 4.9(a). Guide the paper cylinder into the annular optical mounts and acquire the image. This is the radial view MTF test in the sagittal direction.
7	Take the cylinder out and unroll the test pattern. Roll the custom printed test patterns into a cylinder as described in fig. 4.9(b). Guide the paper cylinder into the paper holders and acquire image. This is the radial view MTF test in the tangential direction.
8	Repeat steps 6~8 for all remaining radial view test patterns at different spatial frequencies.

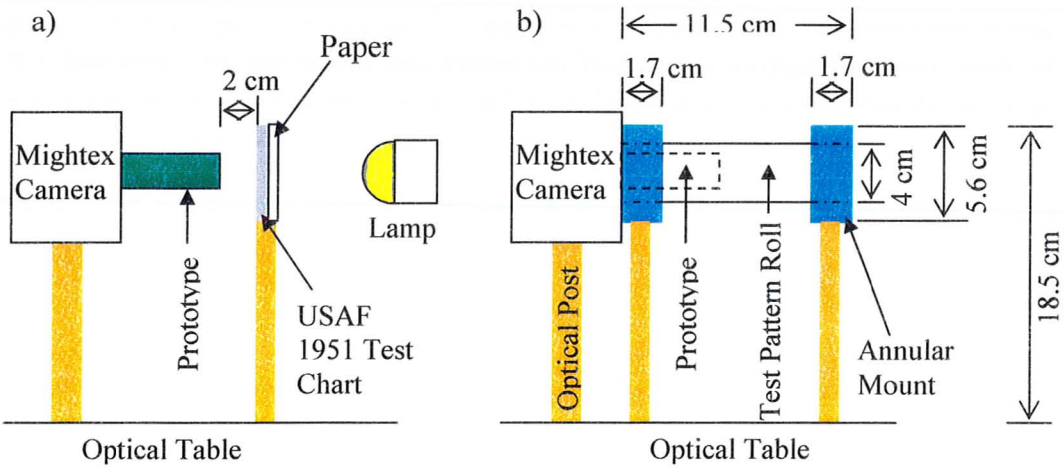

Figure 4.7. Setup blueprint for (a) forward view (b) radial view without the illumination.

As discussed in section 2.4.4, the MTF is a characterization of resolving power that compares the contrast on the image at different spatial frequency. Suppose a region of interest is defined over an area on the image that shows the test pattern and has near uniform illumination. Assuming a linear irradiance and image gray level response, the contrast modulation could then be calculated by using the gray level values from this region of interest. The dynamic range of the gray level values of the acquired monochromatic image is 0 ~ 255 possible levels of gray, with 0 being absolute black and 255 being absolute white. The gray level histogram over a chosen region of interest is collected and the gray levels of the dark and bright patterns would be visually discernable. The dark and bright peaks in the histogram represent the dark and bright parts of the oscillating test pattern. The region of interest and the corresponding histogram for group 2 element 4 of the USAF 1951 test chart from the forward view MTF test is shown in fig. 4.10(a) and fig. 4.10(b), respectively. The region of interest and the corresponding histogram for the radial view sagittal test pattern at 4 lp/mm is shown in fig. 4.11(a) and fig. 4.11(b), respectively. Note the periodic thick lines in fig. 4.11(a) are from the printer, as shown in Appendix C.

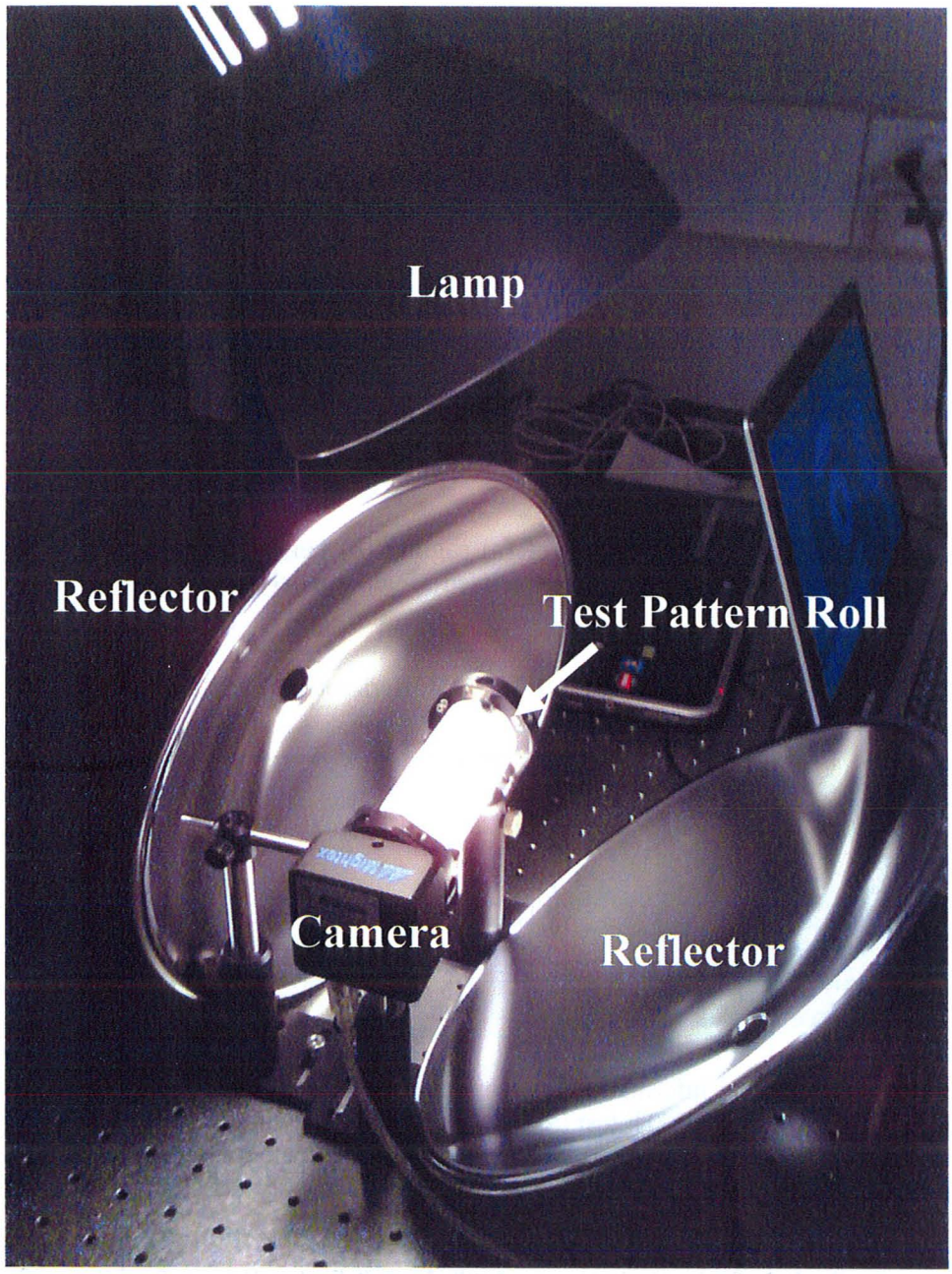

Figure 4.8. Setup photograph for radial view illumination.

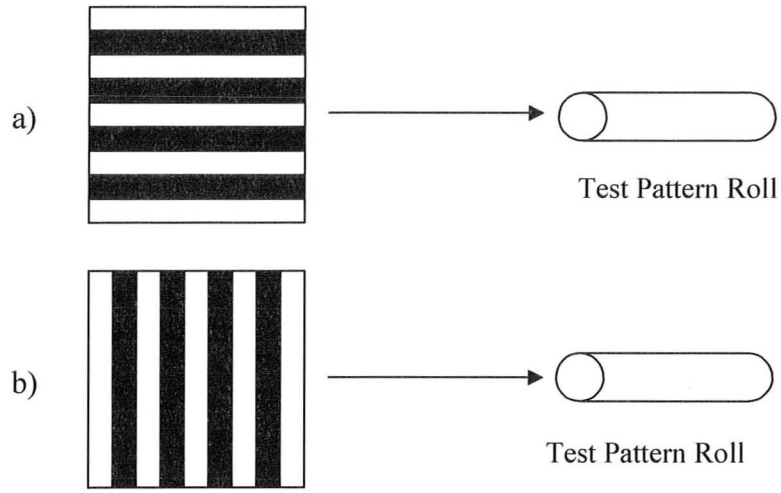

Figure 4.9. The generation of (a) sagittal (b) tangential MTF test patterns from rolling custom printed single spatial frequency test patterns on paper.

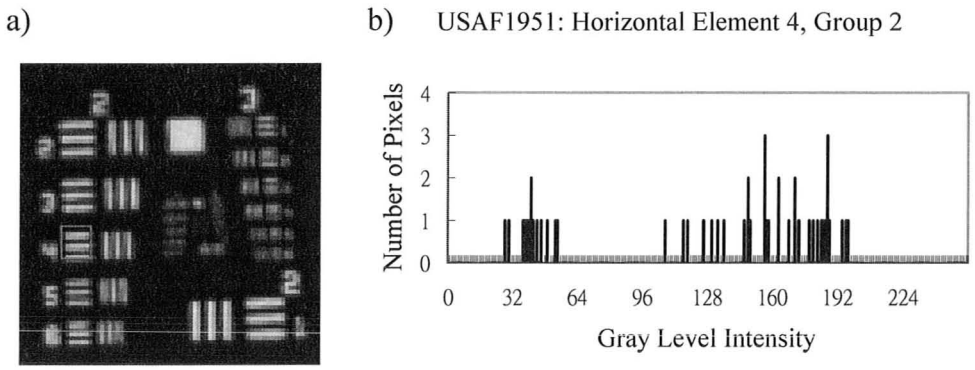

Figure 4.10. Gray level information on group 2 element 4 of the USAF 1951 test chart used for the forward view MTF test (a) is resized at 600% zoom to illustrate the red box, which is the region of interest used in computation of the histogram in (b). The dark and bright gray level peaks are taken to be 41 and 174 out of 0 ~ 255 possible levels of gray.

The computation of the histogram and the selection of the region of interest are performed in ImageJ, an image processing software package that can compute and export histogram data over a selected region in the image. For the forward view test, the region of interest would contain one pattern group element, as shown in fig. 4.10(a). For the radial view test, the region of interest is the yellow rectangular region bounded by vertices (r,c)=(250,1000), (250,1050), (290,1050), (290,1000), as shown in fig. 4.11(a); this region is chosen as the region of interest for all radial view MTF calculations because the illumination

inside the marked yellow box is close to uniform across the test pattern set, which would help with the consistency of the tests. Note that r is the row coordinate, c is column coordinate, $(r,c) = (1,1)$ is the top left pixel in the image, and $(r,c) = (1024,1280)$ is the bottom right pixel in the image.

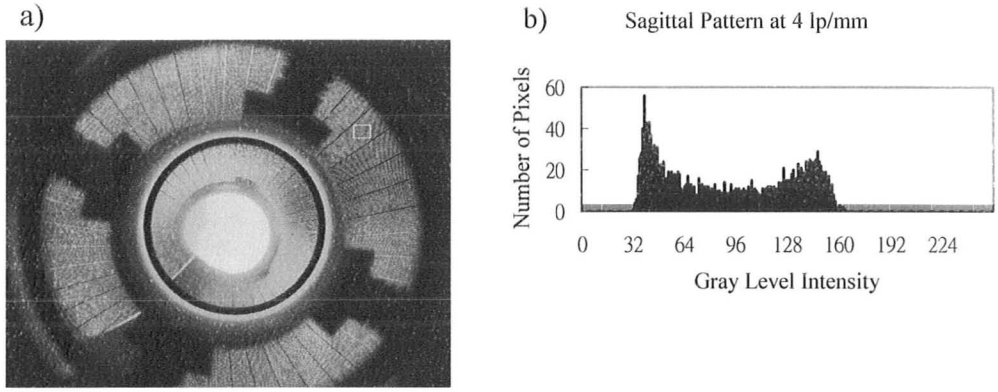

Figure 4.11. Gray level information on group 2 element 4 of the USAF 1951 test chart used for the forward view test (a) is resized at 75% zoom to illustrate the yellow box, which is the region of interest used (b) histogram for the sagittal test pattern at 4 lp/mm. The dark and bright gray level peaks are taken to be 39 and 146 out of 0 ~ 255 possible levels of gray.

4.3.2 Results

All images are acquired with unity gain and 300 ms exposure time unless otherwise specified. Fig. 4.12 is the acquired image from the forward view MTF test and fig. 4.13 is the acquired image from the sagittal radial view MTF test at 2 lp/mm. Both figures are resized to 300 pixels per inch without pixel resample for publication purposes. With reference to the setup blueprint in fig. 4.7 and fig. 4.8, it can be seen that all test patterns are back illuminated. Therefore the illumination of the test patterns depends on the amount of black print on the paper. The Mightex camera setting of unity gain and 300 ms exposure time is found to provide acceptable illumination to all test chart patterns. This setting is empirically determined to provide adequate illumination across all test patterns. The forward view and radial view measurements are summarized in table 4.11 and table 4.12. The acquired image from the forward view MTF test and all associated histograms are shown in Appendix D. The acquired image from the radial view MTF test and all associated histograms are shown in Appendix E. The dynamic range of the image is 0 ~ 255 levels of gray. The dark and bright gray level peaks are manually selected according to the shape of the histograms similar to the manner shown in fig. 4.10(b) and fig. 4.11(b). The modulation contrast is calculated according to Eq. (2.9), with the *max* and *min* being the dark and bright gray level peaks, respectively.

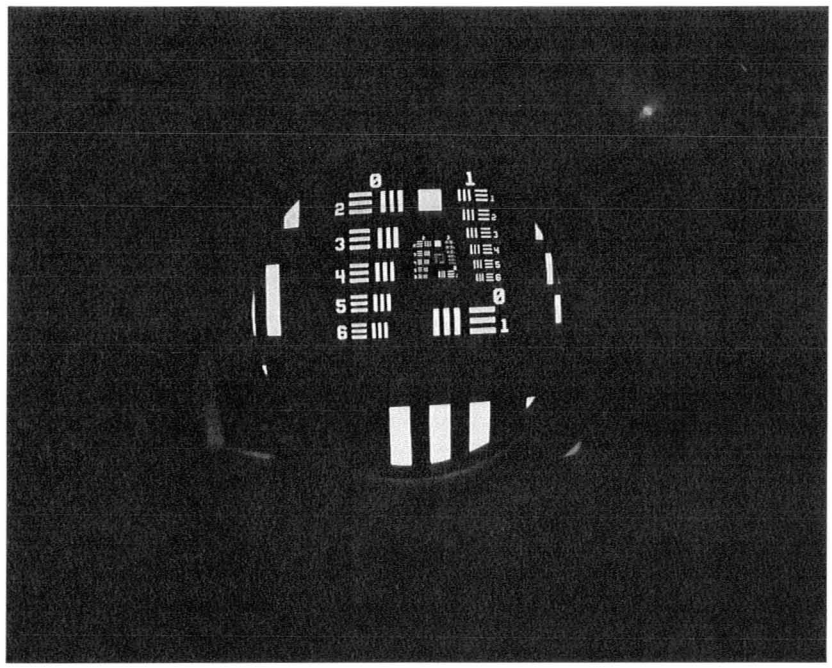

Figure 4.12. Acquired image of the forward view.

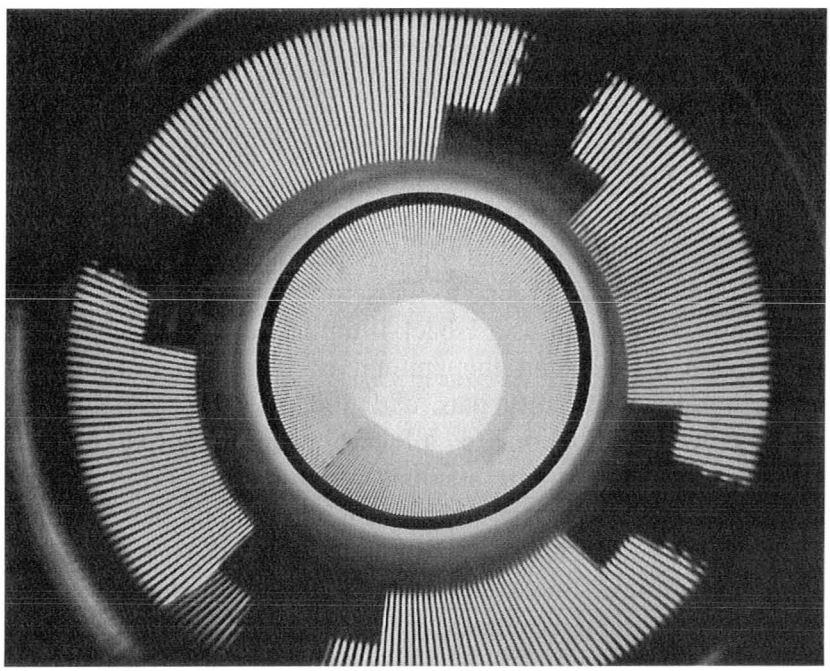

Figure 4.13. Acquired image of the radial view sagittal test pattern at 2 lp/mm object spatial frequency.

Table 4.11. Forward view MTF measurement results.

Location [1]	Object Spatial Frequency (lp/mm)	Image Spatial Frequency (lp/mm)	Dark Intensity	Bright Intensity	Modulation
G3E1S	8	130.4	51	113	0.38
G3E1T	8	130.4	64	110	0.26
G2E6S	7.13	116.219	62	166	0.46
G2E6T	7.13	116.219	68	157	0.40
G2E5S	6.35	103.505	77	160	0.35
G2E5T	6.35	103.505	56	164	0.49
G2E4S	5.66	92.258	41	174	0.62
G2E4T	5.66	92.258	67	181	0.46
G2E3S	5.04	82.152	45	185	0.61
G2E3T	5.04	82.152	49	187	0.58
G2E2S	4.49	73.187	26	189	0.76
G2E2T	4.49	73.187	33	178	0.69
G2E1S	4	65.2	24	194	0.78
G2E1T	4	65.2	34	188	0.69
G1E6S	3.56	58.028	18	191	0.83
G1E6T	3.56	58.028	20	184	0.80
G1E5S	3.17	51.671	19	192	0.82
G1E5T	3.17	51.671	19	191	0.82

[1] Bar pattern location given in GxEyd where x is group number, y is element number, d indicates the direction of testing; T for tangential, S for sagittal. For the forward MTF test, sagittal is in the horizontal direction and tangential is in the vertical direction.

Table 4.12. Radial view MTF measurement results.

Orientation	Object Spatial Frequency (lp/mm)	Image Spatial Frequency (lp/mm)	Dark Intensity	Bright Intensity	Modulation
Sagittal	0.5	8.75	23	161	0.75
Sagittal	1	17.5	24	159	0.74
Sagittal	2	35	33	159	0.66
Sagittal	3	52.5	39	156	0.60
Sagittal	4	70	39	146	0.58
Sagittal	5	87.5	40	143	0.56
Sagittal	6	105	46	123	0.46
Tangential	0.5	8.75	71	159	0.38
Tangential	1	17.5	68	153	0.38
Tangential	2	35	92	132	0.18
Tangential	3	52.5	N/A [1]	N/A [1]	0
Tangential	4	70	N/A [1]	N/A [1]	0
Tangential	5	87.5	N/A [1]	N/A [1]	0
Tangential	6	105	N/A [1]	N/A [1]	0

[1] The bright and dark gray levels cannot be distinguished from the histogram.

With reference to the setup blueprint in fig. 4.7 and fig. 4.8, it can be seen that all test patterns are back illuminated. Therefore the illumination of the test

patterns depends on the amount of black print on the paper. The Mightex camera setting of unity gain and 300 ms exposure time is found to provide acceptable illumination to all test chart patterns. This setting is empirically determined to provide adequate illumination across all test patterns. The forward view and radial view measurements are summarized in table 4.11 and table 4.12. The acquired image from the forward view MTF test and all associated histograms are shown in Appendix D. The acquired image from the radial view MTF test and all associated histograms are shown in Appendix E. The dynamic range of the image is 0 ~ 255 levels of gray. The dark and bright gray level peaks are manually selected according to the shape of the histograms similar to the manner shown in fig. 4.10(b) and fig. 4.11(b). The modulation contrast is calculated according to Eq. (2.9), with the *max* and *min* being the dark and bright gray level peaks, respectively.

$$Modulation = \frac{\max - \min}{\max + \min} \tag{2.9}$$

4.3.3 Discussion

The first major limitation of this method of MTF measurement stems from the assumption that the CMOS image detector would generate image gray levels in a linearly proportional manner from the irradiance collected on the CMOS imager chip. For future work, it may be possible to calibrate this behaviour by replacing the CMOS camera from the manufactured prototype by an optical power meter at the location of the image plane. A variable power light source may be used to provide different illumination intensities and a series of irradiance measurements on the optical power meter could be recorded for comparison with the gray level obtained from the CMOS camera under the same set of illumination intensities. The second major limitation is related to the finite pixel pitch of 5.2 μm on the CMOS imager chip. The pixel pitch of 5.2μm could be treated as a spatial sampling period, which translates to a spatial sampling frequency of 192.3 lp/mm. From information theory, the Nyquist spatial frequency of a Nyquist sampling rate of 192.3 lp/mm is 96.15 lp/mm, where Nyquist frequency is the highest frequency that could be theoretically reconstructed without ambiguity or aliasing. Test patterns with image spatial frequency above 96.15 lp/mm would undergo aliasing, thus reliable MTF testing of the optical design cannot be carried out above the Nyquist spatial frequency using the approach in this chapter. With reference to table 4.10 and table 4.11, the test patterns on the USAF 1951 smaller than group 2 element 4 would have an image spatial frequency higher than 96.15 lp/mm. The custom printed test patterns used for the radial view tests would exceed 96.15 lp/mm for the test pattern with 6 lp/mm object spatial frequency. For this reason, the measurements with image spatial frequency above 96.15 lp/mm

are excluded from the comparison against the simulated MTF. Other limitations include the fact the CMOS imager have a finite dynamic range, or the resolution pattern object may not be well defined enough with a laser printer specified to print at 600 dots per inch printing quality. Some lines are printed thicker than the others as shown in the scanned images of the custom printed test patterns in Appendix C.

The simulated nominal MTF plots from fig. 4.4 show the MTF performance is different across the FOV, therefore the field positions of the test objects need to be estimated so that a proper selection of the various simulated nominal MTF curves for comparison with the test results can be made. The regions of interest used to calculate the histogram are measured from the image center to estimate their corresponding image height. The definition of image height is discussed in section 2.1.1 to be the distance from the optical axis to the intersection location of the chief ray and the image surface. The measured image height would then be compared to the simulated image height from the ray trace simulation. In the ray trace simulation, 4 field points are used to generate the sagittal and tangential MTF simulation results in the MTF plots from fig. 4.4. Therefore by determining the field points that have similar image heights as the measured image heights, the appropriate MTF curve could be selected from the ray trace data results for comparison.

Although the acquired image should theoretically be centered about the optical axis of the system, tolerance induced errors may have caused a shift in image centers. The periphery of the FOV of the prototype imaging system is traced using the oval selection tool in ImageJ and the circular region is saved as a mask image. The traced region is shown in fig. 4.14. The mask image is then analyzed in MATLAB^{TM} to locate the centroid of the circular region. This centroid is essentially the image coordinate that represents the optical axis in the acquired image. Due to the presence of clipping at the bottom of the acquired image, the acquired image is zero padded to increase the height to an appropriate amount as shown in fig. 4.14. The center of the acquired image is (r,c) = (640,512) and the calculated centroid is (r,c) = (647,561.5), where r is the row coordinate, c is column coordinate. The image coordinates are set up such that (r,c) = (1,1) at the top left corner and (r,c) = (1024,1280) at the bottom right corner of the image.

The centroids of each test pattern are computed using a similar method where the region of interests used to obtain the histograms of the test patterns are used for the mask image generation. The distance between the centroid of the region of interest and the image center is then computed and converted from pixels to millimetres by using the fact the pixel pitch of the CMOS chip is 5.2 μm. This converted distance would be the image height. The image height of all test patterns used in this thesis work is summarized in table 4.13. The image heights

of the field points used in the ray trace simulation to generate the MTF curves in fig. 4.4 are summarized in table 4.14.

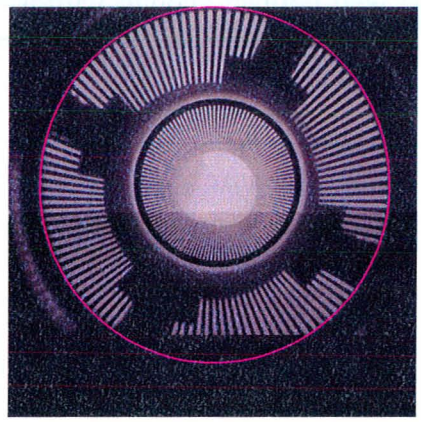

Figure 4.14. The magenta outline is similar to the oval selection tool used in ImageJ to generate the mask image.

Table 4.13. Calculated image height for each test pattern.

Test Pattern [1]	ROI Centroid (*r*,*c*)	Image Spatial Frequency (lp/mm)	Image Height (pixels)	Image Height (mm)
G1E5S	(621,528.5)	51.671	132.6	0.69
G1E6S	(600.5,526.5)	58.028	126.65	0.66
G2E1S	(605.5,587.5)	65.2	74.00	0.38
G2E2S	(652.5,636)	73.187	91.66	0.48
G2E3S	(638,636.5)	82.152	77.22	0.40
G2E4S	(625,636)	92.258	64.45	0.34
G2E5S	(612.5, 635.5)	103.505	52.28	0.27
G2E6S	(602.5, 635.5)	116.219	42.58	0.22
G3E1S	(656,587)	130.4	111.94	0.58
G1E5T	(621,545.5)	51.671	117.65	0.61
G1E6T	(605.5,542)	58.028	112.01	0.58
G2E1T	(605.5,601.5)	65.2	63.29	0.33
G2E2T	(653,624)	73.187	94.35	0.49
G2E3T	(638.5,625.5)	82.152	79.95	0.42
G2E4T	(625,626)	92.258	66.88	0.35
G2E5T	(613,626.5)	103.505	55.43	0.29
G2E6T	(602.5, 627.5)	116.219	45.40	0.24
G3E1T	(656, 594)	130.4	108.35	0.56
All radial Tests [2]	(270.5,1025.5)	8.75~105	477.43	2.48

[1] Bar pattern location given in GxEyd where x is group number, y is element number, d indicates the direction of testing; T for tangential, S for sagittal. For the forward view testing, sagittal is in the horizontal direction and tangential is in the vertical direction.

[2] All radial tests have the same region of interest as described in fig. 4.11.

The forward view test patterns have image heights between 0.38 mm to 0.58 mm. The nearest simulation field points have field angles of 0° and 12° with an image height of 0 mm and 0.6 mm. The simulated tangential MTF at field angles 0° and 12° and the measured forward view MTF are shown in fig. 4.15. The simulated sagittal MTF at field angles 0° and 12° as well as the measured forward view MTF are shown in fig. 4.16.

Table 4.14. Image height of each field point used in the MTF simulation.

Simulation View	Specified Field Angle [1]	Image Height (mm)
Forward View	0°	0
Forward View	12°	0.6
Forward View	16°	0.79
Forward View	25°	1.23
Radial View	-26°	2.66
Radial View	-30°	2.49
Radial View	-40°	2.08
Radial View	-49°	1.72

[1] This is the field angle specified in the Zemax™ simulation files, which are used to identify the field points in the simulated MTF plots in fig. 4.4 and simulated spot diagrams in fig. 4.5.

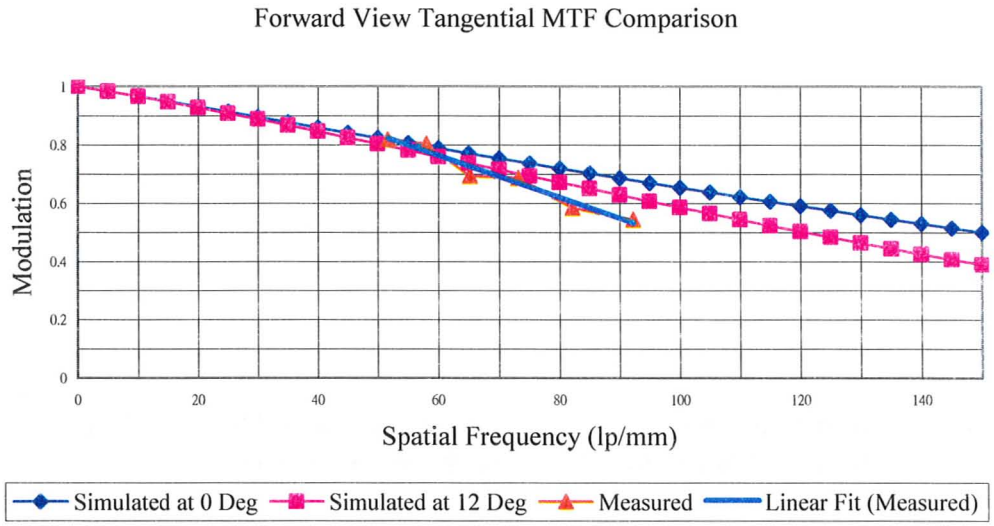

Figure 4.15. Tangential MTF comparison of forward view optics.

It can be seen that the simulated MTF curves at 0° and 12° are very similar, and the measured MTF is similar to a shifted version of the simulated curves. At lower spatial frequencies, the measured performance is very similar to the simulated performance. This is unexpected since there is usually a 5%~30% tolerance induced performance degradation associated with optical systems [1]. At higher spatial frequencies, the measured performance becomes worse than

predicted. The variance in the trend may be attributed to the low number of pixels used to sample each of the regions of interest in each forward view measurement. Low number of pixels implies low population in the histogram, which leads to a noisy measurement. This is due to the small size of each of the USAF1951 test patterns used for the measurement. For future work, perhaps larger test patterns of fixed frequency could be used such that the region of interest could be made larger in the image, which would increase the number of pixels within the region of interest.

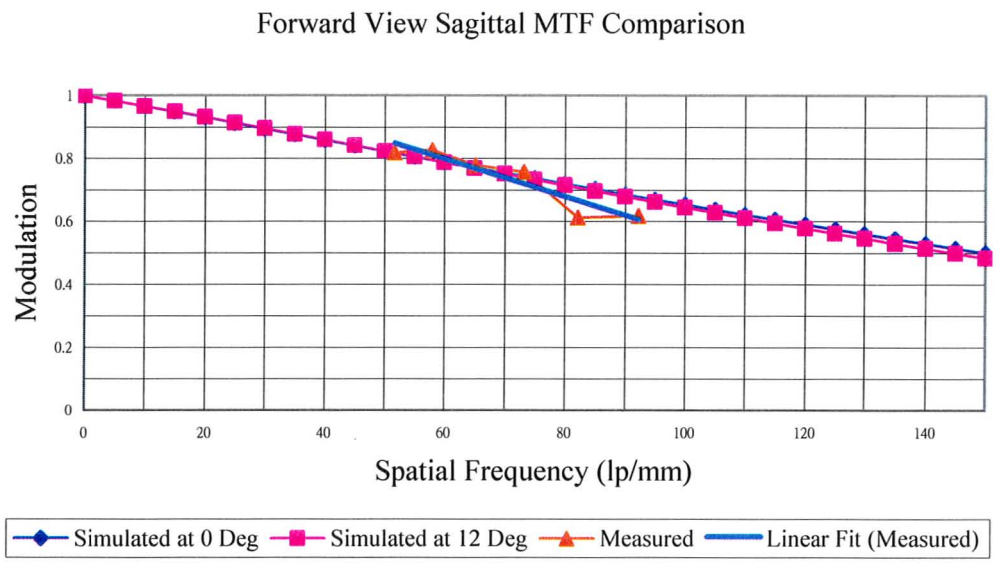

Figure 4.16. Sagittal MTF comparison of forward view optics.

All radial view test patterns used the same region of interest in their modulation calculations, which has an image height of 2.48 mm. The nearest simulated field point has a field angle of -30° with an image height of 2.49 mm. The simulated tangential MTF at the field angle of -30° and the measured radial view MTF are shown in fig. 4.17. The simulated sagittal MTF at the field angle of -30°and the measured radial view MTF are shown in fig. 4.18.

It can be seen in fig. 4.17 that the simulated MTF curves at -30° and the measured MTF are very different for the tangential direction. The measured sagittal MTF performance in fig. 4.18 is an expected shift from the simulated MTF. The apparent disagreement between the measured and expected in the tangential direction can be explained by the data acquired from the Monte Carlo tolerance simulation results. Recall from section 4.2.3 that Monte Carlo tolerance simulations are conducted at 30 lp/mm and 60 lp/mm for the radial view optics, 35 lp/mm and 70 lp/mm for the forward view optics. The evaluation criterion is

averaged MTF, which is given by Eq. (4.2). The computation of the averaged MTF for all measured and simulated data is shown in table. 4.15.

$$MTF_{avg} = \frac{MTF_{tangential} + MTF_{sagittal}}{2} \tag{4.2}$$

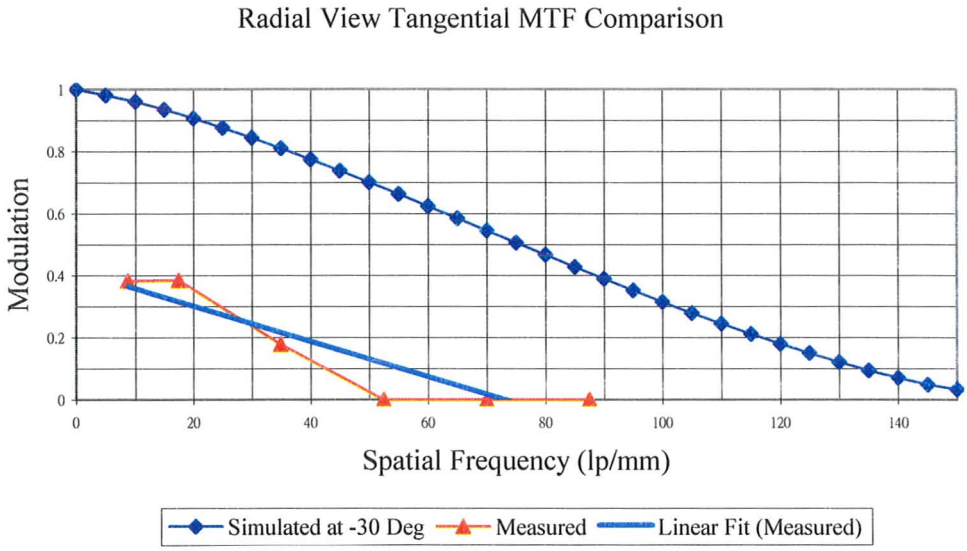

Figure 4.17. Tangential MTF comparison of radial view optics.

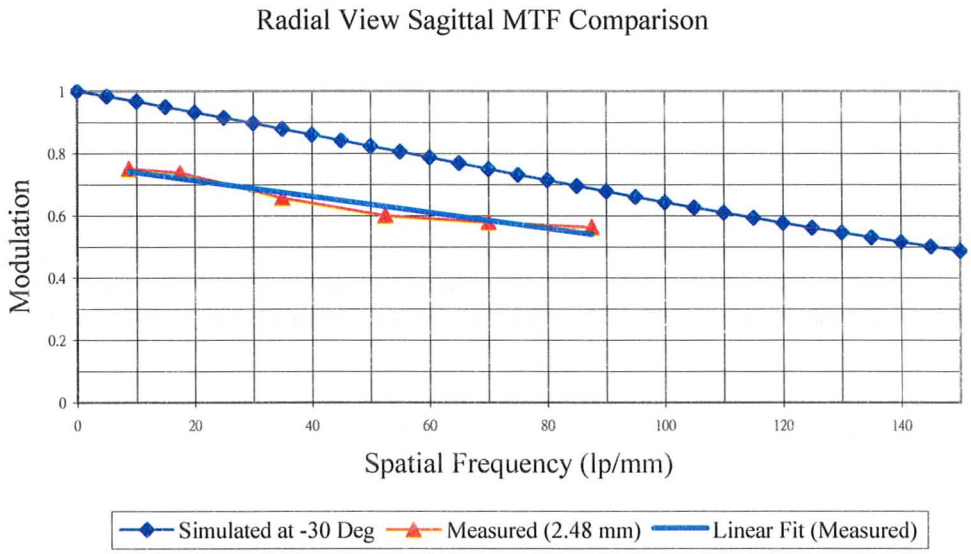

Figure 4.18. Sagittal MTF comparison of radial view optics.

Table 4.15. Measured and Monte Carlo tolerance simulated average MTF.

Data Source [1]	Image Spatial Frequency (lp/mm)	Tangential Modulation [2]	Sagittal Modulation [2]	Average Modulation [3]					
				Measured	90%	80%	50%	20%	10%
F-S	70	N/A	N/A	-	> 0.46	> 0.49	> 0.53	> 0.61	> 0.62
F-M	73.187	0.69	0.76	0.725	-	-	-	-	-
R-S	30	N/A	N/A	-	> 0.45	> 0.52	> 0.68	> 0.79	> 0.81
R-M	35	0.18	0.66	0.42	-	-	-	-	-
R-S	60	N/A	N/A	-	> 0.21	> 0.27	> 0.45	> 0.61	> 0.63
R-M	52.5	0	0.60	0.3	-	-	-	-	-

[1] *S* denotes *simulation*, *F* denotes *forward view*, *R* denotes *radial view*.

[2] The evaluation criterion from tolerance simulations is averaged MTF, intermediate sagittal and tangential values are unavailable.

[3] The Monte Carlo simulation result is given in terms of probabilities of achieving different modulation scores at the specified spatial frequency.

From table 4.15, it can be seen that the Monte Carlo tolerance results predicted a similar modulation to the measure MTF results. The large performance degradation present in fig. 4.17 for the radial view in the tangential direction is undetected during the design phase since the averaged MTF provides no additional insight into whether the sagittal or tangential MTF would both be similar to their averaged score. Although an averaged MTF score of > 0.45 with 90% probability at 30 lp/mm seems fairly close to the design criteria laid out in table 4.1, it did not constrain the design to enforcing achieving a similar MTF score in both the sagittal and tangential directions. For future work, additional tolerance simulations should also be conducted in the sagittal and tangential directions to avoid a similar outcome of large differences in resolving power between the two directions.

With references to fig. 4.15, fig. 4.16, table 4.11, and table 4.15, the measured forward view modulation is exceptionally good. The modulation at an image spatial frequency of 70 lp/mm predicted by the Monte Carlo simulation is > 0.46 with 90% probability, which is significantly more pessimistic compared to the measured modulation of 0.725 at 73.187 lp/mm from group 2 element 2 on the USAF 1951. One explanation for this behaviour may be that the tolerances used for simulation are actually more relaxed than the tolerances used in the actual manufacturing. From table 4.4, several of the lenses unique to the forward view optics group are assigned more relaxed tolerances in hopes of lowering the production cost. ITRC, the optics shop commissioned to fabricate and assemble the prototype, may have used the most stringent tolerances for all lenses, e.g. the airspace and thickness tolerance may be set 0.05 mm instead of the simulated value of 0.1 mm. This may help with streamlining the tolerance inspection

process. In addition, the Monte Carlo simulation probability profile is set to be parabolic, where there is larger probability distributed near the maximum magnitude of the specified tolerance [5]. This is chosen to bring about a rigorous and pessimistic tolerance simulation to ensure the manufactured prototype would achieve the MTF criteria set out in table 4.1.

4.4 Radiometry: Simulations & Measurements

The irradiance of the prototype is simulated using the same procedure as outlined in section 3.5. The target thesis application has an emphasis on the radial view light collection, so only the radial view is considered in this section. The simulation package used here is LightTools™, and fictitious point sources with 100 watts evenly distributed over its entire projection sphere are used as field points along the gastrointestinal (GI) tract wall. The FOV range simulated is shown in fig. 4.19. The field position range used here corresponds to the FOV range used in the sequential ray trace simulations used to design the prototype.

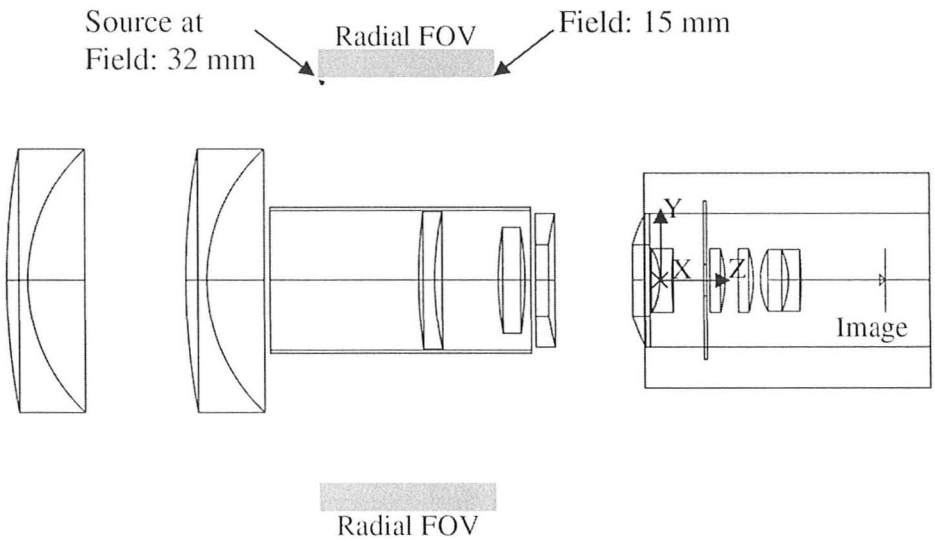

Figure 4.19. Radiometry simulation setup for radial view optical design. The simulated point source is located at the field position of 32 mm from global axis in the negative z direction in this figure. Other field positions in table 4.16 are sampled from the region shade in gray, which represents the radial view FOV. The PMMA tube emulates the sidewall of the endoscope.

For the verification of this experiment, one LED (Futurlec LED3R) is positioned at each of the radiometry simulation field points shown in table 4.16. Two images are acquired for each LED position; one with high gain (five) to serve as a mask image of the location of the LED in the image, one with unity gain for the actual measurement. One sample image set is shown in fig. 4.20 for

radiometry test at the field position of 18 mm. The gray level of the measurement image is averaged across the region described by the mask image. These averaged gray levels across the simulation field points provide a relative comparison to the irradiance simulation conducted in LightTools™. The LED is connected in series to two 1.5V alkaline batteries and a 1 kOhm resistor. The simulation and measurement results are summarized in table 4.16 with the acquired images in Appendix F.

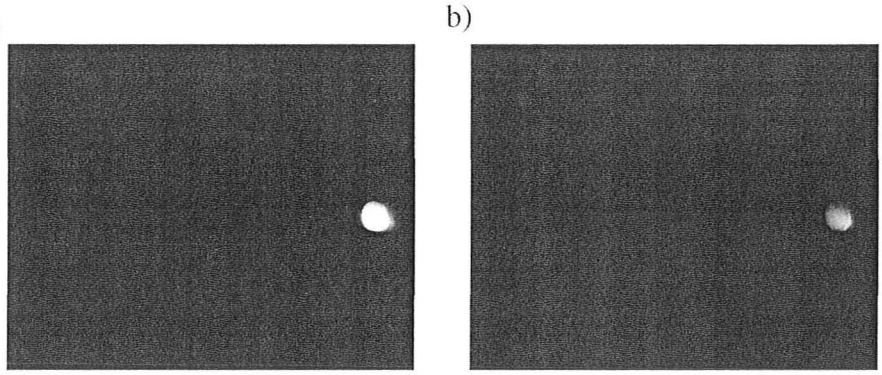

Figure 4.20. Acquired images resized at 50% zoom for field position 18 mm. (a) mask image (b) measurement image. The mean gray level intensity in the measurement image is 88.11 over the region of interest in defined by the mask image. The dynamic range of the image is 0 ~ 255 discrete levels of gray.

Table 4.16. Simulated and measured radiometry results.

Field Position (mm)	Simulated (mW/mm^2)	Measured (Averaged Gray level) [1]	Simulated (Normalized)	Measured (Normalized)
15	22.48	69.07	1.00	0.78
18	21.21	88.11	0.94	1.00
20	19.40	80.75	0.86	0.92
25	14.34	67.87	0.64	0.77
32	3.014	44.49	0.13	0.50

[1] Averaged over the region of interest described by the mask image. The dynamic range of the image is 0 ~ 255 discrete levels of gray.

The simulated and measured data are normalized and plotted in fig. 4.21. With the exception of the first field point, the simulated fallout curve is similar at field positions closer to the mirrors. This method of characterizing illumination of an imaging system is limited by the dynamic range and response of the CMOS image sensor in the camera. The LED is cylindrical in shape with diameter 2 mm and height 3 mm. At the first field position of 15 mm, it is only partially visible due to physical obstruction with the lens barrel. This limited the range of adjustable orientation of the LED at that field position, and it is possible the LED

is not oriented in an optimized direction to transfer most of its light to the radial view optics, which caused a decrease in gray level intensity on the image. Other smaller light sources such as fibre optics did not provide adequate illumination.

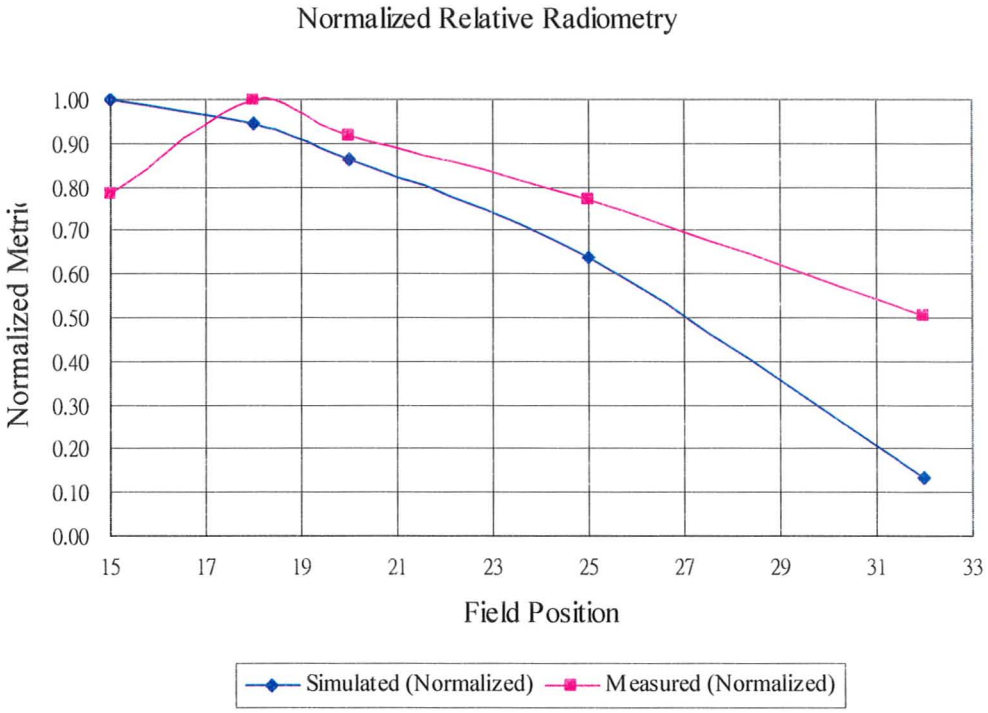

Figure 4.21. Acquired images resized at 50% zoom for field position 18 mm. (a) mask image (b) measurement image. The mean gray level intensity in the measurement image is 88.11 over the region of interest in defined by the mask image.

4.5 Reference

1. Robert E. Fischer, Biljana Tadie-Galeb, Paul R. Yoder (2008). *Optical System Design*. McGraw-Hill Professional.
2. SCHOTT North America Inc. (2009). *Inquiry Glass Overview Excel Table*. Retrieved Nov. 14, 2009. http://www.us.schott.com/advanced_optics/english/download/schott_optical_glass_catalogue_excel_2009.xls
3. Edmund Optics (2010). *Optics and Optical Components*. Edmund Optics.
4. Warren J. Smith (2004). *Modern Lens Design*. MgGraw Hill Professional.
5. ZEMAX Development Corporation (2008). *ZEMAX Optical Design Program User's Guide*. ZEMAX Development Corporation.
6. Frank L. Pedrotti, Leno M. Pedrotti, Leno S. Pedrotti (2006). *Introduction to Optics*, Benjamin Cummings.

Chapter 5
View Synthesis Algorithms

The target thesis application is diagnostic screening of the gastrointestinal (GI) tract using autofluorescence imaging in a non-real-time setting. Due to the narrow field of view (FOV) of the radial view optics, the interpretation of the acquired images could be better achieved if the images are stitched together to form a mosaic map of the areas traversed by the endoscope. In order to perform automated stitching of the acquired imagery without parallax artifacts, the radial view should be converted to a known image projection that could be calibrated and characterized [1]. Since the acquired images are ultimately used for human interpretation, it may be beneficial if a perspective projection view could be synthesized from the acquired image. This is because perspective view describes the method of image projection the human brain is most used to [2]. It would also be beneficial if the objects imaged in the radial view could be displayed without the intrinsic parallax distortion present in perspective projection, so view projections similar to the orthographic view of 3D computer-aided drafting and design CAD are also investigated. This chapter would address the topic of view synthesis from the imagery acquired by the manufactured prototype, in particular, a perspective projection based algorithm and an estimated orthographic projection based algorithm are proposed. The MATLAB^{TM} code for the perspective projection and the estimated orthographic projection view synthesis algorithm are in Appendix G.

View synthesis algorithms essentially map every pixel on the image to be synthesized to a position on the raw image. Existing panoramic catadioptric imaging system literatures have described approaches to the perspective view synthesis problem, but they often model the refractive optics as ideal perspective or orthographic cameras and focus on the mirror geometry [3]. Although there has been some investigation into combining optical simulation packages with panoramic catadioptric imaging system design [4], the majority of the view synthesis algorithms are not designed to fully utilize information from optical design packages. Due to the short range of object distances encountered in the radial view and the availability of optical design packages, ray trace simulations could be feasibly conducted across those object distances. A different approach than Ref. [3] to perspective view synthesis is taken for this thesis work, which would be the topic of discussion in section 5.1.

Another image synthesis method based on orthographic projection is discussed in section 5.2. This approach requires additional knowledge of the object depth from the optical axis, but ultimately achieves a more convenient interpretation of the scene.

5.1 Perspective View Synthesis Algorithm

As discussed in section 2.3.1, that the perspective view is an image projection where all the rays that define the image pass through a single point, which is referred as the single-viewpoint (SVP) constraint. The radial view optical design of this thesis work is based on a folded parabolic mirror form that satisfies this SVP constraint; thus the synthesis of a perspective view from the images acquired by the manufactured prototype described in chapter 4 should be possible.

The basis of perspective view is that objects along the same line of sight would be imaged onto the same point on the imaging plane. The approach used by Ref. [3] is to use conic section mathematics and the perspective projection camera model to calculate the ray paths across the mirrors. This method is not preferred when ray trace data is available, since the pinhole camera model is less accurate than ray traced data. The flow chart of the perspective view synthesis algorithm is illustrated in fig. 5.1. The image acquired from the prototype is the *raw image* and the image to be synthesized using perspective projection is the *perspective image.* As discussed in section 4.3.3, the image center of a perfect prototype is (r,c) = (640,512) but the image center of the manufactured prototype is calculated to be (r,c) = (647,561.5), where r is the row coordinate, c is column coordinate. The image coordinates are set up such that (r,c) = (1,1) at the top left corner and (r,c) = (1024,1280) at the bottom right corner of the image.

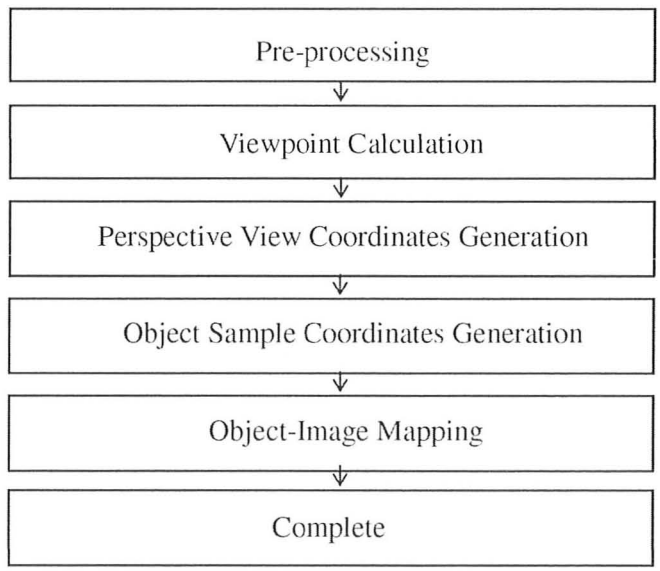

Figure 5.1. Perspective view synthesis algorithm flow chart.

Recall from section 2.3.2 that a plenoptic function is essentially describes the information acquired by a pinhole camera with 360° FOV. If the radial view optics is SVP constrained, the optics would functionally image the world through an effective viewpoint; the acquired image would contribute to the construction of

a plenoptic function at that effective viewpoint. If the same viewpoint is to also serve as the effective viewpoint of the perspective image, it would imply that the perspective image could directly sample from the plenoptic function of optics helped construct. This is the logic to perspective view synthesis used in this thesis work, which would require the effective viewpoint of the synthesized image to be placed at the effective viewpoint of the optical system.

In the *pre-processing* step, a database of ray trace information relating field point positions and corresponding image point positions is created at different object depths, as shown in fig. 5.2. It is discussed in section 2.1.1 that field points are simulated object points in a ray trace simulation. The image point position is taken to be the centroid of the spot diagram from the field point.

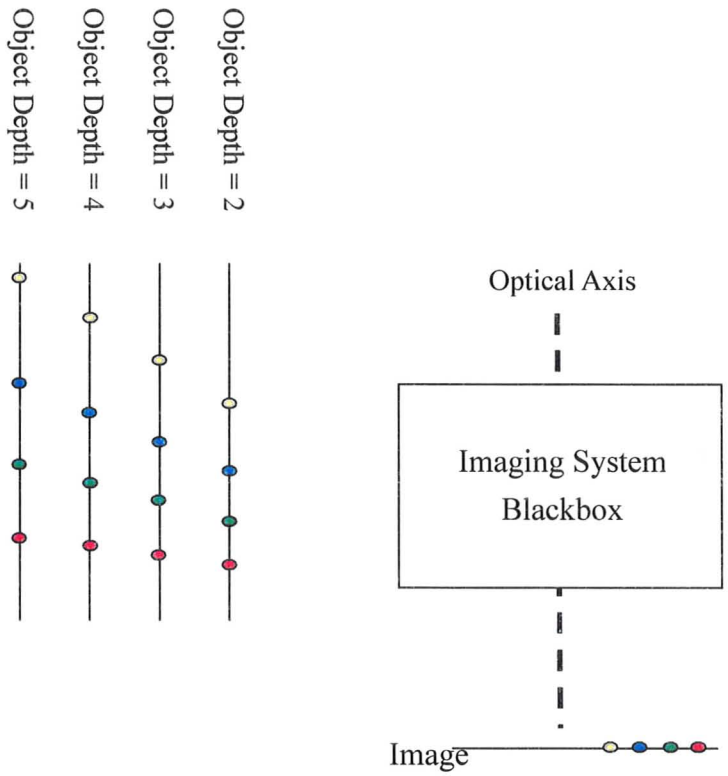

Figure 5.2. The raytrace database would store the relationship between field positions and their corresponding image positions. Object points with the same colour would map to the same coloured image point. The points on the image are uniformly sampled.

Due to the rotationally symmetric nature of the radial view optical design, the object is not located on a plane but on a cylinder concentric to the optical system as shown in fig. 5.3; this is referred to as the *object cylinder*. The database is then reorganized to group together the object points that have the same image

position. The *pre-processing* step is discussed in more detail in section 5.1.1.

In the *viewpoint calculation* step, the effective viewpoint of the radial view optical design is calculated from the ray trace database. As discussed earlier, the effective viewpoint of the synthesized perspective image would be placed at the effective viewpoint of the radial view optics. If the radial view optical design does not satisfy the SVP constraint, a profile of viewpoint against object locations would be built, and the centroid of the locus of viewpoints could be computed and assigned as the effective viewpoint of the perspective image. This step is discussed in section 5.1.2.

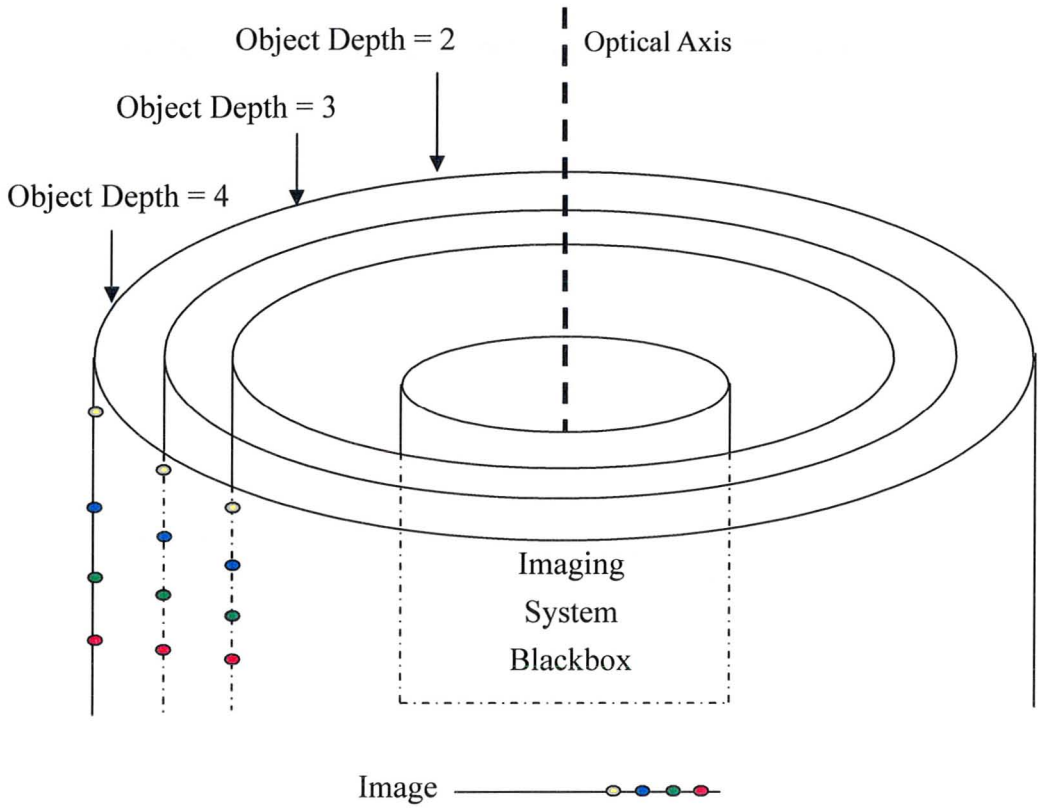

Figure 5.3. The object at a fixed depth forms a cylinder around the imaging system.

In the *perspective view coordinates generation* step, user inputs that describe the perspective view to be synthesized such as zoom, image size, and view orientation would be used to compute the object space locations of each pixel in the perspective view to be synthesized. This step computes the sampling plane of the perspective view on the world and it is discussed in section 5.1.3.

In the *object sample coordinates generation* step, lines of sight connecting the effective viewpoint and each of the view coordinates are projected towards the object cylinders and a collision detection algorithm described in Ref. [5] would be

used to record the intersection location. The intersection location would be referred to as the *object sample points*.

In the *Object-Image Mapping* step, each object sample points would be mapped to an image position using interpolation algorithms and the raytrace database constructed in the pre-processing step. The mapped image position would then undergo coordinate conversion from millimetres to pixels and adjusted for mechanical decenter errors on the manufactured prototype. This step provides a mapping between every pixel in the perspective image and their corresponding positions on the object cylinder.

5.1.1 Pre-process

The database is generated by tracing rays from 36 different field point locations across a custom defined FOV over 10 different object depths at 1 mm apart. This effectively samples the entire depth of field of the prototype design with 36 field positions for each depth. The depth of field of the prototype design is 2 mm ~ 11 mm measured from the outer dummy surface, as specified in table 4.4. MATLAB™ is used to calculate suitable field positions, which is then imported into Zemax™ as field positions. The maximum number of field points Zemax™ can simulate at once is 12, thus a macro routine is written to expedite this process. The custom defined FOV used here is larger than the design FOV used in chapter 4 to allow rays outside the design FOV to be traced. These rays would be used in the event significant decenter error is present in the manufactured prototype, which would cause a shift in the FOV. The data is then organized such that image positions would be associated with object positions across the 10 depths that have the same image position. These image positions are then uniformly sampled across image space using the MATLAB™ *spline()* interpolation function for better organization. The complete database is conceptually described in fig. 5.2, but with 36 object points per depth, 10 depths in total.

5.1.2 Viewpoint Calculation

Although the radial optics is designed using a SVP constrained mirror configuration, the question of whether the actual radial optical design is SVP constrained would have to be addressed in order to proceed with the view synthesis algorithm development. When all possible lines of sight within the FOV of the optical system intersect the optical axis at a common location, the system is said to be SVP constrained. If this is not the case, the objects and viewpoint are not related by a linear line of sight, but with a curve. Therefore non-linear fitting may have to be used to profile the relationship between the viewpoint and the objects seen through the viewpoint, as illustrated in fig. 5.4.

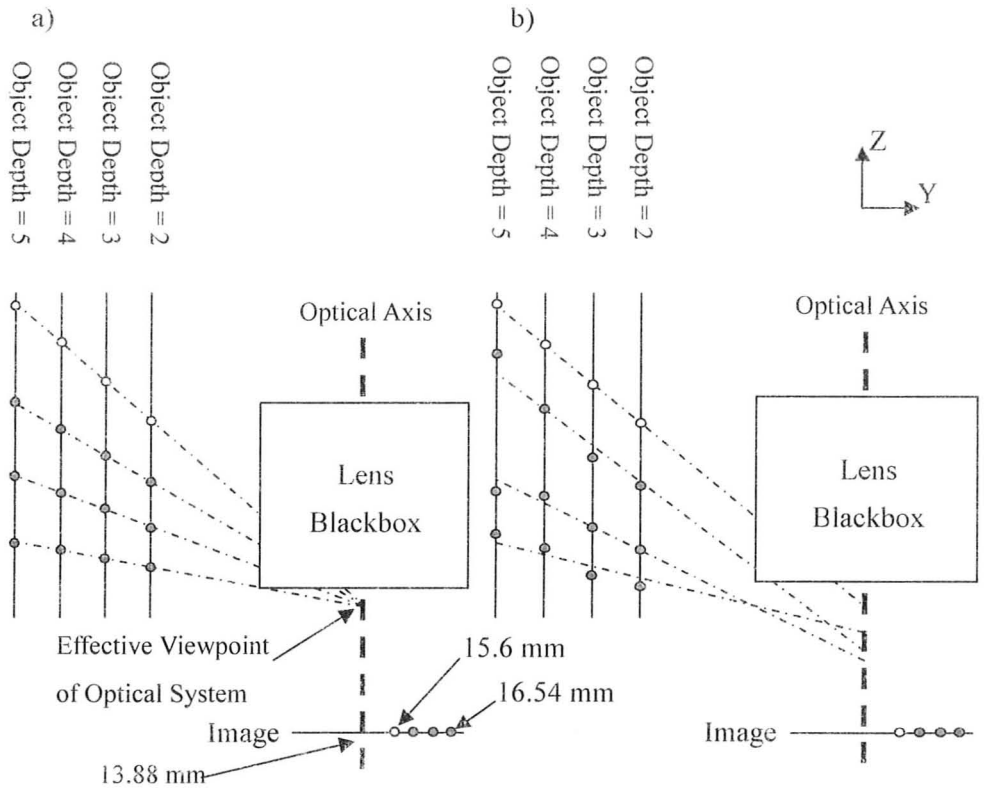

Figure 5.4. The possible outcome of the viewpoint calculation step (a) all objects points across depth with the same corresponding image point form a line of sight that would intersect the optical axis at a location shared by other lines of sight formed by other object points; this is the effective viewpoint (b) a more general case where object points across depth with the same corresponding image point do not form a straight line, and the objects may be better described using curves.

In this step, the points are first fitted with a linear trend to compute the corresponding viewpoints using back projection. If the positions of these back projected viewpoints are very different, then the points would be re-fitted with polynomial curves. Fortunately, the positions of the back projected viewpoints are found to be within 20 microns apart in the operational FOV, which meant the prototype design could practically be treated as a SVP constrained imaging system, and a non-linear fit is unnecessary. The viewpoint locations along the optical axis and the image position are shown in fig. 5.5. The optical axis is located at y =13.88 mm. The operational FOV of the radial view optics utilizes the region between y = 15.6 mm ~ 16.54 mm on the image surface. Recall that additional rays outside of this operational region are traced during the generation of the ray trace database as discussed in section 5.1.1. Since these rays are not included in the optical design process because they are outside of the design FOV, they are

unconstrained by the lens optimization routine. This implies their aberration is uncontrolled and may be significant. When the aberration is significant, the centroid of the spot diagram would deviate from that of an ideal perspective projection; this is essentially the distortion aberration. As shown in fig. 5.5, rays with image heights that are far from the operational image height of y = 15.6 mm ~ 16.54 mm do not satisfy the single-viewpoint constraint.

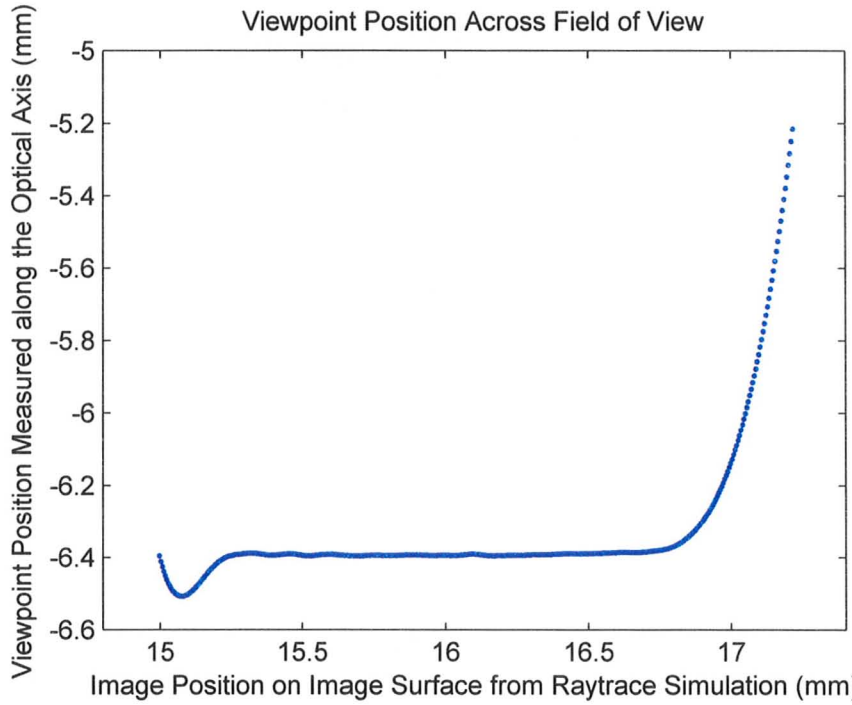

Figure 5.5. Viewpoint location and their corresponding image positions using only raytrace simulation data.

5.1.3 Perspective View Coordinates Generation

The user inputs that describe the perspective image to be synthesized are used to compute its corresponding location in object space. Each pixel in the perspective image is assigned a 3D position and is referred to as the *view coordinate,* and these coordinates make up a planar surface referred to as the *view plane*. The view plane is planar because the perspective image is planar. The view plane and the effective viewpoint would together define the regions of the world the perspective image would be sampling from, as shown in fig. 5.6. This is similar to the concept of the perspective camera model described in section 2.3.3 and fig. 2.6(b) where a plane is placed in front of the pinhole camera; the location of the plane and the pinhole would together dictate the regions of the world the image would be sampling from.

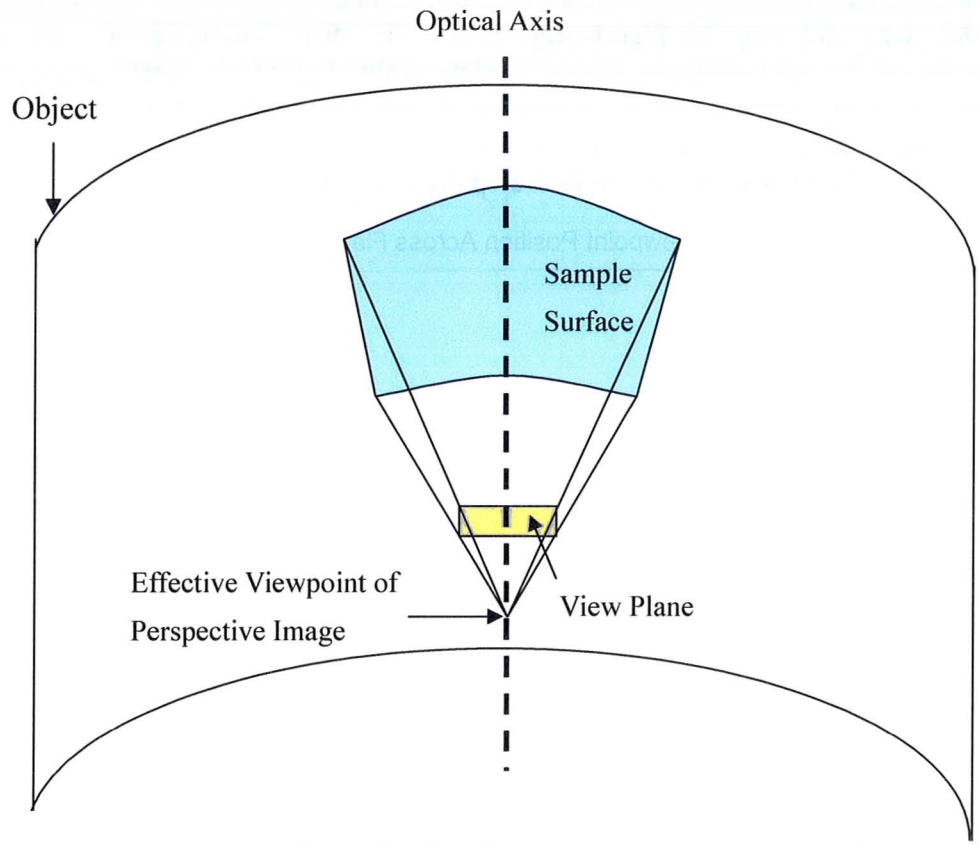

Figure 5.6. View plane and sample plane in object space. The view coordinates define the view plane, which could be used with the effective viewpoint to define the region of the world the resultant perspective image would sample from.

5.1.4 Object Sample Coordinates Generation

With reference to fig. 5.6, this step computes the corresponding object position on the sample plane from forward projecting rays that pass through the effective viewpoint and each view coordinate position on the view plane. These rays would intersect the object cylinder at positions computed by a custom implementation of the collision detection algorithm in Ref. [5]. The computed intersection positions are referred to as *object sample coordinates* and the surface they define is the *object sample surface*.

Each of the 10 sampled object depths has different object cylinders with different radiuses. The choice of the object cylinder from these 10 depths could be arbitrary, as long as the same object cylinder is used for the object-image mapping step. This is because the prototype optical system satisfies the SVP constraint, which implies objects at different depths that lie on the same line of sight from the effective viewpoint would all map to a common image point. The calculated

sample coordinates is shown in fig. 5.7. It has a shape similar to the sample surface illustrated in fig. 5.6. In fig. 5.7, the outline of the object sample surface is not rectangular due to its projection onto the object cylinder at an oblique angle, e.g. the effective viewpoint is located at z = -6.4 mm and so the perspective view to be synthesized is looking upwards in the positive z direction.

5.1.5 Object-Image Mapping

The raytrace database would map the object sample coordinates calculated in the previous step to their corresponding image coordinates. These image coordinates only describe radial distance from the image center. The angular information would be calculated from user specified orientation of the perspective image. The radial and angular information could then be converted to row and column coordinates to be used with the raw image.

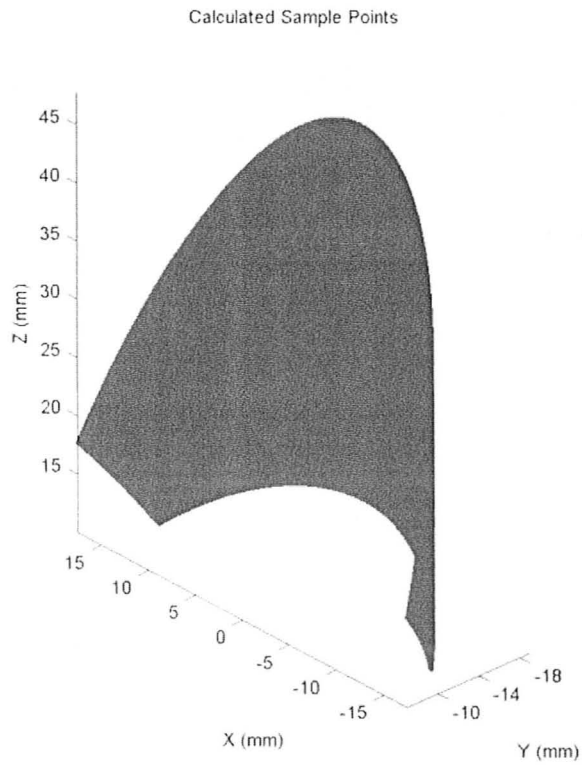

Figure 5.7. Calculated sample points in object space.

5.1.6 Results

Two acquired images are used to demonstrate this algorithm, as shown in fig. 5.8. The test scene in fig. 5.8(a) is a McMaster University business card rolled around the prototype. The test scene in fig. 5.8(d) is the 0.5 lp/mm tangential MTF

test used in chapter 4, which has straight parallel black lines when the test pattern paper is flattened, as shown in Appendix C.

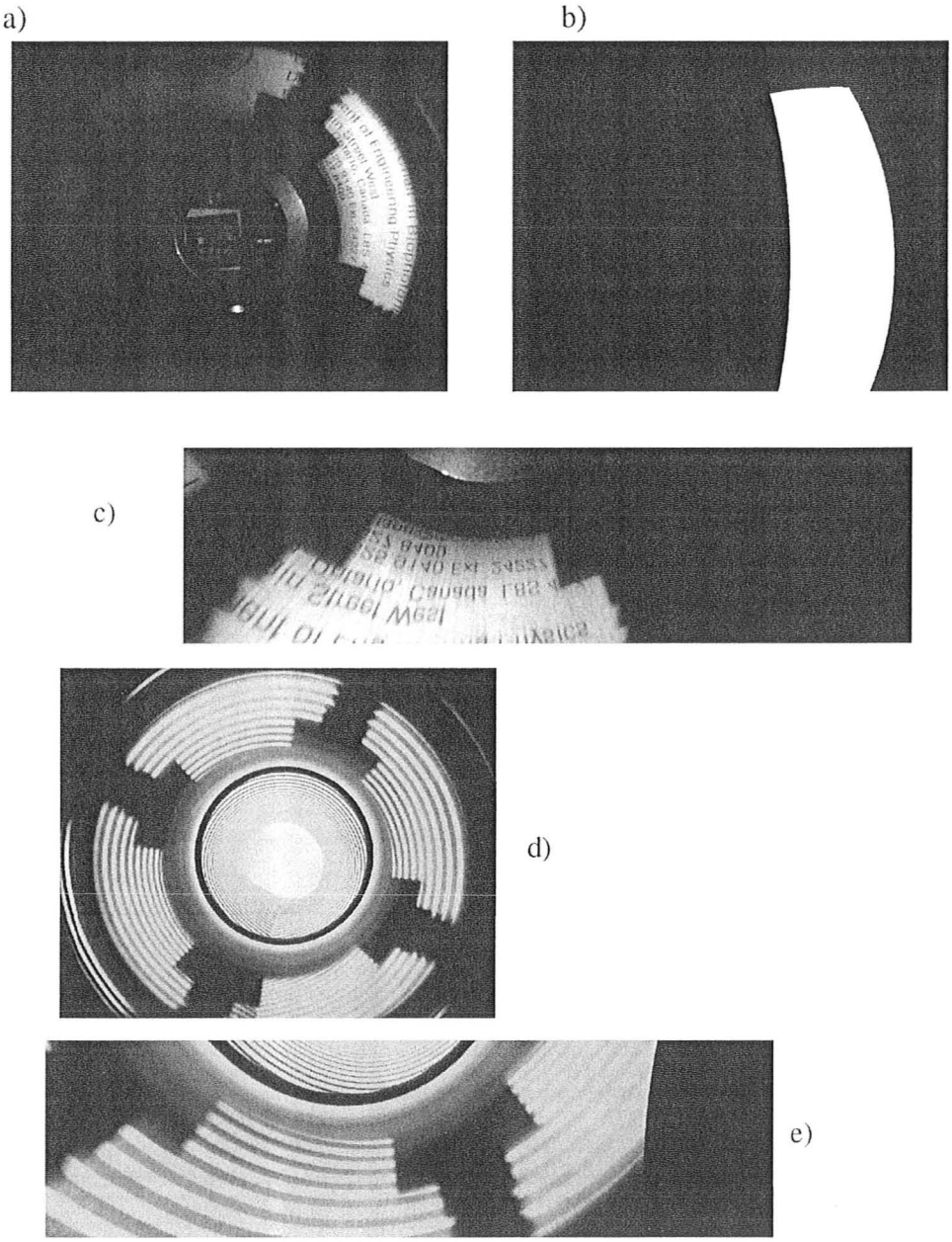

Figure 5.8. (a) mask image (b) acquired image with McMaster business card (c) synthesized perspective image (d) acquired image with 0.5 lp/mm test pattern (e) synthesized perspective image.

The synthesized images in fig. 5.8(c) and fig. 5.8(e) are not much different from the acquired image. The straight lines from the test pattern in fig. 5.8(d) do not appear straight. This is because the effective viewpoint of the optical system is found to be along the optical axis (z direction) at z = -6.4 mm, as shown in fig. 5.4(a). The FOV of the prototype has z coordinates above z = 12 mm. The effective viewpoint is located at least 18.4 mm away from the object it is imaging. This is analogous to an observer looking upwards at the bottom of a deep dried well; the horizontal brick lines along the walls of the well would appear curved to the viewer even though they appear to be straight when the viewer is next to it. It may be possible to generate views that have a closer viewpoint position to the FOV range of the radial view, but the new viewpoint would not coincide with the viewpoint of the radial optical design, thus other view synthesis methods would need to be employed.

5.2 Estimated Orthographic View Synthesis

When the object depth does not change significantly, or when knowledge of the depth position of the scene object is available, an estimated orthographic view may be synthesized. This may be the situation for the target thesis application where the distance from the sidewall of the endoscope to the GI tract wall may not change much in the narrower regions of the small intestine. For object scenes where the depth varies significantly, there may be ambiguity in the actual location of the object, as shown in fig. 5.9. In fig. 5.9(b), the horizontal lines of sight describe orthographic projection. Notice the line of sight drawn at the top which passes by the yellow and blue object points located at different object depths; this is marked by the arrows. The pixel that corresponds to that line of sight in the synthesized image would not be able to make a decision on which image point from the raw image to sample from, unless knowledge of the object depth at that line of sight is available to the view synthesis algorithm.

The cause of this problem is that the manufactured prototype samples the world from a finite viewpoint location of z = -6.4 mm on the optical axis, as shown in fig. 5.9(a), thus view synthesis using a different effect viewpoint location than that of the prototype would lead to the ambiguous situation shown in fig. 5.9(b). Therefore the algorithm proposed in this section can only provide an estimate of the true orthographic view.

5.2.1 Algorithm Approach

This algorithm is similar to the one proposed in section 5.1, but without the calculation of the effective viewpoint of the prototype system, nor the collision detection algorithm with the object cylinder. The same pre-processing module is used to generate the ray trace database. The algorithm flow chart is illustrated in fig. 5.10.

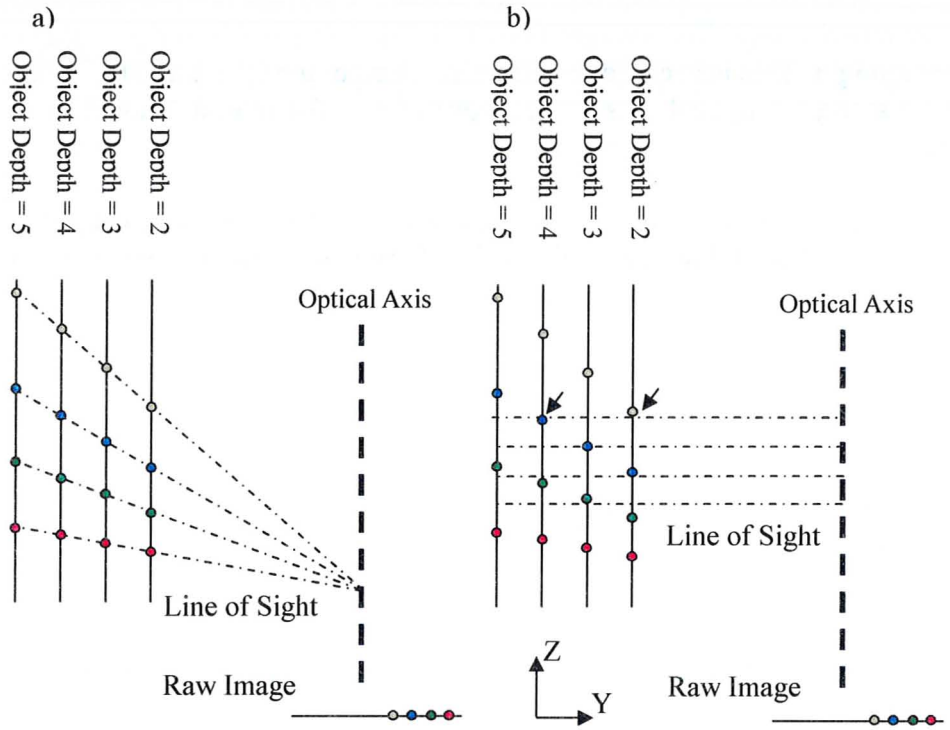

Figure 5.9. Estimated orthographic projection vs. perspective projection. (a) perspective projection with the same viewpoint as the optical system (b) orthographic projection where the viewpoint is located at infinity.

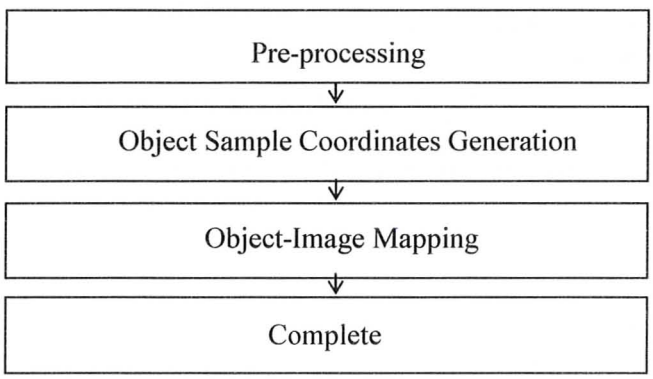

Figure 5.10. Estimated orthographic view synthesis algorithm flow chart.

Due to the nature of the orthographic projection, the z coordinates of the image position and object positions are identical when the magnification of the orthographic projection is set to unity; this is shown in fig. 5.9(b). The synthesized image can be defined directly on the object cylinder since the view coordinates and object sample coordinates are the same. The calculated object

sample points are then mapped to the corresponding raw image locations using the same *Object-Image Mapping* module described in section 5.1.5.

5.2.2 Results

The same test images used in the perspective view synthesis are used for the estimated orthographic view synthesis, with the results shown in fig. 5.11.

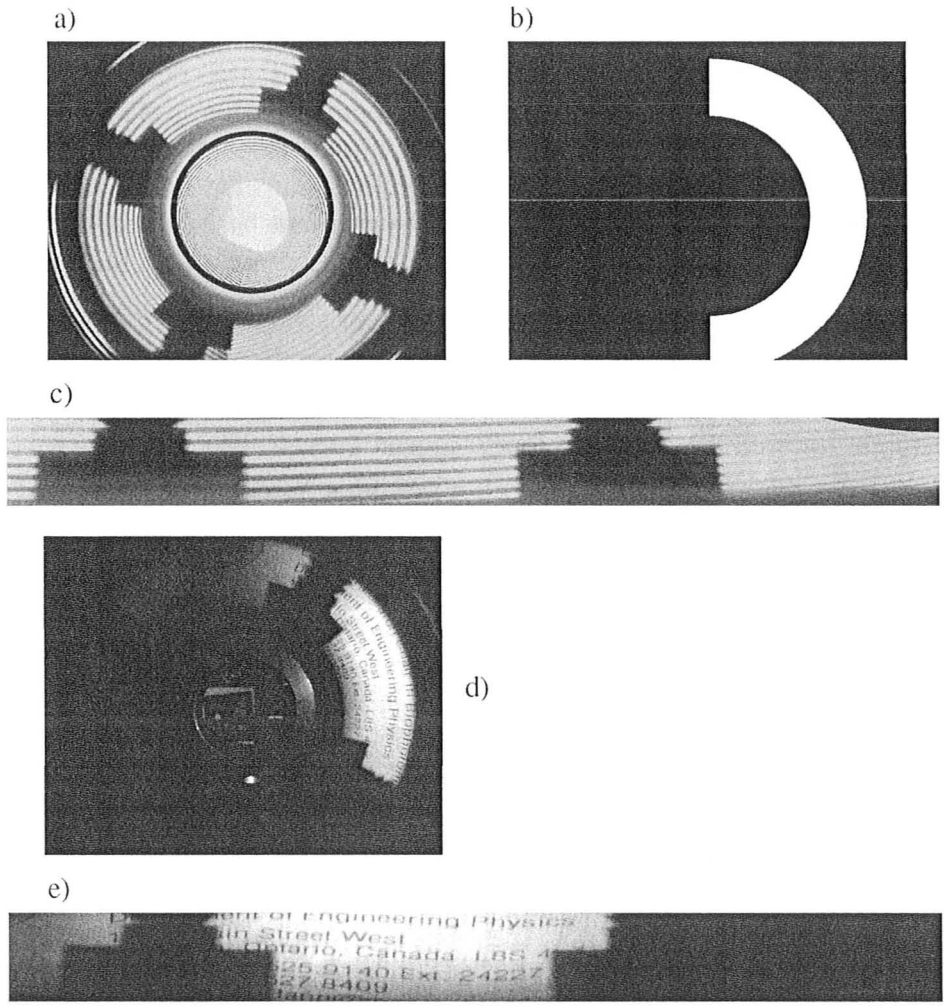

Figure 5.11. (a) mask image (b) acquired image with 0.5 lp/mm test pattern (c) synthesized estimated orthographic image (d) acquired image with McMaster business card (e) synthesized estimated orthographic image.

The estimated orthographic view synthesis algorithm is run with the object depth set to 19.88 mm from the optical axis and with 180° field of view. The 0.5 lp/mm MTF test pattern in fig. 5.11(a) is setup according to fig. 4.7(b), which

corresponds to an object depth of 20 mm. From fig. 5.11(c), the straight and parallel black lines of the 0.5 lp/mm MTF test pattern are successfully unwrapped to almost straight lines. The setup of the business card test scene in fig. 5.11(d) is not as accurately held in place in the equipment setup as the MTF test pattern, but the synthesized image in fig. 5.11(e) have the appearance of being less distorted than the perspective view synthesis result in fig. 5.8(c).

5.3 Discussion

The perspective view synthesis algorithm in section 5.1 is theoretically valid for objects within the operating depth of field and FOV range of the prototype imaging system since the prototype optical design is SVP constrained and thus objects along the line of sight that passes through the viewpoint are mapped to a common image point. The availability of a perspective view from the prototype imaging system implies that multi-viewpoint based 3D reconstruction algorithms such as structure from motion may be possible [6]; this may have applications in other research fields such as laparoscopic surgery or tunnel inspection.

The estimated orthographic view algorithm in section 5.2 has the advantage of displaying more useful information on the surrounding object, mainly the fact that straight lines on the object no longer appear curved. The disadvantage is that the proposed algorithm is only an estimation of a true orthographic projection where ambiguity in actual object positions may arise as shown in fig. 5.9(b).

5.4 References

1. Fay Huang, Reinhard Klette, Karsten Scheibe (2008). *Panoramic Imaging: Sensor-Line Cameras and Laser Range-Finders*. John Wiley & Sons Ltd.
2. David Salomon (1999). *Computer graphics and geometric modeling*. Springer.
3. S. K. Nayar (1997). Catadioptric Omnidirectional Camera. 1997 *IEEE Computer Society Conference on Computer Vision and Pattern Reconition*, 482-488.
4. Gurunandan Krishnan, S. K. Nayar (2010). Cata-Fisheye Camera for Panoramic Imaging. *IEEE Workshop on Applications of Computer Vision, WACV 2008*, 1-8.
5. Christer Ericson (2005). *Real-Time Collision Detection*. Morgan Kaufmann
6. Richard Hartley (2004). *Multiple View Geometry in Computer Vision*. Cambridge University Press.

Chapter 6
Conclusion

Two endoscope objective designs are proposed in this thesis work: a 1:1 scale design and a 3:1 scale design. Both designs are capable of viewing objects to the front and radial directions of the endoscope in a simultaneous manner. The proposed 1:1 scale design provides a more practical method of collecting light from objects along the gastrointestinal (GI) wall under the assumption the GI tract is collapsed on the endoscope. The simulated image quality is similar to the simulated performance of several wide-angle endoscope objective designs described in Ref. [1-6]. The performance summary for the reference designs and proposed designs are in table 6.1 and table 6.2, respectively.

Table 6.1. Performance summary of reference designs.

	Reference Designs					
Features	[1]	[2]	[3]	[4]	[5]	[6]
EFL (mm)	1	1.84	0.5	1	0.5	1
Full FOV (deg)	133	133	116	116	80	110
F-number	2.42	1.96	3.01	4.1	3.99	4.93
EPR (mm)	0.21	0.32	0.084	0.12	0.06	0.1
NA, object space	0.01	0.02	0.008	0.011	0.006	0.002
NA, image space	0.21	0.26	0.17	0.12	0.13	0.1
RMS spot size, on-axis (μm)	1.4	1.2	1.9	2.2	0.9	2.2
Airy Disc Radius (mm)	4.2	3.2	2.9	6.3	4.1	3.5
Number of elements	8	8	3	7	3	6
Track length (mm)	7.72	9.01	2.9	6.7	3.2	9.9
Shortest ROC (mm)	0.87	0.85	-0.75	0.85	0.61	0.93
RMS spot size at full field (μm)	4.8	5.6	5.9	4.1	4.2	5.9

As shown in table 6.2, the numerical aperture for the proposed 1:1 scale design is the largest across all simulated designs, which shows the proposed prototype has a larger light collection angle than the simulated reference designs. The Airy disc and root mean square (RMS) spot size is a measure of image quality, where the larger of the two quantities would describe the size of the simulated blur radius from imaging a point object. The Airy disc radius describes the blur due to diffraction effects and increases as the aperture stop diameter is decreased. It can be seen in table 6.1 that the reference designs have such small aperture stop diameters that the Airy disc radius approach that of the RMS spot size. The speculated purpose of the small aperture stop diameters in the reference designs is to lower the aberrations encountered in off-axis object points. This is speculated from the fact their on-axis and full field RMS spot sizes are very different. For the proposed 1:1 scale design, the Airy disc is the smallest among all simulated

designs in table 6.1. This implies the proposed 1:1 scale design would suffer less from the diffraction induced performance degradation than the other designs.

Table 6.2. Performance summary of the proposed 1:1 scale and 3:1 scale designs; (R) is radial view and (F) is forward view.

	Proposed Designs			
Features	1:1 (R)	1:1 (F)	3:1 (R)	3:1 (F)
EFL (mm)	1.12	0.9	3.52	2.81
Full FOV (deg)	20	44	23	50
F-number	2.46	2.99	4.14	4.26
EPR (mm)	0.19	0.15	0.42	0.33
NA, object space	0.026	0.014	0.016	0.008
NA, image space	0.16	0.17	0.12	0.12
RMS spot size, on-axis [1] (μm)	4.0	1.9	3.2	1.9
Airy Disc Radius (mm)	2.1	2.1	3	3
Number of elements [2]	6	10	7	11
Track length (mm)	13.74	19.48	38.27	83.07
Shortest ROC (mm)	1.84	1.84	6.18	6.18
RMS spot size at full field [3] (μm)	4.04	1.58	2.98	3.04

[1] Measured at the field point closest to the radial optics
[2] The two mirrors are considered as two elements
[3] Measured at the field point furthest to the radial optics

In terms of physical dimension, the proposed 1:1 scale design is suitable for use with catheter based endoscopes, but its track length of 19.48 mm is too long to practically fit inside the footprint of a capsule endoscope. Although it is possible to scale the entire design down to 50% of the original size, the fabrication and mechanical assembly requirements of the lens may become unrealistic. Several precision optics shops verbally specified the manufacture limit of their fabrication process is in the range of 2 mm or 1 mm for the radius of curvature, but from table 6.1, it would seem that endoscope designs with radius of curvature as small as 0.61 mm could be fabricated. The shortest radius of curvature for the proposed 1:1 scale design is 1.84 mm, which would become 0.92 mm if the design is scaled down to 50% of the original size. This thesis work followed the suggestion of the optics shops and kept the radius of curvature above 1 mm.

The proposed 1:1 scale design could benefit from having larger magnification, as its image dimension is only 2 mm × 2 mm. Typical capsule endoscopes could have a diameter of 11 mm [7]. The field of view position of the radial view could also benefit if it is closer to the region near the two folded mirrors to further reduce the distance between the object and the radial view optics. Decrease in the source to collection optics distance would aid in irradiance collection as shown in the radiometry simulations of section 3.5.

The proposed 1:1 scale and 3:1 scale designs contain the most number of elements. The feasibility of manufacturing the 3:1 scale design with 11 elements

as well as the performance degradation due to tolerance is described in chapter 4. It is concluded that the actual image performance of the radial view imaging system can be predicted by Monte Carlo based tolerance simulations.

For future prototype designs, Monte Carlo tolerance simulations should be iterated across multiple spatial frequencies. The simulated performance after the inclusion of tolerance serves as a much better prediction of the actual performance than the nominal modulation transfer function (MTF) simulation results, as documented in chapter 4. The evaluation criterion should also be set to evaluating the MTF in both the tangential and sagittal directions, as opposed to an averaged score of the two. This would prevent the MTF in one direction being significantly better than the other direction, as is the case with the manufactured prototype.

Construction of dedicated verification apparatus should be a priority for future verification work on the manufactured prototype. The radial view test setup currently utilize custom printed test patterns on paper that can be quickly assembled and disassembled on optical mounts as described in fig. 4.7(b), and the illumination described in fig. 4.8. The illumination method is based on backlighting the test target paper to create diffuse light to achieve uniformity in illumination. Construction of new illumination test systems could use miniature light emitting diodes (LEDs) on a strip of flexible material that would wrap around the prototype. Although the illumination generated from this type of setup would not be as uniform as the back light setup used in chapter 4, it is a more realistic setup that approximates the actual operation of the endoscope. Construction of a scaled-up synthetic GI tract with known object details on the walls, twists and bends along its length, as well as varying diameter would help to acquire imagery from a more realistic environment.

Two preliminary view synthesis algorithms are investigated in chapter 5, where the estimated orthographic projection algorithm achieved better success in terms of scene interpretation than the perspective projection algorithm. Future work for the view synthesis portion of this project could include investigations into other view synthesis approaches where the viewpoint of the synthesized image is located at a different position than the effective viewpoint of the radial view optics. The problem of view synthesis is an on-going research topic in the area of image-based rendering [8,9]. Literature from that research area could serve as a starting point to the view synthesis algorithm of the proposed design; just as literature from panoramic imaging using curved mirrors are used in the optical design of this thesis work. Mosaic map generation from the raw acquired images or the synthesized views is also another research area worthy of investigation due to the interpretation benefits it could provide to the human operator.

6.1 References

1. Patent: US 6956703, Objective Lens for Endoscope, 18-10-2005.

2. Patent: US 6994668, Four-Group Endoscope Objective Lens, 7-2-2006.
3. Patent: US 7027231, Endoscope Objective Lens, 11-4-2006.
4. Patent: US 7085064, Object Lens and Endoscope using it, 1-8-2006.
5. Patent: US 7218454, Endoscope Objective Lens, 15-5-2007.
6. Patent: US 7486449, Objective Lens for Endoscope, and Imaging Apparatus for Endoscope using the same, 3-2-2009.
7. Moussa Kfouri, Ognian Marinov, Paul Quevedo, Naser Faramarzpour, Student Member, Shahram Shirani, Louis W. C. Liu, Qiyin Fang, M. Jamal Deen (2008). Toward a Miniaturized Wireless Fluorescence-Based Diagnostic Imaging System. *IEEE Journal of Selected Topics in Quantum Electronics*, 14(1), 226-234.
8. K. Tanaka, K. Otsuka, M. Hirayama, E. Kondo (2005). View synthesis on mobile robot image database. *2005 IEEE International Conference on Robotics and Biomimetics*, 455-461.
9. S. M. Seitz, C. R. Dyer (1995). Physically-Valid View Synthesis by Image Interpolation. *Proc. Workshop on Representation of Visual Scenes*, 18-25.

Appendix A
Chief Raytrace MATLAB™ Code

A.1 main.m

```
clear all
%% Description
% Given a range of k and range of c, generate k,c sampling coordinates and
% simulate with specified starting and ending radius.

%% How parameters are chosen for each surface
% menually vary k and c while fixing starting and ending radius. The range
% of k and c were chosen such that the total length (in optical axis
% direction, taken to be z axis in global coordinate system) would remain
% less than CAPSULE_LENGTH. This was done manually so there may be some
% cases where it slightly goes out of bound.

% NOTE: all position coordinates are relative to a common, global coordinate
% system.

% Vary variable M to vary sampling of the k,c plane (warning, each
% sampling of the k,c plane would generate 3 saved plots and 1 text file
% summarizing the simulation at that specified (k,c) pair). In other words,
% M changes the number of cases to be simulated.

% Vary in.N to change the sampling of the mirror. This changes the number
% of rays traced per plot.

CAPSULE_LENGTH=22;
in.surface_mode=1;
SVP_flag=1; % >0 for true, <0 for false
cam_start=3; %for nonSVP configurations
cam_end=13; %for nonSVP configurations
if SVP_flag>0
    cam_start=-5;
    cam_end=-5;
end

M=4; %sampling of k,c plane %(M must be positive integer, non-zero)
out_len=zeros(1,M*M);
out_H=zeros(1,M*M);
out_P=zeros(1,M*M);
kc_plane=zeros(2,M*M);

in.start_r=1;
in.end_r=4.5;
in.N=10;
in.cylinder_r=7.5;

switch in.surface_mode
    case 1
        %for ellipse, note R1 is end_r, R2 is star_r, which is opposite,
        %k>0, c>0
        k_start=100;
        k_end=300;
        c_start=5;
        c_end=15;
        %cam_start=-5;
```

```
        %cam_end=-5;
    case 2
        %for hyperbolic, k>2, c>0
        k_start=3;
        k_end=16;
        c_start=3;
        c_end=13;
        %cam_start=-5;
        %cam_end=-5;
    case 3
        %for cone, c=0, k=>2
        k_start=2.5;
        k_end=8;
        c_start=0;
        c_end=0;
        %cam_start=3;
        %cam_end=13;
    case 4
        % for sphere, k>0,c=0
        k_start=50; %corresponds to radius of 5
        k_end=200; %corresponds to radius of 10
        c_start=0;
        c_end=0;
        %cam_start=15;
        %cam_end=24;
end
step_k=(k_end-k_start)/(M-1);
step_c=(c_end-c_start)/(M-1);
step_cam=(cam_end-cam_start)/(M-1);

index=1;
c=c_start;
cam_dist=cam_start;
for a=1:M
    k=k_start;
    for b=1:M
    in.k=k;
    in.c=c;
    in.cam_dist=cam_dist;
    ret=engine(in, CAPSULE_LENGTH,a,b);

    %H=(omni z direction FOV range)
    %P=(position of the top of omni FOV)

    out_len(index)=ret.total_length;
    out_H(index)=ret.H;
    out_P(index)=ret.P;
    kc_plane(1,index)=k;
    if in.cam_dist <-1
        kc_plane(2,index)=c;
    else
        kc_plane(2,index)=in.cam_dist;
    end

    index=index+1;
    k=k+step_k;
    end
    c=c+step_c;
    cam_dist=cam_dist+step_cam;
end

figure,plot3(kc_plane(1,:),kc_plane(2,:),out_H,'.');
title('omnidirectional FOV range (z component)')
```

```
axis equal
xlabel('k')
if in.cam_dist <-1
    ylabel('c')
else
    ylabel('nonSVP: camera distance')
end
saveas(gcf,'000000FOVRangePlot.fig')

figure,plot3(kc_plane(1,:),kc_plane(2,:),out_len,'.');
title('setup length in z component (pinhole to far end of mirror)')
axis equal
xlabel('k')
if in.cam_dist <-1
    ylabel('c')
else
    ylabel('nonSVP: camera distance')
end
saveas(gcf,'000000SetupLengthPlot.fig')

figure,plot3(kc_plane(1,:),kc_plane(2,:),out_P,'.');
title('position of the top edge of the FOV (z component)')
axis equal
xlabel('k')
if in.cam_dist <-1
    ylabel('c')
else
    ylabel('nonSVP: camera distance')
end
saveas(gcf,'000000FOVStartPositionPlot.fig')
```

A.2 engine.m

```
%% Functional form of maincone.m
function qreturn = engine(in, CAPSULE_LENGTH,step_x,step_y)
start_r=in.start_r;
end_r=in.end_r;
N=in.N;

cam_dist=in.cam_dist;
cylinder_r=in.cylinder_r;
surface_mode=in.surface_mode;

k=in.k;
c=in.c;
concavity=1; %1 for convex, else concave. this function is broken right now.

switch surface_mode
    case 1
        %for ellipse, note R1 is end_r, R2 is star_r, which is opposite
        %convention of the other cases.
        be=sqrt(k/2);
        ae=sqrt((2*k+c^2)/4);

        z=0;
        max_cut_off=be*sqrt(1-(z-c/2)^2/ae^2);
        % check if practical
        T=-ae*sqrt((1-start_r^2/be^2))+c/2;
        %

        concavity=0;
        ret=getEllipse( start_r, end_r ,N,k,concavity,c);
        preset1=sprintf(' ellipse: cut off radius at z=0 plane is %.3f ',max_cut_off);
```

```
    case 2 %for hyperbolic
        ah=(c/2)*sqrt((k-2)/k);
        bh=(c/2)*sqrt(2/k);
        % check if practical
        T=-ah*sqrt(1+end_r^2/bh^2)+c/2;
        %
        preset1=sprintf(': hyperbolic: ');
        ret=getHyperbola( start_r, end_r ,N,k,concavity,c);

    case 3 %for cone
        c=0;
        % check if practical
        T=-end_r*sqrt((k-2)/2);
        %
        ret=getCone( start_r, end_r ,N,k,concavity);
        preset1=sprintf(' cone: ');
    case 4 % for sphere
        c=0;
        % check if practical
        if concavity==1
            T=sqrt(k/2-end_r^2);
        else
            T=-1*sqrt(k/2-end_r^2);
        end
        %
        ret=getSphere2( start_r, end_r ,N,k,concavity,c);
        preset1=sprintf(' sphere: ',k);
end


% check capsule length
if cam_dist<-1
    total_length=c-T;
else
    total_length=cam_dist-T;
end
if total_length >CAPSULE_LENGTH
    'too long'
    passstring='the capsule is too long for given input parameters\n\r '
else
    passstring=sprintf('the capsule length is %.2f\n\r ',total_length);
end
%end of check

if cam_dist <-1
    cam_dist=c;
end
preset2=sprintf('startr=%.2f endr=%.2f N=%d k=%.2f concavity=%d c=%.2f
camdist=%.2f',start_r,end_r,N,k,concavity,c,cam_dist);

pinhole=[0;0;cam_dist];
[junk N_pts]=size(ret.m);
out=zeros(3,N_pts);
world_out=zeros(3,N_pts);
topZ=0;
bottomZ=0;
for pp=1:N_pts
%k=36
    m=ret.m(:,pp);


    a=m-pinhole;
```

```
    %z^2+x^2+y^2=k/2;
    n=ret.n(:,pp);
    x=n(1); y=n(2); z=n(3);
    %n=n/norm(n);


    %find the azimeth and elevation angles of the normal
    phi=atan2(y,x);
    theta=atan2(sqrt(x^2+y^2),z);

    Rz = EulerR( 'z',phi );
    Ry = EulerR( 'y',theta );

    n_=Ry'*Rz'*n;
    a_=Ry'*Rz'*(pinhole-m);
    %a_=Ry'*Rz'*a;
    %out2=Rz*Ry*[0;0;norm(n)]

    %% look only at the x-y plane to get output phi angle`
    %a_=[1;1;1];
    p=[a_(1);a_(2)];
    %p=[-1;0];
    R180=PlanarR(pi);
    pout=R180*p;
    alpha=atan2(pout(2),pout(1));

    %% look only at the r-z plane to get output elevation angle

    r_sqrd=p(1)^2+p(2)^2;
    r=sqrt(r_sqrd);
    theta1=atan2(r,a_(3));

    %if theta1>0
     %   beta=pi/2-(pi-theta1);
    %else
    %    beta=pi/2-(-1*pi-theta1);
    %end

    Rz1 = EulerR( 'z',alpha );
    Ry1 = EulerR( 'y',theta1 );
    %o=[pout(1);pout(2);a_(3)];
    o=Rz1*Ry1*[0;0;norm(a_)];
    out(:,pp)=Rz*Ry*o;

    %% cylinder collision detection.
%algorithm from "Real Time Collision Detection" PG 192. By C.Ericson.
%n in book is u here, P is at origin => m in book is m here.
%a  is c1,  b is c2, c is c3 in the equadratic expression.
%note the equadratic root expression is correct in the book since the
%factor of 2 wasn't included in b.
    u=out(:,pp);
    d=[0;0;50*cylinder_r];
    %(arbitrarily choose any point but hte origin on the z axis to define cylinder axis.)

    c1=dot(d,d)*dot(u,u)-dot(u,d)^2;
    c2=dot(d,d)*dot(m,u)-dot(u,d)*dot(m,d);
    c3=dot(d,d)*(dot(m,m)-cylinder_r^2)-dot(m,d)^2;

    if c1== 0
        %case reflected ray is parallel to cylinder.
        world_out(:,pp)=[0;0;0];
    else
        t1=(-c2+sqrt(c2^2-c1*c3))/c1;
```

```
        t2=(-c2-sqrt(c2^2-c1*c3))/c1;
        if t1>0
            t=t1;
        else
            t=t2;
        end
        world_out(:,pp)=m+t*u;
    end

end

bottomZ=min(min(world_out(3,:)));
topZ=max(max(world_out(3,:)));
%show reflected ray and normal
name1=strcat(preset1,preset2);
if step_x>9
    stringx=sprintf('%d',step_x);
else
    stringx=sprintf('0%d',step_x);
end
if step_y>9
    stringy=sprintf('%d',step_y);
else
    stringy=sprintf('0%d',step_y);
end
stringCaseNum=strcat(stringx,stringy);
figure,
hhh=quiver3(ret.m(1,:),ret.m(2,:),ret.m(3,:),out(1,:),out(2,:),out(3,:));
title('Reflected Rays (Rem: all chief rays)')
axis equal
stringtemp=strcat(stringCaseNum,'Reflected.fig');
saveas(hhh,stringtemp)
close(gcf);

figure,
yyy=quiver3(ret.m(1,:),ret.m(2,:),ret.m(3,:),ret.n(1,:),ret.n(2,:),ret.n(3,:));
title('normal of mirror')
axis equal
stringtemp=strcat(stringCaseNum,'normal.fig');
saveas(yyy,stringtemp)
close(gcf);

figure,
zzz=plot3(ret.m(1,:),ret.m(2,:),ret.m(3,:),'.',world_out(1,:),world_out(2,:),world
_out(3,:),'.');
title('mirror points and world points')
axis equal
stringtemp=strcat(stringCaseNum,'cylindercollision.fig');
saveas(gcf,stringtemp)
close(gcf);

stringtemp=strcat(stringCaseNum,'IO_parameters.txt');
fid = fopen(stringtemp,'w');
fprintf(fid,name1);
fprintf(fid,'\n\r');
fprintf(fid,' T(bottom position of mirror)=%.3f\n H(omni z direction FOV range)=%.3f\n
P(position of the top of omni FOV)=%.2f \n\r',T,abs(topZ-bottomZ),topZ);
fprintf(fid,' max capsule length designated as %.2f \n\r',CAPSULE_LENGTH);
fprintf(fid,passstring);
fprintf(fid,'startr is R1, endr is R2, N relates to sampling of the mirror surface for
ray tracing \n\r');
fprintf(fid,'k, c relate to surface, c is camera position for SVP correct
configuration\n\r');
```

```
fprintf(fid,'cam_dist is actual pinhole camera distance.\n\r');
fprintf(fid,'T is height of simulated mirror (function of R1,R2,k,c)\n\r');
fprintf(fid,'H is height of omnidirectional FOV, P is the beginning of the
omnidirectional FOV\n\r');
fprintf(fid,'concavity of 1 means convex mirror, else concave\n\r');
fprintf(fid,'all positions referenced to a common global coordinate system.\n\r');
fclose(fid);

qreturn.total_length=total_length;
qreturn.H=abs(topZ-bottomZ); %H=(omni z direction FOV range)
qreturn.P=topZ;% P=(position of the top of omni FOV)
end
```

A.3 getEllipse.m

```
function qreturn = getEllipse( start_r, end_r ,N,k,concavity,c)
%get sphere
%always start with the vertice above the plane z=0, i.e. z>0
%theta measured from positive z axis.
%concavity == 1 for convex, else concave
    step_r=(end_r-start_r)/N;
    step_phi=2*pi/N;
    qreturn.m=zeros(3,N);
    qreturn.n=zeros(3,N);
    g=1;
    phi=0;
    r=start_r;
    be=sqrt(k/2);
    ae=sqrt((2*k+c^2)/4);
    cons=1+c^2/(2*k);
    for a=0:N
        for b=0:N
            %surface calculation of sphere
            qreturn.m(1,g)=r*cos(phi);
            qreturn.m(2,g)=r*sin(phi);
            qreturn.m(3,g)=-ae*sqrt(1-r^2/be^2)+c/2;
            %normal calculation of sphere
            if concavity==1
                %case normal vector pointing outwards from centre (origin)
                qreturn.n(1,g)=2*qreturn.m(1,g)*cons;
                qreturn.n(2,g)=2*qreturn.m(2,g)*cons;
                qreturn.n(3,g)=2*qreturn.m(3,g)-c;
            else
                qreturn.n(1,g)=-2*qreturn.m(1,g)*cons;
                qreturn.n(2,g)=-2*qreturn.m(2,g)*cons;
                qreturn.n(3,g)=-2*qreturn.m(3,g)+c;
            end
            g=g+1;
            phi=phi+step_phi;
        end
        r=r+step_r;
    end
end
```

A.4 getHyperbola.m

```
function qreturn = getHyperbola( start_r, end_r ,N,k,concavity,c)
%get sphere
%always start with the vertice above the plane z=0, i.e. z>0
%theta measured from positive z axis.
%concavity == 1 for convex, else concave
    step_r=(end_r-start_r)/N;
```

```
    step_phi=2*pi/N;
    qreturn.m=zeros(3,N);
    qreturn.n=zeros(3,N);
    g=1;
    phi=0;
    r=start_r;
    ah=sqrt((k-2)/k)*c/2;
    bh=sqrt(2/k)*c/2;
    for a=0:N
        for b=0:N
            %surface calculation of sphere
            qreturn.m(1,g)=r*cos(phi);
            qreturn.m(2,g)=r*sin(phi);
            qreturn.m(3,g)=-ah*sqrt(1+r^2/bh^2)+c/2;

            %normal calculation of sphere
            if concavity==1
                %case normal vector pointing outwards from centre (origin)
                qreturn.n(1,g)=(k-2)*qreturn.m(1,g);
                qreturn.n(2,g)=(k-2)*qreturn.m(2,g);
                qreturn.n(3,g)=c-2*qreturn.m(3,g);
            else
                qreturn.n(1,g)=-(k-2)*qreturn.m(1,g);
                qreturn.n(2,g)=-(k-2)*qreturn.m(2,g);
                qreturn.n(3,g)=-2*qreturn.m(3,g);
            end
            g=g+1;
            phi=phi+step_phi;
        end
        r=r+step_r;
    end
end
```

A.5 getCone.m

```
function qreturn = getCone( start_r, end_r ,N,k,concavity)
%get sphere
%always start with the vertice above the plane z=0, i.e. z>0
%theta measured from positive z axis.
%concavity == 1 for convex, else concave
    step_r=(end_r-start_r)/N;
    step_phi=2*pi/N;
    qreturn.m=zeros(3,N);
    qreturn.n=zeros(3,N);
    g=1;
    phi=0;
    r=start_r;
    for a=0:N
        for b=0:N
            %surface calculation of sphere
            qreturn.m(1,g)=r*cos(phi);
            qreturn.m(2,g)=r*sin(phi);
            qreturn.m(3,g)=-r*sqrt((k-2)/2);

            %normal calculation of sphere
            if concavity==1
                %case normal vector pointing outwards from centre (origin)
                qreturn.n(1,g)=(k-2)*qreturn.m(1,g);
                qreturn.n(2,g)=(k-2)*qreturn.m(2,g);
                qreturn.n(3,g)=-2*qreturn.m(3,g);
            else
                qreturn.n(1,g)=-(k-2)*qreturn.m(1,g);
                qreturn.n(2,g)=-(k-2)*qreturn.m(2,g);
```

```
                qreturn.n(3,g)=-2*qreturn.m(3,g);
            end
            g=g+1;
            phi=phi+step_phi;
        end
        r=r+step_r;
    end
end
```

A.6 getSphere2.m

```
function qreturn = getSphere2( start_r, end_r ,N,k,concavity,c)
%get sphere
%always start with the vertice above the plane z=0, i.e. z>0
%theta measured from positive z axis.
%concavity == 1 for convex, else concave
    step_r=(end_r-start_r)/N;
    step_phi=2*pi/N;
    qreturn.m=zeros(3,N);
    qreturn.n=zeros(3,N);
    g=1;
    phi=0;
    r=start_r;
    cons=k/2;
    for a=0:N
        for b=0:N
            %surface calculation of sphere
            qreturn.m(1,g)=r*cos(phi);
            qreturn.m(2,g)=r*sin(phi);

            %normal calculation of sphere
            if concavity==1
                %case normal vector pointing outwards from centre (origin)
                qreturn.m(3,g)=sqrt(cons-r^2);
                qreturn.n(1,g)=qreturn.m(1,g);
                qreturn.n(2,g)=qreturn.m(2,g);
                qreturn.n(3,g)=qreturn.m(3,g);
            else
                qreturn.m(3,g)=-1*sqrt(cons-r^2);
                qreturn.n(1,g)=-1*qreturn.m(1,g);
                qreturn.n(2,g)=-1*qreturn.m(2,g);
                qreturn.n(3,g)=-1*qreturn.m(3,g);
            end
            g=g+1;
            phi=phi+step_phi;
        end
        r=r+step_r;
    end
end
```

A.7 EulerR.m

```
function qreturn = EulerR( direction,a )
%Elementary Rotational matrix using Euler angles.
%direction is a character specifying which elementary axis to use
%'z', 'y', or 'x'
    ca=cos(a);
    sa=sin(a);
    switch direction
          case {'z'}
            R=[ca -sa 0; sa ca 0; 0 0 1];
          case 'y'
```

```
            R=[ca 0 sa; 0 1 0; -sa 0 ca];
        case 'x'
            R=[1 0 0; 0 ca -sa; 0 sa ca];
        otherwise
            disp('Unknown axis.')
            R=zeros(3,3);
    end
    qreturn=R;
end
```

A.8 PlanarR.m

```
function qreturn = PlanarR( a )
%Elementary Rotational matrix using Euler angles.
%direction is a character specifying which elementary axis to use
%'z', 'y', or 'x'
    ca=cos(a);
    sa=sin(a);
    qreturn=[ca, sa; -sa, ca];
end
```

Appendix B
Tolerance Simulation Summary

Mnemonics:
TFRN: Tolerance on curvature in fringes.
TTHI: Tolerance on thickness.
TSDX: Tolerance on surface decentering in x.
TSDY: Tolerance on surface decentering in y.
TSTX: Tolerance on surface tilt in x (degrees).
TSTY: Tolerance on surface tilt in y (degrees).
TIRR: Tolerance on irregularity (fringes).
TIND: Tolerance on Nd index of refraction.
TABB: Tolerance on Abbe number.
TEDX: Tolerance on element decentering in x.
TEDY: Tolerance on element decentering in y.
TETX: Tolerance on element tilt in x (degrees).
TETY: Tolerance on element tilt in y (degrees).
Units are Millimeters.
All changes are computed using root-sum-square (RSS) differences.
S: Sagittal
T: Tangential

B1. Forward View, Averaged Diffractive MTF at 35 lp/mm

Criterion	Diffraction MTF average S&T at 35.0000 cycles per mm
Mode	Sensitivities
Sampling	3
Nominal Criterion	0.85522637
Test Wavelength	0.6328

Worst offenders:

Type			Value	Criterion	Change
TEDY	10	11	-0.05000000	0.84651226	-0.12177497
TEDY	10	11	0.05000000	0.84651226	-0.12177497
TEDX	10	11	-0.05000000	0.84651226	-0.12177497
TEDX	10	11	0.05000000	0.84651226	-0.12177497
TSDY	10		-0.05000000	0.84734760	-0.11581965
TSDY	10		0.05000000	0.84734760	-0.11581965
TSDX	10		-0.05000000	0.84734760	-0.11581965
TSDX	10		0.05000000	0.84734760	-0.11581965
TSDY	18		-0.05000000	0.84806829	-0.11041884
TSDY	18		0.05000000	0.84806829	-0.11041884
TSDX	18		-0.05000000	0.84806829	-0.11041884
TSDX	18		0.05000000	0.84806829	-0.11041884
TIRR	16		-3.00000000	0.84930638	-0.10045302
TIRR	17		3.00000000	0.84932363	-0.10030711
TIRR	19		-3.00000000	0.84950214	-0.09878388
TIRR	15		3.00000000	0.84966910	-0.09733738

TIRR	14	-3.00000000	0.85012668	-0.09325646
TIRR	13	3.00000000	0.85090551	-0.08586015
TIND	17	0.01000000	0.85127113	-0.08215600
TIND	18	-0.01000000	0.85157018	-0.07899601

Estimated Performance Changes based upon Root-Sum-Square method:

Nominal MTF	0.85522637
Estimated change	-0.52203811
Estimated MTF	0.67741298

Compensator Statistics:
Change in back focus:

Minimum	-0.262686
Maximum	0.279243
Mean	0.000068
Standard Deviation	0.027974

Monte Carlo Analysis:
Number of trials: 50
Initial Statistics: Parabolic Distribution
Number of traceable Monte Carlo files generated: 50

Nominal	0.85522637		
Best	0.85067462	Trial	16
Worst	0.72022464	Trial	3
Mean	0.79259745		
Std Dev	0.03037092		

Compensator Statistics:
Change in back focus:

Minimum	-0.597743
Maximum	0.446867
Mean	-0.004505
Standard Deviation	0.269822
90% >	0.74122084
80% >	0.76505361
50% >	0.79874724
20% >	0.81832734
10% >	0.82504789

B2. Forward View, Averaged Diffractive MTF at 70 lp/mm

Criterion	Diffraction MTF average S&T at 70.0000 cycles per mm
Mode	Sensitivities
Sampling	3
Nominal Criterion	0.67602981
Test Wavelength	0.6328

Worst offenders:

Type			Value	Criterion	Change
TEDY	10	11	-0.05000000	0.65537986	-0.16581176
TEDY	10	11	0.05000000	0.65537986	-0.16581176
TEDX	10	11	-0.05000000	0.65537986	-0.16581175
TEDX	10	11	0.05000000	0.65537986	-0.16581175
TIRR	17		3.00000000	0.65656800	-0.16104272

TIRR	16	-3.00000000	0.65657517	-0.16101350
TSDY	18	-0.05000000	0.65716934	-0.15857100
TSDY	18	0.05000000	0.65716934	-0.15857100
TSDX	18	-0.05000000	0.65716934	-0.15857100
TSDX	18	0.05000000	0.65716934	-0.15857100
TIRR	19	-3.00000000	0.65726738	-0.15816413
TSDY	10	-0.05000000	0.65731428	-0.15796911
TSDY	10	0.05000000	0.65731428	-0.15796911
TSDX	10	-0.05000000	0.65731428	-0.15796911
TSDX	10	0.05000000	0.65731428	-0.15796911
TIRR	15	3.00000000	0.65774310	-0.15617398
TIND	17	0.01000000	0.65885772	-0.15140281
TIRR	14	-3.00000000	0.65934537	-0.14926480
TIRR	13	3.00000000	0.66181828	-0.13788717
TIND	18	-0.01000000	0.66209233	-0.13656516

Estimated Performance Changes based upon Root-Sum-Square method:

Nominal MTF	0.67602981
Estimated change	-0.79296367
Estimated MTF	0.00000000

Compensator Statistics:
Change in back focus:

Minimum	-0.262686
Maximum	0.279243
Mean	0.000068
Standard Deviation	0.027974

Monte Carlo Analysis:
Number of trials: 50
Initial Statistics: Parabolic Distribution
Number of traceable Monte Carlo files generated: 50

Nominal	0.67602981		
Best	0.63801234	Trial	20
Worst	0.41034575	Trial	11
Mean	0.53788839		
Std Dev	0.06000854		

Compensator Statistics:
Change in back focus:

Minimum	-0.604315
Maximum	0.598548
Mean	0.040689
Standard Deviation	0.266730
90% >	0.46061768
80% >	0.48809009
50% >	0.53455501
20% >	0.60533161
10% >	0.61862961

B3. Radial View, Averaged Diffractive MTF at 30 lp/mm

Criterion Diffraction MTF average S&T at 30.0000 cycles per mm

Mode			Sensitivities		
Sampling			4		
Nominal Criterion			0.86589867		
Test Wavelength			0.6328		
Worst offenders:					
Type			Value	Criterion	Change
TEDY	5	6	0.05000000	0.79314349	-0.34742467
TSDY	5		0.05000000	0.79885761	-0.33407636
TEDY	5	6	-0.05000000	0.80513673	-0.31864611
TSDY	5		-0.05000000	0.81088786	-0.30371265
TEDY	8	9	-0.05000000	0.84022487	-0.20929086
TSDY	9		-0.05000000	0.84022487	-0.20929086
TEDY	10	11	-0.05000000	0.84252464	-0.19983176
TSDY	11		-0.05000000	0.84252464	-0.19983176
TSDY	13		0.05000000	0.84688313	-0.18047013
TSTX	9		-0.20000000	0.85004814	-0.16492014
TSDY	9		0.05000000	0.85048334	-0.16266096
TEDY	8	9	0.05000000	0.85048334	-0.16266096
TSTX	11		-0.20000000	0.85123913	-0.15865826
TIND	10		0.01000000	0.85136247	-0.15799508
TSTX	5		0.20000000	0.85268327	-0.15070415
TEDY	10	11	0.05000000	0.85298206	-0.14900370
TSDY	11		0.05000000	0.85298206	-0.14900370
TIRR	14		3.00000000	0.85395247	-0.14333764
TETX	12	14	-0.20000000	0.85501210	-0.13687514
TSTX	14		-0.20000000	0.85538953	-0.13449631

Estimated Performance Changes based upon Root-Sum-Square method:

Nominal MTF	0.86589867
Estimated change	-0.86633144
Estimated MTF	0.00000000

Compensator Statistics:
Change in back focus:

Minimum	-0.278057
Maximum	0.296079
Mean	0.000106
Standard Deviation	0.033957

Monte Carlo Analysis:
Number of trials: 50
Initial Statistics: Parabolic Distribution

Nominal	0.86589867		
Best	0.82987789	Trial	23
Worst	0.29322651	Trial	45
Mean	0.65267095		
Std Dev	0.14812317		

Compensator Statistics:
Change in back focus:

Minimum	-0.684442
Maximum	0.677583
Mean	-0.032713

Standard Deviation	0.328241
90% >	0.44859480
80% >	0.52413255
50% >	0.67910888
20% >	0.79237058
10% >	0.81162563

B4. Forward View, Averaged Diffractive MTF at 60 lp/mm

Criterion	Diffraction MTF average S&T at 60.0000 cycles per mm
Mode	Sensitivities
Sampling	4
Nominal Criterion	0.68768855
Test Wavelength	0.6328

Worst offenders:

Type			Value	Criterion	Change
TEDY	5	6	-0.05000000	0.51025896	-0.46103290
TSDY	5		-0.05000000	0.52456968	-0.44468213
TEDY	5	6	0.05000000	0.55576928	-0.40501364
TSDY	5		0.05000000	0.56636460	-0.39005984
TSDY	13		0.05000000	0.61603257	-0.30564591
TSDY	9		0.05000000	0.63083393	-0.27379572
TEDY	8	9	0.05000000	0.63083393	-0.27379572
TEDY	10	11	0.05000000	0.63948916	-0.25292125
TSDY	11		0.05000000	0.63948916	-0.25292125
TSDY	9		-0.05000000	0.64092575	-0.24925835
TEDY	8	9	-0.05000000	0.64092575	-0.24925835
TSDY	11		-0.05000000	0.64481971	-0.23900436
TEDY	10	11	-0.05000000	0.64481971	-0.23900436
TSDY	12		-0.05000000	0.64627541	-0.23503966
TSTX	9		0.20000000	0.65459957	-0.21074854
TIND	10		-0.01000000	0.65560677	-0.20759407
TSTX	5		-0.20000000	0.65563222	-0.20751371
TSTX	14		-0.20000000	0.65652990	-0.20465588
TSDX	5		0.05000000	0.65857058	-0.19799073
TSDX	5		-0.05000000	0.65857058	-0.19799073

Estimated Performance Changes based upon Root-Sum-Square method:

Nominal MTF	0.68768855
Estimated change	-1.23607444
Estimated MTF	0.00000000

Compensator Statistics:

Change in back focus:

Minimum	-0.278057
Maximum	0.296079
Mean	0.000106
Standard Deviation	0.033957

Monte Carlo Analysis:

Number of trials: 50

Initial Statistics: Parabolic Distribution

Nominal	0.68768855		
Best	0.68816750	Trial	36
Worst	0.11331762	Trial	43
Mean	0.43339927		
Std Dev	0.16442716		
Compensator Statistics:			
Change in back focus:			
Minimum	-0.544278		
Maximum	0.769625		
Mean	0.022282		
Standard Deviation	0.300006		
90% >	0.21209679		
80% >	0.27310240		
50% >	0.45237084		
20% >	0.60588376		
10% >	0.62693044		

Appendix C
Custom Test Patterns for Radial View MTF Tests

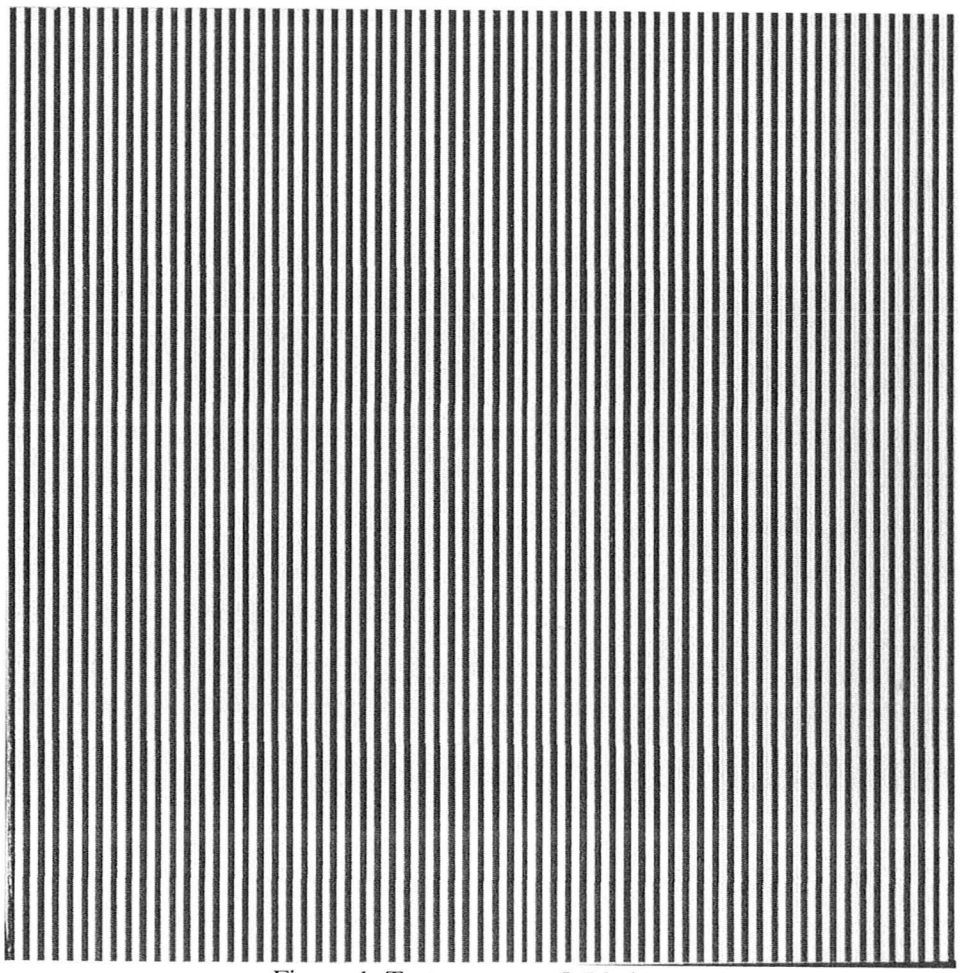

Figure 1. Test pattern at 0.5 lp/mm.

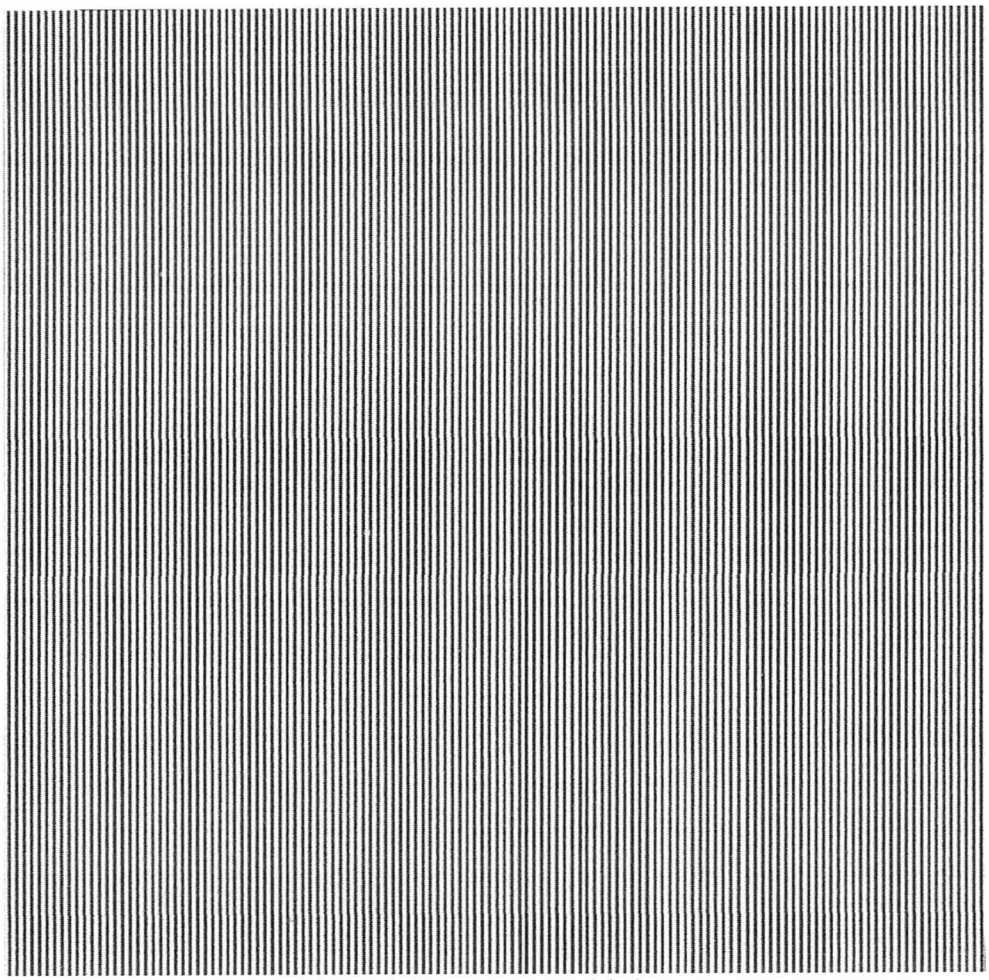

Figure 2. Test pattern at 1 lp/mm.

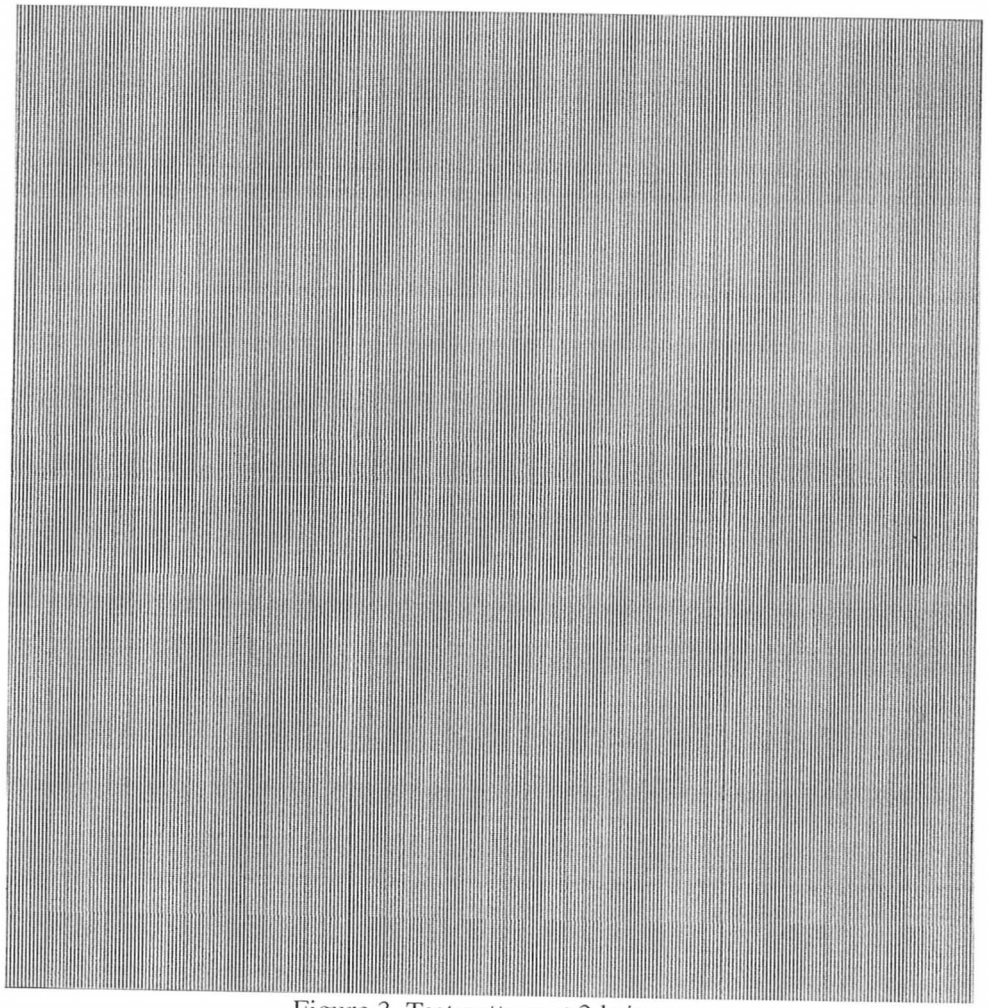

Figure 3. Test pattern at 2 lp/mm.

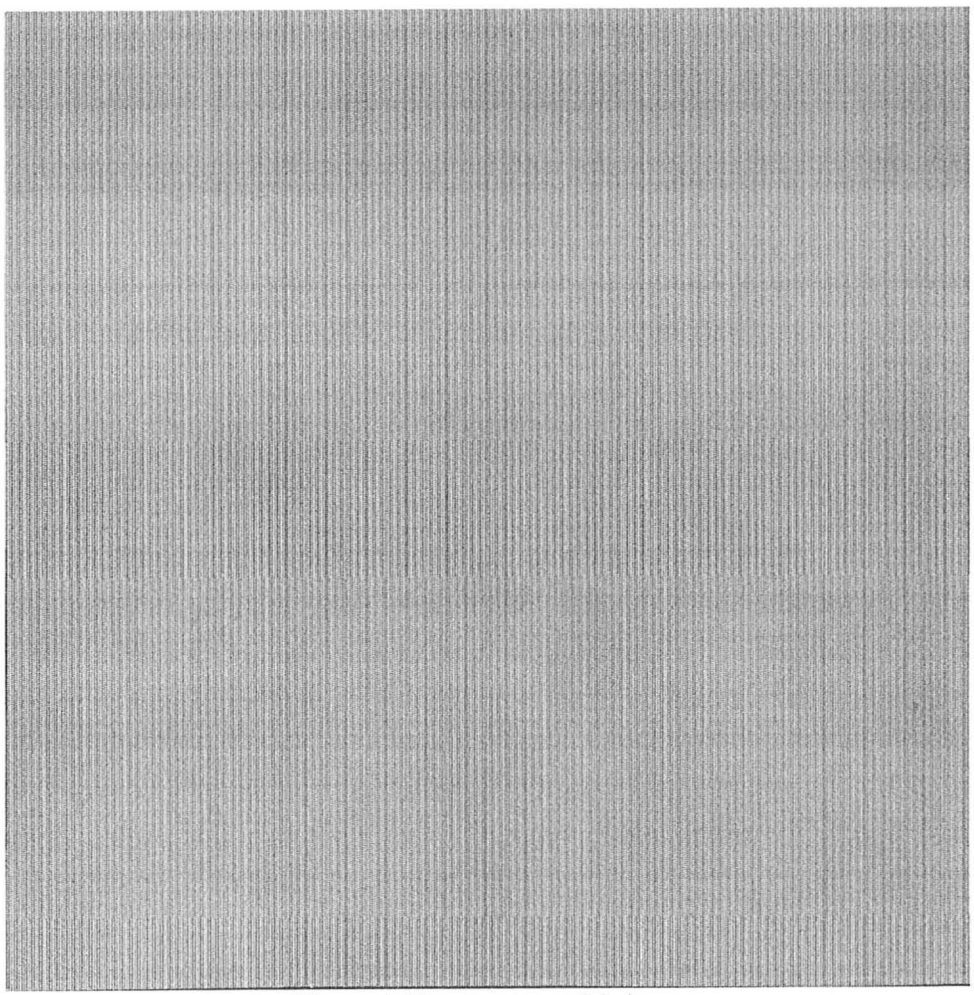

Figure 4. Test pattern at 3 lp/mm.

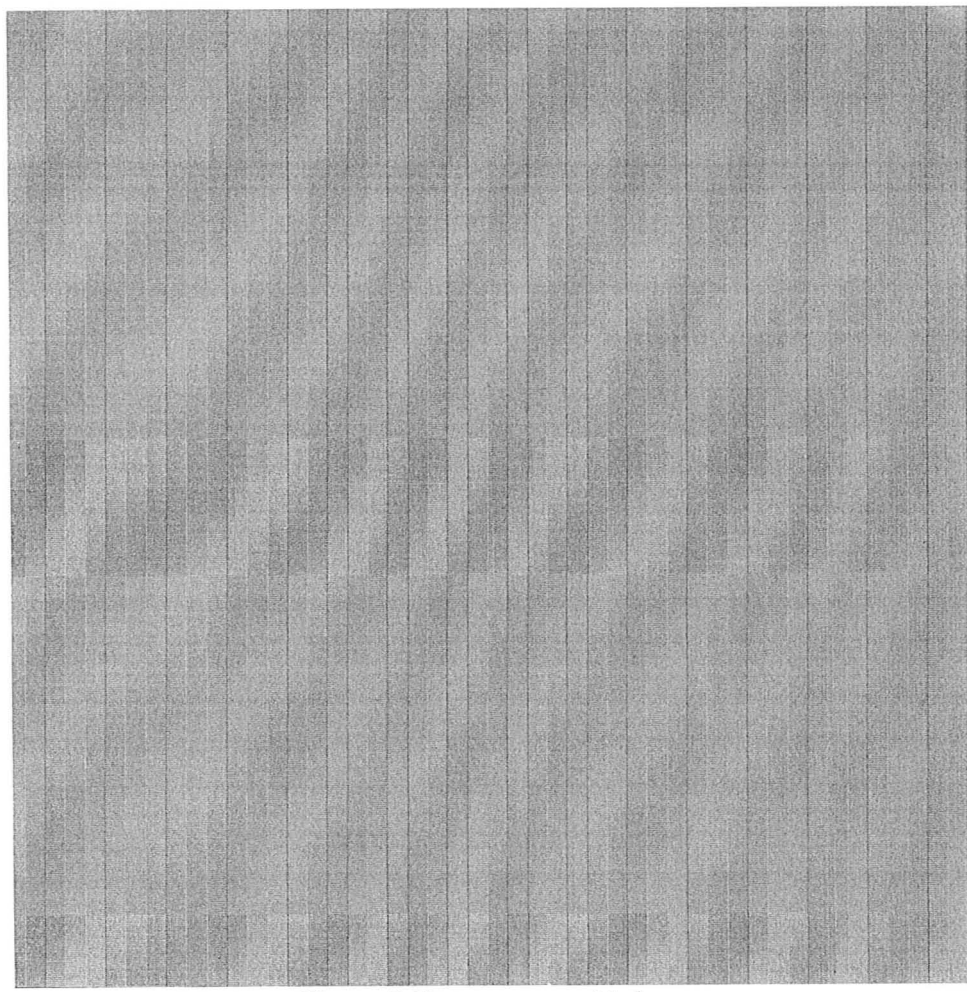

Figure 5. Test pattern at 4 lp/mm.

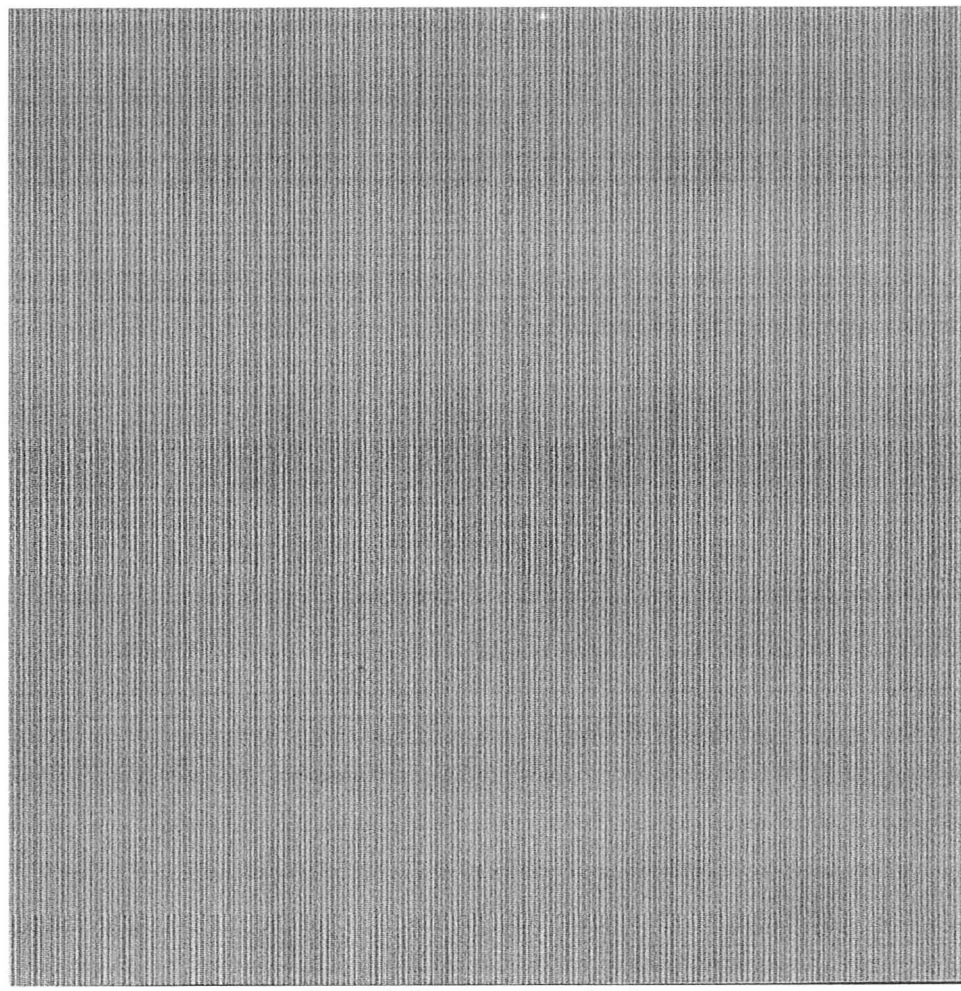

Figure 6. Test pattern at 5 lp/mm.

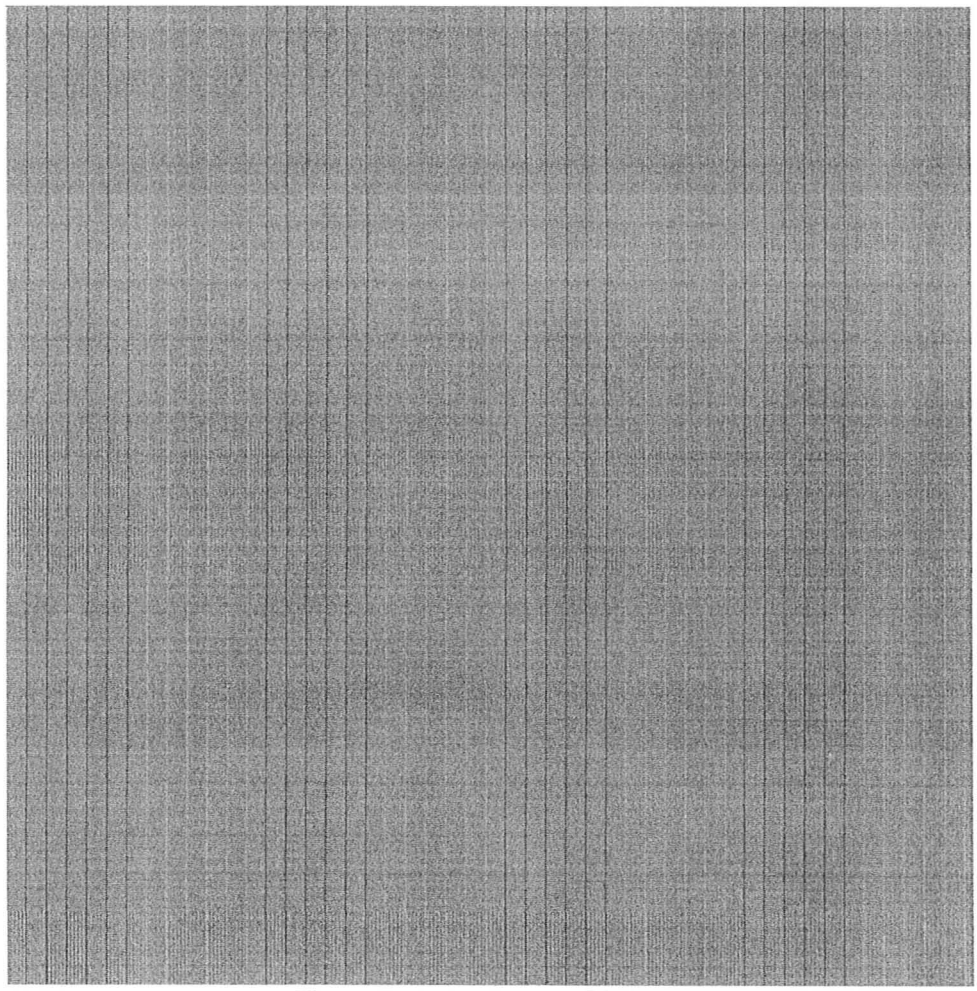

Figure 7. Test pattern at 6 lp/mm.

Appendix D
Acquired Images for Forward View MTF Tests

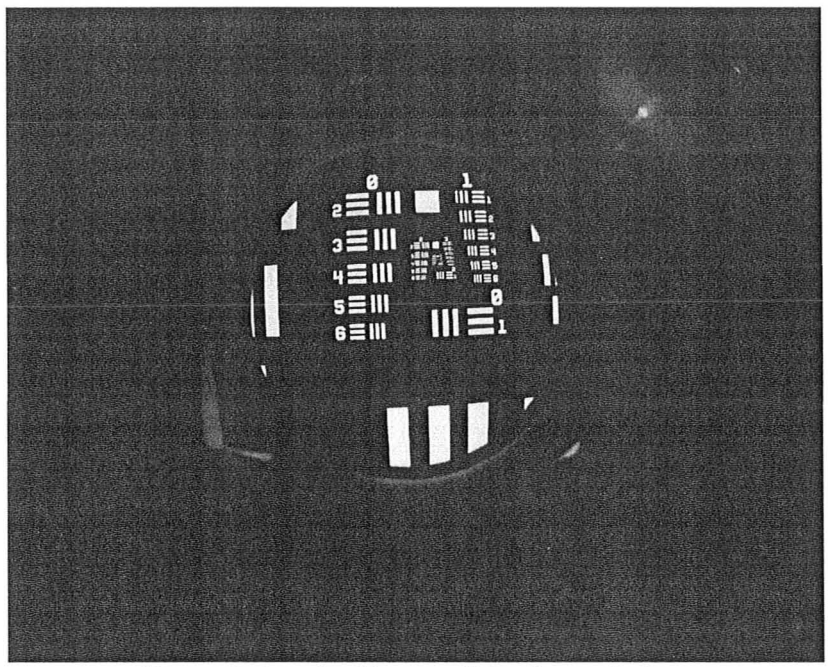

Figure 1. Acquired image of the forward view.

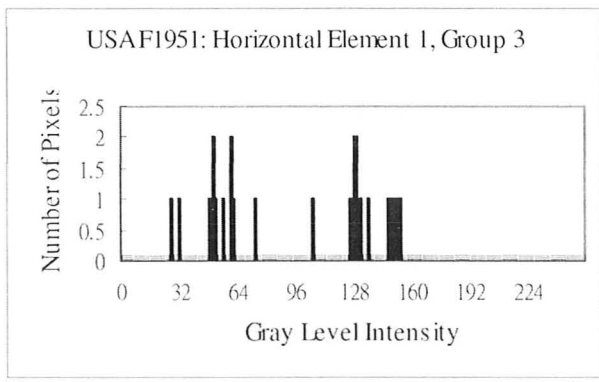

Figure 2. Histogram for the horizontal bar pattern at group 3, element 1. The dark and bright gray level peaks are taken to be 51 and 113.

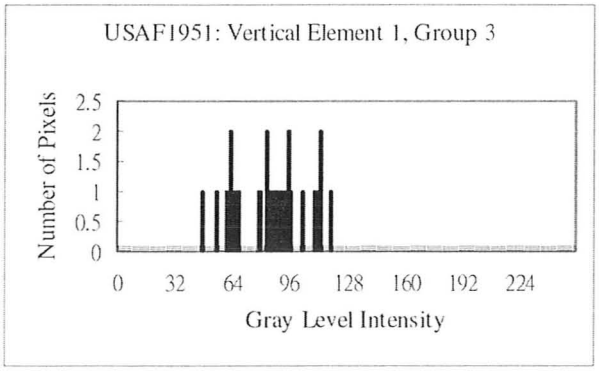

Figure 3. Histogram for the vertical bar pattern at group 3, element 1. The dark and bright gray level peaks are taken to be 64 and 110.

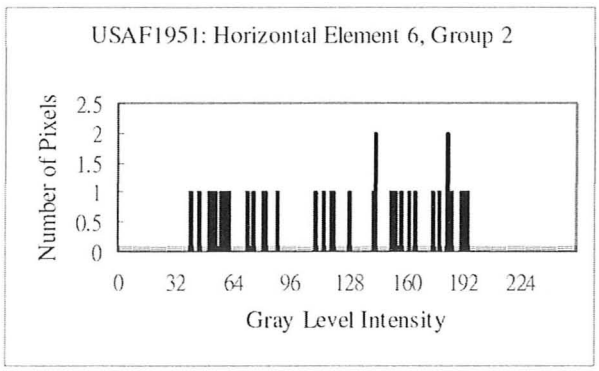

Figure 4. Histogram for the horizontal bar pattern at group 2, element 6. The dark and bright gray level peaks are taken to be 62 and 166.

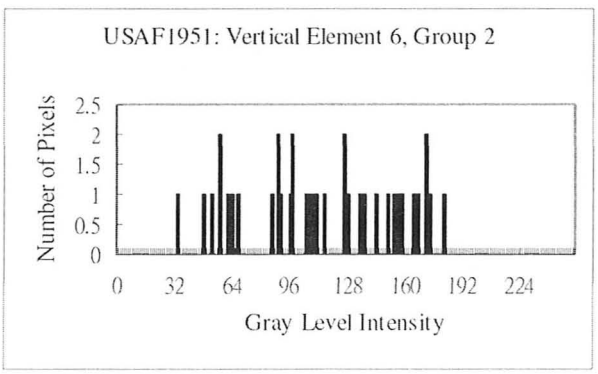

Figure 5. Histogram for the vertical bar pattern at group 2, element 6. The dark and bright gray level peaks are taken to be 68 and 157.

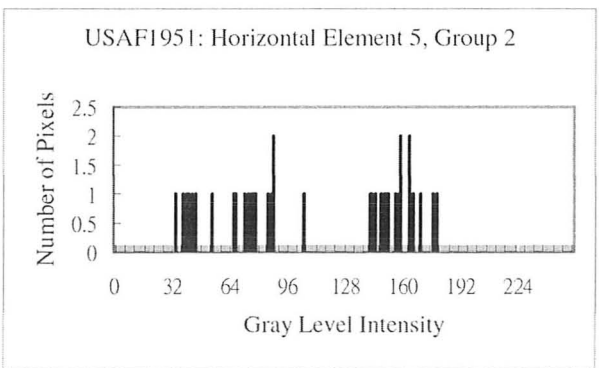

Figure 6. Histogram for the horizontal bar pattern at group 2, element 5. The dark and bright gray level peaks are taken to be 77 and 160.

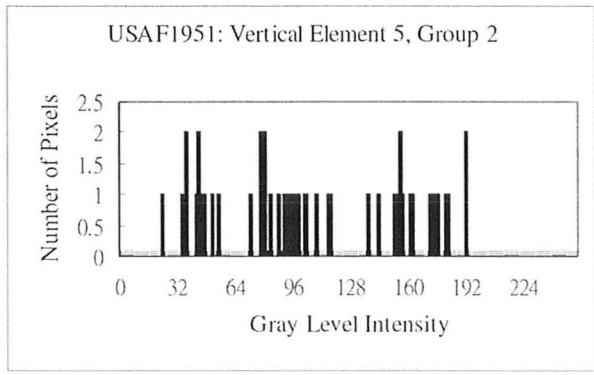

Figure 7. Histogram for the vertical bar pattern at group 2, element 5. The dark and bright gray level peaks are taken to be 56 and 164.

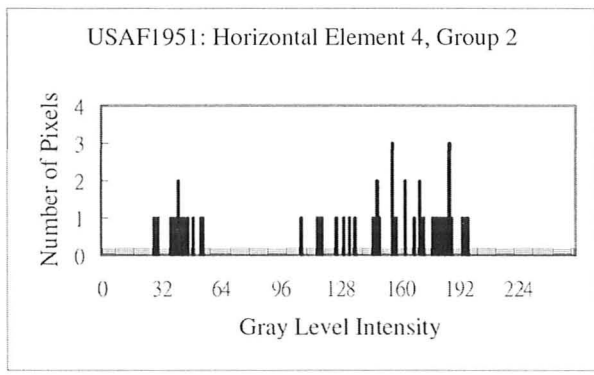

Figure 8. Histogram for the horizontal bar pattern at group 2, element 4. The dark and bright gray level peaks are taken to be 41 and 174.

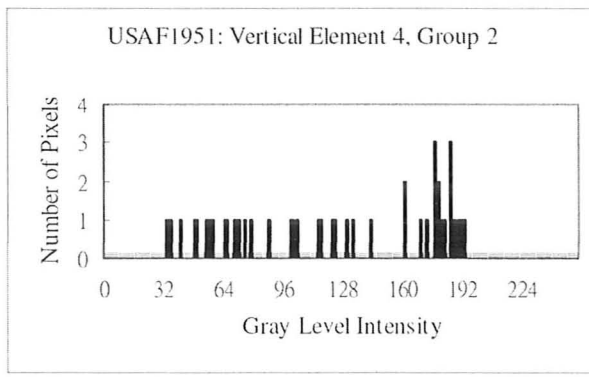

Figure 9. Histogram for the vertical bar pattern at group 2, element 4. The dark and bright gray level peaks are taken to be 67 and 181.

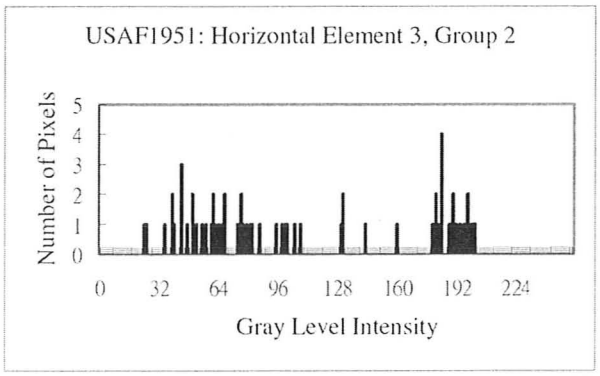

Figure 10. Histogram for the horizontal bar pattern at group 2, element 3. The dark and bright gray level peaks are taken to be 45 and 185.

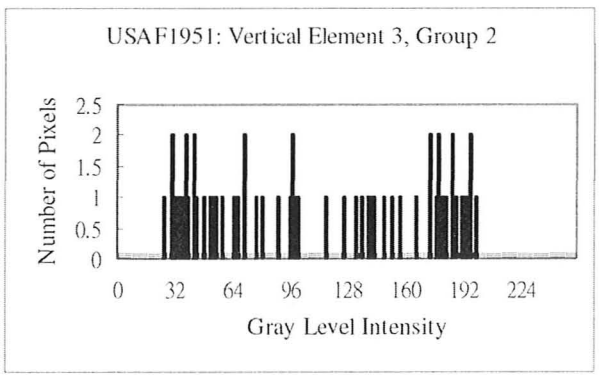

Figure 11. Histogram for the vertical bar pattern at group 2, element 3. The dark and bright gray level peaks are taken to be 49 and 187.

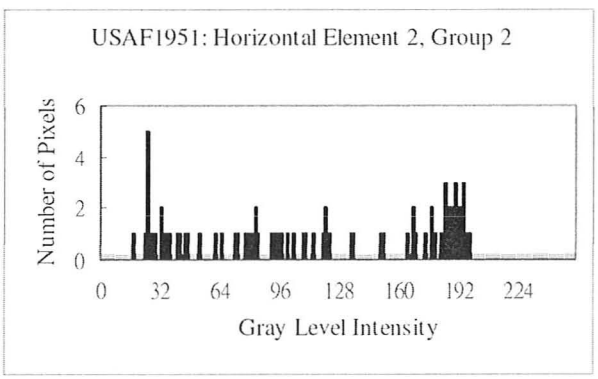

Figure 12. Histogram for the horizontal bar pattern at group 2, element 2. The dark and bright gray level peaks are taken to be 26 and 189.

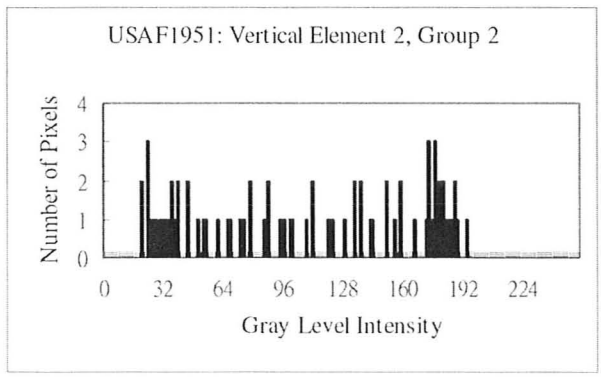

Figure 13. Histogram for the vertical bar pattern at group 2, element 2. The dark and bright gray level peaks are taken to be 33 and 178.

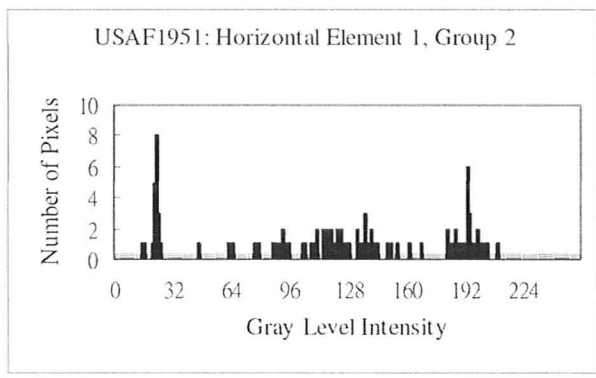

Figure 14. Histogram for the horizontal bar pattern at group 2, element 1. The dark and bright gray level peaks are taken to be 24 and 194.

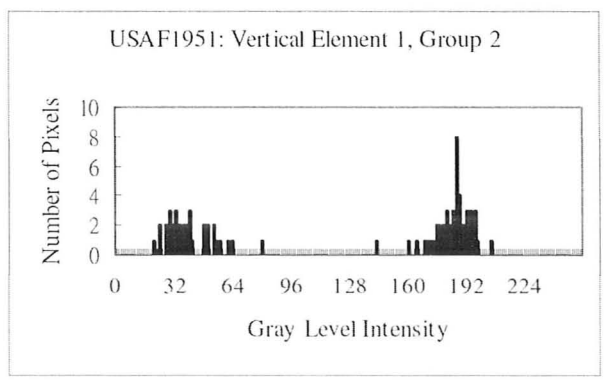

Figure 15. Histogram for the vertical bar pattern at group 2, element 1. The dark and bright gray level peaks are taken to be 34 and 188.

Appendix E
Acquired Images for Radial View MTF Tests

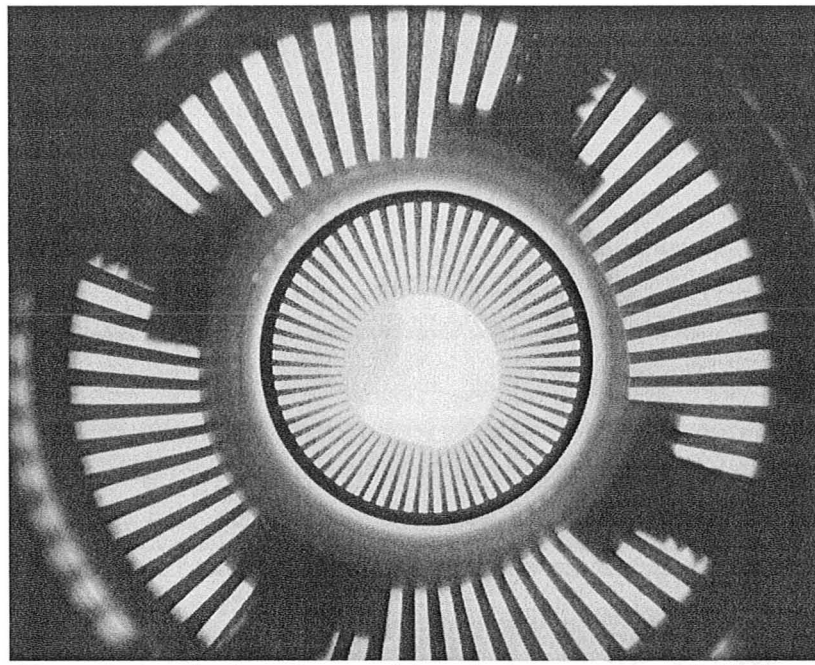

Figure 1. Acquired test image with sagittal test pattern at 0.5 lp/mm.

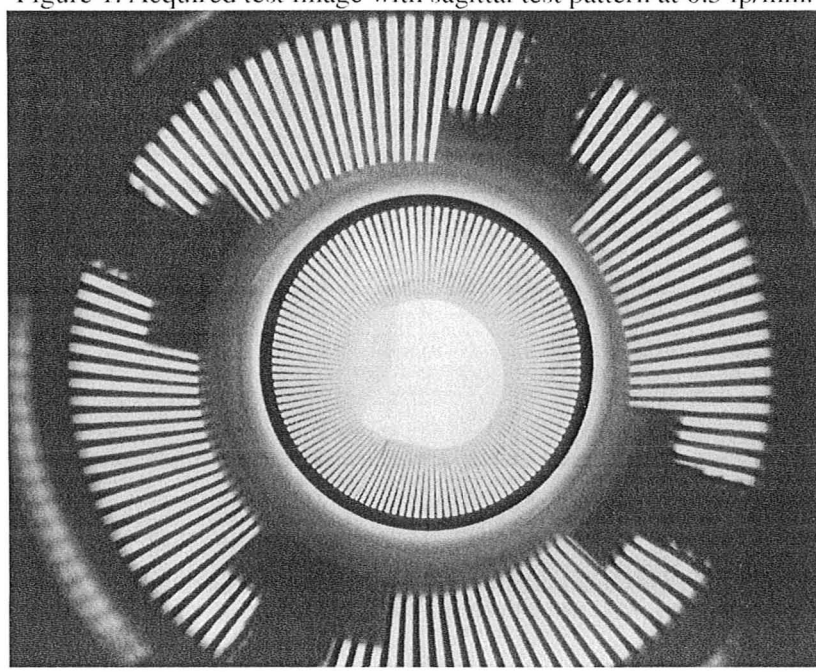

Figure 2. Acquired test image with sagittal test pattern at 1 lp/mm.

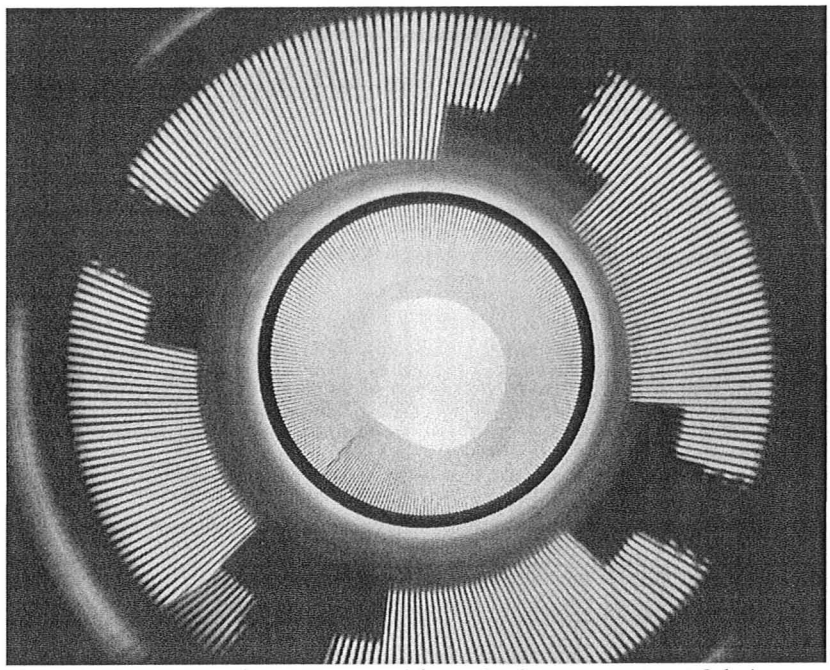

Figure 3. Acquired test image with sagittal test pattern at 2 lp/mm.

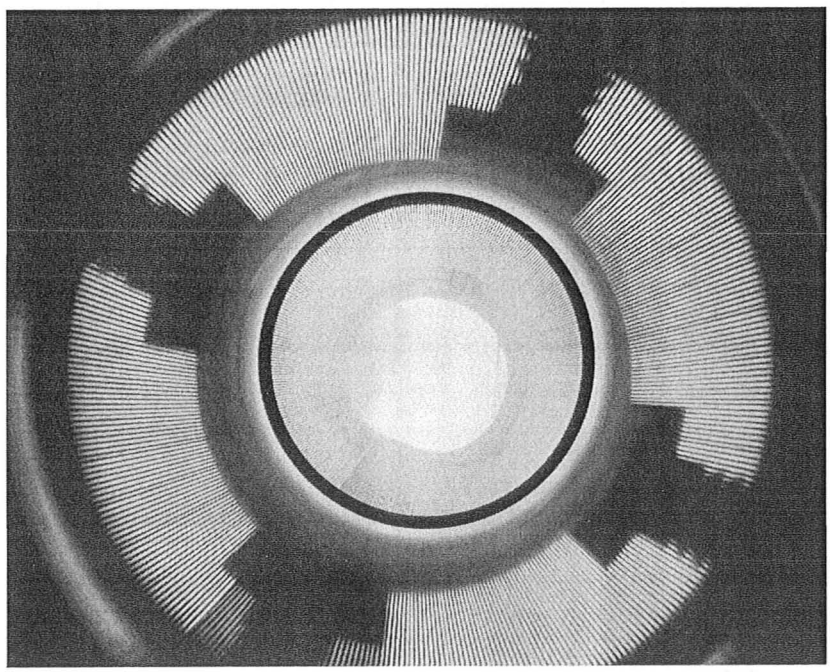

Figure 4. Acquired test image with sagittal test pattern at 3 lp/mm.

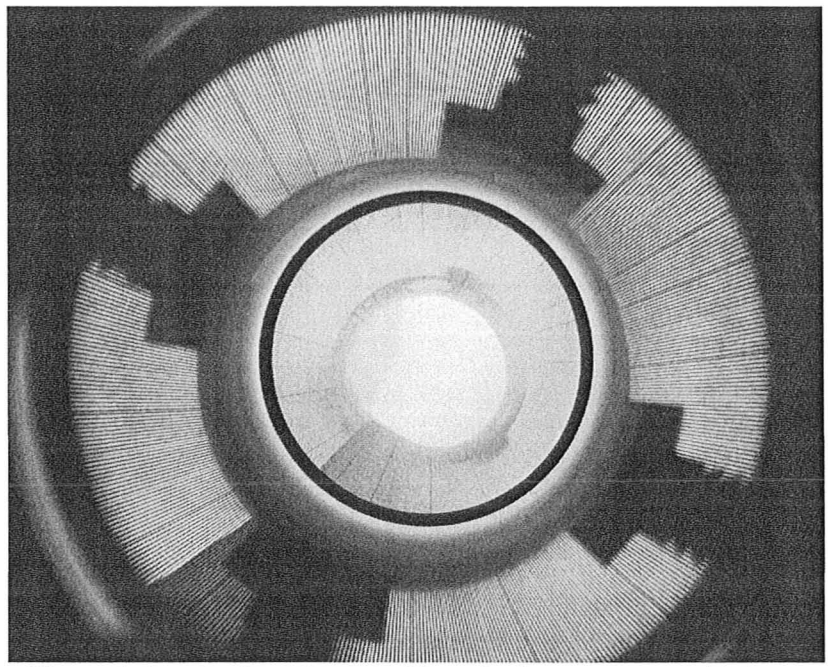

Figure 5. Acquired test image with sagittal test pattern at 4 lp/mm.

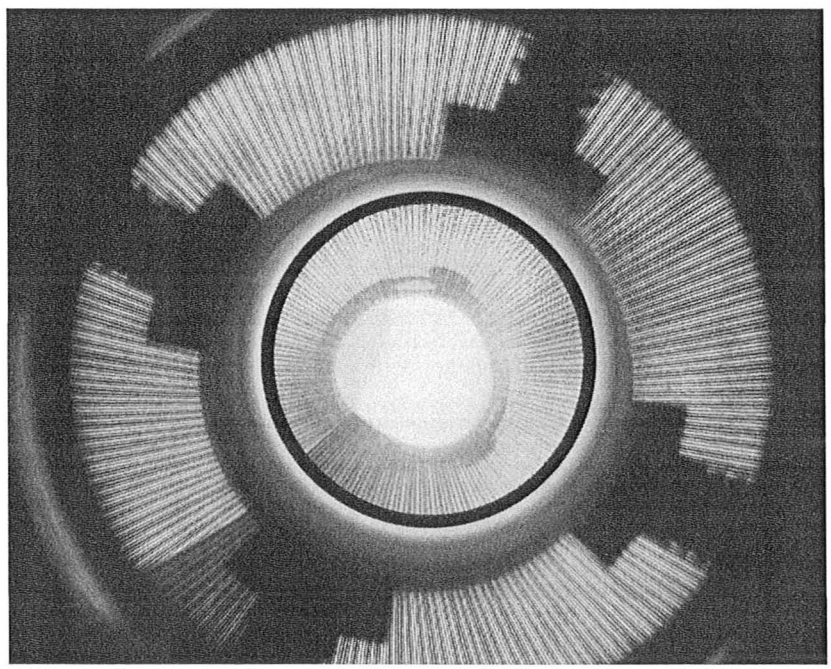

Figure 6. Acquired test image with sagittal test pattern at 5 lp/mm.

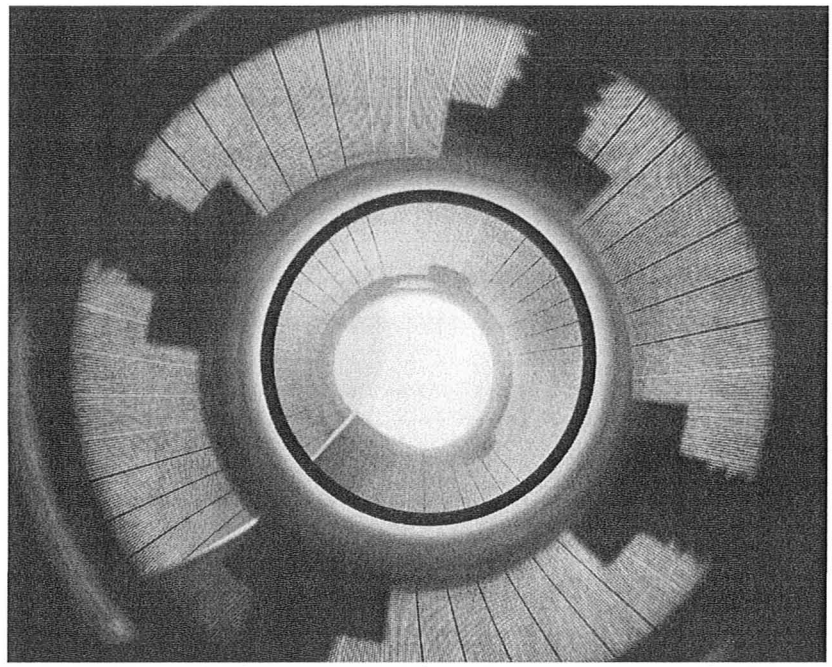

Figure 7. Acquired test image with sagittal test pattern at 6 lp/mm.

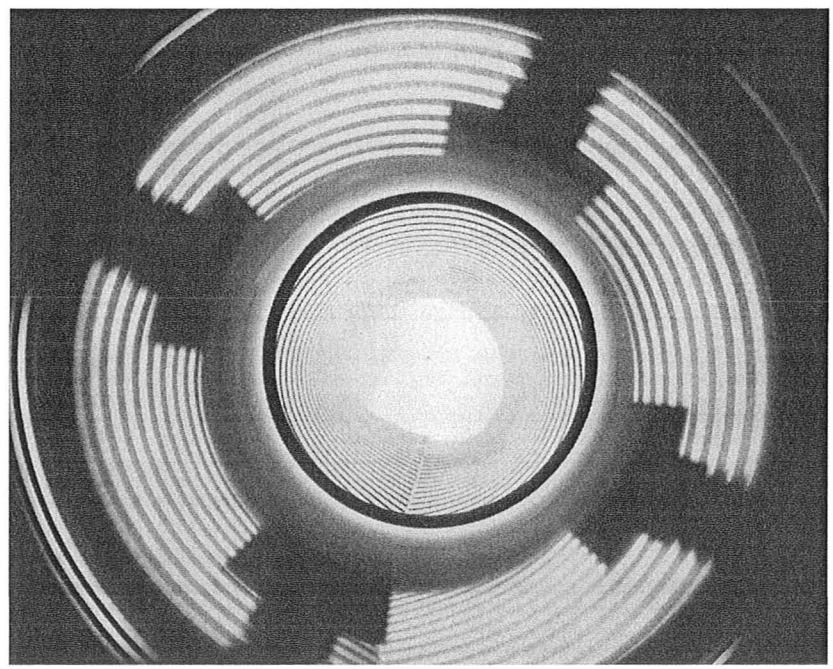

Figure 8. Acquired test image with tangential test pattern at 0.5 lp/mm.

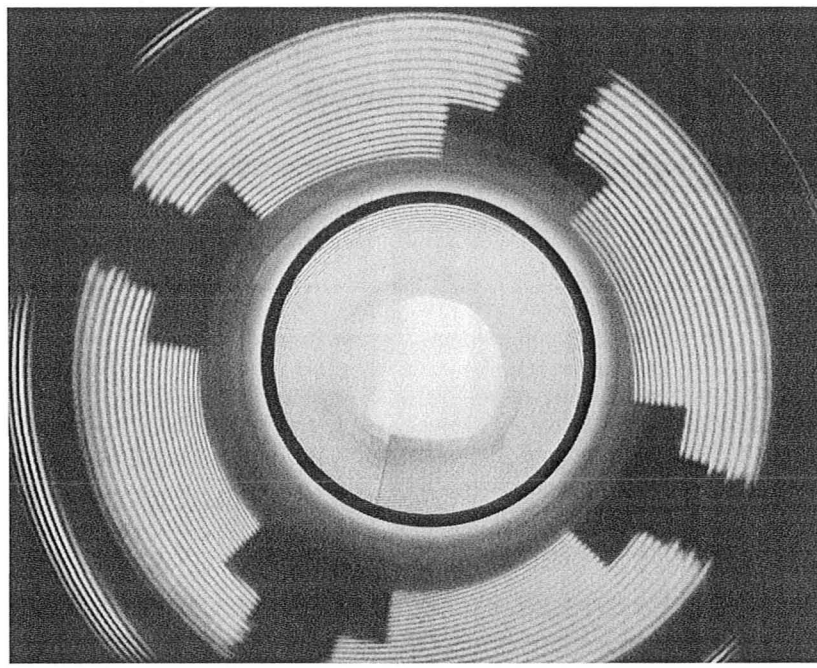

Figure 9. Acquired test image with tangential test pattern at 1 lp/mm.

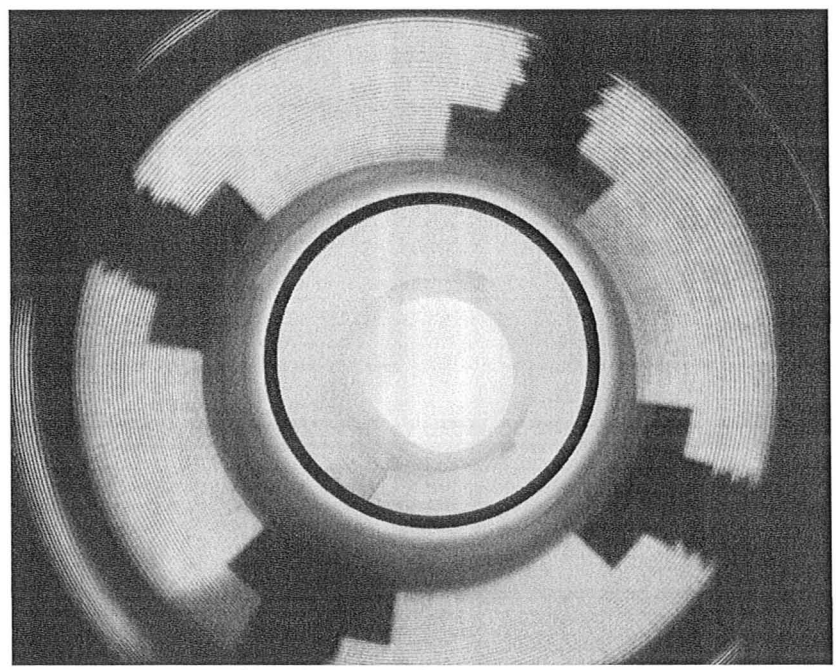

Figure 10. Acquired test image with tangential test pattern at 2 lp/mm.

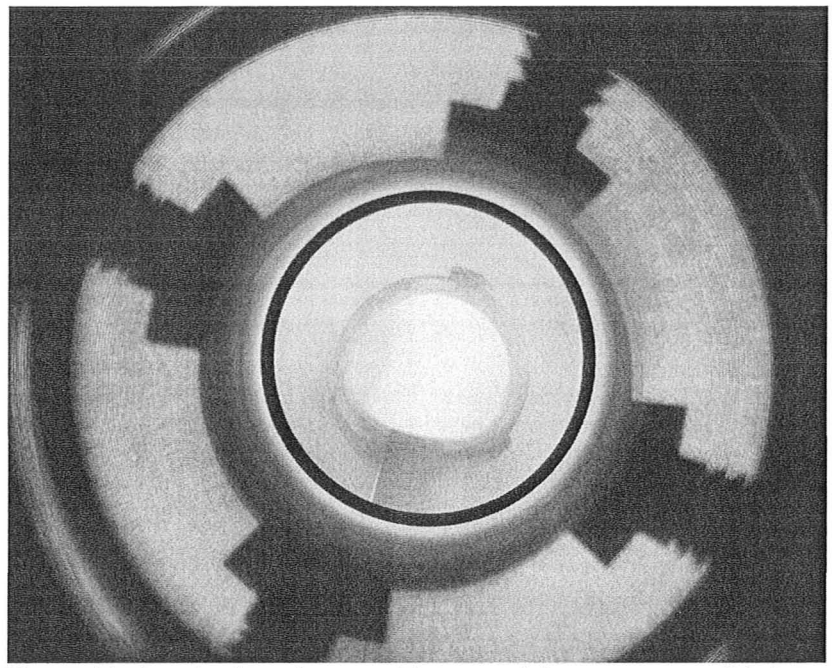

Figure 11. Acquired test image with tangential test pattern at 3 lp/mm.

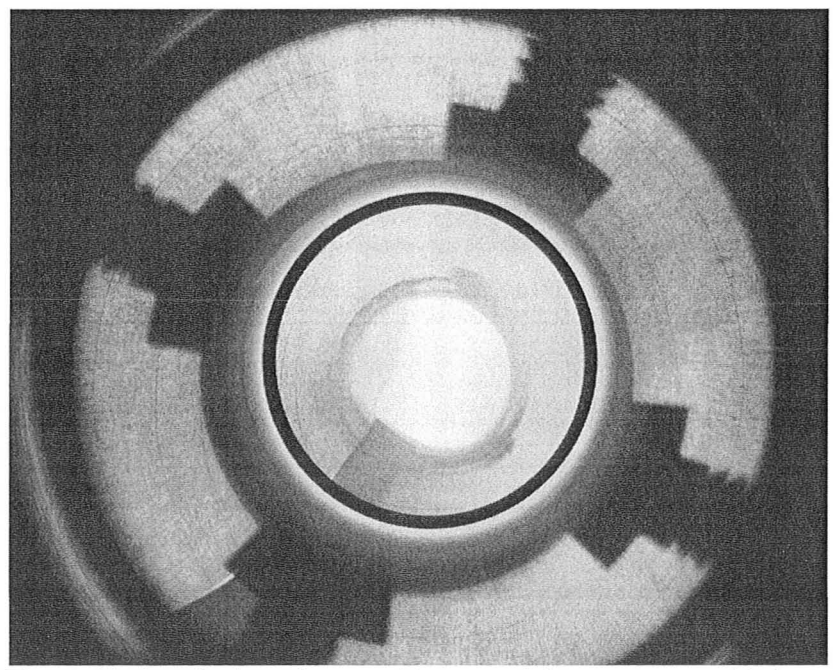

Figure 12. Acquired test image with tangential test pattern at 4 lp/mm.

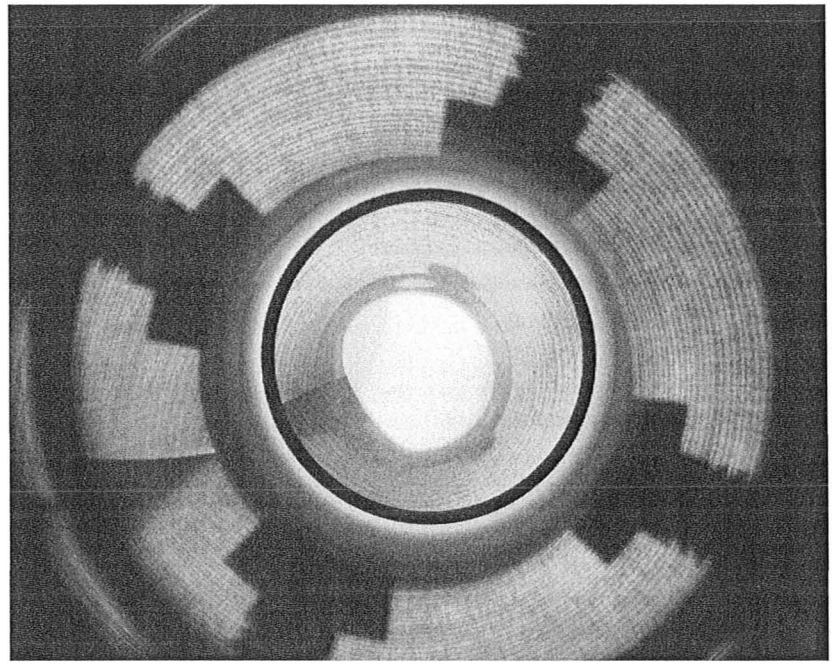

Figure 13. Acquired test image with tangential test pattern at 5 lp/mm.

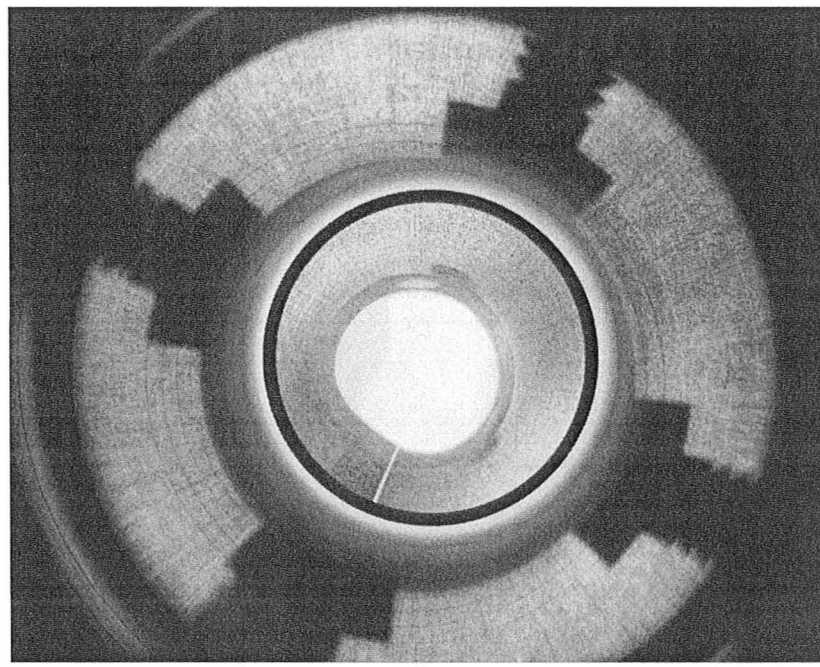

Figure 14. Acquired test image with tangential test pattern at 6 lp/mm.

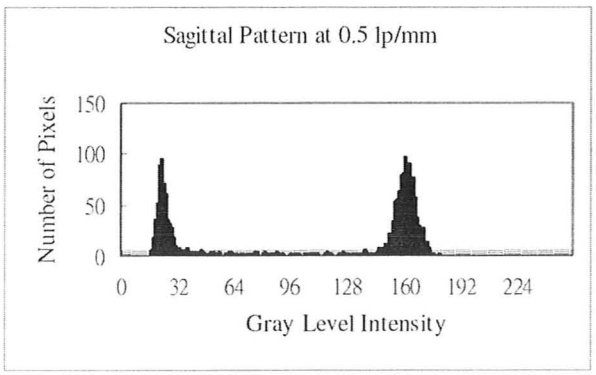

Figure 15. Histogram for the sagittal test pattern at 0.5 lp/mm. The dark and bright gray level peaks are taken to be 23 and 161.

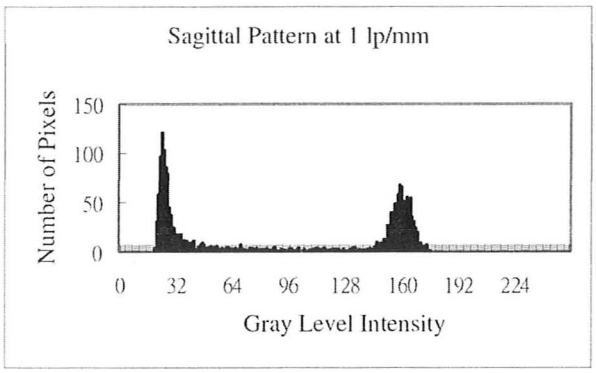

Figure 16. Histogram for the sagittal test pattern at 1 lp/mm. The dark and bright gray level peaks are taken to be 24 and 159.

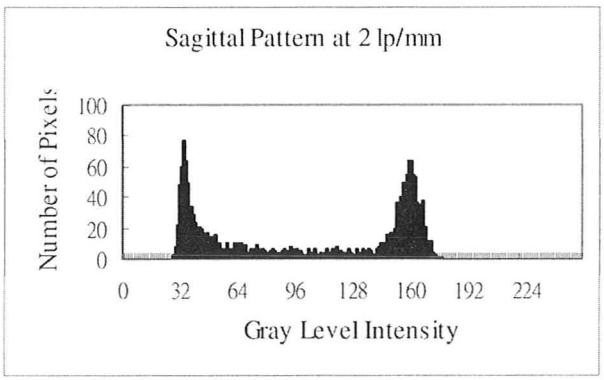

Figure 17. Histogram for the sagittal test pattern at 2 lp/mm. The dark and bright gray level peaks are taken to be 33 and 159.

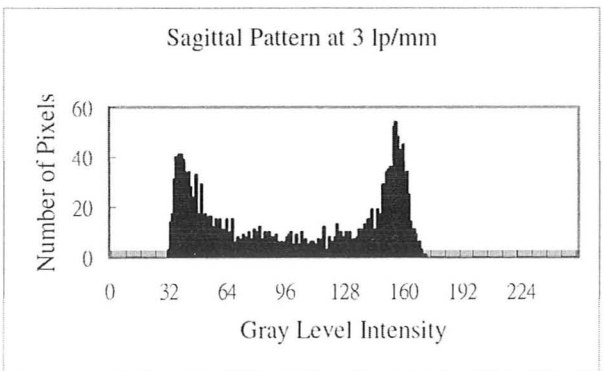

Figure 18. Histogram for the sagittal test pattern at 3 lp/mm. The dark and bright gray level peaks are taken to be 39 and 156.

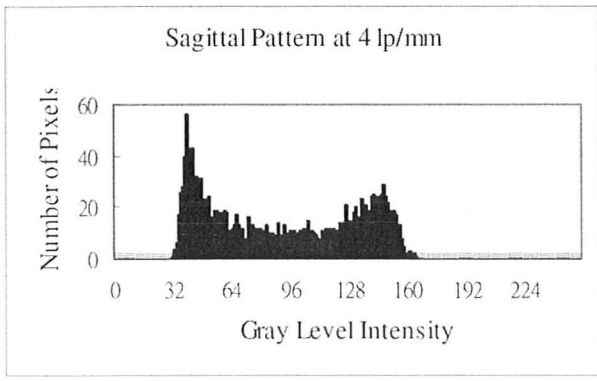

Figure 19. Histogram for the sagittal test pattern at 4 lp/mm. The dark and bright gray level peaks are taken to be 39 and 146.

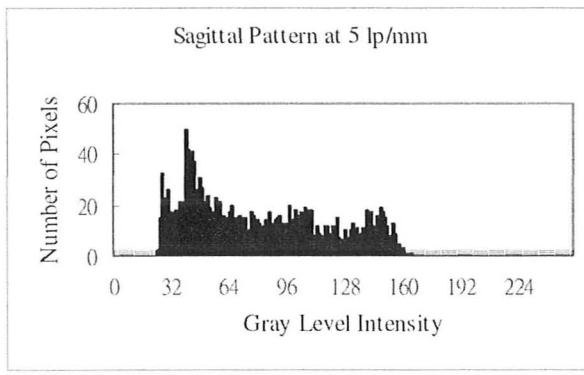

Figure 20. Histogram for the sagittal test pattern at 5 lp/mm. The dark and bright gray level peaks are taken to be 40 and 143.

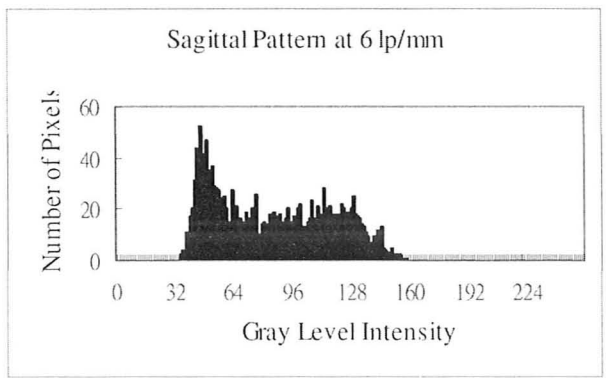

Figure 21. Histogram for the sagittal test pattern at 6 lp/mm. The dark and bright gray level peaks are taken to be 46 and 123.

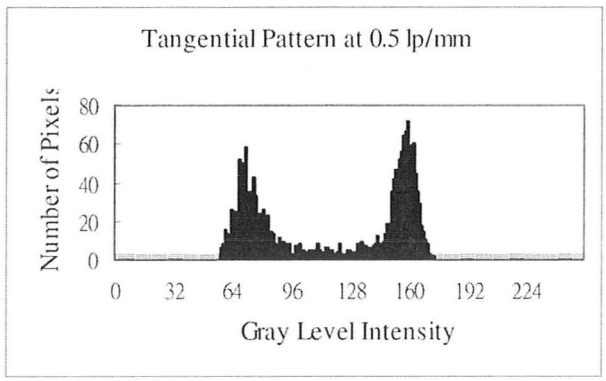

Figure 22. Histogram for the tangential test pattern at 0.5 lp/mm. The dark and bright gray level peaks are taken to be 71 and 159.

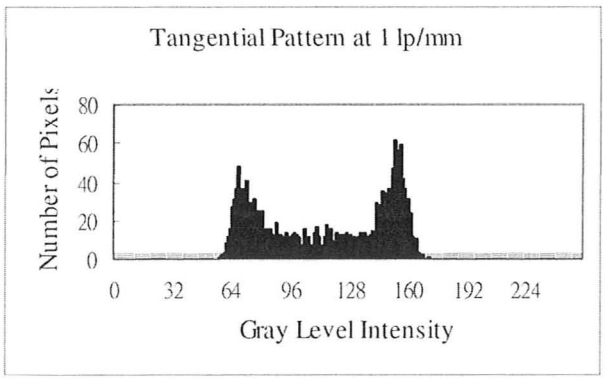

Figure 23. Histogram for the tangential test pattern at 1 lp/mm. The dark and bright gray level peaks are taken to be 68 and 153.

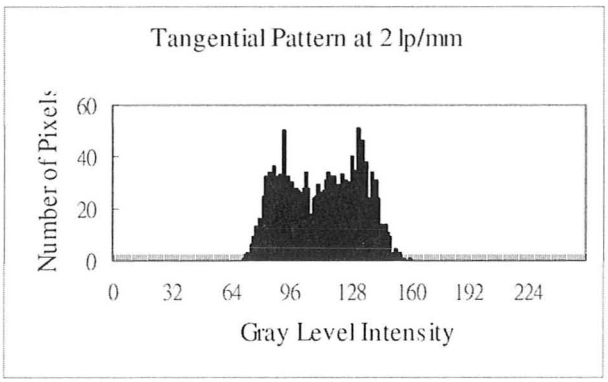

Figure 24. Histogram for the tangential test pattern at 2 lp/mm. The dark and bright gray level peaks are taken to be 92 and 132.

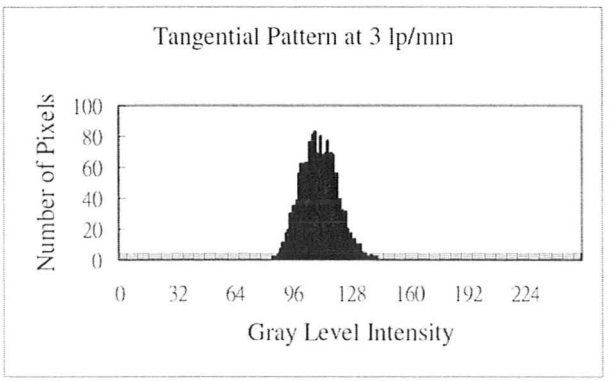

Figure 25. Histogram for the tangential test pattern at 3 lp/mm. Cannot distinguish the darker and brighter peaks.

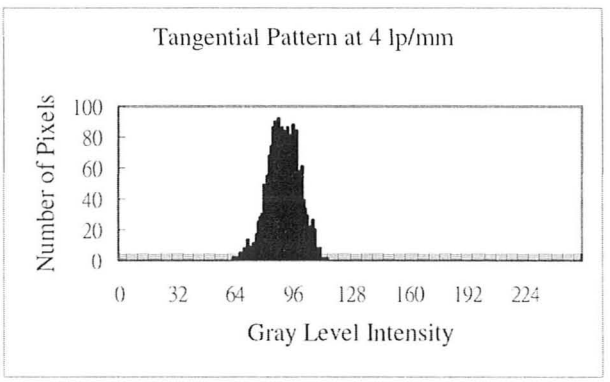

Figure 26. Histogram for the tangential test pattern at 4 lp/mm. Cannot distinguish the darker and brighter peaks

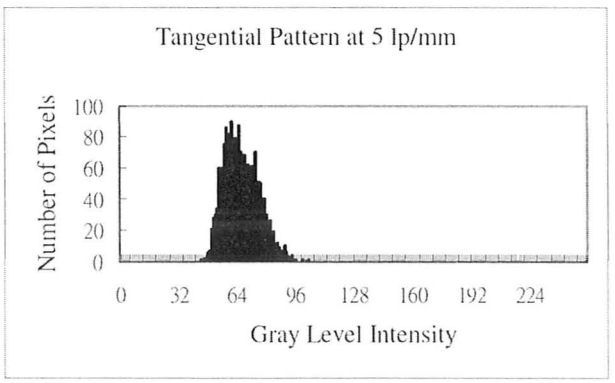

Figure 27. Histogram for the tangential test pattern at 5 lp/mm. Cannot distinguish the darker and brighter peaks.

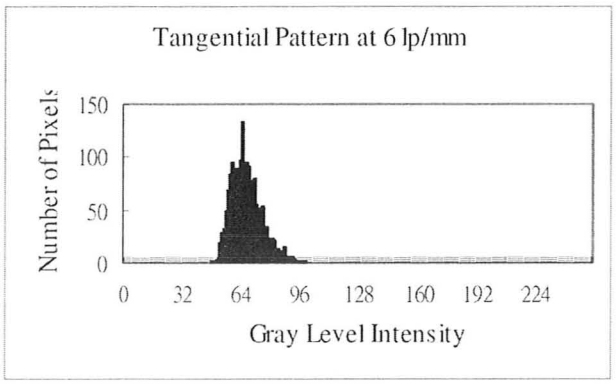

Figure 28. Histogram for the tangential test pattern at 6 lp/mm. Cannot distinguish the darker and brighter peaks.

Appendix F
Acquired Images for Radiometry Tests

All acquired images used an exposure of 375 ms and resized to 300 pixels per inch for publication purposes. The measurement images used a gain of 1 and the mask images used a gain of 5. All figures here are scaled to 50%.

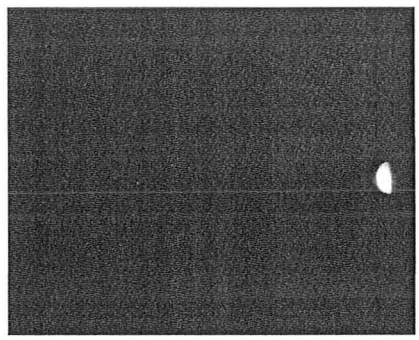

Figure 1. Mask image at field position 15 mm.

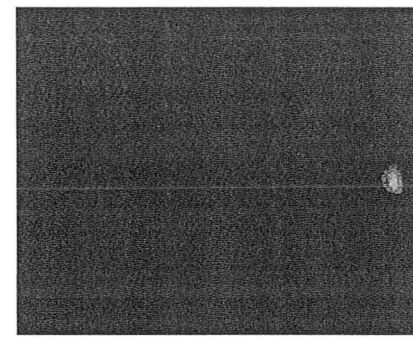

Figure 2. Measurement image at field position 15 mm. Mean gray level intensity is 69.07.

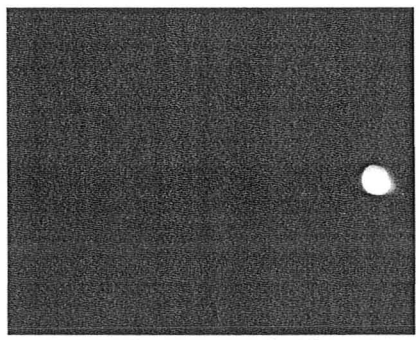

Figure 3. Mask image at field position 18 mm

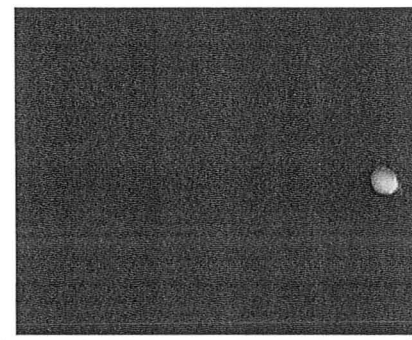

Figure 4. Measurement image at field position 18 mm. Mean gray level intensity is 88.11.

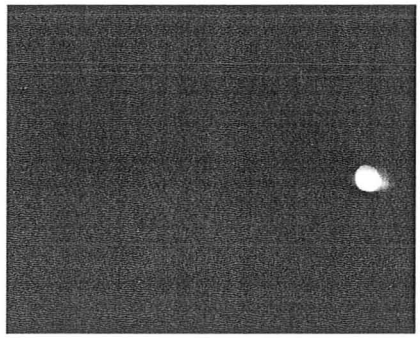

Figure 5. Mask image at field position 20 mm.

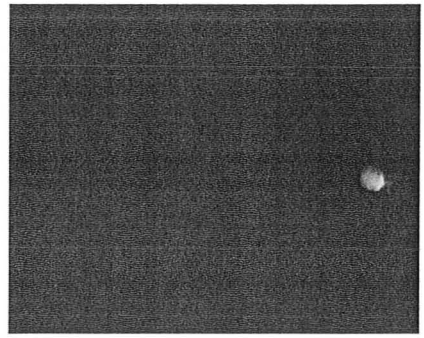

Figure 6. Measurement image at field position 20 mm. Mean gray level intensity is 80.75.

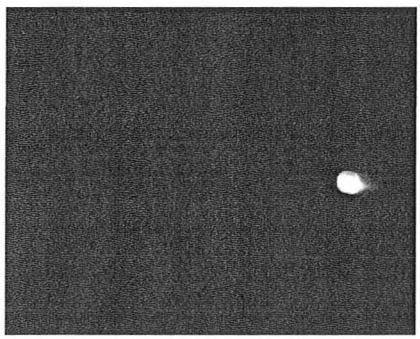

Figure 7. Mask image at field position 25 mm.

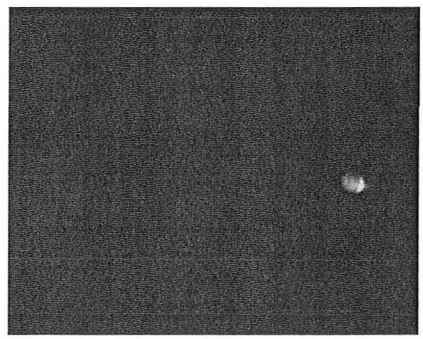

Figure 8. Measurement image at field position 25 mm. Mean gray level intensity is 67.87

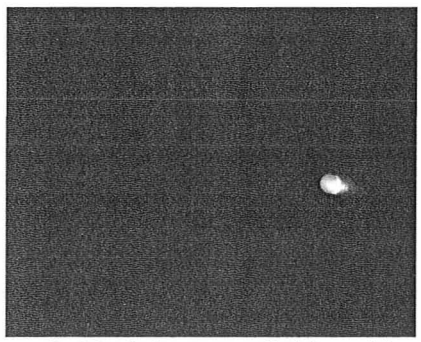

Figure 9. Mask image at field position 32 mm.

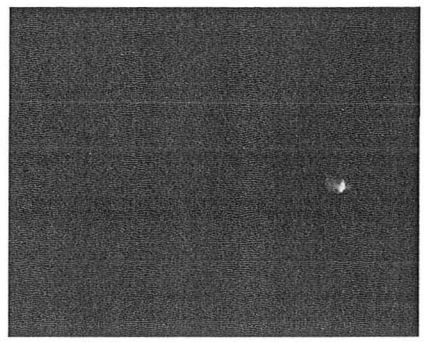

Figure 10. Measurement image at field position 32 mm. Mean gray level intensity is 44.49.

Appendix G
View Synthesis MATLAB™ Code

G.1 Perspective View Synthesis Algorithm

```
%%
% This is the perspective view synthesis implementation
% By Roy Wang
%
%% Initial variables setup
clear all
ndepth=10;
imgcc=13.88;
%sample from 10 object depths: depths z= -2 to z=-11. Coordinate layout is
%z= 13.88 is optical axis, z=0 is capsule sidewall, z= -2 ~ -11 is the
%depth of field of the prototype design.
T00=zeros(3,ndepth);
T00(:,1)=[0;0;-2];
T00(:,2)=[0;0;-3];
T00(:,3)=[0;0;-4];
T00(:,4)=[0;0;-5];
T00(:,5)=[0;0;-6];
T00(:,6)=[0;0;-7];
T00(:,7)=[0;0;-8];
T00(:,8)=[0;0;-9];
T00(:,9)=[0;0;-10];
T00(:,10)=[0;0;-11];
T15=[0; -24.39; 13.88];
% rotational matrice. Object surface is Surf.00. Image surface is Surf.15.
R00=eye(3);
R15=[1 0 0; 0 0 -1; 0 1 0];

%% image alignment block
% find position of each pixel on the raw image (rc image coordinate system)
% in the object space (xyz global coordinate system)
% load the image acquired from the prototype
raw_file=imread('card2.bmp');
[height width]=size(raw_file);
% shifted image center as described in chapter 4
cc=[647,562];
h_offset=height/2-cc(1); %measured in pixels, up is negative
w_offset=width/2-cc(2); %measured in pixels, left is negative
% units in micron,
pos_st_c=13880-5.2*(cc(2)-0.5);
pos_st_r=0+5.2*((height-cc(1))+0.5);
row_pos(1,1)=pos_st_r;
col_pos(1,1)=pos_st_c;
for r=1:height
    for c=1:width
        row_pos(r,1)=pos_st_r-(r-1)*5.2;
        col_pos(1,c)=pos_st_c+(c-1)*5.2;
    end
end
% Generate the uniformly sampled image coordinates across the image space.
% Name the output as xx. This is for the end of the pre-process step
if cc(2)>(width/2)
    % case where image is right shifted. xx range should be based on the left
    % quadrant (M-s + M) search, (M+s + M) start&end. M midpoint == 13880
```

```
    for a=1:width
        if col_pos(a) < (2*13880-15000)
            inds=a;
        end
    end
    xstart=2*13880-col_pos(inds);
    xend=2*13880-col_pos(1);
else
    %case image is left shifted
    for a=1:width
        if col_pos(a) < (15000)
            inds=a;
        end
    end
    xstart=col_pos(inds);
    xend=col_pos(width);
end
xx_raw=xstart:5.2:xend; % units microns. Pixel pitch of 5.2 microns.
xx=xx_raw/1000; % units millimetres

%% Pre-process Step
% First import the ray trace data stored in text files generated by Zemax.
nfield=12; % field points per file
Nf_obj=3;  % 3 files per depth, 36 field points in total per depth.
Start_FOV=-20;
End_FOV=-60;
step=(End_FOV-Start_FOV)/(Nf_obj*nfield);
Fld_t=zeros(ndepth,nfield*Nf_obj);
Obj_t=zeros(ndepth,nfield*Nf_obj);
Img_t=zeros(ndepth,nfield*Nf_obj);
G00x_t=zeros(ndepth,nfield*Nf_obj);
G00y_t=zeros(ndepth,nfield*Nf_obj);
G00z_t=zeros(ndepth,nfield*Nf_obj);
G15x_t=zeros(ndepth,nfield*Nf_obj);
G15y_t=zeros(ndepth,nfield*Nf_obj);
G15z_t=zeros(ndepth,nfield*Nf_obj);
G00x=zeros(1,nfield*Nf_obj);
G00y=zeros(1,nfield*Nf_obj);
G00z=zeros(1,nfield*Nf_obj);
G15x=zeros(1,nfield*Nf_obj);
G15y=zeros(1,nfield*Nf_obj);
G15z=zeros(1,nfield*Nf_obj);
% Sort the raytrace data text files alphabetically, then read them.
directory= 'jul.14.raytrace.results\';
filenames = dir([directory '*.txt']);
num_files = length(filenames);
g=0;
i=1;
for h = 1:ndepth
    for g=0:(Nf_obj-1)
        Fld1=zeros(nfield*Nf_obj,2);
        Obj1=zeros(nfield*Nf_obj,3);
        Img1=zeros(nfield*Nf_obj,3);
        G00=zeros(nfield*Nf_obj,3);
        G15=zeros(nfield*Nf_obj,3);
        filename = [directory filenames(i).name];
        fid = fopen(filename,'rt');
        for a=1:nfield
            ii = textscan(fid, '%s %f %f %f', 1);
            Fld1(a,1)=ii{1,3};
            Fld1(a,2)=ii{1,4};
            jj = textscan(fid, '%s %f %f %f %f', 1);
            Obj1(a,1)=jj{1,3};
```

```
            Obj1(a,2)=jj{1,4};
            Obj1(a,3)=jj{1,5};
            kk = textscan(fid, '%s %f %f %f %f', 1);
            Img1(a,1)=kk{1,3};
            Img1(a,2)=kk{1,4};
            Img1(a,3)=kk{1,5};
            % for reading the carriage return seperating entries
            en=fscanf(fid,'%d');
            L00=transpose(Obj1(a,:));
            L15=transpose(Img1(a,:));
            st_ind=g*nfield; %starting index
            dummy=(R00*L00+T00(:,h))';
            G00x(st_ind+a)=dummy(1);
            G00y(st_ind+a)=dummy(2);
            G00z(st_ind+a)=dummy(3);
            dummy=(R15*L15+T15)';
            G15x(st_ind+a)=dummy(1);
            G15y(st_ind+a)=dummy(2);
            G15z(st_ind+a)=dummy(3);
        end
        fclose(fid);
        i=i+1;
    end
    G00x_t(h,:)=G00x;   % object position output
    G00y_t(h,:)=G00y;
    G00z_t(h,:)=G00z;
    G15x_t(h,:)=G15x;   % image position output
    G15y_t(h,:)=G15y;
    G15z_t(h,:)=G15z;
end
% Reorganize database such that the image positions are uniformly sampled
% using interpolation.
[junk num]=size(xx);
cs=zeros(ndepth, num);
for h=1:ndepth
    a15=G15z_t(h,:)';
    a00=G00y_t(h,:)';
    cs(h,:) = spline(a15,a00,xx);
end
% End of Pre-processing Step

%% Viewpoint Calculation Step
viewpoint15z=zeros(num,1);
for n=1:num
    %find current object depth
    depth_vec=G00z_t(:,1)';
    %fit polynomial of degree 1; linear fit
    coeffs=polyfit(depth_vec,cs(:,n)',1);
    %use euqation of a straight line to backproject the viewpoint;
    % i.e. "y = mx+b"
    viewpoint15z(n)=coeffs(1)*imgcc+coeffs(2);
end
vp_mid=median(viewpoint15z);
% End of Viewpoint Calculation

%% Perspective View Coordinates Generation Step
pfocal=7; %user zoom setting to 7 mm
gamma=180; % azimuth full FOV on raw image, in degrees
azi_orientation=-90*pi/180;
obj_pts=zeros(num,1);
for n=1:num
    xn=-5;
    coeffs=polyfit(depth_vec,cs(:,n)',1);
```

```
    obj_pts(n)=coeffs(1)*xn+coeffs(2);
end
tol=0.02; %viewpoint height drift tolerance in mm
obj_pts1=obj_pts-vp_mid;
figure, plot(xx,obj_pts1,'.')
for n=1:num
    if viewpoint15z(n) < (vp_mid-tol)
        st_bound=n;
    end

    if  viewpoint15z(n) < (vp_mid+tol)
        end_bound=n;
    end
end
st_bound=st_bound+1;
end_bound=end_bound+1;
obj_a= obj_pts1(st_bound);
obj_b= obj_pts1(end_bound);
xx_a=xx(st_bound);
xx_b=xx(end_bound);
%determine perspective image coordinates (grid).
d=0.5; % sampling control, range is 0 to 100%
arc1=gamma*2*pi*(xx_a-imgcc)/180; %short (central) arc
arc2=gamma*2*pi*(xx_b-imgcc)/180; %long (periphery) arc
arc2_pos=gamma*2*pi*(abs(imgcc-row_pos(1)))/(180*1000);
imP_w=floor((arc1+(arc2-arc1)*d)/0.0052); %unit in pixels
a0=imgcc-xn;
y0=obj_a;
x0=obj_b;
h=sqrt(a0^2+y0^2);
beta=atan2(x0,a0);
alpha=(asin(y0/h)-beta)/2;
theta_rot=(alpha+beta)*180/pi;
t=-1*theta_rot*pi/180;
R_rot=[cos(t) -1*sin(t); sin(t) cos(t)];
v1_0=[-1*(pfocal); 0];
v1=R_rot*v1_0;
v2_0=[-1*(pfocal); pfocal*tan(alpha)];
v2=R_rot*v2_0;
v3_0=[-1*(pfocal); -1*pfocal*tan(alpha)];
v3=R_rot*v3_0;
top=sqrt((v1(1)-v2(1))^2+(v1(2)-v2(2))^2);
bot=sqrt((v1(1)-v3(1))^2+(v1(2)-v3(2))^2);
elev_pos=top+bot;
imP_h=floor(elev_pos/0.0052);
% generate view coordinate surface
imP_y=zeros(imP_h,imP_w); %output coordinates prior to rotation
imP_z=zeros(imP_h,imP_w);
imP_x=zeros(imP_h,imP_w);
imP_y1=zeros(imP_h,imP_w); %ouput coordinates of the rotated perspective image
imP_z1=zeros(imP_h,imP_w);
imP_x1=zeros(imP_h,imP_w);
%prep row direction
if mod(imP_h,2)<1 %case even # of pixels in the row direction
    %middle is v2 in VP frame
    cc_r = floor(imP_h/2);
    pos_st_r1=0+0.0052*(imP_h-cc_r+0.5);
else
    cc_r = ceil(imP_h/2);
    pos_st_r1=0+0.0052*(imP_h-cc_r);
end
%prep column direction
if mod(imP_w,2)<1 %case even # of pixels in the row direction
```

```
    %middle is v2 in VP frame
    cc_c = floor(imP_w/2);
    pos_st_c1=0-0.0052*(cc_c-0.5);
else
    cc_c = ceil(imP_w/2);
    pos_st_c1=0-0.0052*cc_c;
end
t=-1*theta_rot*pi/180;
R3x_rot=[1 0 0; 0 cos(t) -1*sin(t); 0 sin(t) cos(t)];
imP_y(1,1)=pos_st_r1;
imP_x(1,1)=pos_st_c1;
for r=1:imP_h
    for c=1:imP_w
        imP_x(r,c)=pos_st_c1+(c-1)*0.0052; %imP plane prior to rotation
        imP_y(r,c)=-1*pfocal;
        imP_z(r,c)=pos_st_r1-(r-1)*0.0052;
        temp=R3x_rot*[imP_x(r,c);imP_y(r,c);imP_z(r,c)];
        imP_x1(r,c)=temp(1); %rotated plane
        imP_y1(r,c)=temp(2);
        imP_z1(r,c)=temp(3);
    end
end
% end of view coordinates generation

%% Object Sample Coordinate Generation Step
% Collision detection algorithm taken from PG196 of "Real Time Collision
% Detection"
P=[0,0,0]; Q=[0,0,60];
de=Q-P; de=de/norm(de);
%start the ray at viewpoint, which is the origin of the current
%local coordinate system (LCS)
A=[0,0,0];
mm=A-P;
dxm=cross(de,mm);
%xn measured in current LCS' y direction at ray trace depth plane 0
r2=13.88-xn;
spd_v=r2^2*dot(de,de);
elev_ptx=zeros(imP_h,imP_w);
elev_pty=zeros(imP_h,imP_w);
elev_ptz=zeros(imP_h,imP_w);
imP_rad_pt=zeros(imP_h,imP_w);
obj_rad_pt=zeros(imP_h,imP_w);
for r=1:imP_h
    for c=1:imP_w
    B=[imP_x1(r,c),imP_y1(r,c),imP_z1(r,c)];
    nn=B-A;
    dxn=cross(de,nn);
    ad=dot(dxn,dxn);
    bd=dot(dxm,dxn);
    cd=dot(dxm,dxm)-spd_v;
    t_roots=roots([ad 2*bd cd]);
    t_take=max(t_roots);
    elev_pt=mm+t_take*nn;
    elev_ptx(r,c)=elev_pt(1);
    elev_pty(r,c)=elev_pt(2);
    elev_ptz(r,c)=elev_pt(3);
    imP_rad_pt(r,c)=sqrt(imP_x1(r,c)^2+imP_y1(r,c)^2);
    obj_rad_pt(r,c)=sqrt(elev_pt(1)^2+elev_pt(2)^2);
    end
end
wx = reshape(elev_ptx,1,imP_h*imP_w); % output object sample coordinates
wy = reshape(elev_pty,1,imP_h*imP_w);
wz = reshape(elev_ptz,1,imP_h*imP_w);
```

```
%% Object-Image Mapping Step
[junk num]=size(xx);
imP_rad_coord=zeros(imP_h, imP_w);
obj_pts1;
st_bound;
end_bound;
% use raytrace database on the object sample x-y-z coordinates to get the
% corresponding image radius
for h1=1:imP_h
    imP_rad_coord(h1,:) = spline(obj_pts1,xx,elev_ptz(h1,:)); %inverse of ray trace
readout processing
end
% Compute image x-y position from image radius
azi_phi=zeros(imP_h,imP_w);
imR_x=zeros(imP_h,imP_w);   imR_x1=zeros(imP_h,imP_w);
imR_y=zeros(imP_h,imP_w);   imR_y1=zeros(imP_h,imP_w);
for r=1:imP_h
    for c=1:imP_w
        xpart=elev_ptx(r,c);
        ypart=-1*elev_pty(r,c);
        azi_phi(r,c)=atan2(ypart,xpart)+azi_orientation;
        imR_x(r,c)=(imP_rad_coord(r,c)-imgcc)*cos(azi_phi(r,c));
        imR_y(r,c)=(imP_rad_coord(r,c)-imgcc)*sin(azi_phi(r,c));

        % output x-y coordinate
        imR_x1(r,c)=(imP_rad_coord(r,c)-imgcc)*cos(azi_phi(r,c)-azi_orientation);
        imR_y1(r,c)=(imP_rad_coord(r,c)-imgcc)*sin(azi_phi(r,c)-azi_orientation);
    end
end
% Compute the image space r-c coordinates from object space x-y coordinates
cc=[647,562];
height_pos=height*0.0052;
width_pos=width*0.0052;
ck0=[height_pos/2 -1*width_pos/2]; %(r,c) format, debug
ck=[cc(1)*0.0052 -1*cc(2)*0.0052]; %(r,c) format
imR_c=(imR_x-ck(2))/0.0052;
imR_c=floor(imR_c);
imR_r=(-1*(imR_y-ck(1)))/0.0052;
imR_r=floor(imR_r);
% Synthesize the perspective image using the acquired raw image at the r-c
% coordinates
imP_final=zeros(imP_h,imP_w);
imP_final=cast(imP_final,'uint8');
imP_finalr=zeros(imP_h,imP_w);
imP_finalc=zeros(imP_h,imP_w);
for r=1:imP_h
    for c=1:imP_w
        rv=imR_r(r,c);
        cv=imR_c(r,c);
        imP_finalr(r,c)=rv;
        imP_finalc(r,c)=cv;
        if (rv> height) || (rv<1) || (cv >width) || (cv<1)
            imP_final(r,c)=0;
        else
            imP_final(r,c)=raw_file(rv,cv);
        end
    end
end
figure, imshow(imP_final)
title('perspective view')
```

G.2 Estimated Orthographic View Synthesis Algorithm

```
%%
% This is the estimated orthographic view synthesis implementation
% By Roy Wang
%
%% Initial variables setup
clear all
ndepth=10;
imgcc=13.88;
%sample from 10 object depths: depths z= -2 to z=-11. Coordinate layout is
%z= 13.88 is optical axis, z=0 is capsule sidewall, z= -2 ~ -11 is the
%depth of field of the prototype design.
T00=zeros(3,ndepth);
T00(:,1)=[0;0;-2];
T00(:,2)=[0;0;-3];
T00(:,3)=[0;0;-4];
T00(:,4)=[0;0;-5];
T00(:,5)=[0;0;-6];
T00(:,6)=[0;0;-7];
T00(:,7)=[0;0;-8];
T00(:,8)=[0;0;-9];
T00(:,9)=[0;0;-10];
T00(:,10)=[0;0;-11];
T15=[0; -24.39; 13.88];
% rotational matrice. Object surface is Surf.00. Image surface is Surf.15.
R00=eye(3);
R15=[1 0 0; 0 0 -1; 0 1 0];

% Align image
% find position of each pixel on the raw image (rc image coordinate system)
% in the object space (xyz global coordinate system)
% load the image acquired from the prototype
raw_file=imread('0.51p.azi345.bmp');
%raw_file=imread('card2.bmp');
[height width]=size(raw_file);
% shifted image center as described in chapter 4
cc=[647,562];
h_offset=height/2-cc(1); %measured in pixels, up is negative
w_offset=width/2-cc(2); %measured in pixels, left is negative
% units in micron
pos_st_c=13880-5.2*(cc(2)-0.5);
pos_st_r=0+5.2*((height-cc(1))+0.5);
row_pos(1,1)=pos_st_r;
col_pos(1,1)=pos_st_c;
for r=1:height
    for c=1:width
        row_pos(r,1)=pos_st_r-(r-1)*5.2;
        col_pos(1,c)=pos_st_c+(c-1)*5.2;
    end
end
% Generate the uniformly sampled image coordinates across the image space.
% Name the output as xx. This is for the end of the pre-process step
if cc(2)>(width/2)
    % case where image is right shifted. xx range should be based on the left
    % quadrant (M-s + M) search, (M+s + M) start&end. M midpoint == 13880
    for a=1:width
        if col_pos(a) < (2*13880-15000)
            inds=a;
        end
    end
    xstart=2*13880-col_pos(inds);
    xend=2*13880-col_pos(1);
```

```
else
    %case image is left shifted
    for a=1:width
        if col_pos(a) < (15000)
            inds=a;
        end
    end
    xstart=col_pos(inds);
    xend=col_pos(width);
end

xx=13:0.028:30; % units millimeters.
%Set the pixel pitch of the synthesized view to be 28 microns

%% Pre-process Step
% First import the ray trace data stored in text files generated by Zemax.
nfield=12; % field points per file
Nf_obj=3; % 3 files per depth, 36 field points in total per depth.
Start_FOV=-20;
End_FOV=-60;
step=(End_FOV-Start_FOV)/(Nf_obj*nfield);
FLD_pos=zeros(Nf_obj,nfield);
for u=1:Nf_obj

FLD_pos(u,:)=(step*(u-1)*nfield+Start_FOV):step:(Start_FOV+step*u*nfield-step);
end
Fld_t=zeros(ndepth,nfield*Nf_obj);
Obj_t=zeros(ndepth,nfield*Nf_obj);
Img_t=zeros(ndepth,nfield*Nf_obj);
G00x_t=zeros(ndepth,nfield*Nf_obj);
G00y_t=zeros(ndepth,nfield*Nf_obj);
G00z_t=zeros(ndepth,nfield*Nf_obj);
G15x_t=zeros(ndepth,nfield*Nf_obj);
G15y_t=zeros(ndepth,nfield*Nf_obj);
G15z_t=zeros(ndepth,nfield*Nf_obj);
G00x=zeros(1,nfield*Nf_obj);
G00y=zeros(1,nfield*Nf_obj);
G00z=zeros(1,nfield*Nf_obj);
G15x=zeros(1,nfield*Nf_obj);
G15y=zeros(1,nfield*Nf_obj);
G15z=zeros(1,nfield*Nf_obj);
% Sort the raytrace data text files alphabetically, then read them.
directory= 'jul.14.raytrace.results\';
filenames = dir([directory '*.txt']);
num_files = length(filenames);
g=0;
i=1;
for h = 1:ndepth
    for g=0:(Nf_obj-1)
        Fld1=zeros(nfield*Nf_obj,2);
        Obj1=zeros(nfield*Nf_obj,3);
        Img1=zeros(nfield*Nf_obj,3);
        G00=zeros(nfield*Nf_obj,3);
        G15=zeros(nfield*Nf_obj,3);
        filename = [directory filenames(i).name];
        fid = fopen(filename,'rt');
        for a=1:nfield
            ii = textscan(fid, '%s %f %f %f', 1);
            Fld1(a,1)=ii{1,3};
            Fld1(a,2)=ii{1,4};
            jj = textscan(fid, '%s %f %f %f %f', 1);
            Obj1(a,1)=jj{1,3};
            Obj1(a,2)=jj{1,4};
```

```
            Obj1(a,3)=jj{1,5};
            kk = textscan(fid, '%s %f %f %f %f', 1);
            Img1(a,1)=kk{1,3};
            Img1(a,2)=kk{1,4};
            Img1(a,3)=kk{1,5};
             % for reading the carriage return seperating entries
            en=fscanf(fid,'%d');
            L00=transpose(Obj1(a,:));
            L15=transpose(Img1(a,:));
            st_ind=g*nfield; %starting index
            dummy=(R00*L00+T00(:,h))';
            G00x(st_ind+a)=dummy(1);
            G00y(st_ind+a)=dummy(2);
            G00z(st_ind+a)=dummy(3);
            dummy=(R15*L15+T15)';
            G15x(st_ind+a)=dummy(1);
            G15y(st_ind+a)=dummy(2);
            G15z(st_ind+a)=dummy(3);
        end
        fclose(fid);
        i=i+1;
    end
    G00x_t(h,:)=G00x; % object position output
    G00y_t(h,:)=G00y;
    G00z_t(h,:)=G00z;
    G15x_t(h,:)=G15x; % image position output
    G15y_t(h,:)=G15y;
    G15z_t(h,:)=G15z;
end
% Reorganize database such that the image positions are uniformly sampled
% using interpolation.
[junk num]=size(xx);
%depth set to the 4th entry, which has the object depth of 19.88 mm from
%the optical axis
depth= 4;
b15=G15z_t(depth,:)';
b00=G00y_t(depth,:)';
cs=zeros(num);
csb = spline(b00,b15,xx);
[junk imP_h]=size(csb);
azi_orientation=-90*pi/180;

%% Object Sample Coordinate Generation Step
azi_start=0;
azi_end=180;
elev_start=0.25;
elev_end=0.75;
orientation=0;
% The object is fixed by the annular optical mounts with diameter 40 mm
radius=20; % units mm
dummy=azi_start:0.028:azi_end;
[junk imP_w]=size(dummy);
xypts=zeros(2,imP_w);
d_theta=dummy*pi/180;
for a32=1:imP_w
    xypts(1,a32)=radius*cos(d_theta(a32));
    xypts(2,a32)=radius*sin(d_theta(a32));
end
f=orientation*pi/180;
RrR=[cos(f) -1*sin(f); sin(f) cos(f)];
xypts2=RrR*xypts;

%% Object-Image Mapping Step
```

```
[junk num]=size(xx);
imP_rad_coord=zeros(imP_h, imP_w);
for h1=1:imP_w
    imP_rad_coord(:,h1) = csb;
end
azi_phi=zeros(imP_h,imP_w);
azi_phi_d=zeros(imP_h,imP_w);
imR_x=zeros(imP_h,imP_w);    imR_x1=zeros(imP_h,imP_w);
imR_y=zeros(imP_h,imP_w);    imR_y1=zeros(imP_h,imP_w);
for r=1:imP_h
    for c=1:imP_w
        xpart=xypts2(1,c);
        ypart=xypts2(2,c);
        azi_phi(r,c)=atan2(ypart,xpart)+azi_orientation;
        azi_phi_d(r,c)=(atan2(ypart,xpart)+azi_orientation)*180/pi;
        imR_x(r,c)=(imP_rad_coord(r,c)-imgcc)*cos(azi_phi(r,c));
        imR_y(r,c)=(imP_rad_coord(r,c)-imgcc)*sin(azi_phi(r,c));
        imR_x1(r,c)=(imP_rad_coord(r,c)-imgcc)*cos(azi_phi(r,c)-azi_orientation);
        imR_y1(r,c)=(imP_rad_coord(r,c)-imgcc)*sin(azi_phi(r,c)-azi_orientation);
    end
end
cc=[647,562];
imR_c=imR_x/0.0052+cc(1);
imR_c=floor(imR_c);
imR_r=imR_y/0.0052+cc(2);
imR_r=floor(imR_r);

%% construct intensity values of imP from raw image
imP_final=zeros(imP_h,imP_w);
imP_final=cast(imP_final,'uint8');
imP_finalr=zeros(imP_h,imP_w);
imP_finalc=zeros(imP_h,imP_w);
for r=1:imP_h
    for c=1:imP_w
        rv=imR_r(r,c);
        cv=imR_c(r,c);
        imP_finalr(r,c)=rv;
        imP_finalc(r,c)=cv;
        if (rv> height) || (rv<1) || (cv >width) || (cv<1)
            imP_final(r,c)=0;
        else
            imP_final(r,c)=raw_file(rv,cv);
        end
    end
end
figure, imshow(imP_final)
title('Estimated Orthographic View')
```